

THE FLORIDA STATE UNIVERSITY  
COLLEGE OF ARTS AND SCIENCES

MEASUREMENT OF POLARIZATION OBSERVABLES IN  $\vec{\gamma}p \rightarrow p\pi^+\pi^-$  USING  
CIRCULAR BEAM AND LONGITUDINAL TARGET POLARIZATION AND  
THE CLAS SPECTROMETER AT JEFFERSON LABORATORY

By

SUNGKYUN PARK

A Dissertation submitted to the  
Department of Physics  
in partial fulfillment of the  
requirements for the degree of  
Doctor of Philosophy

Degree Awarded:  
Summer Semester, 2013

Sungkyun Park defended this dissertation on July 1, 2013.

The members of the supervisory committee were:

Volker Crede  
Professor Directing Thesis

Tomasz Plewa  
University Representative

Paul Eugenio  
Committee Member

Simon Capstick  
Committee Member

Todd Adams  
Committee Member

The Graduate School has verified and approved the above-named committee members, and certifies that the dissertation has been approved in accordance with the university requirements.

To my parents, Yangsoon Kang and Youngsik Park, and my sister, Seoyeon Park,  
who supported me so well during this process.

# ACKNOWLEDGMENTS

The first person I would like to thank is my advisor, Dr. Volker Credé for all the great advices and supports throughout my time here at Florida State University. Nothing would have been possible without his guidance. I would also like to thank the former and current people in Hadronic Nuclear Physics Group, Dr. Paul Eugenio, Dr. Alexander Ostrovidov, Dr. Charles Hanretty, Dr. Mukesh Saini, Dr. Andrew Wilson, Nathan Sparks, Priyashree Roy, Aristeidis Tsaris, Hussein Al Ghoul, Christopher Pederson. I thank Dr. Paul Eugenio to introduce me to my advisor and to help familiarize me with Jefferson Laboratory. I thank Dr. Charles Hanretty to help me build up the kinematic fitting part and Dr. Andrew Wilson to help me develop the Q-factor method in my analysis code. I wish to thank Dr. Mukesh Saini for his kindness and friendship.

Next, I would like to thank the people in FROST working group, Dr. Eugene Pasyuk, Dr. Mike Dugger, Dr. Steffen Strauch, Dr. Franz Klein, Dr. Barry Ritchie, Dr. Patrick Collins, and Natalie Walford, etc. I thank Dr. Eugene Pasyuk for his tireless work helping more. From the very beginning of the FROST experiment, Dr. Eugene Pasyuk was always there to answer my questions about experiments. The advice of Dr. Mike Dugger is very useful to understand the detailed part of the FROST experiment. I also thank Dr. Steffen Strauch and Dr. Franz Klein to give the useful advices during the FROST meeting. I would like to thank my committee members for their work in reading and considering this thesis, Dr. Simon Capstick, Dr. Todd Adams, Dr. Tomasz Plewa.

Lastly but most importantly, I would like to thank my parents, Yangsoon Kang and Youngsik Park, and my sister, Seoyeon Park. They give me the source to go head to head without giving up in my life.

# TABLE OF CONTENTS

List of Tables . . . . .	viii
List of Figures . . . . .	x
Abstract . . . . .	xxvi
Zusammenfassung . . . . .	xxviii
<b>1 Introduction and Overview</b>	<b>1</b>
1.1 Quark Model . . . . .	1
1.2 Quantum Chromodynamics (QCD) . . . . .	4
1.3 Nucleon Resonances . . . . .	5
1.3.1 Constituent Quark Models . . . . .	7
1.3.2 Missing Resonance Problem . . . . .	8
1.3.3 Polarization Observables . . . . .	14
<b>2 FROST Experiment</b>	<b>16</b>
2.1 CEBAF Electron Accelerator . . . . .	17
2.2 Broad-Range Photon Tagging Facility . . . . .	18
2.3 CLAS Spectrometer . . . . .	21
2.3.1 Start Counter (ST) . . . . .	22
2.3.2 Torus Magnet . . . . .	23
2.3.3 Drift Chamber (DC) . . . . .	24
2.3.4 Time of Flight Counters (TOF) . . . . .	26
2.3.5 Electromagnetic Calorimeters (EC) . . . . .	26
2.4 Frozen Spin Target (FROST) . . . . .	27
<b>3 Data Reconstruction</b>	<b>33</b>
3.1 Reconstruction . . . . .	34
3.2 Calibration . . . . .	35
<b>4 Data Selection</b>	<b>42</b>
4.1 Pre-Event Selection . . . . .	42
4.2 Reaction Channel and General Event Selection . . . . .	44
4.3 Photon and Particle Identification . . . . .	45
4.3.1 Photon Selection . . . . .	45
4.3.2 Proton and Pion Selection . . . . .	46

4.4	Kinematic Fitting . . . . .	48
4.4.1	Confidence Level . . . . .	48
4.4.2	Pulls . . . . .	49
4.5	Corrections . . . . .	50
4.5.1	Energy Loss Correction (ELoss) . . . . .	50
4.5.2	Photon Beam Correction . . . . .	51
4.5.3	Momentum Correction . . . . .	54
4.6	Basic Cuts . . . . .	58
4.6.1	Vertex Cut . . . . .	58
4.6.2	Accidental Cuts . . . . .	59
4.6.3	Confidence Level Cut . . . . .	60
4.6.4	Removing Bad Time-of-flight Paddles . . . . .	61
4.6.5	Event Distributions after Applying All Cuts and Corrections . . . . .	63
4.7	Beam and Target Polarization . . . . .	65
4.7.1	Photon Beam Polarization . . . . .	65
4.7.2	Beam Charge Asymmetry . . . . .	69
4.7.3	Target Polarization . . . . .	70
4.7.4	Confirm the Information of the Beam and Target Polarization . . . . .	73
4.8	Normalization Factor . . . . .	75
4.9	Dilution Factor . . . . .	78
4.9.1	Phase Space Scale Factor . . . . .	80
4.9.2	Q-factor Method . . . . .	81
<b>5</b>	<b>DATA Analysis</b>	<b>91</b>
5.1	General Data Analysis . . . . .	91
5.1.1	Binning and Definition of Angles . . . . .	91
5.1.2	Observables with Circular Beam and Longitudinal Target Polarization . . . . .	93
5.2	Polarization observable $\mathbf{I}^\odot$ . . . . .	93
5.2.1	Beam Helicity Asymmetry . . . . .	93
5.2.2	Average Beam Asymmetry . . . . .	97
5.2.3	Comparison . . . . .	100
5.3	Polarization Observable $\mathbf{P}_z$ . . . . .	102
5.3.1	Target Asymmetry . . . . .	102
5.3.2	Average Target Asymmetry . . . . .	104
5.3.3	Comparison . . . . .	107
5.4	Polarization Observable $\mathbf{P}_z^\odot$ . . . . .	108
5.4.1	Helicity Difference . . . . .	108
5.4.2	Average Helicity Difference . . . . .	109
5.4.3	Comparison . . . . .	112
5.5	Systematic Uncertainties . . . . .	113

<b>6</b>	<b>Conclusions</b>	<b>114</b>
6.1	Systematic check of the Symmetry of the Observables . . . . .	114
6.2	Comparison of the Polarization Observables with Models . . . . .	118
<b>Appendix A Beam and Target Polarization</b>		<b>123</b>
A.1	Beam and Target Polarization . . . . .	123
<b>Appendix B Beam Charge Asymmetry</b>		<b>125</b>
B.1	Beam Charge Asymmetry . . . . .	125
<b>Appendix C Background Effect in the Butanol Target</b>		<b>127</b>
C.1	Background Effect in the Butanol Target . . . . .	127
<b>Appendix D Error Propagation</b>		<b>131</b>
D.1	Error Propagation . . . . .	131
<b>Appendix E Average Polarization Observables</b>		<b>134</b>
E.1	Average Polarization Observable $\mathbf{I}^\odot$ . . . . .	134
E.1.1	Average Polarization Observable $\mathbf{I}^\odot$ for the Butanol Data . . .	134
E.1.2	Average Polarization Observable $\mathbf{I}^\odot$ for the Butanol Data Weighted by Q-factor . . . . .	139
E.2	Average Polarization Observable $\mathbf{P}_z$ . . . . .	144
E.2.1	Average Polarization Observable $\mathbf{P}_z$ for the Butanol Data Weighted by Q-factor . . . . .	144
E.3	Average Polarization Observable $\mathbf{P}_z^\odot$ . . . . .	149
E.3.1	Average Polarization Observable $\mathbf{P}_z^\odot$ for the Butanol Data Weighted by Q-factor . . . . .	149
Bibliography . . . . .		154
Biographical Sketch . . . . .		157

# LIST OF TABLES

1.1	Quark classification according to the key properties of the six quarks, such as total angular momentum, $J$ , the electric charge, $Q$ (in units of electron charge $e$ ), and isospin ( $I_3$ as a flavor quantum number). . . . .	3
2.1	Examples of materials for DNP targets. . . . .	28
3.1	Names, sizes and directories of output files containing reconstructed events.	35
3.2	The purpose of each calibration. . . . .	36
4.1	The dataset of the g9a experiment classified according to a wide variety of characteristics, such as the target polarization, the beam polarization, the electron beam energy, dates, and run numbers. The data with the circularly-polarized beam is grouped in periods with similar run conditions. . . . .	43
4.2	Identification of the $\gamma p \rightarrow p\pi^+\pi^-$ channel using different topologies. Reconstructed particles are identified by the <b>PID</b> information from the <b>GPID</b> bank. . . . .	44
4.3	The parameters used in the FSU photon beam correction. . . . .	53
4.4	The momentum binning of the proton and pion for the momentum correction and the correction factors applied in this analysis. . . . .	55
4.5	Means and $\sigma$ 's of pull distributions made to integrate with the momentum bins referenced in Table 4.4 after applying all corrections. . . . .	56
4.6	The information of the bad time-of-flight paddles. . . . .	62
4.7	Møller measurements of the electron-beam polarization. . . . .	66
4.8	The average degrees of circular polarization in FROST g9a. . . . .	68
4.9	The mean and error of the beam-charge asymmetries, $\bar{a}_c$ , calculated in each period. . . . .	70

4.10	The definition of the direction of the target polarization used in the g9a experiment. The first plus sign in L++ means the direction of the holding magnet and the second indicates the direction of the proton polarization. . . . .	71
4.11	The direction of the target polarization before and after correcting initial inconsistencies. After the correction, the direction of the target polarization in period 4 and 5 is reversed. The arrow $\Rightarrow$ ( $\Leftarrow$ ) means the target polarization is parallel (anti-parallel) to the beam direction. . .	71
4.12	Average target polarization with the statistical and systematic error per period and the ratio between the different target polarizations. This ratio of the different target polarization is used in Equation 5.12. . . .	72
4.13	Helicity signal from the TGBI-bank latch1 for the two half-wave-plate positions. In the table, the sign $+(-)$ means the beam polarization is parallel (anti-parallel) to the beam direction. . . . .	73
4.14	The condition of the beam and target polarization of each period used in this analysis. . . . .	74
4.15	The normalization factor used in combination-32, combination-45, and combination-67. . . . .	77
4.16	The kinematic variables $\Gamma_i$ and their ranges $\Delta_i$ used in the Q-factor method. . . . .	82
5.1	The dataset used to calculate the average observable $\mathbf{I}^\odot$ . . . . .	98
5.2	The dataset used to calculate the average observable $\mathbf{P}_z$ . . . . .	104
5.3	The dataset used to calculate the average observable $\mathbf{P}_z^\odot$ . . . . .	109
5.4	Systematic contributions to the uncertainties in polarization observables. There is the list of systematic errors studied for publishing. . .	113

# LIST OF FIGURES

1.1	Classification of baryons and mesons according to charge and the strangeness. Charge is determined by the diagonal line and strangeness is determined by the horizontal line. . . . .	2
1.2	Artist view of the interior of a proton. The three valence quarks are surrounded by quark-antiquark pairs and gluons that form the main fraction of the mass of the proton. . . . .	4
1.3	Summary of measurements of the QCD coupling constant $\alpha_s$ as a function of the exchanged gluon momentum $Q$ . The curves are QCD predictions for the combined world average value of $\alpha_s$ . . . . .	6
1.4	The proton is composed of three constituent quarks. Current quarks are surrounded by a cloud of virtual quarks and gluons. Points of red, blue, and green colors are virtual quarks; the others are gluons. . . . .	7
1.5	Schematic representation of the nucleon, $P_{11}(939)$ , and the three lowest lying nucleon resonances in a simplified constituent quark model. The convention for naming the baryon resonances in this figure is from Equation 1.1. . . . .	8
1.6	The spectrum of $N^*$ resonances using one-gluon exchange for short-range interaction. The left side of each column shows the resonances predicted by the model, while the corresponding right side with the blocks represents experimental measurements. The height of the blocks illustrates the uncertainty in the mass measurement. The number of *'s denotes the ranking of the state according to the PDG. Resonances with four stars are well-established, those with three stars have solid evidence supporting their existence, states with two stars have little evidence, and excited states with one star have even less supporting evidence. . . . .	9
1.7	A model of the baryon used in CQMs. In this model, the baryon is treated as an object with two independent oscillators, $\rho$ and $\lambda$ . . . . .	10
1.8	Total cross section for $\gamma p$ reaction with contributions of individual channels. . . . .	11

1.9	(a) Total photoabsorption and partial cross sections for photoproduction off the proton. (b) Second resonance region in logarithmic scale. . . . .	12
1.10	Nucleon excitation spectrum showing the lowest lying resonances. The black arrows show the mesonic decay of these resonances with width proportional to the branching ratio. The shaded colored areas represent the widths of the resonances. . . . .	13
2.1	An aerial view of the accelerator and the three experimental halls at Jefferson Lab. The Continuous Electron Beam Accelerator Facility (CEBAF) is the racetrack accelerator, and the three mounds located at the bottom of the photograph are the three experimental halls: Hall A, Hall B, and Hall C (left to right). . . . .	16
2.2	Schematic drawing of CEBAF and the three experimental halls. Included are, clockwise from the top, a module in the linac, a steering magnet, and a part of the RF separator. . . . .	17
2.3	A diagram of an RF cavity with the charge gradient produced. . . . .	18
2.4	Overall geometry of the bremsstrahlung photon tagging system. The electrons, which enter from the left, are scattered off the radiator and then are "tagged" while the photons go downstream through the collimator (not shown in this picture). The dashed lines indicate the trajectories made by recoil electrons with various fractional energies. The two planes of the scintillator hodoscope, the E- and T-planes, are shown geometrically. . . . .	19
2.5	Side view schematic of the Tagger and the CLAS spectrometer in Hall B.	20
2.6	Schematic of the CLAS spectrometer. This spectrometer, approximately 8 m in diameter, is housed in experimental Hall B at Jefferson Lab. . . . .	21
2.7	A CAD drawing of the Start Counter used for the g9 experiment. . . . .	22
2.8	(a) Contours of the constant absolute magnetic field for the CLAS toroid magnet in the midplane between two coils and (b) the toroidal magnetic field as seen from a plane centered on the target. The length of the lines indicates the field strength at that point. . . . .	23
2.9	(a) Horizontal cut through the CLAS spectrometer showing two charged particles traveling through the DC in opposite sectors. (b) Vertical cut through the DC transverse to the beam line at the target location. . . . .	24

2.10	The hexagonal Drift Chamber of R3 chamber, showing the layout of its two superlayers. The highlighted drift cells indicate a passing charged particle. The upper right corner shows the edge of the Cherenkov counters. . . . .	25
2.11	(a) A picture of the Time-of-Flight counters revealed when CLAS is opened. TOF can be seen to the far left. The part of the CLAS spectrometer revealed is the region 3 of the Drift Chamber. (b) A diagram of a ToF sector, showing the scintillation counters arranged in four panels and perpendicular to the beam line. At both ends of each paddle are a light guide and a PMT. . . . .	26
2.12	Enlarged diagram of one of the six CLAS electromagnetic calorimeter modules. . . . .	27
2.13	The polarization of an electron and proton by brute force. . . . .	28
2.14	(a) Two phases of $^3\text{He}/^4\text{He}$ mixture in the mixing chamber. (b) An illustration of the operation of the dilution refrigerator for FROST. . .	29
2.15	(a) The illustration of the frozen spin target with 1K pot and 4K pot. The actual butanol target is located on the target material part. (b) A cross section of the target area of FROST: A) primary heat exchanger, B) 1K heat shield, C) holding coil, D) 20 K heat shield, E) outer vacuum can (Rohacell extension), F) polyethylene target, G) carbon target, H) butanol target, J) target insert K) mixing chamber, L) microwave waveguide, M) Kapton coldseal. (c) The floor plan of the frozen spin target with the polarizing magnet. . . . .	30
2.16	(a) Butanol beads formed by supercooling of the liquid nitrogen. (b) Butanol beads placed in the target cup (the green area). . . . .	31
2.17	There are, clockwise from the top, the longitudinal holding magnet with a field strength of approximately 0.56 T, the transverse holding magnet with approximately 0.52 T, and the polarizing magnet with 5.0 T. (b) Magnetic field vs. spin relaxation time for butanol. . . . .	32
2.18	The polarization schedule for the frozen spin target. . . . .	32
3.1	Number of events for the g9a experiment, which utilizes a variety of electron beam energies. The numbers on the top show the electron beam energies in [GeV] used in the g9a experiment. LC indicates longitudinal target polarization and circular beam polarization, and LL indicates longitudinal target polarization and linear beam polarization. . . . .	33
3.2	Schematic view of regions and superlayers in CLAS DC. . . . .	37

3.3	Typical arrangement of electrodes in a drift-chamber cell. . . . .	38
3.4	Left: Portion of a Region 3 sector showing the layout of its two superlayers. A passing charged particle is indicated by the highlighted drift cells that have fired. Right: Schematic diagram showing a charged particle track. The individual hexagonal drift cells are identified by a dashed line around the perimeter of each. . . . .	38
3.5	(a) Drift time measured in superlayer 1 of sector 1. (b) Relation between fitted DOCA and drift times in superlayer 1 of sector 1. . . . .	39
3.6	(a) Fitting the plot between fitted <i>DOCA</i> and drift times in superlayer 1 of sector 1, as shown in Figure 3.5 (b), to calculate the drift velocity function in the "dc3" software package. (b) Relation between drift times and the residual in superlayer 1 of sector 1. . . . .	40
3.7	Average DC residuals before starting (the top) and after finishing (the bottom) DC calibration in the g9a dataset. . . . .	41
4.1	Coincidence-time distribution of tagged photons for the raw data (dotted histogram) and after applying all $\gamma p \rightarrow p\pi^+\pi^-$ selection cuts (solid histogram). Events of the center bins filled in black indicate the candidates for the final selection. . . . .	46
4.2	Distribution of $\Delta\beta = \beta_c - \beta_m$ made from protons (a) and pions (plus and minus) (b), where $\beta_c$ is calculated based on the particle's assumed mass. Events of the center peak filled in red are selected after applying the $ \beta_c - \beta_m  \leq 3\sigma$ cut. . . . .	47
4.3	(a) Measured $\beta_m$ versus the measured momentum for the double-pion photoproduction events read from GPID on a logarithmic color scale. Notice the stripes for pions at the top, followed by protons. (b) Measured $\beta_m$ versus the measured momentum after applying the cut based on the difference $\Delta\beta = \beta_c - \beta_m$ . Events with pions and protons are clearly distinguished after applying the cut. . . . .	48
4.4	Example of fit results coming from a fit to a fully reconstructed $\gamma p \rightarrow p\pi^+\pi^-$ final state. (a) Shows an example of a confidence level distribution. A confidence level distribution (working with real data) peaks toward zero but flattens out toward one. (b) Shows an example of a pull distribution (the photon energy pull). Ideally, a pull distribution has the Gaussian distribution in shape around the origin with a mean ( $\mu$ ) of zero and a sigma ( $\sigma$ ) of one. . . . .	50

4.5	Missing-mass distributions before (dotted blue histogram) and after (solid red histogram) applying energy-loss-correction made in Topology $\gamma p \rightarrow p\pi^+(\pi^-)$ from the butanol target (a) and carbon target (b). The vertical lines denote the mass of the $\pi^-$ . The energy-loss correction makes the peak shape noticeably narrower and the peak position is also corrected. Since, however, the peak position is not positioned at the $\pi^-$ mass exactly, another correction is needed in the butanol target. . . .	51
4.6	The photon beam correction on $E_e = 1.645$ GeV dataset at ASU (a) and $E_e = 2.478$ GeV dataset (b). $E_{\gamma TRUE}$ is the photon energy returned by the kinematic fitting and $E_{\gamma measured}$ is the measured photon energy from the data. . . . .	52
4.7	The difference between the calculated photon energy $E_{cal.\gamma}$ and measured photon energy $E_{mea.\gamma}$ after applying the ASU photon beam correction. . . . .	53
4.8	The difference between the calculated photon energy $E_{cal.\gamma}$ and measured photon energy $E_{mea.\gamma}$ , after applying energy-loss correction and all photon-beam correction. This figure is made for the topology $\gamma p \rightarrow p\pi^+\pi^-$ with no missing mass and the data from the butanol target. On the $x$ -axis, $E_{e-}$ is the electron beam energy used in the g9a experiment. As the tagging system of the Hall-B can tag photon energies from 20% to 95% of the incident electron beam energy, the data on the $x$ -axis covers a range from 0.2 to 0.95. . . . .	54
4.9	Examples of momentum distributions of final-state particles in the g9a dataset. . . . .	55
4.10	Pull and confidence-level distributions after applying all corrections in the butanol target. The green dotted line is made from the raw data. After the energy-loss correction is applied to the raw data, the red dashed line is obtained. One after another, photon-beam correction and momentum-correction are applied on the dataset and the blue solid histograms are obtained. These pulls and the confidence-level distribution are from Topology $\gamma p \rightarrow p\pi^+\pi^-$ ( ) with a 5% confidence level cut applied. The lines represent fitting the data to a Gaussian function, the mean and $\sigma$ of which can be found in Table 4.5. . . . .	57

4.11	(a) The vertex $z$ -position (axis along the beam line) of all reconstructed particles showing the positions of the three kinds of targets. The red line denotes the data with all $p\pi^+\pi^-$ events. The blue line denotes events after applying basic cuts. The carbon data with all $p\pi^+\pi^-$ events is fitted with a Breit-Wigner to check the distribution of carbon events. (b) A comparison of the $z$ -vertex reconstruction from the MVRT and TBTR bank is shown on a log- $z$ color scale. Lines indicating the target cut regions are shown in the dashed red boxes. . . . .	58
4.12	The distributions of the variable NGRF and TAGRID used in the g9a experiment. . . . .	60
4.13	(a) The distribution of confidence level values for the topology $\gamma p \rightarrow p\pi^+(\pi^-)$ generated from the butanol target. The confidence-level cut selects the events whose confidence level is greater than 0.05, as shown in the colored region. (b) The missing mass distribution made from the same topology and target as in Figure 4.13 (a). The black dashed line is made after applying all cuts and corrections without the confidence-level cut and the blue solid histogram indicates the good events after applying the confidence-level cut of 5% on the black dashed histogram. The colored area includes events whose confidence level is less than 0.05. . . . .	61
4.14	The paddle distributions of the time-of-flight counters in the six sectors. The red dashed line is the average of the six sectors' counts in the paddle distribution. . . . .	62
4.15	Missing-mass distributions for the four different topologies. The $\pi^-$ particle is missing in all $p\pi^+\pi^-$ events (a), the $\pi^+$ particle is missing (b), the $p$ particle is missing (c), and there are no particles missing (d). The black solid line is made from the butanol target after applying all corrections. The histogram filled in light blue indicates the good events after applying all basic and accidental cuts and corrections without the confidence-level cut. The red dashed histogram includes events whose confidence level is greater than 0.05. The distribution in (d) is made as a function of the squared missing mass. . . . .	64
4.16	Circular polarization of the photon beam as a function of photon energy. . . . .	65
4.17	The average degree of circular polarization of the photon beam as a function of the center-of-mass energy for electron beam energies 1.645 GeV (a) and 2.427 GeV (b). . . . .	67
4.18	Distribution of beam-charge asymmetries for the analyzed runs. . . . .	69
4.19	Target polarization versus run number measured in the g9a experiment. . . . .	70

4.20	Values of target polarization versus run number measured in the g9a experiment and their averages (the blue line) made per period. . . . .	72
4.21	The distribution of the number of photons as a function of photon energy saved in the “gflux” file. In this picture, there are seven periods and each period has 100 and 25-MeV wide bins in the range from 0.4875 to 2.9875 GeV, respectively. Period 5 has the largest number of photons. . . . .	75
4.22	The ratio of the number of photons between periods with the target polarizations parallel ( $\Rightarrow$ ) and anti-parallel ( $\Leftarrow$ ) to the beam. . . . .	76
4.23	Illustration of the signal and background events in the butanol data from the g9a experiment. . . . .	78
4.24	(a) The missing mass distribution for the topology $\gamma p \rightarrow p\pi^+(\pi^-)$ from the butanol and carbon target. The black line describes the butanol events from the g9a experiment and the red line denotes the carbon events from the g9b experiment. (b) The fitted missing mass distribution using a mixed function of a Gaussian and a Chebyshev polynomial (blue line). The green dotted line denotes the Chebyshev polynomial in the mixed fitting function. The colored area includes events whose confidence level is less than 0.05. The data are selected from $W \in [1.575, 1.625]$ GeV; the beam polarization is anti-parallel to the beam and the target polarization is anti-parallel to the beam direction. . . . .	79
4.25	The missing squared-mass distribution for Topology $\gamma p \rightarrow p\pi^+(\pi^-)$ from the butanol target (a) and from the carbon target (b). The blue-shaded regions indicate $MM^2 < -0.2$ GeV <sup>2</sup> and should contain only events for bound nucleons. . . . .	80
4.26	The comparison of the $\pi^+$ $W$ versus $\phi_{\pi^+}^*$ from the butanol and carbon data in the reaction $\gamma p \rightarrow p\pi^+(\pi^-)$ . The phase space (a) is from the butanol data of the g9a experiment, and the phase space (b) is from the carbon data of the g9b experiment. . . . .	81
4.27	(a) The $\pi^+$ phase space scale factor on two dimensional distribution of the $\pi^+$ $W$ versus $\phi_{\pi^+}^*$ (b) The missing mass distribution with the free-proton and bound-nucleon distribution calculated using the phase space scale factors given in (a). The black line describes the butanol events for Topology $\gamma p \rightarrow p\pi^+(\pi^-)$ and the center-of-mass energy $W \in [1.575, 1.625]$ GeV from the g9a experiment, and the red line is the carbon events from the g9b experiment. The yellow line is the scaled carbon distribution, and the blue dashed line is the free-proton distribution made by the phase space scale factors. . . . .	82

4.28	(a) The missing mass distributions made from the 300 nearest events selected from butanol (black dots) and carbon (green line) data in Topology $\gamma p \rightarrow p\pi^+(\pi^-)$ , $W \in [1.575,1.625]$ GeV, and Period 7. (b) Fitting the butanol's missing mass distribution (black dots) using a combination of the signal (red line) and carbon background (blue dashed line) function. . . . .	83
4.29	Fitting the missing-mass distribution from the butanol data in Topology $\gamma p \rightarrow p\pi^+(\pi^-)$ , $W \in [1.575,1.625]$ GeV, and Period 7 using a Voigt function. The $\Gamma$ parameter taken in this fitting is used as a fixed value in the Q-factor method. . . . .	84
4.30	(a) The normalized $\chi^2$ distribution from the Q-factor method (b) The comparison of scaled carbon distribution between the phase space scale factor and Q-factor method. . . . .	85
4.31	The missing-mass distribution with the free-proton and bound-nucleon distribution calculated by the Q-factor method. The black and red line denote the butanol (the g9a experiment) and carbon (the g9b experiment) data for Topology $\gamma p \rightarrow p\pi^+(\pi^-)$ and $W \in [1.575,1.625]$ GeV used in Figure 4.27, respectively. The yellow line and the green line denote the scaled carbon distribution and the free-proton distribution by the method described in Section 4.9.1, respectively. . . . .	86
4.32	The missing-mass distribution with the free-proton and bound-nucleon distribution calculated in Q-factor method in Topology $\gamma p \rightarrow p\pi^+(\pi^-)$ , the center-of-mass energy range $W \in [1.475,1.625]$ GeV, and Period 7, and their $\chi^2$ distribution. . . . .	87
4.33	The missing-mass distribution with the free-proton and bound-nucleon distribution calculated in Q-factor method in Topology $\gamma p \rightarrow p\pi^+(\pi^-)$ , the center-of-mass energy range $W \in [1.625,1.775]$ GeV, and Period 7, and their $\chi^2$ distribution. . . . .	88
4.34	The missing-mass distribution with the free-proton and bound-nucleon distribution calculated in Q-factor method in Topology $\gamma p \rightarrow p\pi^+(\pi^-)$ , the center-of-mass energy range $W \in [1.775,1.925]$ GeV, and Period 7, and their $\chi^2$ distribution. . . . .	89
4.35	The missing-mass distribution with the free-proton and bound-nucleon distribution calculated in Q-factor method in Topology $\gamma p \rightarrow p\pi^+(\pi^-)$ , the center-of-mass energy range $W \in [1.925,2.075]$ GeV, and Period 7, and their $\chi^2$ distribution. . . . .	90

5.1	A diagram describing the kinematics of the reaction $\gamma p \rightarrow p\pi^+\pi^-$ . The blue plane represents the center-of-mass production plane composed of the initial photon and proton, while the red plane represents the decay plane formed by two of the final-state particles. In the diagram, $k$ is the initial photon and the particle $p$ denotes the polarized target proton. $a$ , $b_1$ , and $b_2$ are the three particles of the final state. If we assume that particle $a$ is the recoiling proton, $b_1$ and $b_2$ should be the two pions: $\pi^+$ and $\pi^-$ . $\Theta_{c.m.}$ denotes the angle between the initial proton and the particle $a$ in the center-of-mass system. $\phi^*$ and $\theta^*$ indicate the azimuthal and polar angles of the particle $b_1$ in the rest frame of $b_1$ and $b_2$ . . . .	92
5.2	Examples of $\phi^*$ angular distributions in the helicity frame of the beam polarization parallel (a) and anti-parallel (b) to the beam axis for the center-of-mass energy $W \in [1.675, 1.725]$ GeV in the topology $\gamma p \rightarrow p\pi^+(\pi^-)$ . The data with the target polarization parallel (antiparallel) to the beam axis are from Period 6 (Period 7). . . . .	95
5.3	CLAS-integrated azimuthal angular distributions in the helicity frame of helicity-plus events $N(\phi^*, \rightarrow)$ and helicity-minus events $N(\phi^*, \leftarrow)$ for the center-of-mass energy $W \in [1.675, 1.725]$ GeV in the topology $\gamma p \rightarrow p\pi^+(\pi^-)$ . . . . .	96
5.4	The polarization observable $\mathbf{I}^\odot$ calculated from Equation 5.12 is compared with the same observable published in the g1c experiment. The dataset is the same as in Figure 5.2. . . . .	96
5.5	Polarization observables $\mathbf{I}^\odot$ from the three kinds of period-combinations in the topology $\gamma p \rightarrow p\pi^+(\pi^-)$ (a) and the topology $\gamma p \rightarrow p\pi^-(\pi^+)$ (b) for the center-of-mass energy $W \in [1.675, 1.725]$ GeV and their average in each topology. The polarization observable $\mathbf{I}^\odot$ in each period-combination and each topology is derived from Equation 5.12. . . . .	98
5.6	The beam asymmetries from the topology 1, 2, and 4 and average, called FROST-average. The polarization observable $\mathbf{I}^\odot$ analyzed in the g9a experiment is also compared with data published. . . . .	99
5.7	(a)-(c) Comparisons (differences) between results for the polarization observables $\mathbf{I}^\odot$ from different period-combinations integrated over all energies in Topology $\gamma p \rightarrow p\pi^+(\pi^-)$ . The distributions are centered at zero, suggesting consistency among the results from different period-combinations. . . . .	100

5.8	(a)-(c) Comparisons (differences) between results for the polarization observables $\mathbf{I}^\odot$ from different topologies integrated over all energies. The distributions are centered at zero, suggesting consistency among the results from different topologies. (d) Comparisons (differences) between results for the polarization observables $\mathbf{I}^\odot$ from the g9a experiment and the g1c experiment, integrated over all energies. . . . .	101
5.9	Example of the $\phi^*$ angular distributions in the helicity frame of the target polarization parallel (a) and antiparallel (b) to the beam axis. The data are selected for $W \in [1.725,1.775]$ GeV, combination-67, and Topology $\gamma p \rightarrow p\pi^+(\pi^-)$ . . . . .	103
5.10	CLAS-integrated azimuthal angular distribution in $N(\phi^*, \Rightarrow)^Q$ and $N(\phi^*, \Leftarrow)^Q$ for the center-of-mass energy $W \in [1.725,1.775]$ GeV and the topology $\gamma p \rightarrow p\pi^+(\pi^-)$ . . . . .	103
5.11	The polarization observable $\mathbf{P}_z$ calculated from Equation 5.18. The dataset is the same as that used in Figure 5.10. . . . .	104
5.12	Polarization observables $\mathbf{P}_z$ of three kinds of period-combinations in Topology $\gamma p \rightarrow p\pi^+(\pi^-)$ (a) and Topology $\gamma p \rightarrow p\pi^-(\pi^+)$ (b) for the center-of-mass energy $W \in [1.725,1.775]$ GeV and their average in each topology. . . . .	105
5.13	The average target asymmetry of the topology 1 and topology 2 and their average, called FROST-average. The data are shown for the center-of-mass energy $W \in [1.725,1.775]$ GeV. . . . .	106
5.14	Comparisons (differences) between results for the polarization observables $\mathbf{P}_z$ from different period-combinations integrated across all energies in Topology $\gamma p \rightarrow p\pi^+(\pi^-)$ . . . . .	107
5.15	Comparisons (differences) between results for the polarization observables $\mathbf{I}^\odot$ from different topologies integrated across all energies. . . . .	107
5.16	CLAS-integrated azimuthal angular distribution in $N(\phi^*, 3/2)$ and $N(\phi^*, 1/2)$ for the center-of-mass energy $W \in [1.675,1.725]$ GeV and the topology $\gamma p \rightarrow p\pi^+(\pi^-)$ . . . . .	108
5.17	The polarization observable $\mathbf{P}_z^\odot$ calculated from Equation 5.20. The dataset is the same as in Figure 5.16. . . . .	109
5.18	Polarization observables $\mathbf{P}_z^\odot$ of three kinds of period-combinations in Topology $\gamma p \rightarrow p\pi^+(\pi^-)$ (a) and Topology $\gamma p \rightarrow p\pi^-(\pi^+)$ (b) for the center-of-mass energy $W \in [1.675,1.725]$ GeV and their average in each topology. . . . .	110

5.19	The average helicity difference of the topology 1 and topology 2 and their average, called FROST-average. The data are shown for the center-of-mass energy $W \in [1.675, 1.725]$ GeV. . . . .	111
5.20	Comparisons (differences) between results for the polarization observables $\mathbf{P}_z^\odot$ from different period-combinations integrated over all energies in Topology $\gamma p \rightarrow p\pi^+(\pi^-)$ . . . . .	112
5.21	Comparisons (differences) between results for the polarization observables $\mathbf{P}_z^\odot$ from different topologies integrated over all energies. . . . .	112
6.1	Measured beam-helicity asymmetry $\mathbf{I}^\odot$ in the reaction $\vec{\gamma}p \rightarrow p\pi^+\pi^-$ for the whole center-of-mass energy range $W \in [1.375, 2.125]$ GeV. The filled symbols denote the average observable $\mathbf{I}^\odot$ from the butanol data and the open symbol the observable $-\mathbf{I}^\odot(2\pi - \phi_{\pi^+}^*)$ from the same dataset. The distribution at the bottom of each energy is the difference between the observable $\mathbf{I}^\odot$ and the observable $-\mathbf{I}^\odot(2\pi - \phi_{\pi^+}^*)$ . . . . .	115
6.2	Measured beam-helicity asymmetry $\mathbf{P}_z$ in the reaction $\vec{\gamma}\vec{p} \rightarrow p\pi^+\pi^-$ for the whole center-of-mass energy range $W \in [1.375, 2.125]$ GeV. The filled symbols denote the average observable $\mathbf{P}_z$ from the butanol data weighted by the Q-factor (Section 4.9.2) and the open symbol the observable $-\mathbf{P}_z(2\pi - \phi_{\pi^+}^*)$ from the same dataset. The distribution at the bottom of each energy is the difference between the observable $\mathbf{P}_z$ and the observable $-\mathbf{P}_z(2\pi - \phi_{\pi^+}^*)$ . . . . .	116
6.3	Measured beam-helicity asymmetry $\mathbf{P}_z^\odot$ in the reaction $\vec{\gamma}\vec{p} \rightarrow p\pi^+\pi^-$ for the whole center-of-mass energy range $W \in [1.375, 2.125]$ GeV. The filled symbols denote the average observable $\mathbf{P}_z^\odot$ from the butanol data weighted by the Q-factor (Section 4.9.2) and the open symbol the observable $\mathbf{P}_z^\odot(2\pi - \phi_{\pi^+}^*)$ from the same dataset. The distribution at the bottom of each energy is the difference between the observable $\mathbf{P}_z^\odot$ and the observable $\mathbf{P}_z^\odot(2\pi - \phi_{\pi^+}^*)$ . . . . .	117
6.4	Comparison between the polarization observable $\mathbf{I}^\odot$ analyzed in the g9a experiment, and the polarization observable $\mathbf{I}^\odot$ published in the g1c experiment (light blue). The data are shown for the whole center-of-mass energy range. All kinematic variables except $\phi_{\pi^+}^*$ and $W$ are integrated over. The red datapoint denotes the observable $\mathbf{I}^\odot$ from the butanol data, and the deep blue datapoint denotes the same observable from the butanol weighted by the Q-factor (Section 4.9.2). The green dots indicate model calculations provided by A. Fix, and the blue dots by W. Roberts. . . . .	120

6.5	The polarization observable $\mathbf{P}_z$ from the g9a experiment for the whole center-of-mass energy range. All kinematic variables except $\phi_{\pi^+}^*$ and $W$ are integrated over. The blue datapoint denotes the observable $\mathbf{I}^\odot$ from the butanol weighted by the Q-factor (Section 4.9.2). The green dots indicate model calculations provided by A. Fix, and the blue dots by W. Roberts. . . . .	121
6.6	The polarization observable $\mathbf{P}_z^\odot$ from the g9a experiment for the whole center-of-mass energy range. All kinematic variables except $\phi_{\pi^+}^*$ and $W$ are integrated over. The blue fullcross denotes the observable $\mathbf{I}^\odot$ from the butanol weighted by the Q-factor (Section 4.9.2). The green dots indicate model calculations provided by A. Fix, and the blue dots by W. Roberts. . . . .	122
A.1	The beam asymmetries of three period-combinations in topology $\gamma p \rightarrow p\pi^+(\pi^-)$ and an average beam asymmetry. . . . .	123
A.2	The target asymmetry made from different target polarizations (a) and from the same target polarization (b). . . . .	124
B.1	Comparisons between the polarization observables $\mathbf{I}^\odot$ before and after applying the beam charge asymmetry. . . . .	126
C.1	(a) The missing mass distribution with the 5 % confidence-level cut for the butanol target. (b) The missing mass distribution fitted with a Gaussian and the second-order Chebyshev polynomial. The data are selected for the center-of-mass energy $W \in [1.575, 1.625]$ GeV and the topology $\gamma p \rightarrow p\pi^+(\pi^-)$ . The hatched area includes events whose the confidence-level is less than 0.05. The light blue line is located at the $\pi^+$ mass $\pm 3\sigma$ of the fitted Gaussian function. The dashed green line is the second-order Chebyshev polynomial function. . . . .	127
C.2	The missing mass distribution of the butanol target made in different CL-cuts. The data are selected for the center-of-mass energy $W \in [1.575, 1.625]$ GeV and the topology $\gamma p \rightarrow p\pi^+(\pi^-)$ . . . . .	128
C.3	The average beam asymmetries made in 1 % CL-cut, 5 % CL-cut, 10 % CL-cut, and 15 % CL-cut and the polarization observable $\mathbf{I}^\odot$ published in g1c experiment. . . . .	129
C.4	Difference and percent error between polarization observable $\mathbf{I}^\odot$ for 5 % CL-cut and other CL-cuts. . . . .	130

D.1	The statistical error contribution on observable $\mathbf{I}^\odot$ from the target polarization (b), from the normalization factor (c), and the beam polarization (d). The sum of these errors is shown in (a). . . . .	133
E.1	The beam asymmetries for the topology $\gamma p \rightarrow p\pi^+(\pi^-)$ and the combination-32. The dataset is for the whole center-of-mass energy range and the butanol data. . . . .	134
E.2	The beam asymmetries for the topology $\gamma p \rightarrow p\pi^+(\pi^-)$ and the combination-45. The dataset is for the whole center-of-mass energy range and the butanol data. . . . .	135
E.3	The beam asymmetries for the topology $\gamma p \rightarrow p\pi^+(\pi^-)$ and the combination-67. The dataset is for the whole center-of-mass energy range and the butanol data. . . . .	135
E.4	The beam asymmetries for the topology $\gamma p \rightarrow p\pi^-(\pi^+)$ and the combination-32. The dataset is for the whole center-of-mass energy range and the butanol data. . . . .	136
E.5	The beam asymmetries for the topology $\gamma p \rightarrow p\pi^-(\pi^+)$ and the combination-45. The dataset is for the whole center-of-mass energy range and the butanol data. . . . .	136
E.6	The beam asymmetries for the topology $\gamma p \rightarrow p\pi^-(\pi^+)$ and the combination-67. The dataset is for the whole center-of-mass energy range and the butanol data. . . . .	137
E.7	The beam asymmetries for the topology $\gamma p \rightarrow p\pi^+(\pi^-)$ and the average combination. The dataset is for the whole center-of-mass energy range and the butanol data. . . . .	137
E.8	The beam asymmetries for the topology $\gamma p \rightarrow p\pi^-(\pi^+)$ and the average combination. The dataset is for the whole center-of-mass energy range and the butanol data. . . . .	138
E.9	The beam asymmetries for the average topology and the average combination. The dataset is for the whole center-of-mass energy range and the butanol data. . . . .	138
E.10	The beam asymmetries for the topology $\gamma p \rightarrow p\pi^+(\pi^-)$ and the combination-32. The dataset is for the whole center-of-mass energy range and the butanol data weighted by Q-factor. . . . .	139

E.11	The beam asymmetries for the topology $\gamma p \rightarrow p\pi^+(\pi^-)$ and the combination-45. The dataset is for the whole center-of-mass energy range and the butanol data weighted by Q-factor. . . . .	139
E.12	The beam asymmetries for the topology $\gamma p \rightarrow p\pi^+(\pi^-)$ and the combination-67. The dataset is for the whole center-of-mass energy range and the butanol data weighted by Q-factor. . . . .	140
E.13	The beam asymmetries for the topology $\gamma p \rightarrow p\pi^-(\pi^+)$ and the combination-32. The dataset is for the whole center-of-mass energy range and the butanol data weighted by Q-factor. . . . .	140
E.14	The beam asymmetries for the topology $\gamma p \rightarrow p\pi^-(\pi^+)$ and the combination-45. The dataset is for the whole center-of-mass energy range and the butanol data weighted by Q-factor. . . . .	141
E.15	The beam asymmetries for the topology $\gamma p \rightarrow p\pi^-(\pi^+)$ and the combination-67. The dataset is for the whole center-of-mass energy range and the butanol data weighted by Q-factor. . . . .	141
E.16	The beam asymmetries for the topology $\gamma p \rightarrow p\pi^+(\pi^-)$ and the average combination. The dataset is for the whole center-of-mass energy range $W \in [1.375, 2.125]$ GeV and the butanol data weighted by Q-factor. . .	142
E.17	The beam asymmetries for the topology $\gamma p \rightarrow p\pi^-(\pi^+)$ and the average combination. The dataset is for the whole center-of-mass energy range and the butanol data weighted by Q-factor. . . . .	142
E.18	The beam asymmetries for the average topology and the average combination. The dataset is for the whole center-of-mass energy range and the butanol data weighted by Q-factor. . . . .	143
E.19	The target asymmetries for the topology $\gamma p \rightarrow p\pi^+(\pi^-)$ and the combination-32. The dataset is for the whole center-of-mass energy range and the butanol data weighted by Q-factor. . . . .	144
E.20	The target asymmetries for the topology $\gamma p \rightarrow p\pi^+(\pi^-)$ and the combination-45. The dataset is for the whole center-of-mass energy range and the butanol data weighted by Q-factor. . . . .	144
E.21	The target asymmetries for the topology $\gamma p \rightarrow p\pi^+(\pi^-)$ and the combination-67. The dataset is for the whole center-of-mass energy range and the butanol data weighted by Q-factor. . . . .	145

E.22	The target asymmetries for the topology $\gamma p \rightarrow p\pi^-(\pi^+)$ and the combination-32. The dataset is for the whole center-of-mass energy range and the butanol data weighted by Q-factor. . . . .	145
E.23	The target asymmetries for the topology $\gamma p \rightarrow p\pi^-(\pi^+)$ and the combination-45. The dataset is for the whole center-of-mass energy range and the butanol data weighted by Q-factor. . . . .	146
E.24	The target asymmetries for the topology $\gamma p \rightarrow p\pi^-(\pi^+)$ and the combination-67. The dataset is for the whole center-of-mass energy range and the butanol data weighted by Q-factor. . . . .	146
E.25	The target asymmetries for the topology $\gamma p \rightarrow p\pi^+(\pi^-)$ and the average combination. The dataset is for the whole center-of-mass energy range and the butanol data weighted by Q-factor. . . . .	147
E.26	The target asymmetries for the topology $\gamma p \rightarrow p\pi^-(\pi^+)$ and the average combination. The dataset is for the whole center-of-mass energy range and the butanol data weighted by Q-factor. . . . .	147
E.27	The target asymmetries for the average topology and the average combination. The dataset is for the whole center-of-mass energy range and the butanol data weighted by Q-factor. . . . .	148
E.28	The helicity differences for the topology $\gamma p \rightarrow p\pi^+(\pi^-)$ and the combination-32. The dataset is for the whole center-of-mass energy range and the butanol data weighted by Q-factor. . . . .	149
E.29	The helicity differences for the topology $\gamma p \rightarrow p\pi^+(\pi^-)$ and the combination-45. The dataset is for the whole center-of-mass energy range and the butanol data weighted by Q-factor. . . . .	149
E.30	The helicity differences for the topology $\gamma p \rightarrow p\pi^+(\pi^-)$ and the combination-67. The dataset is for the whole center-of-mass energy range and the butanol data weighted by Q-factor. . . . .	150
E.31	The helicity differences for the topology $\gamma p \rightarrow p\pi^-(\pi^+)$ and the combination-32. The dataset is for the whole center-of-mass energy range and the butanol data weighted by Q-factor. . . . .	150
E.32	The helicity differences for the topology $\gamma p \rightarrow p\pi^-(\pi^+)$ and the combination-45. The dataset is for the whole center-of-mass energy range and the butanol data weighted by Q-factor. . . . .	151

E.33	The helicity differences for the topology $\gamma p \rightarrow p\pi^-(\pi^+)$ and the combination-67. The dataset is for the whole center-of-mass energy range and the butanol data weighted by Q-factor. . . . .	151
E.34	The helicity differences for the topology $\gamma p \rightarrow p\pi^+(\pi^-)$ and the average combination. The dataset is for the whole center-of-mass energy range and the butanol data weighted by Q-factor. . . . .	152
E.35	The helicity differences for the topology $\gamma p \rightarrow p\pi^-(\pi^+)$ and the average combination. The dataset is for the whole center-of-mass energy range and the butanol data weighted by Q-factor. . . . .	152
E.36	The helicity differences for the average topology and the average combination. The dataset is for the whole center-of-mass energy range and the butanol data weighted by Q-factor. . . . .	153

# ABSTRACT

The study of baryon resonances offers a deeper understanding of the strong interaction, since the dynamics and relevant degrees of freedom hidden within them are reflected by the properties of these states. The baryon resonances have been fairly accurately predicted in the low-energy region (center-of-mass energies  $W < 1.7$  GeV) by constituent quark models. However, at higher masses ( $W > 1.7$  GeV), most of the predicted resonances and experimental findings do not match up. The model calculations even predict more baryon resonances than have been observed experimentally. This issue is referred to as the "missing resonance problem".

Quark model calculations have suggested that some of the missing resonances couple very weakly to  $\pi N$  or  $KN$  modes, but strongly to  $\gamma p$  reactions. Therefore, the missing resonances should be found in photoproduction experiments, not in pion- or kaon-production experiments. Higher-lying excited states at and above 1.7 GeV are generally predicted to have strong couplings to the reaction  $\gamma p \rightarrow p\pi^+\pi^-$  via  $\pi\Delta$  or  $\rho N$  intermediate states. Double-pion photoproduction is, therefore, important for investigating the properties of high-mass resonances. The excited states of the nucleon are usually found as broadly overlapping resonances, which may decay into a multitude of final states involving mesons and baryons. Polarization observables make it possible to isolate single resonances from interference terms.

The CLAS g9a (FROST) experiment, as part of the  $N^*$  spectroscopy program at Jefferson Laboratory, has accumulated photoproduction data using circularly- and linearly-polarized photons incident on a longitudinally-polarized butanol target in the photon energy range 0.3 to 2.4 GeV. The CLAS g9b (FROST) experiment used transverse target polarization, with a similar set of beam polarization as in the g9a experiment. For the g9a experiment, I was serving as the run group chef who is responsible for overseeing the reconstruction of the data. I was also responsible for the drift chamber calibration in the g9a and g9b experiments. This document summarizes how the beam-helicity asymmetry  $\mathbf{I}^\odot$ , the target asymmetry  $\mathbf{P}_z$ , and the helicity difference  $\mathbf{P}_z^\odot$  for the reaction  $\vec{\gamma}\vec{p} \rightarrow p\pi^+\pi^-$  are extracted from photoproduction data, utilizing circular beam and longitudinal target polarization in the g9a experiment.

# ZUSAMMENFASSUNG

Das Studium der Baryon resonanzen liefert ein tieferes Verständnis der starken Wechselwirkung, da die Dynamik sowie die in ihnen versteckten, relevanten Freiheitsgrade die Eigenschaften dieser Zustände widerspiegelt werden. Die Baryon resonanzen wurden ziemlich genau mithilfe von Konstituentenquark-Modellen im niedrigen Energiebereich vorhergesagt (Schwerpunktsenergien  $W < 1.7$  GeV). Bei höheren Massen ( $W > 1.7$  GeV) stimmen die meisten der vorhergesagten Resonanzen nicht mit den experimentellen Befunden überein. Die Modellrechnungen prognostizieren sogar mehr Baryonenresonanzen, als experimentell beobachtet wurden. Dieses Problem wird als "Fehlende-Resonanz-Problem" bezeichnet.

Quark-Modell-Berechnungen haben ergeben, dass sich einige der fehlenden Resonanzen sehr schwach zu  $\pi N$ - oder  $KN$ -Modi, aber stark zu  $\gamma p$ -Reaktionen verbinden. Daher sollten die fehlenden Resonanzen in Photoproduktionsexperimenten und nicht in Pion- oder Kaon-Produktionen zu finden sein. Bei höheren, angeregten Zuständen, die bei 1.7 GeV und darüber liegen, ist im Allgemeinen zu prognostizieren, dass sie starke Verbindungen mit den Zwischenzuständen der Reaktion  $\gamma p \rightarrow p\pi^+\pi^-$  über  $\pi\Delta$  oder  $\rho N$  eingehen. Die Doppel-Pion-Fotoproduktion ist daher für die Untersuchung der Eigenschaften von Resonanzen mit hohen Massen wichtig. Die angeregten Zustände des Nukleons zeigen sich in der Regel als weit überlappende Resonanzen, die in einer Vielzahl von Endzuständen aus Mesonen und Baryonen zerfallen. Polarisations-

beobachtungen machen es möglich, einzelne Resonanzen von den Interferenztermen zu isolieren.

Das CLAS g9a (Frost) Experiment als Teil des  $N^*$  Spektroskopie-Programms am Jefferson-Laboratorium hat Photoproduktionsdaten mit zirkular und linear polarisierten Photonen auf ein in Längsrichtung polarisiertes Butanol-Ziel im Photonen-Energie-Bereich von 0.3 bis 2.4 GeV gesammelt. Beim CLAS g9b (FROST) Experiment wurde eine querliegende Zielpolarisation mit einemähnlichen Satz an Strahlpolarisation wie im g9a Experiment verwendet. Für das g9a Experiment wurde ich als Gruppenleiter eingeteilt, dem die Überwachung der Daten-Rekonstruktion oblag. Ich war ebenfalls für die Kalibrierung der Driftkammer bei den g9a- und den g9b-Experimenten verantwortlich. Dieses Dokument fasst zusammen, wie die Strahl-Helizitätsasymmetrie  $\mathbf{I}^\odot$ , die Ziel-Asymmetrie  $\mathbf{P}_z$ , und der Helizitätsunterschied  $\mathbf{P}_z^\odot$  für die Reaktion  $\vec{\gamma}\vec{p} \rightarrow p\pi^+\pi^-$  aus den Fotoproduktionsdaten unter Verwendung kreisförmiger Strahl- und längsgerichteter Zielpolarisation im g9a Experiment extrahiert wurden.

# CHAPTER 1

## INTRODUCTION AND OVERVIEW

The proton was discovered by Ernest Rutherford from Rutherford's scattering experiment in 1918. The proton is composed of two up quarks and one down quark, and its mass is  $938.272 / c^2$ . The mass of the proton is known to be about 80-100 times greater than the sum of the rest masses of the quarks to make up, while the gluons have zero rest mass. When the overall mass of the proton and the combined masses of these three quarks are compared with each other, more than 98 % of the proton mass cannot be accounted for. The remaining mass of the proton may, thus, be a result of the interaction among the quarks, the quark kinematic energy, and a "sea" of quark anti-quark pairs and gluons.

### 1.1 Quark Model

The atom is a basic unit of matter consisting of a dense central nucleus surrounded by a cloud of negatively-charged electrons. The atomic nucleus itself contains a mix of positively-charged protons and electrically-neutral neutrons. These protons and neutrons are members of a family of particles called "hadrons". Hadrons are composite particles of quarks held together by a strong force, like atoms and molecules are held together by the electromagnetic force. In 1961, M. Gell-Mann and Y. Ne'eman independently classified hadrons using a system called the Eightfold Way. In the Eightfold Way, hadrons with the same spin ( $J$ ) and parity ( $P$ ) are classified as a function of their charge ( $Q$ ) and strangeness ( $S$ ), based on group theory (SU(3)). According to the rules of group theory, the particles are classified in multiplets: baryons with  $J^P = \frac{1}{2}^+$  are contained in an octet, baryons with  $J^P = \frac{3}{2}^+$  are contained in a decuplet, and the vector mesons ( $J^P = 1^-$ ) as well as the pseudoscalar mesons ( $J^P = 0^-$ ) are contained in a flavor singlet and an octet (a nonet). The multiplet structure of mesons, as shown in Figure 1.1 (c) and (d), can be expressed using the combination rules of SU(3) ( $3 \otimes \bar{3} = 1 \oplus 8$ ). Similarly, the octet and decuplet structure of baryons, as shown in Figure 1.1 (a) and (b), can also be explained using all possible combinations of three quarks according to SU(3) ( $3 \otimes 3 \otimes 3 = 1 \oplus 8 \oplus 8 \oplus 10$ ).

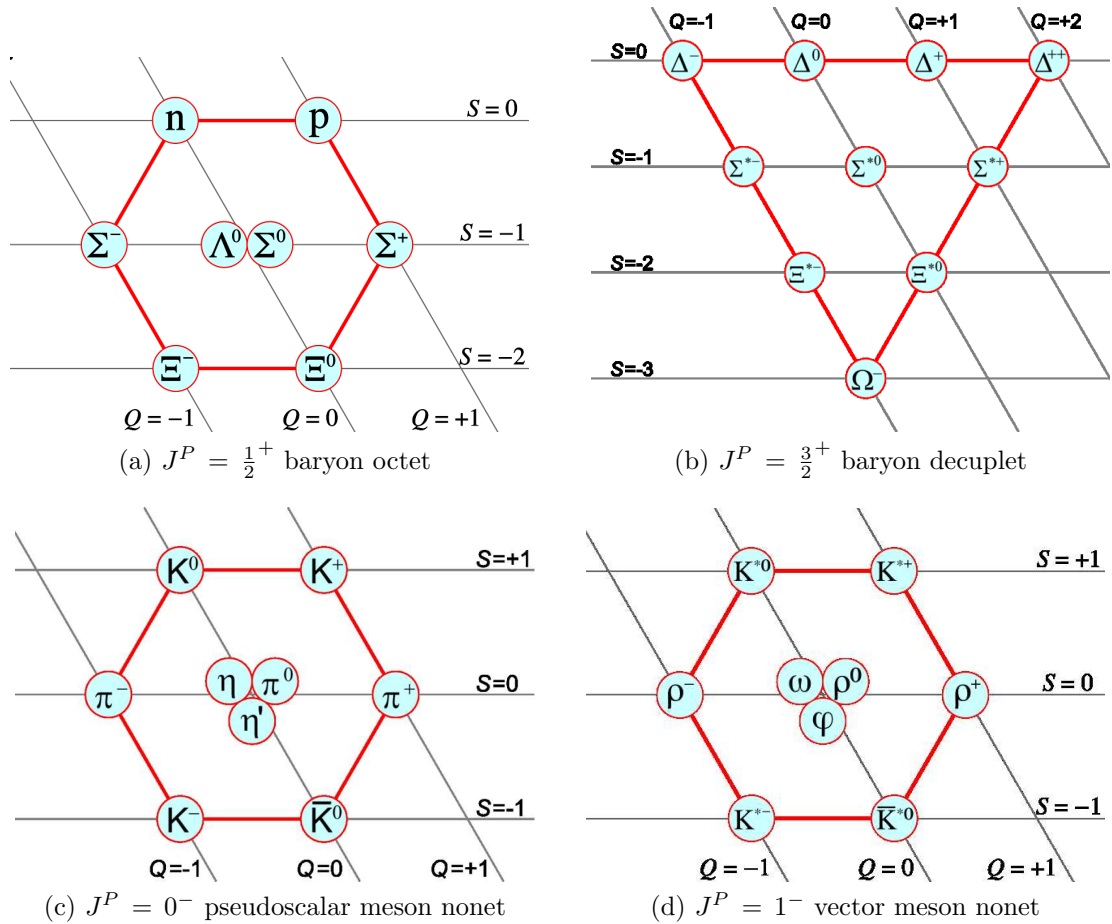


Figure 1.1: Classification of baryons and mesons according to charge and the strangeness. Charge is determined by the diagonal line and strangeness is determined by the horizontal line.

The hadrons were not classified accidentally in the patterns, as shown in Figure 1.1. These patterns would eventually reveal an internal structure of the hadrons. An interpretation of these structures was proposed by Gell-Mann and Zweig independently, in 1964. According to their work, the  $SU(3)$  structure appearing in the classification of hadrons can be easily explained if the hadrons are not treated as fundamental particles but, in fact, are composed of even more elementary constituents, which Gell-Mann called quarks. Table ?? summarizes masses of known quarks and their properties. Hadrons are also categorized into two families according to the number of quarks: baryons and mesons. The quark model asserts that baryons are composed of three quarks ( $qqq$ ), and mesons are composed of a quark and an anti-quark ( $q\bar{q}$ ).

The combination rules of  $SU(3)$  elegantly explain the multiplet structure of the

Table 1.1: Quark classification according to the key properties of the six quarks, such as total angular momentum,  $J$ , the electric charge,  $Q$  (in units of electron charge  $e$ ), and isospin ( $I_3$  as a flavor quantum number) [1].

Name	Symbol	Mass (MeV/ $c^2$ )	Spin ( $J$ )	Charge ( $Q$ )	Isospin ( $I_3$ )
Up	u	1.7 to 3.1	$\frac{1}{2}$	$+\frac{2}{3}$	$+\frac{1}{2}$
Down	d	4.1 to 5.7	$\frac{1}{2}$	$-\frac{1}{3}$	$-\frac{1}{2}$
Charm	c	1,290 +50/-110	$\frac{1}{2}$	$+\frac{2}{3}$	0
Strange	s	100 +30/-20	$\frac{1}{2}$	$-\frac{1}{3}$	0
Top	t	$172,900 \pm 600 \pm 900$	$\frac{1}{2}$	$+\frac{2}{3}$	0
Bottom	b	4,190 +180/-60	$\frac{1}{2}$	$-\frac{1}{3}$	0

hadrons, as shown in Figure 1.1, but contain a problem in the baryon decuplet. The quark content of the three particles located in the corners of the decuplet are  $\Delta^{++} = uuu$ ,  $\Delta^- = ddd$ , and  $\Omega^- = sss$ , and their spins are  $3/2$ . The spins of all quarks in these baryons must be parallel since the spin of each quark is  $1/2$  and, therefore, all quarks must be in the same quantum state. Since the quarks are fermions, they must obey Fermi statistics, and the baryon wave function should be antisymmetric under the exchange of two quarks, which is obviously not the case, and is thus in contradiction with the Pauli exclusion principle. This problem is overcome using a new quantum number, the *color* charge which can take three values: *red*, *green*, and *blue*. In order to overcome the violation of the Pauli exclusion principle, the color part of the wave function is prepared to be antisymmetric under the exchange of two quarks in the wave function being symmetric, so that the total wave function of the baryon is antisymmetric, and the rest of the wave function is symmetric. Color charges mentioned here are used as a property of quarks and gluons in the theory of Quantum Chromodynamics (QCD). The baryon resonances, which reflect the behavior of QCD, are defined by

$$L_{2I2J}(m), J^\pi, \quad (1.1)$$

where  $I$  is the isospin of the particle,  $J$  is the total angular momentum, and  $m$  is the invariant mass of the resonance in units of  $\text{MeV}/c^2$ , and  $\pi$  is the parity of the particle. Since the majority of the baryon resonances was discovered using  $\pi N$  or  $KN$  scattering,  $L$  is named by the relative angular momentum between the pion (or kaon) meson and the nucleon which gave rise to the resonance. This notation not

only shows the properties of the baryon resonance but also how it is produced.

## 1.2 Quantum Chromodynamics (QCD)

The quarks predicted in the quark model have never been observed as massive and charged particles even though it was thought before 1968 that they would be easily detected. In order to test the existence of quarks, new experiments which did not depend on hadron spectroscopy were considered, such as "deep inelastic scattering" (DIS) of leptons by nucleons. The DIS experiments delivered high energy electrons to nucleon targets, and these electrons interacted at a large exchange momentum  $Q$  so that the final state consisted of more particles than the initial lepton and nucleon. In 1968, an important DIS experiment was performed in which 15 GeV electrons was incident on protons at SLAC. This experiment showed that quarks were real and the functions describing the internal structure of the protons did not depend strongly on the exchange momentum  $Q$  [2]. The result of the DIS experiment could not be fully explained with the simple assumption that the protons were made of three pointlike quarks. This fact, on the other hand, was the evidence for point like partons which Feynman called the different constituents of the hadrons.

R. Feynman gave a more comprehensive interpretation of this DIS experiment at SLAC. The proton and other baryons are made of three quarks known as valence

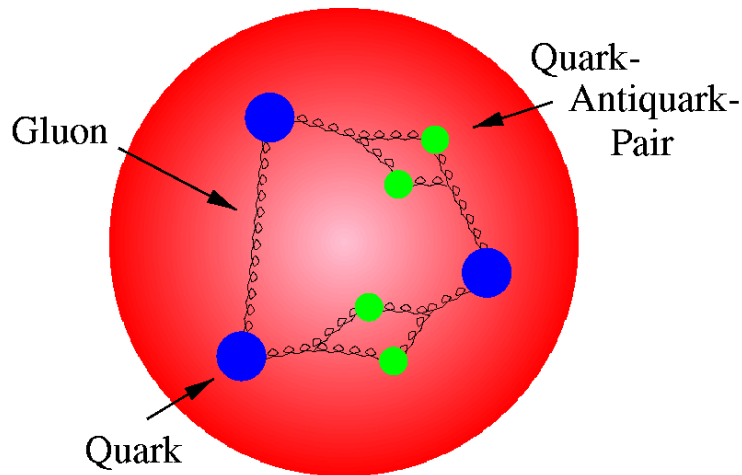


Figure 1.2: Artist view of the interior of a proton. The three valence quarks are surrounded by quark-antiquark pairs and gluons that form the main fraction of the mass of the proton.

quarks, and these quarks contribute the hadron's quantum properties. In addition to these quarks in the hadron, there are virtual quark-antiquark ( $q\bar{q}$ ) pairs known as sea quarks ( $q_s$ ) as revealed by DIS. Moreover, there are some neutral, spin 1 partons in the nucleon, which are now known as gluons. Sea quarks form when a gluon of the hadron's color field splits. These virtual quark-antiquark pairs exist only shortly, and they typically annihilate each other within the interior of the hadron. These sea quarks do not contribute to the quantum properties of the hadron. The proton is based on three valence quarks and numerous virtual quark-antiquark pairs bound by gluons, as shown in Figure 1.2.

In nature, there exist four known fundamental forces: gravity, the electromagnetic force, the weak nuclear force, and the strong nuclear force. The theory of Quantum Chromodynamics (QCD) describes the strong interactions between quarks and gluons which make up hadrons, like the electromagnetic interactions which are described by the exchange of photons between two charged particles. In QCD, however, the force between two quarks has different properties than the electromagnetic force and this difference leads to the dramatically different behavior of the nuclear strong force.

First, the force between two quarks does not diminish with distance as does the electromagnetic force. That is, the attractive force between two quarks does not decrease as the distance between quarks increases, but quite the contrary, the force increases. If enough energy is provided to separate two quarks, new quark pairs will be created in the process. As a result of this condition, quarks cannot exist alone and are bound into hadrons such as baryons and mesons. This property is called "confinement". Second, the force between two quarks diminishes at very small distance so that it is approximately possible to treat the quarks inside the hadrons as free, non-interacting particles. This is called "asymptotic freedom". This means that the QCD coupling constant,  $\alpha_s$  decreases as the energy of system increases, as shown in Figure 1.3.

## 1.3 Nucleon Resonances

At very high energies, deep inelastic scattering experiments make it easier to probe the inner structure of the nucleons composed of three valence quarks surrounded by numerous quark-antiquark pairs, from the sea of quarks bound together by gluons, as shown in Figure 1.2. When the exchange momentum  $Q$  is great, the asymptotic freedom of QCD occurs and the mathematics of the gauge theory is greatly simplified. That is, QCD can be treated in a perturbative way, expanded in powers of the strong coupling constant  $\alpha_s$  which is very small at such high energies. In this regime of perturbative QCD (pQCD), the quarks in the hadrons are treated essentially as free-moving, non-interacting quarks, and calculations of QED, used to describe the

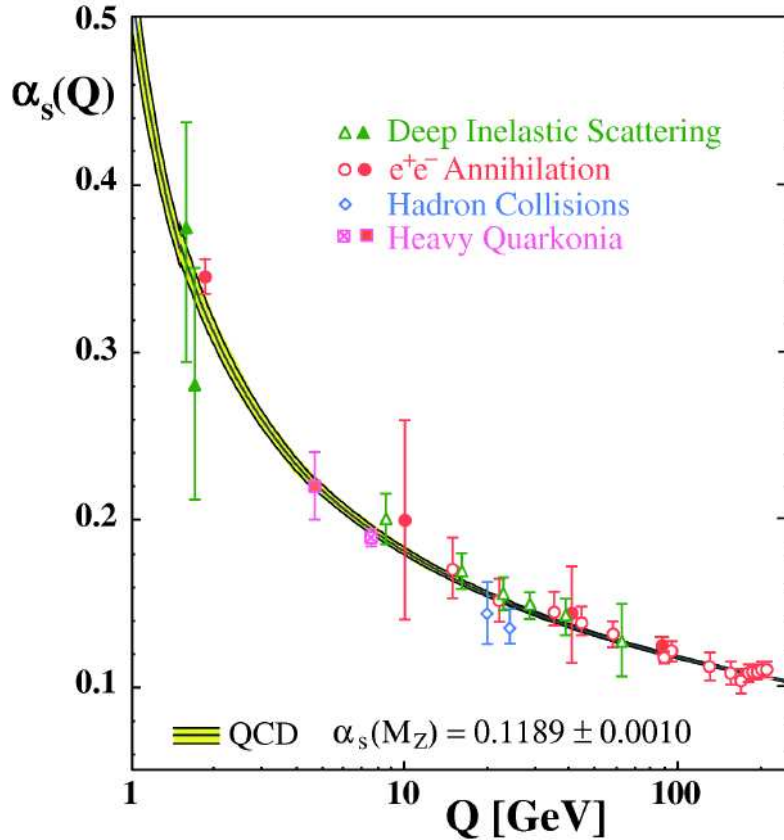


Figure 1.3: Summary of measurements of the QCD coupling constant  $\alpha_s$  as a function of the exchanged gluon momentum  $Q$ . The curves are QCD predictions for the combined world average value of  $\alpha_s$  [3].

interaction between photon and electron, can be applied to calculations of pQCD. In the low energy regime at which the nucleon resonances can be observed, it is not possible to apply this perturbative method to QCD, since the strong coupling constant becomes large. The description of hadrons would be provided by a non-perturbative treatment of QCD in which the coupling constant cannot be expanded in terms of  $\alpha_s$ . This energy regime, where the theory of perturbative QCD cannot provide solutions for nucleon excitations, is a highly important region to study.

It is an immensely difficult task to provide theoretical solutions to non-perturbative QCD. In order to overcome this problem, a very promising and well-established method called a Lattice QCD has been suggested. This method uses a grid of space-time points to simplify the path integral calculations included in QCD and has shown promising results. The main limitation encountered by Lattice QCD comes in the

form of the hardware used to carry out the calculations. In order to extract testable predictions from the theory, large amounts of computational power are required.

### 1.3.1 Constituent Quark Models

Constituent quark models (CQMs) are the most successful models for making predictions about the properties of baryon resonances in the non-perturbative region of QCD. CQMs do not describe the baryons based on their full internal structure, but postulate that the baryons are made of so-called constituent quarks only. In the low- or medium-energy region of QCD, where asymptotic freedom does not exist, the sea quarks and virtual gluons, described in Figure 1.2, cannot be ignored. As previously mentioned, the baryon is comprised of three quarks called the "valence quarks". These valence quarks, when they have only their bare masses, are called current quarks, and these current quarks are then "dressed" with the interactions of the sea quarks and gluons to make constituent quarks.

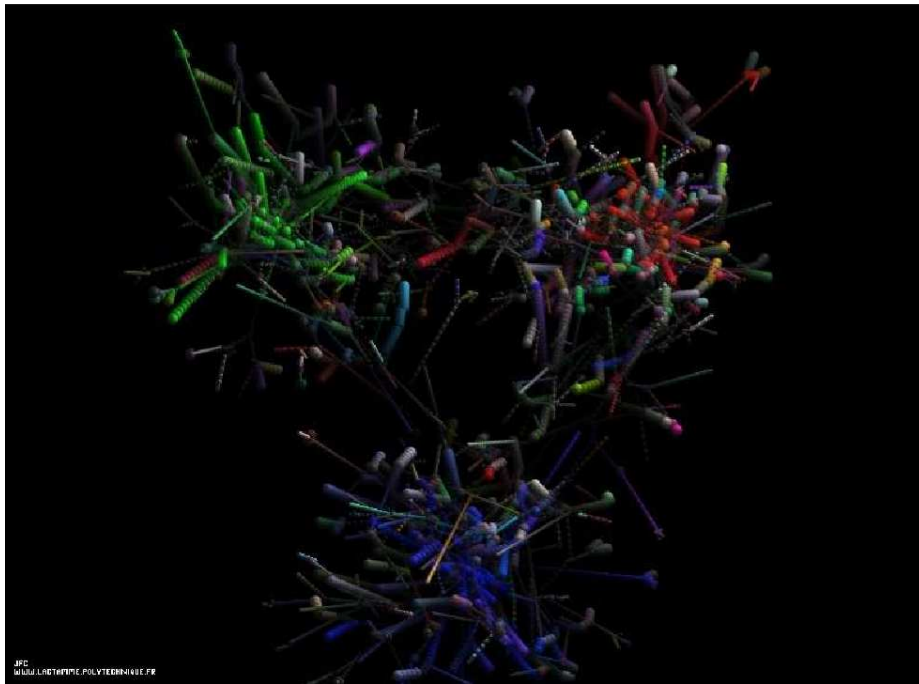


Figure 1.4: The proton is composed of three constituent quarks. Current quarks are surrounded by a cloud of virtual quarks and gluons. Points of red, blue, and green colors are virtual quarks; the others are gluons.

As an example, the proton is made of two u and one d constituent quarks, as shown in Figure 1.4. In this point of view, the constituent quarks cannot be defined

as point-particles any longer and, since they are the only subcomponents of the proton, these quarks share the total mass of the proton in CQMs. As a consequence, the constituent quark masses are much heavier than the bare quark masses given in Table ??, so that their masses are between 220 and 330 MeV for the u and d quarks. There are three prominent examples of CQMs according to how the models treat the short-range interactions among the three constitute quarks within the hadron: one-gluon exchange [4], goldstone boson exchange [5], or instanton exchange [6]. Figure 1.6 represents an example of the constituent quark model, developed by S. Capstick and N. Isgur using a gluon as the mediator for the short-range interactions.

Figure 1.5 shows how three quarks in a harmonic oscillator potential are arranged in the lightest resonances of the nucleon spectrum. The nucleon ground state  $P_{11}(939)$ , as shown in Figure 1.5, is the lowest energy state with the spin of two quarks aligned and the third spin in the other direction in the  $1s$  state. The first excited state  $P_{33}$  (1232), referred to as the  $\Delta$  resonance, is obtained by flipping the spin of the third quark so that the three quarks remain on the  $1s$  state but now with all their spins aligned. The next resonances,  $S_{11}(1535)$  and  $D_{13}(1520)$ , are obtained by moving one quark on the  $1p$  state. At higher energies, an arbitrary number of resonances can be built using this procedure.

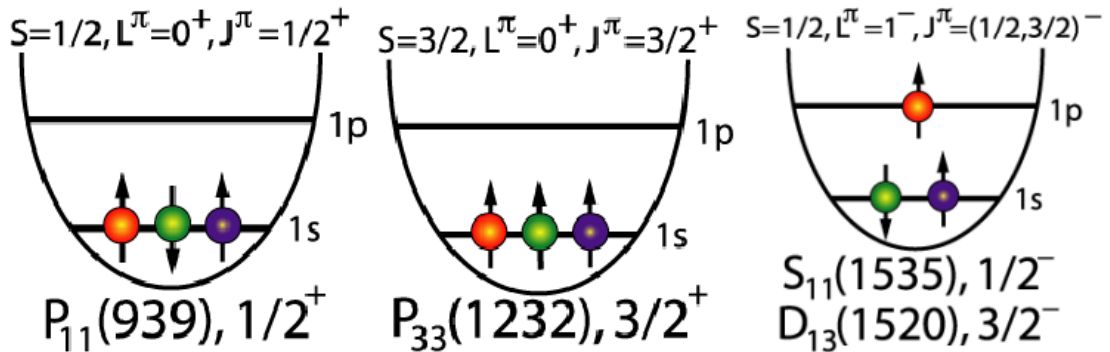


Figure 1.5: Schematic representation of the nucleon,  $P_{11}(939)$ , and the three lowest lying nucleon resonances in a simplified constituent quark model. The convention for naming the baryon resonances in this figure is from Equation 1.1.

### 1.3.2 Missing Resonance Problem

Figure 1.6 shows spectrum of  $N^*$  with model predictions and experimental findings. The baryon resonances have been fairly accurately predicted in the low-energy region (center-of-mass energy,  $W < 1.7$  GeV) by CQMs. However, at higher masses

( $W > 1.7$  GeV), most of the predicted resonances and experimental measurements do not match up. These model calculations even predict more baryon resonances than have been observed experimentally. This issue is referred to as the "missing resonance problem".

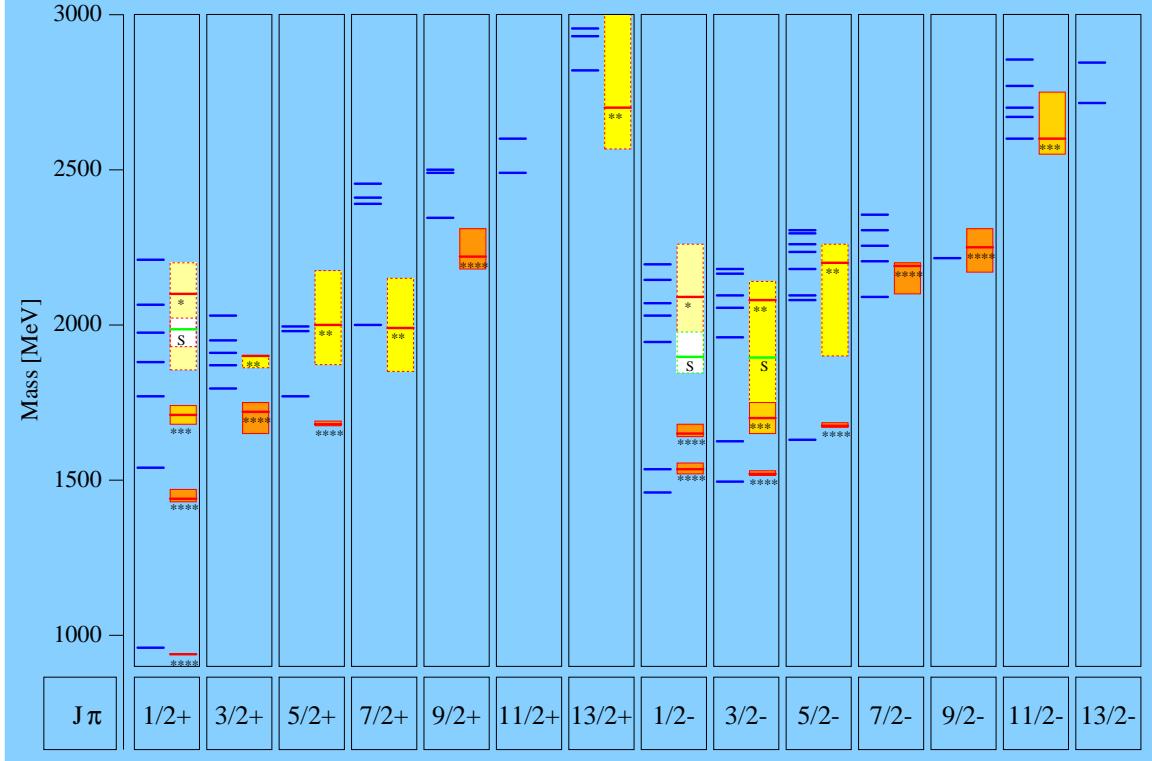


Figure 1.6: The spectrum of  $N^*$  resonances using one-gluon exchange for short-range interaction. The left side of each column shows the resonances predicted by the model, while the corresponding right side with the blocks represents experimental measurements. The height of the blocks illustrates the uncertainty in the mass measurement. The number of \*'s denotes the ranking of the state according to the PDG. Resonances with four stars are well-established, those with three stars have solid evidence supporting their existence, states with two stars have little evidence, and excited states with one star have even less supporting evidence [4].

The CQMs mentioned up to this point primarily describe the baryons as particles composed of three constituent quarks in the excited baryon spectrum. If there is a model with a lesser number of effective degrees of freedom, the number of predicted resonances could be less. Two of the three constituent quarks in the baryon are antisymmetric in color and spin components. These two quarks form a strongly-bound quark pair, called diquark, by freezing the  $\rho$  oscillator, as shown in Figure 1.7. Cal-

culations of the excited states in the diquark-quark model can be simplified, and the number of degrees of freedom for the model will be decreased considerably. However, the number of resonances predicted from the diquark-quark model is still too large. There may be two possibilities which explain this discrepancy between model predictions and experimental measurements. The first is that CQMs still predict too many resonances, and further constraints should be added in CQMs to decrease the number of effective degrees of freedom. Alternatively, additional resonances might exist but couple very weakly with particles commonly used to excited nucleons made from data accumulated until now. This weak coupling makes it difficult to observe additional missing resonance in experiments.

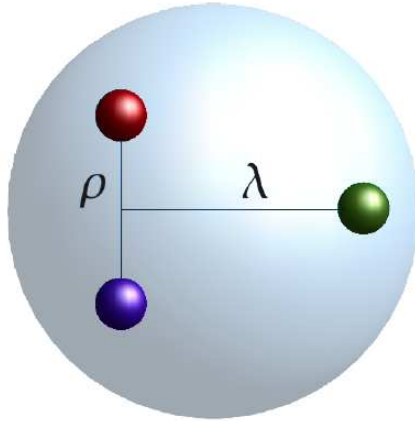


Figure 1.7: A model of the baryon used in CQMs. In this model, the baryon is treated as an object with two independent oscillators,  $\rho$  and  $\lambda$  [7].

Most of the data was accumulated from pion or kaon production, in which nucleons are excited with beams of long-lived mesons, like  $\pi^+$ ,  $\pi^-$ ,  $K^+$ , and  $K^-$ . Quark model calculations have suggested that some of the missing resonances couple very weakly to  $\pi N$  or  $KN$  modes but these states couple strongly to  $\gamma p$  reactions, the missing resonances would not have been found in the pion- or kaon-production experiment. Therefore, photoproduction experiments can be the clue to solving the missing resonance problem. Before 2005, the experiments related to photoproduction have been done at fairly low energies  $E_\gamma < 1.07$  GeV (center-of-mass energy,  $W < 1.70$  GeV), as shown in Figure 1.8, and the missing resonance problem appears in the region above  $W \sim 1.70$  GeV, as shown in Figure 1.6. If the photoproduction data at these higher energies are analyzed, more baryon resonances will be revealed. This will help decide the existence of the missing resonances. Figure 1.8 shows the total cross sections for  $\gamma p$  reaction as well as cross sections in several channels. Channels with quasi 2-body final states such as  $K\Lambda$ ,  $K\Sigma$ ,  $N\omega$ , and  $N\pi$  are primarily involved in these baryon

spectrum made in  $\gamma p$  reaction. The 3-body final states, like  $N\pi\pi$ , especially account for most of cross sections above  $E_\gamma \sim 1.07$  GeV, as shown in Figure 1.8. The  $\gamma p$  reaction data with 3-body final states provide a good opportunity to discover the missing high-mass resonances.

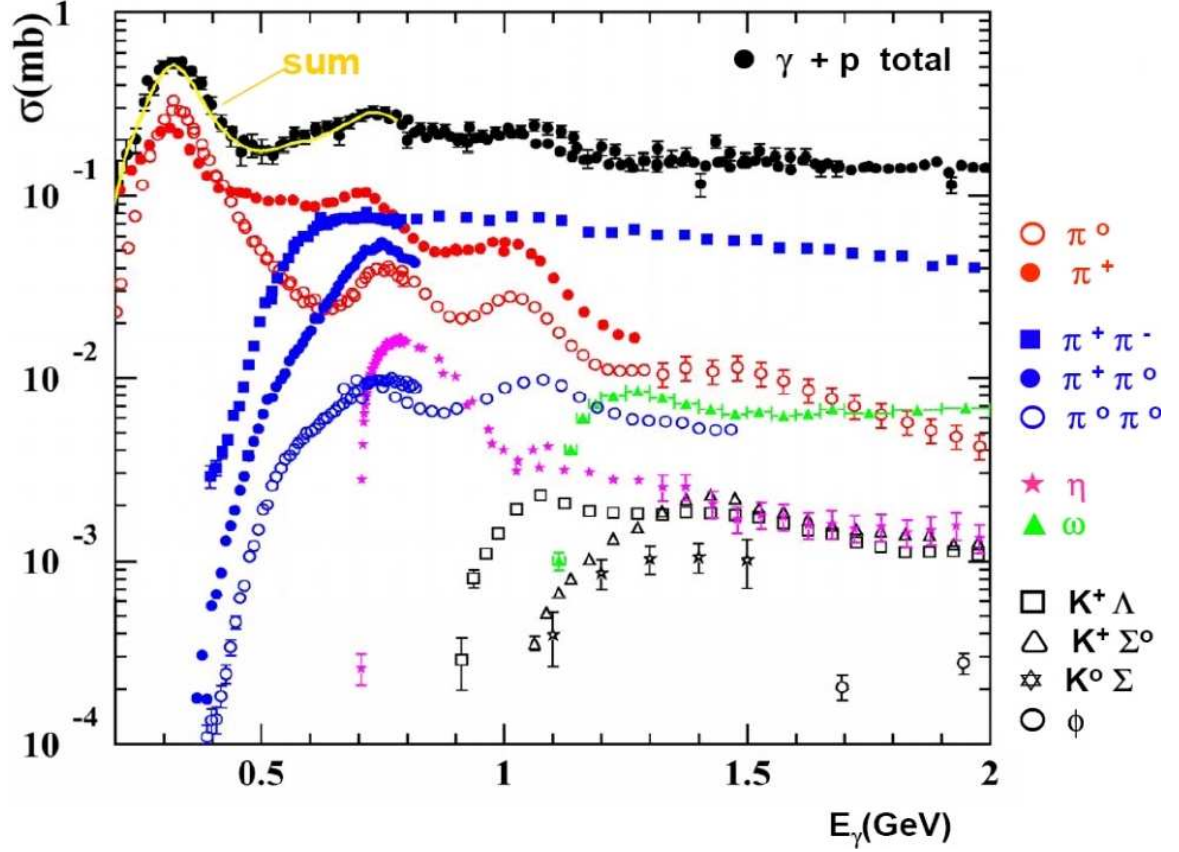


Figure 1.8: Total cross section for  $\gamma p$  reaction with contributions of individual channels.

Most of the high-lying resonances in the  $N\pi\pi$  channels are predicted to decay into excited intermediate states rather than directly to the ground state via single-meson emission. Therefore the missing resonances can be found in the intermediate state leading to a final state with two mesons, like  $\gamma p \rightarrow N^* \rightarrow \Delta^{++}\pi^- \rightarrow p\pi^+\pi^-$ . CQMs have given at least 150 MeV as the theoretical width of these missing resonances. However, calculations of the decays of these resonances into 2-body final states like  $K\Lambda$ ,  $K\Sigma$ ,  $N\omega$ , and  $N\pi$  result in very narrow partial widths. This indicates that the final state with  $N\pi\pi$  channels dominates more than a 2-body final state at the high energies.

Figure 1.9 (a) shows a broad structure called the "second resonance region" above the energy range of the  $\Delta$  resonance,  $P_{33}(1232)$ , at incident photon energies between 0.5 and 0.9 GeV. The second resonance region has a more complex structure than the peak corresponding to the  $\Delta$  resonance,  $P_{33}(1232)$ . Three nucleon resonances,  $P_{11}(1440)$ ,  $D_{13}(1520)$ , and  $S_{11}(1535)$ , have primarily overlapped in the second resonance region. The tails from the  $\Delta$  resonance,  $P_{33}(1232)$  and additional higher resonances are included as well. This second resonance region also consists of a complicated superposition of the different reaction channels which differ in their energy dependence. Figure 1.9 shows the total cross section for  $\gamma p$  reaction, and the partial cross sections of the different reaction channels. The partial channels add up precisely to the total cross section. The total cross section in the energy range corresponding to the  $\Delta$  resonance,  $P_{33}(1232)$ , originates entirely in single pion production. The production of two pions and  $\eta$  mesons is only allowed in the second resonance region, due to the kinematic particle thresholds. Most of the rise of the cross section in the second resonance region, as shown in Figure 1.9 (b), comes from double pion production. The partial cross section of the double pion production is very useful to understand the complicated second resonance region.

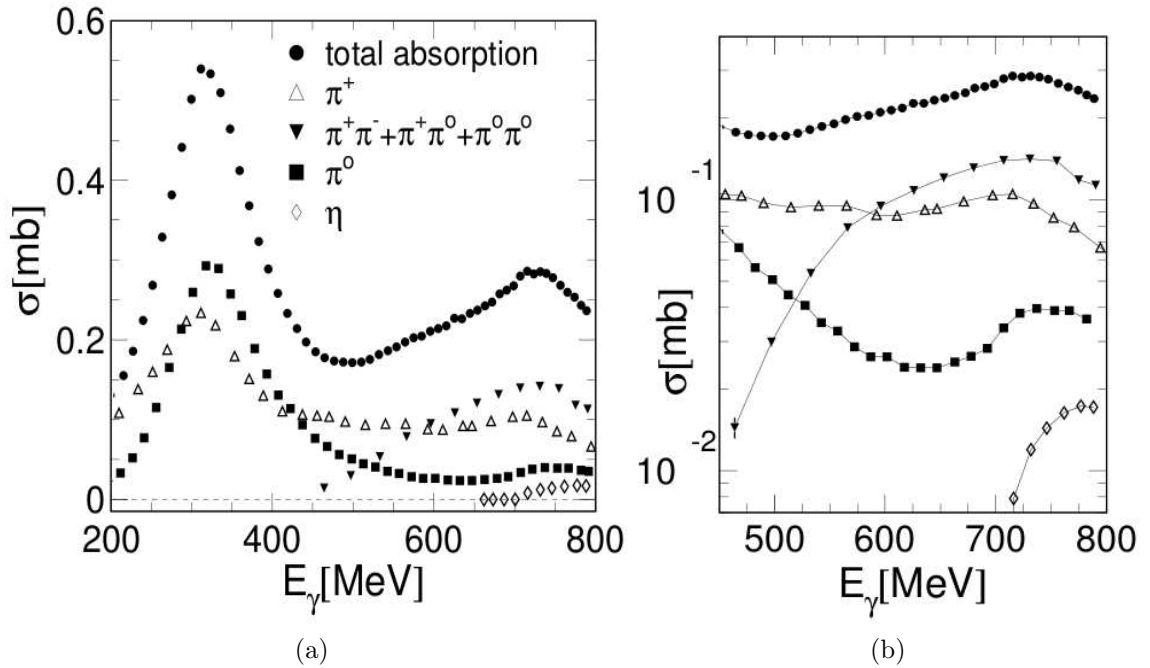


Figure 1.9: (a) Total photoabsorption and partial cross sections for photoproduction off the proton. (b) Second resonance region in logarithmic scale [8].

Hadron spectroscopy experiments produce the excited baryon states, and measure properties of these resonances as precisely as possible to test quark models. The emission of mesons via the strong interaction is usually the most common decay mode

for all resonances. Figure 1.10 shows the lowest lying nucleon resonances with their respective mesonic decay channels. Since these resonances have very short life times, their widths in the mass measurement are quite broad, with widths on the order of 100 MeV. This implies that the individual resonances in the excited baryon spectrum should be not only broad but also overlapping. These general characteristics of individual resonances make it difficult to identify the resonances contained in the excited baryon spectrum. In Figure 1.10, the  $P_{33}(1232)$  resonance is isolated at 1232 MeV. However, other resonances are laid quite close to this neighborhood and thus are overlapped strongly, especially  $P_{11}(1440)$ ,  $D_{13}(1520)$ , and  $S_{11}(1535)$  in the second resonance region. For this reason, it is difficult to study the excitation spectra alone in an effort to present an accurate description of individual resonances.

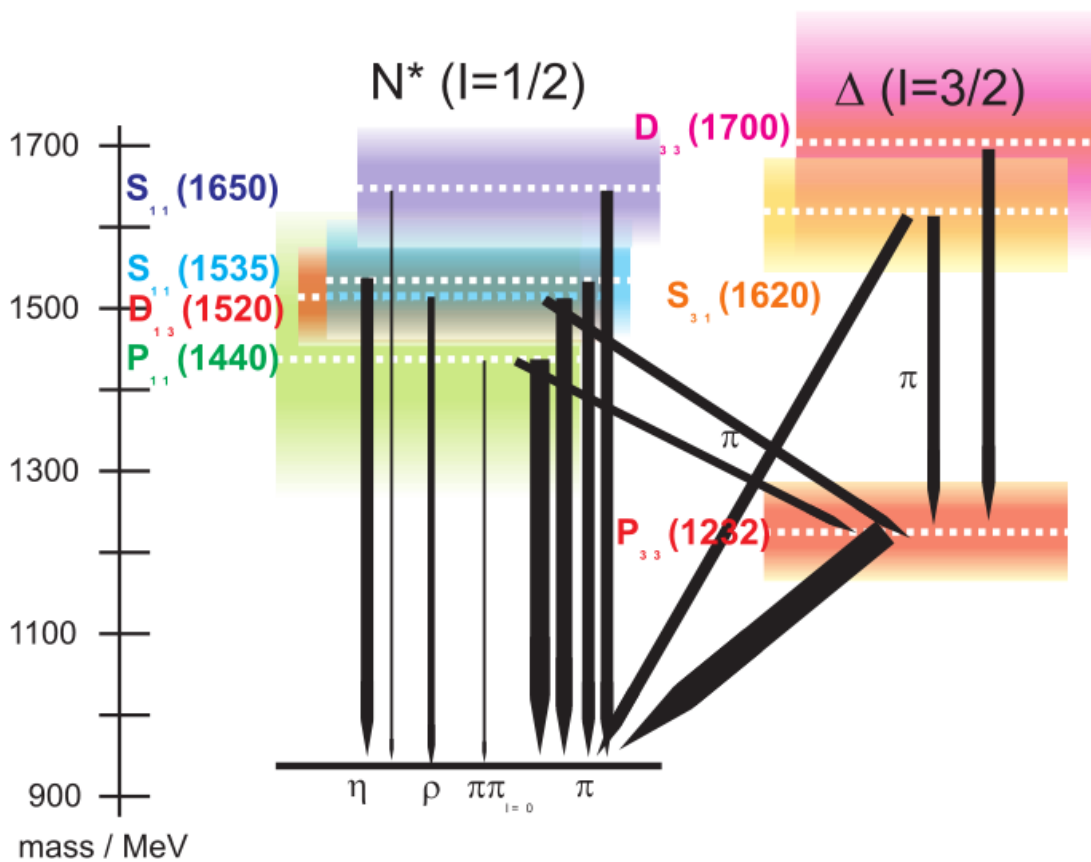


Figure 1.10: Nucleon excitation spectrum showing the lowest lying resonances. The black arrows show the mesonic decay of these resonances with width proportional to the branching ratio. The shaded colored areas represent the widths of the resonances [9].

### 1.3.3 Polarization Observables

In order to study individual resonances from an area in which several resonances are overlapped, like the second resonance region, measurable quantities called polarization observables are a very useful tool to evaluate  $N^*$  parameters, since polarization observables are very sensitive to small resonant contributions. After model-dependent theoretical values related to polarization observables are extracted from the model calculations, these theoretical values can be compared with the experimentally measured values. Resonance contributions can be explored by omitting or including them in model observables. Precisely determined polarization observables give very stringent constraints to the models, and help us understand the underlying processes present in double pion photoproduction.

Differential cross section data are not sensitive to adding or omitting these small resonant couplings. However, their interferences with the dominant amplitude will reveal more clearly resonances with a small contribution to the cross section, and these interference terms can be isolated via polarization observables. For example,  $D_{13}(1520)$  resonance can reveal itself in the beam-asymmetry data of  $\eta$  production by its interference with the dominant amplitude of  $S_{11}(1535)$ . In the general polarization experiment there are three different polarizations considered: beam, target, and recoil. First, the incoming photon is able to be polarized 0 or linearly. The target nucleon can be polarized, and in this case two polarizations can be taken into account: the polarization before (target polarization) and after interaction (recoil polarization). Therefore, there are single, double, and triple polarization experiments, depending on the number of polarizations observed. The theoretical description of the general triple polarization case, involving 64 polarization observables in double-meson photoproduction, has been given by W. Roberts and T. Oed [10].

In a double-polarization experiment, the differential cross section for single-meson production,  $d\sigma/dx_i$ , is given by :

$$\begin{aligned} \frac{d\sigma}{dx_i} = \sigma_0 \{ & 1 - \delta_l \Sigma \cos 2\phi \\ & + \Lambda_x (-\delta_l \mathbf{H} \sin 2\phi + \delta_{\odot} \mathbf{F}) \\ & - \Lambda_y (-\mathbf{T} + \delta_l \mathbf{P} \cos 2\phi) \\ & - \Lambda_z (-\delta_l \mathbf{G} \sin 2\phi + \delta_{\odot} \mathbf{E}) \}. \end{aligned} \quad (1.2)$$

where  $x_i$  are kinematic variables, as described in Section 5.1.1, and  $\sigma_0$  is the unpolarized cross section.  $\delta_{\odot}$  is the degree of a circular polarization in the photon beam, while  $\delta_l$  is the degree of a linear polarization. Here,  $\vec{\Lambda}$  denotes the polarization of the initial nucleon;  $\Lambda_x$  and  $\Lambda_y$  for transverse polarization, and  $\Lambda_z$  for longitudinal polarization. There are 7 polarization observables obtainable from the analysis of a single-meson final state:  $\Sigma$ ,  $\mathbf{H}$ ,  $\mathbf{F}$ ,  $\mathbf{T}$ ,  $\mathbf{P}$ ,  $\mathbf{G}$ , and  $\mathbf{E}$ . In the case of single-meson

photoproduction, two independent kinematic variables are needed.

The analysis of a channel with two final state mesons requires three additional terms as kinematic variables. These additional variables are used to describe the decay plane which can be formed for every reaction in which the two final state pions occur, and the orientation of the decay plane with respect to the production plane<sup>1</sup>. The analysis of a double-meson final state requires a great deal more observables than a single-meson final state. For  $\gamma p \rightarrow p \pi \pi$ , without measuring the polarization of the recoiling nucleon, the differential cross section can be written as: [10] :

$$\begin{aligned} \frac{d\sigma}{dx_i} = \sigma_0 \{ & (1 + \vec{\Lambda}_i \cdot \vec{\mathbf{P}}) \\ & + \delta_{\odot} (\mathbf{I}^{\odot} + \vec{\Lambda}_i \cdot \vec{\mathbf{P}}^{\odot}) \\ & + \delta_l [\sin 2\beta (\mathbf{I}^s + \vec{\Lambda}_i \cdot \vec{\mathbf{P}}^s) \\ & + \cos 2\beta (\mathbf{I}^c + \vec{\Lambda}_i \cdot \vec{\mathbf{P}}^c)] \}. \end{aligned} \quad (1.3)$$

The two-meson final state equation, as referenced in Equation 1.3, contains 15 polarization observables.  $\mathbf{I}^{\odot}$ ,  $\mathbf{I}^s$ , and  $\mathbf{I}^c$  are observables which arise from the beam polarization. The observable  $\mathbf{I}^{\odot}$  describes the beam asymmetry for an unpolarized target and a circularly-polarized photon beam. The polarization observable  $\mathbf{I}^c$  is equivalent to  $\Sigma$  in Equation 1.2. The observables  $\vec{\mathbf{P}}$  represent the target asymmetry that arises if only the target nucleon is polarized, and  $\vec{\mathbf{P}}^{\odot}$  as well as  $\vec{\mathbf{P}}^{s,c}$  represent the polarization observables if, in addition to the target nucleon, the incoming photon is also polarized, either circularly or linearly, respectively. The observable  $\mathbf{I}^{\odot}$  in double-pion photoproduction data has been published. It has been analyzed from CLAS g1c data [11] and MAMI, TAPS, and A2 Collaboration data [12]. The observable  $\mathbf{P}_z^{\odot}$ , equivalent to  $\mathbf{E}$  in Equation 1.2 for single pion photoproduction, has been also published in double-pion photoproduction data from GDH and A2 Collaboration data [13].

The differential cross section for  $\gamma p \rightarrow p \pi \pi$ , in the case of a circularly-polarized beam on a longitudinally polarized target in the g9a experiment, can be written as:

$$\frac{d\sigma}{dx_i} = \sigma_0 \{ (1 + \Lambda_z \cdot \mathbf{P}_z) + \delta_{\odot} (\mathbf{I}^{\odot} + \Lambda_z \cdot \mathbf{P}_z^{\odot}) \}. \quad (1.4)$$

The number of polarization observables, as referenced in Equation 1.4, has been reduced from 15 to 3. The polarization observable  $\mathbf{I}^{\odot}$  related to a beam-helicity asymmetry, the observable  $\mathbf{P}_z$  related to a target asymmetry, and the observable  $\mathbf{P}_z^{\odot}$  related to the helicity difference can be determined from this dataset.

---

<sup>1</sup>The production plane and decay plane are defined in Figure 5.1.

# CHAPTER 2

## FROST EXPERIMENT

The data used in this analysis were taken as part of the g9a run period at the Thomas Jefferson National Accelerator Facility (JLab) in Newport News, Virginia. In the name "*g9a*", the "*g*" refers to a photoproduction experiment, the "*9*" indicates that it was the ninth approved experiment in Hall B, and the "*a*" denotes the first iteration of the "*g9*" experiment. Figure 2.1 shows the three experimental halls in the foreground along with the CEBAF electron accelerator. A new experimental hall for the 12 GeV upgrade program, Hall D housing the GlueX experiment is located in the north of the CEBAF electron accelerator.



Figure 2.1: An aerial view of the accelerator and the three experimental halls at Jefferson Lab. The Continuous Electron Beam Accelerator Facility (CEBAF) is the racetrack accelerator, and the three mounds located at the bottom of the photograph are the three experimental halls: Hall A, Hall B, and Hall C (left to right).

Hall B provides a unique set of experimental devices for the FROzen Spin Target (FROST) experiment. First, the CEBAF Large Acceptance Spectrometer (CLAS) [14]

is a nearly- $4\pi$  spectrometer. Second, the broad-range photon tagging facility at JLab [15], can tag photon energies over a range of from 20% to 95% of the incident electron energy, and is capable of operation with beam energies up to 5.5 GeV. The remaining element which is indispensable for the double polarization experiment is the frozen-spin target [16].

## 2.1 CEBAF Electron Accelerator

The Continuous Electron Beam Accelerator Facility (CEBAF) at JLab has two superconducting radio-frequency (RF) linear accelerators, 1.4 km in length, to deliver electron beam up to 6 GeV to the three experimental halls and these linacs are connected at each end with recirculation arcs. Figure 2.2 shows the accelerator with the racetrack shape which consists of a 45-MeV injector, two anti-parallel linear accelerators (LINACs), and 9 recirculating arcs (4 at one end and 5 at the other).

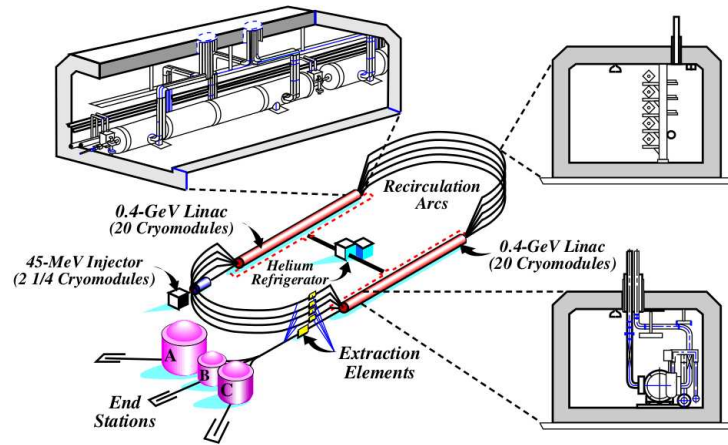


Figure 2.2: Schematic drawing of CEBAF and the three experimental halls. Included are, clockwise from the top, a module in the linac, a steering magnet, and a part of the RF separator [14].

The injector consists of two electron guns: a thermionic gun and a polarized gun. In the g9a experiment, the polarized electron gun was used to produce polarized electrons by illuminating a strained Gallium Arsenide (GaAs) photocathode with a 1497 MHz gain-switched diode laser operated at 780 nm [17]. The electrons produced in the injector are longitudinally polarized, with the degree of polarization reaching up to 85%. The process of making polarized electron beam begins with a circularly polarized photon beam. The circularly-polarized photons are made from an unpolarized laser through the use of two Pocket cells, which are composed of a quarter-wave plate and a half-wave plate. The strained GaAs cathode uses the photoelectric effect

to turn circularly-polarized photons into longitudinally-polarized electrons. A 5 MeV Mott polarimeter measured the polarization of the electron at the injection point. After the extraction of the electrons from the photocathode,  $2\frac{1}{4}$  superconducting radio-frequency (RF) cavities, as shown in Figure 2.3, are used to accelerate the electrons to 45 MeV. An optical chopper is then used to separate cleanly the 2 ns bunches prior to injecting them into the LINACs. Each LINAC is equipped with 20 cryomodules, and each cryomodule is made of 20 superconducting RF cavities, as shown in Figure 2.3.

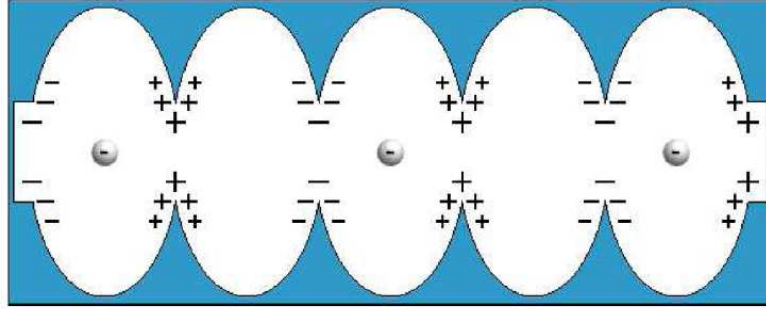


Figure 2.3: A diagram of an RF cavity with the charge gradient produced.

The RF cavities of the LINACs to accelerate the electrons produce a standing electromagnetic wave in phase with the bundles of electrons. This electromagnetic wave makes a charge gradient to serve as the source of the acceleration in the RF cavity. Figure 2.3 shows that the RF cavity maintains the standing electromagnetic wave such that there is a negative electric field filed behind the electrons, and a positive electric field in front of the electrons. Therefore each LINAC is able to accelerate the electrons up to 600 MeV in energy with each pass through the LINAC. Two  $180^\circ$  arcs with a radius of 80 m complete the circuit between each linear accelerator. Several quadrupole and dipole magnets are used to steer and focus the beam as it passes through the accelerator. The electron beam is continuously generated with 45 MeV at the injector, and accelerated through the two linacs so that electrons gain  $\approx 1.2$  GeV for each trip they take around the accelerator. Each Hall can choose to extract the beam after any number of passes, up to five only. After the beam reaches the desired energy, it is delivered to one or more of the experimental halls.

## 2.2 Broad-Range Photon Tagging Facility

The g9a experiment uses the tagged bremsstrahlung method to create and identify the energy of the photon. Figure 2.4 show the photon tagging system (tagger)

in Hall B to tag photons with energies ranging from 20 % to 95 % of the incident electron beam energy [15].

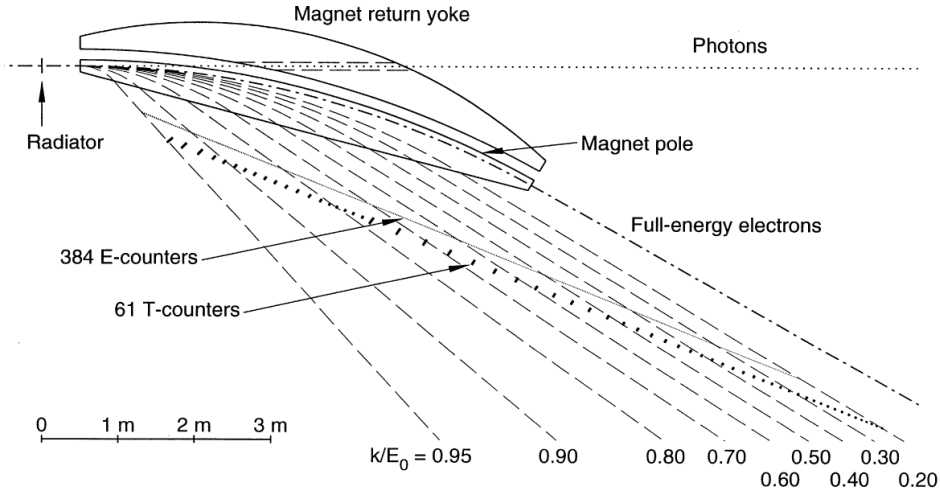


Figure 2.4: Overall geometry of the bremsstrahlung photon tagging system. The electrons, which enter from the left, are scattered off the radiator and then are "tagged" while the photons go downstream through the collimator (not shown in this picture). The dashed lines indicate the trajectories made by recoil electrons with various fractional energies. The two planes of the scintillator hodoscope, the E- and T-planes, are shown geometrically.

Electrons from the CEBAF accelerator strike the radiator upstream from the tagger and scatter off, producing photons via bremsstrahlung radiation. In this process, the incoming electrons interact with the electromagnetic field of the nuclei of the radiator material. When the electron of incident energy  $E_0$  encounters this field, it feels a braking force and emits a bremsstrahlung photon into the target material located at the center of the CLAS spectrometer, as shown in Figure 2.5. Since the energy transferred to the nucleus is negligible, the reaction obeys the energy conservation relation :

$$E_\gamma = E_0 - E_e, \quad (2.1)$$

where  $E_e$  is the energy of the outgoing electron and  $E_\gamma$  is the energy of the emitted bremsstrahlung photon. Since  $E_0$  can be determined from the accelerator, a measurement of the outgoing electron energy by a magnetic spectrometer thus provides a determination of the photon energy. The radiator for the tagger is usually a thin Gold or Carbon foil, and radiators with different thicknesses can be moved into position to change the intensity of the photon beam. Circularly-polarized photon beam produced from the longitudinally-polarized electron beam. Linearly polarized photons can be

produced via coherent bremsstrahlung of the incoming electrons interacting with a well-oriented diamond radiator.

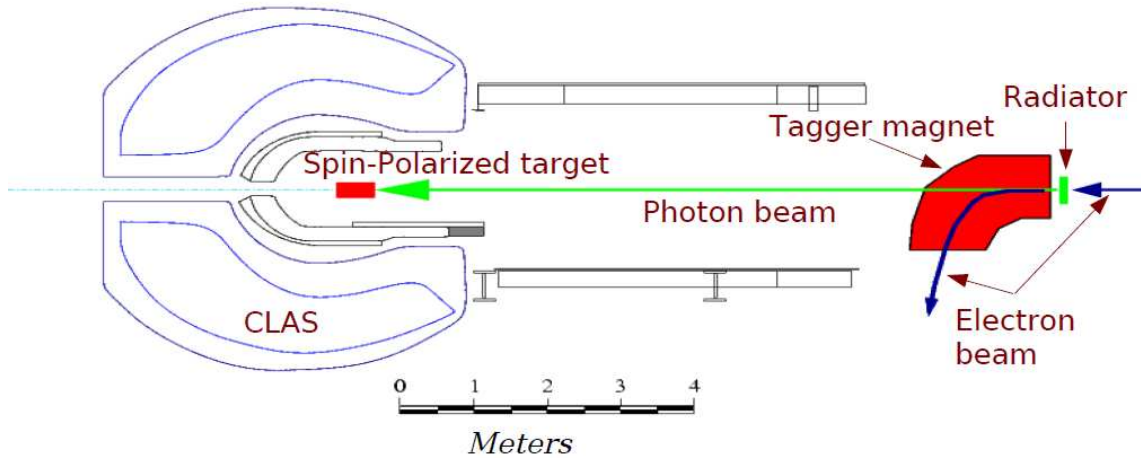


Figure 2.5: Side view schematic of the Tagger and the CLAS spectrometer in Hall B.

Between the radiator and the target material, as shown in Figure 2.5, there is a tagger magnet, which is a C-shaped magnet with an open-yoke design capable of producing a magnetic field up to 1.75 T. After passing through the radiator, the beam will be a mixture of non-interacting electrons, recoil electrons, and photons. The Tagger Magnet is used to bend the recoil electrons towards the two scintillator planes, which are composed of an E-counter plane (for measuring the electron energy) and T-counter plane (for measuring the time), as shown in Figure 2.4. Unscattered electrons are bent out of the beamline and guided directly into the Taggers beam dump, bypassing the E- and T-counters.

The first plane of scintillators, referred to as the "E-counters" in Figure 2.4, is used to determine the momentum of the recoiling electrons and is aligned with the optical focal point of the tagger magnet. The E-counter plane is made of 384 plastic scintillators that are 20 cm long and 4 mm thick, with widths varying from 6 to 18 mm. These scintillators are arranged in an overlapping manner with one scintillator covering 1/3 of its neighbors width, therefore creating 767 separate energy channels. The trajectory followed by an electron in the magnetic field is governed by its momentum. Thus, by determining which paddle an electron passed through, we can calculate its momentum. The momentum of the recoil electron can then be used to obtain the energy of the photon. The energy resolution of the E-counter plane is 0.1 % of the incident electron beam energy. The second plane of scintillators, referred to as the "T-counters" in Figure 2.4, is used to make accurate timing measurements of the

recoiling electrons. The determination of the time at which a photon arrived at the target is crucial to any analysis involving photoproduction. A timing resolution of 300 ps or greater is required to associate the measured time of an electron with the corresponding electron bunch, and therefore to determine the photon time at the target center. The T-counter plane is positioned parallel to the E-counter plane and consists of 61 scintillator counters, 2 cm thick, which vary in length from 20 cm at the high electron momentum end to 9 cm at the low-momentum end. The spectrometer was able to tag photons ranging from 20 - 95 % of the incident electron beam energy.

## 2.3 CLAS Spectrometer

The CEBAF Large Acceptance Spectrometer (CLAS), as shown in Figure 2.7, is used to detect particles produced by interactions of the photon beam with the target located near the center of the CLAS spectrometer.

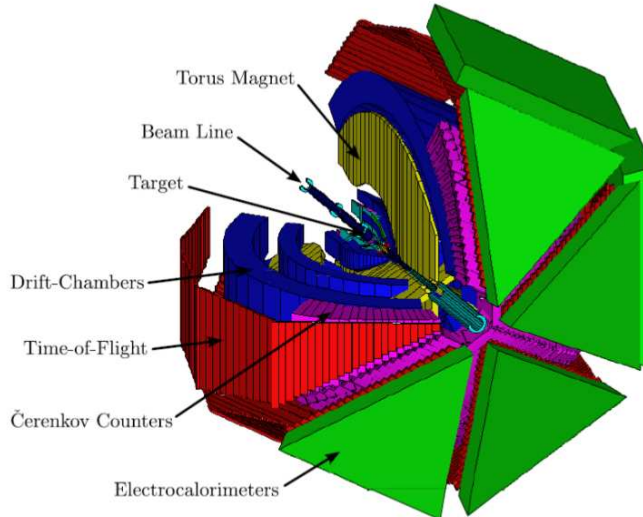


Figure 2.6: Schematic of the CLAS spectrometer. This spectrometer, approximately 8 m in diameter, is housed in experimental Hall B at Jefferson Lab.

The CLAS spectrometer arranged symmetrically around the beam axis is based on six superconducting coils producing a toroidal magnetic field, and azimuthally divided into six independent sectors within this superconducting toroidal magnet. Even though the CLAS spectrometer has almost  $4\pi$  angular coverage in the solid angle, there are dead regions, where the CLAS spectrometer cannot measure particles due to the presence of structures like the beamline, the toroidal magnet's support structure and others. In reality, the spectrometer covers between  $8^\circ < \theta < 145^\circ$

in its polar angle, and  $-25^\circ < \phi < 25^\circ$  along its azimuthal angle, for each sector. Each sector is composed of multi-wire drift chambers (DC) to determine charged-particle trajectories, scintillation counters (SC) for time-of-flight measurement, gas Cherenkov counters (CC) for the identification of recoil electrons in electroproduction experiments, and an electromagnetic calorimeter (EC) for electron, photon and neutron energy measurement and detection. Close to the target region, a sub-nanosecond time coincidence of the tagging spectrometer with a counter (ST) measures the start time of a particle trajectory to better than 25 ps. Since Cherenkov counters are not used in our analysis, it will not be discussed here. Each detector subsystem of the CLAS spectrometer will be described in detail in the following sections.

### 2.3.1 Start Counter (ST)

In run periods using a photon beam instead of an electron beam, the mini-torus<sup>1</sup> is replaced with the Hall B Start Counter. This Start Counter, as seen in Figure 2.7, is located at the center of the CLAS spectrometer and surrounds the target. It provides a precise start time for every trigger recorded by the CLAS spectrometer as well as a time of the hadronic interaction in the target.

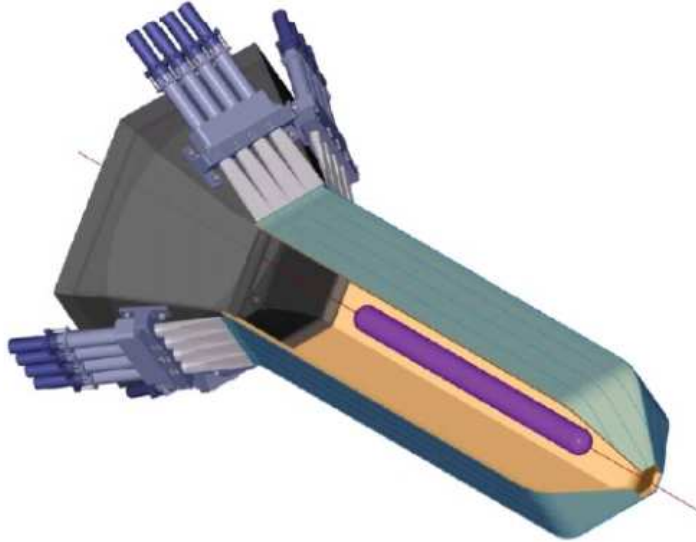


Figure 2.7: A CAD drawing of the Start Counter used for the g9 experiment.

The Start Counter has six identical sectors, matching the six-sector geometry of the CLAS spectrometer. Each of these sectors is made of four scintillator paddles,

---

<sup>1</sup>The mini-torus is used only for run periods using an electron beam, and prevents the electrons in the beam from reaching the drift chambers.

giving a total of twenty-four paddles for the entire structure. The forward tips of the scintillators are bent to form the nose cone of the Start Counter. PMTs, which are attached to the other end of the scintillators, are used as solid light-guides to collect the scintillation light produced on passage of a particle through it. Each paddle is 502 mm long, 29 mm wide, and 2.15 mm thick, which, along with the wrapping and the support material, gives a total thickness of about  $0.26 \text{ g/cm}^2$ . A charged particle traversing the paddle causes light to be produced inside the scintillator. This light is reflected from the mirror film and makes its way to the light guide attached to the PMT. At the PMT, the photo-signal is collected, converted, and amplified and then the ADC and TDC values of this photo-signal are recorded to be used later in the analysis. This Start Counter is capable of providing a fast timing signal ( $\sim 25 \text{ ps}$ ) for the CLAS trigger that, when coupled with the information from the tagger and time-of-flight systems, can be used to reduce greatly the accidental trigger rate. It also helps determine information about velocities of charged particles when combined with information from the time-of-flight system in the CLAS spectrometer. When compared with the RF time, the Start Counter yields the start time of the particle trajectory to better than 25 ps accuracy.

### 2.3.2 Torus Magnet

The torus magnet is composed of six individual superconducting coils around the electron beam line. Figure 2.8 shows the mapping of the magnetic field produced by the CLAS Torus Magnet.

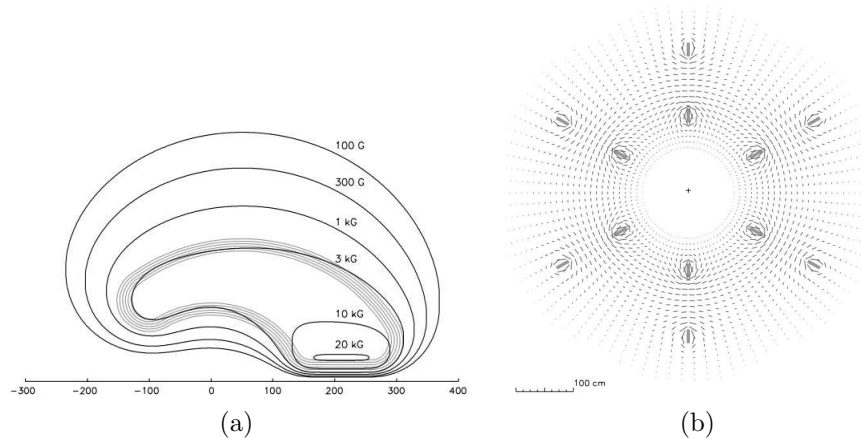


Figure 2.8: (a) Contours of the constant absolute magnetic field for the CLAS toroid magnet in the midplane between two coils and (b) the toroidal magnetic field as seen from a plane centered on the target. The length of the lines indicates the field strength at that point.

The magnetic field created by the CLAS Torus Magnet makes the charged particles bend towards or away from the beamline, depending on the charge of the particle and the polarization of the torus, while leaving their azimuthal angle practically unchanged. The magnetic field thus allows one to analyze the momentum of the charged particles. This magnetic field also provides a magnetic field-free region around the target, which allows for the use of dynamically polarized targets. The maximum designed current in the torus coils is 3860 A, corresponding to the integral magnetic field of 2.5 Tm in the forward direction, and 0.6 Tm at a polar angle of  $90^\circ$ . When the current is positive, the magnetic field bends the negative charged particle toward the beam line; therefore, the data taken with positive torus current are called inbending data, whereas the data taken with a negative torus current are called outbending data. The g9a data were taken at a torus current of 1920 A as inbending data.

### 2.3.3 Drift Chamber (DC)

The momentum of charged particles is determined by tracking the particles through the field generated by the toroidal magnet, as shown in Figure 2.8. Each sector of the CLAS spectrometer consists of three sets of Drift Chamber, as shown in Figure 2.9.

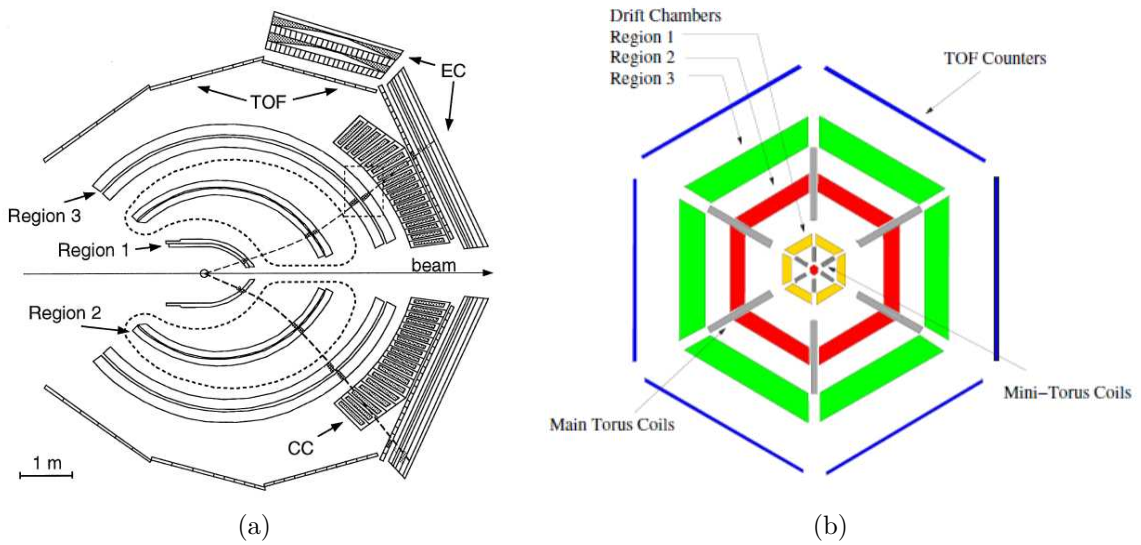


Figure 2.9: (a) Horizontal cut through the CLAS spectrometer showing two charged particles traveling through the DC in opposite sectors. (b) Vertical cut through the DC transverse to the beam line at the target location.

From the curvature of the trajectory of charged particles, as shown in Figure 2.9 (a), the sign of the charge  $q$  of the particle, and the radius of the curvature  $R$  can be de-

terminated. The magnetic field  $B$  is known from the field maps, as shown in Figure 2.8, and therefore, using the knowledge of the supplied current, the momentum  $p$  can be determined from the relation  $p = qBR$ . The charged particles can be tracked using three separate DC regions: region 1 (R1), region 2 (R2), and region 3 (R3). The R1 chambers are located close to the target in an area of low magnetic field. The R2 chambers are larger and reside between the torus coils in an area of high magnetic field. Finally, the R3 chambers are the largest, located radially outside of the torus magnet.

Each DC region is divided into two separate superlayers. Each superlayer consists of six layers, except for superlayer 1 in R1 which consists of only 4 layers. The DC has one anode sense wire at a positive potential surrounded by six cathode wires in an hexagonal shape at a negative potential, as shown in Figure 2.10. The DC is filled with an 88–12% mixture of argon and  $CO_2$  to improve the operating lifetime and system safety. Therefore, as the charged particle passes through the gas in the DC, it ionizes the atom and produces ion pairs. The negative ions drift to the sense wire and create a voltage pulse on the sense wire. The pulse is presented to the time-to-digital converters (TDC) for digitization. The online data acquisition system measures and stores these raw TDC times.

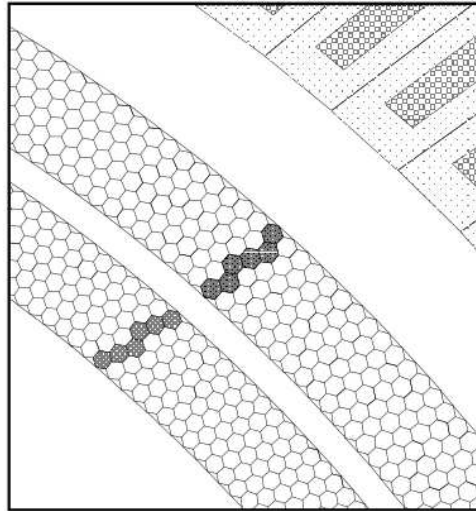


Figure 2.10: The hexagonal Drift Chamber of R3 chamber, showing the layout of its two superlayers. The highlighted drift cells indicate a passing charged particle. The upper right corner shows the edge of the Cherenkov counters.

### 2.3.4 Time of Flight Counters (TOF)

The time information of charged particles crossing the Drift Chambers is measured by the time-of-flight (TOF) scintillation paddles and the transit time for the particles passing through the magnetic field area. It can be measured when this passing time is combined with the time of a hadronic interaction in the target. The track length can be calculated by using the tracking information from the Drift Chamber system, and the  $\beta$  is defined by the equation  $\beta = v/c$ . Once  $\beta$  and  $p$  are given, the mass of the particle can be calculated, and thus particles are identified such as pions, protons, kaons, etc. To determine the masses of all charged particles originating from a hadronic interaction, the TOF counters, as shown in Figure 2.11 (a), cover a polar angle from  $8^\circ$  to  $142^\circ$ , and nearly the entire azimuthal angle. Each one of the six panels of the TOF counts contains 57 scintillator paddles of varying lengths and widths. To provide 100% detection efficiency of minimum ionizing particles, each paddle is made 2 inches thick and the signals from the scintillators are collected via photo-multiplier tubes (PMTs) mounted at each end of the bars.

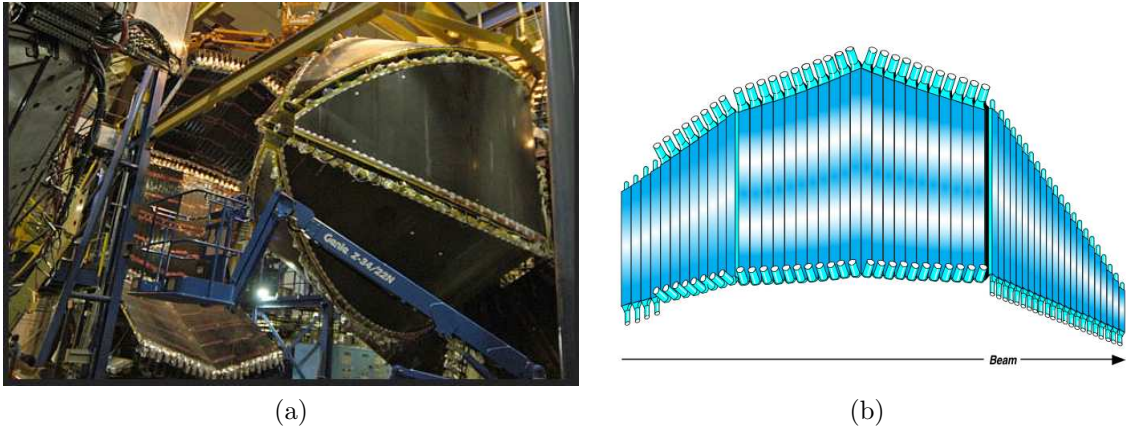


Figure 2.11: (a) A picture of the Time-of-Flight counters revealed when CLAS is opened. TOF can be seen to the far left. The part of the CLAS spectrometer revealed is the region 3 of the Drift Chamber. (b) A diagram of a ToF sector, showing the scintillation counters arranged in four panels and perpendicular to the beam line. At both ends of each paddle are a light guide and a PMT.

### 2.3.5 Electromagnetic Calorimeters (EC)

The forward electromagnetic calorimeter (EC) detects electrons with energies above 500 MeV, photons with energies above 200 MeV (for the reconstruction of  $\pi^0$  and  $\eta$  mesons), and also detects neutrons. The EC covers laboratory scattering angles from  $0$  to  $45^\circ$ . There are six EC modules matching the CLAS sector geometry. Each EC module has 39 layers in an alternating sandwich arrangement of scintillator

strips and lead sheets. Each layer of scintillator with the shape of a nearly equilateral triangle is a 10 mm thickness followed by a 2.2 mm thick lead sheet. Each scintillator layer consists of 36 strips parallel to one side of the triangle. Each successive layer is rotated through  $120^\circ$ , effectively creating three orientations (labeled U, V, and W) with each orientation containing 13 layers, as shows in Figure 2.12.

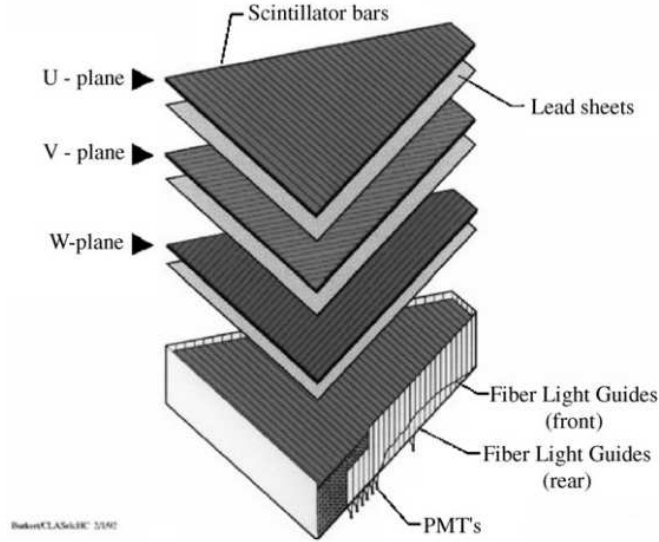


Figure 2.12: Enlarged diagram of one of the six CLAS electromagnetic calorimeter modules.

## 2.4 Frozen Spin Target (FROST)

The previous Hall B polarized target was able to polarize protons in  $^{15}\text{NH}_3$  or deuterons in  $^{15}\text{ND}_3$  only longitudinally, and covered scattering angles up to  $55^\circ$  from the beam. However, the Frozen Spin Target (FROST) can be both longitudinally and transversely polarized, having a  $4\pi$  angular coverage in the scattering angle. The FROST target can also reach polarization values over 80 % at a base temperature of 28 mK [18] [19]. In order to polarize the protons within the target material. A technique called dynamic nuclear polarization (DNP), as shown in Figure 2.13, is used. In the DNP method, free electrons in the target material are polarized by brute force polarization [20] :

$$P = \tanh\left(\frac{\vec{\mu} \cdot \vec{B}}{kT}\right), \quad (2.2)$$

To achieve the high degree of polarization, a maximized B field and minimized temperature are required. At JLab, the DNP process is performed at a "moderate" temperature of approximately 0.3 K using 5.0 T polarizing magnet, where the

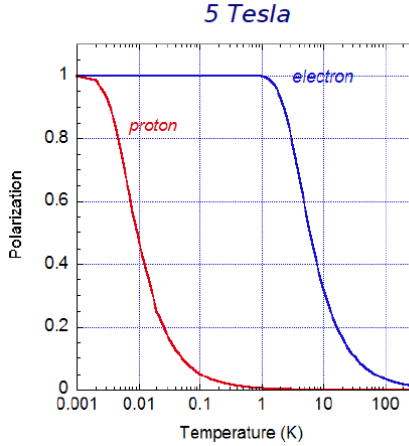


Figure 2.13: The polarization of an electron and proton by brute force.

time required to polarize an electron is short (ms) and the time for a nucleus is long (minutes), as shown in Figure 2.13. Then the spin polarization of electrons, spread throughout the target mixture, is transferred to the nuclei of the target material using microwaves. Mutual electron-nucleus spin flips rearrange the nuclear Zeeman populations to favor one spin state over the other. However, the disadvantage of the DNP method is that a large magnet for the experiment is required, and a choice of target material is very limited. Thus, materials for DNP targets should adhere to some choice of target material: a maximum polarization, a resistance to ionization from radiation, a minimum number of unpolarizing nucleon. Table 2.1 shows conditions of materials for DNP targets considered for the FROST experiment.

Table 2.1: Examples of materials for DNP targets.

Name	Dopant	$f = \tilde{N}/N_{\text{total}}$	Radiative resistance
Polyethylene, $C_2H_4$	chemical	0.12	low
Polystyrene, $C_8H_8$	chemical	0.07	low
Propandiol, $C_3H_6(OH)_2$	chemical	0.11	moderate
Butanol, $C_4H_9OH$	chemical	0.13	moderate
Ammonia, $^{15}NH_3$	radiation	0.17	high
Lithium Hydride, $^7LiH$	radiation	0.12	very high

The FROST experiment uses three kinds of meson production targets: the FROST target, a graphite (carbon) target, and a polyethylene ( $CH_2$ ) target. The FROST experiment uses butanol as the ideal target material. The carbon and polyethylene

targets are useful for various systematics checks, and for the determination of the contribution of bound nucleons in the butanol data. FROST has the capability of polarizing the butanol target by the DNP, as mentioned earlier. Another important characteristic of FROST is that it can also freeze this polarization via a cooling of the target material and usage of a small holding magnet field. In order for the spin polarization of the butanol target to be frozen, a temperature of at least 50 mK for the FROST is required. The FROST uses a  $^3\text{He}/^4\text{He}$  dilution refrigerator to accomplish this cooling process for the butanol target. Refrigeration below 4.2 K is performed by the method of evaporative cooling. Below 0.8 K, the mixing chamber in the dilution refrigerator can separate into two phases, as shown in Figure 2.14 (a): a dilute phase of a  $^3\text{He}$ -poor region and concentrated phase of a  $^3\text{He}$ -rich region. The two phases of the  $^3\text{He}/^4\text{He}$  mixture in the mixing chamber have different specific heats: 106 J/(mol·K) for dilute phase and 22 J/(mol·K) for the concentrated phase. The  $^3\text{He}$  atoms then move from the concentrated phase (a  $^3\text{He}$ -rich region) to the dilute phase (a  $^3\text{He}$ -poor region) with the heat energy exchange with the surroundings. Removing the  $^3\text{He}$  from the dilute phase causes the  $^3\text{He}$  atoms in the concentrated phase to absorb the heat from its surroundings and dissolve into the dilute phase in order to re-establish a thermal equilibrium. This process occurs in the mixing chamber of the FROST where the butanol target exists. When this evaporation of  $^3\text{He}$  into  $^4\text{He}$  occurs, heat is taken from the target material. This process is implemented around FROST, as shown in Figure 2.14 (b).

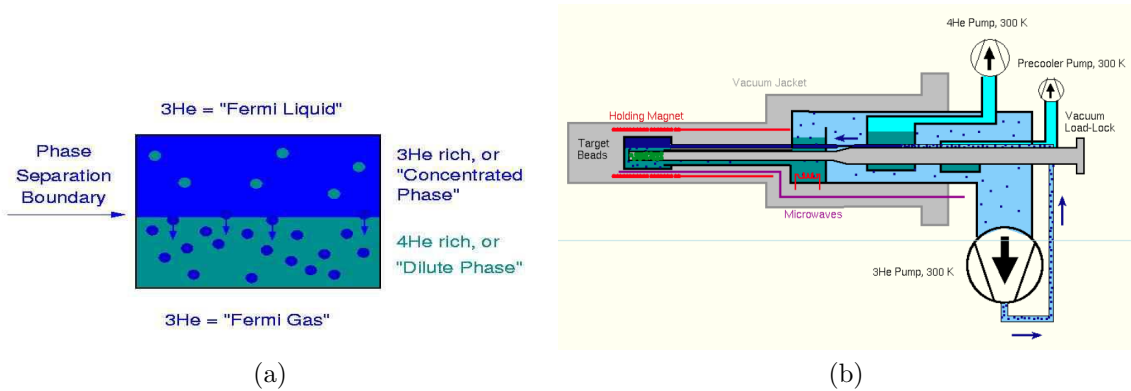


Figure 2.14: (a) Two phases of  $^3\text{He}/^4\text{He}$  mixture in the mixing chamber. (b) An illustration of the operation of the dilution refrigerator for FROST.

Figure 2.15 (a) and (c) show the design for the frozen spin target. The temperature for cooling the butanol target falls step by step in the several parts of the FROST. The temperature in the 4K pot of the FROST, as shown in Figure 2.15 (a), is about 4.2 K. The FROST has approximately 1.5 K in the 1K pot. In the distillation chamber, the FROST has roughly 0.7 K. Finally, the temperature near the butanol target is about

30 mK by the DNP process. Figure 2.15 (b) describes the structure of the FROST near the mixing chamber, with three kinds of targets. In Figure 2.15 (b), the carbon and polyethylene are located on the end caps of the 1 K heat shield and the 20 K heat shield, respectively, downstream from the butanol target. The butanol target of the FROST is composed of supercooled butanol ( $C_4H_9OH$ ) beads, 5%  $H_2O$ , and 0.5% TEMPO ( $C_9H_{18}NO$ ). In order to create these butanol beads, the butanol is doped with the paramagnetic TEMPO used for the DNP process and then make the formation of the beads by supercooling in liquid nitrogen, as shown in Figure 2.16 (a).

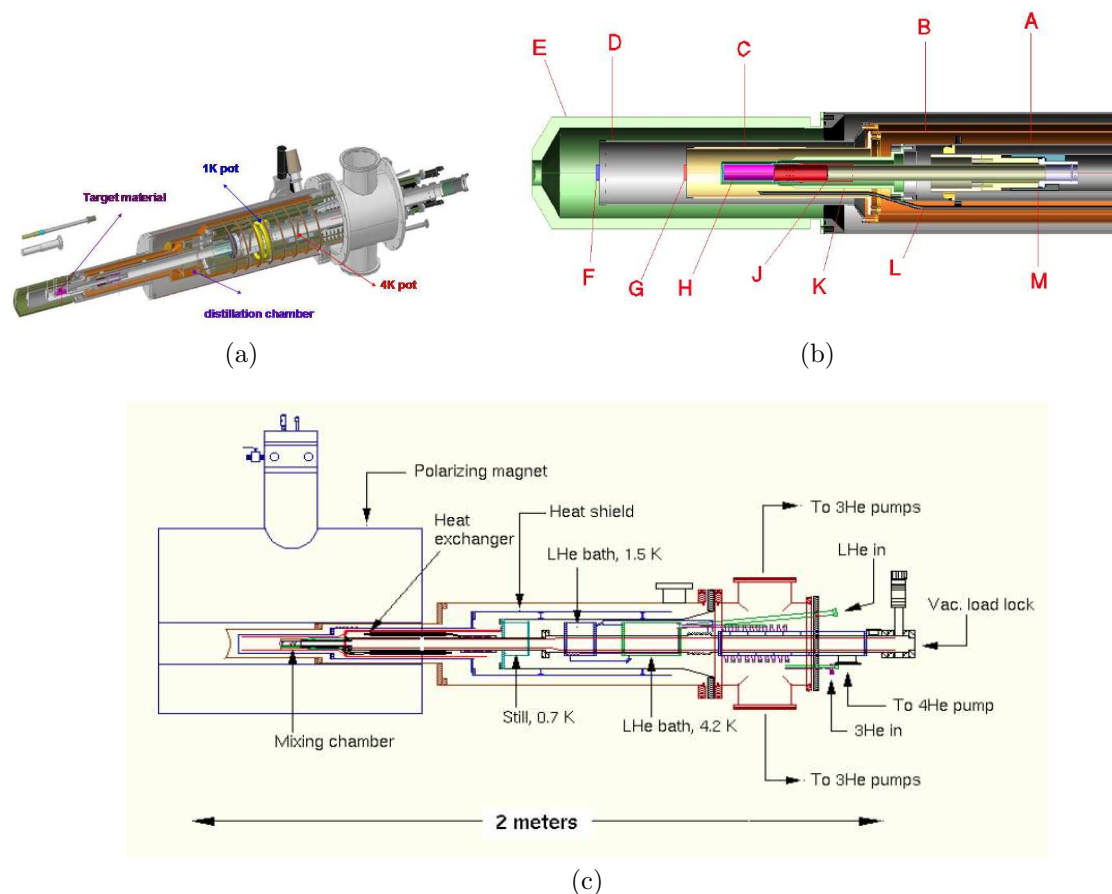


Figure 2.15: (a) The illustration of the frozen spin target with 1K pot and 4K pot. The actual butanol target is located on the target material part. (b) A cross section of the target area of FROST: A) primary heat exchanger, B) 1K heat shield, C) holding coil, D) 20 K heat shield, E) outer vacuum can (Rohacell extension), F) polyethylene target, G) carbon target, H) butanol target, J) target insert K) mixing chamber, L) microwave waveguide, M) Kapton coldseal. (c) The floor plan of the frozen spin target with the polarizing magnet.

In order to retain effectively their polarizations after freezing the butanol beads, a relatively small "holding magnet" with extremely low temperature is used. There are two types of the "holding magnet" for the FROST experiment, as shown in Figure 2.17 (a): The first type is the longitudinal holding magnet which produces a magnetic field, either parallel or anti-parallel to the beamline, used in the g9a experiment. The Second type is the transverse holding magnet with racetrack shaped coils, which produces a magnetic field perpendicular to the beamline, used in the g9b experiment. Figure 2.17 (b) shows that the optimized value of the magnetic field for the maximum relaxation time in the butanol is around 0.5 T. Therefore, the longitudinal holding magnet has approximately 0.56 T as a magnetic field, and the transverse holding magnet has about 0.52 T.

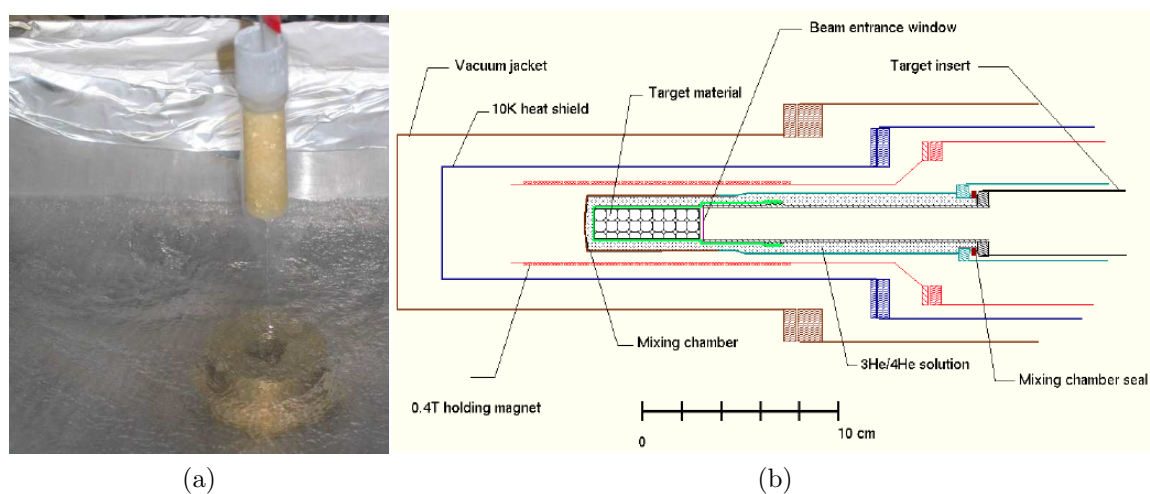


Figure 2.16: (a) Butanol beads formed by supercooling of the liquid nitrogen. (b) Butanol beads placed in the target cup (the green area).

The butanol target is cooled to approximately 0.5 K and dynamically polarized outside the spectrometer using a highly homogeneous magnetic field of about 5.0 T. And then, the microwaves are turned on for electron polarization to be transferred to protons. Once protons in the butanol target are polarized, the butanol target is then cooled to a low temperature of 30 mK, enough to preserve the nuclear polarization in a more moderate holding field of about 0.5 T. The target is then moved back into the spectrometer, and data acquisition with the tagged photon beam can commence. The target polarization then decays exponentially during the data acquisition phase of the experiment. After polarization decays to about 50 % of its initial value, the butanol target is repolarized via the DNP process at 5 T. Repolarization of the butanol target is necessary every 4 to 5 days. The repolarization schedule is seen in Figure 2.18.

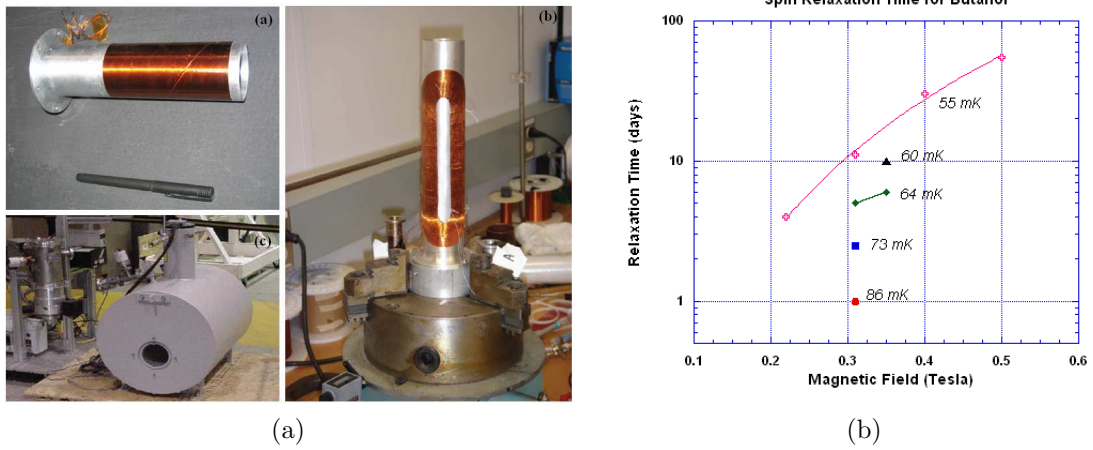


Figure 2.17: (a) There are, clockwise from the top, the longitudinal holding magnet with a field strength of approximately 0.56 T, the transverse holding magnet with approximately 0.52 T, and the polarizing magnet with 5.0 T. (b) Magnetic field vs. spin relaxation time for butanol [21].

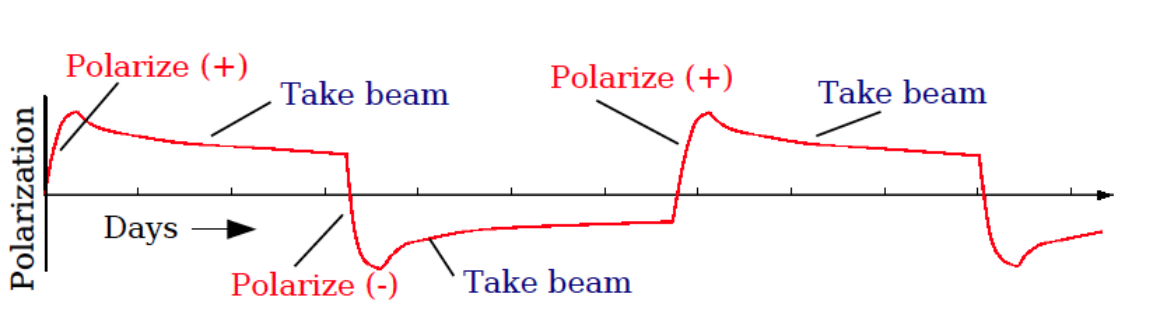


Figure 2.18: The polarization schedule for the frozen spin target.

# CHAPTER 3

## DATA RECONSTRUCTION

The first iteration of the g9 dataset (g9a experiment) utilizing longitudinal target polarization was collected from November 3, 2007 to February 12, 2008, and the second iteration (g9b experiment) utilizing transverse target polarization was taken from March to August, 2010. Because the dataset used in this analysis is from the g9a experiment, the reconstruction and calibration process discussed in this chapter will refer primarily to the g9a experiment. The real time of the data acquisition in the g9a experiment was only 72 days. Figure 3.1 shows the number of events accumulated during this data acquisition period.

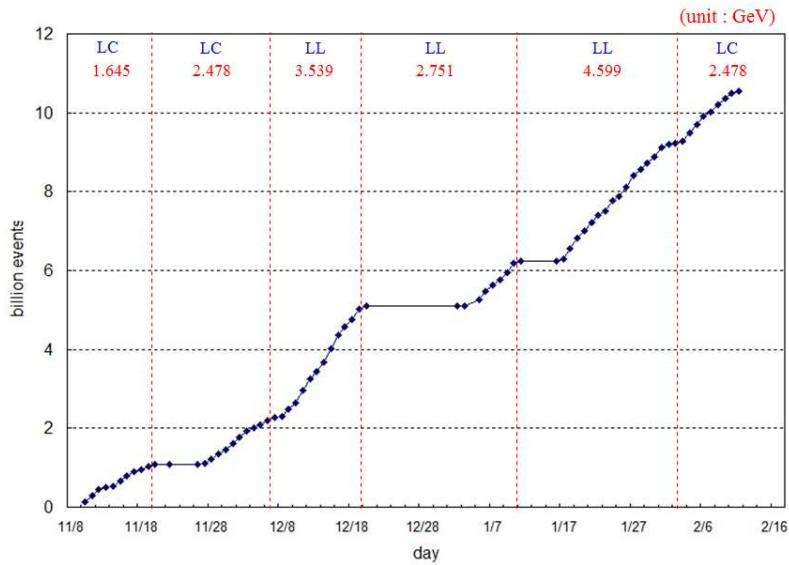


Figure 3.1: Number of events for the g9a experiment, which utilizes a variety of electron beam energies. The numbers on the top show the electron beam energies in [GeV] used in the g9a experiment. LC indicates longitudinal target polarization and circular beam polarization, and LL indicates longitudinal target polarization and linear beam polarization.

The raw Hall B data were acquired in units called runs<sup>1</sup>. A total of 603 runs was accumulated during the g9a data recording. One run may consist of several files of a fixed size of 2 Gb containing about  $0.87 \times 10^6$ . The possible settings for the beam polarization in the g9 experiment are circular and linear, and those for the target polarization are longitudinal and transverse. In the first iteration of the g9 experiment, only longitudinal target polarization was used, with a circularly- or linearly-polarized beam. The second iteration used transverse target polarization, with a similar set of beam polarization as in the g9a experiment.

### 3.1 Reconstruction

The information included in the raw data from the FROST experiment consists of charge-to-digital converter and time-to-digital converter channel IDs and values. The data are then reconstructed to convert these into physical quantities such as particle IDs, positions, angles, energies and momenta. This process takes of the order of 15 h per  $10^6$  events on a mid-range Linux PC. During the FROST experiment,  $1.05 \times 10^{10}$  events were accumulated; it would require approximately 6500 years to reconstruct all the raw data using just a single Linux PC. Jefferson Lab has a computer system called the "batch farm", which consists of dual CPU computers connected by high-speed Ethernet. The word "cooking" is used to describe the reconstruction process, which refers to running the CLAS reconstruction code on many raw data files by sending them to the JLab farm [22]. For each experiment a "chef" is chosen to manage the cooking process. I was serving as the chef for the g9a experiment. The process of reconstructing the raw data requires careful maintenance and good organizational skills.

The cooking process attempts to convert digital information into physical information. For the g9a dataset, the raw data are cooked by using `USER_ANA`, which is the FORTRAN-based reconstruction software for the CLAS spectrometer. The `USER_ANA` program is configured via a tcl file, `COOK.TCL`, that sets up the names of an input and an output file, and switches on or off the required parameters that manage the cooking process. The FROST data are saved in the BOS format<sup>2</sup> [23] after they are acquired.

The raw data from the g9a experiment consist of 17,676 BOS files. Because each file is approximately 2 Gb in size, the g9a experiment accumulated a total of about 35 TB of data. Each BOS file name has the usual format, `clas_xxxxx.Ayy`, where the first and second number represents the run number and its extension, respec-

---

<sup>1</sup>At JLab, the word 'run' has two meanings. A run can mean a time interval during which data are collected, assuming there is no change in the experimental conditions. A run is also the unit of the data accumulated during this time interval.

<sup>2</sup>The BOS format is based on a so-called bank structure.

tively. The original BOS files are processed into and reorganized several output files in the reconstruction process. A single BOS output file containing the reconstructed events is more than 3 Gb in size; thus, it is split into two or even three files. They are expressed in the usual format, `cooked_xxxxx.Ayy.Bzz`, where the third number represents additional file information. The reconstruction process prepares log files that contain information on the progress of the cooking and any errors that happened during cooking. Table 3.1 is illustrative of the name, file size and directory of the output files for the input file `clas_055521.A10`.

Table 3.1: Names, sizes and directories of output files containing reconstructed events.

Description	Nomenclature	Size	Directory
Input File	<code>clas_055521.A10</code>	2 Gb	Silo tape
BOS Output	<code>cooked_055521.A10.B00</code>	2 Gb	BOS
	<code>cooked_055521.A10.B01</code>	2 Gb	
	<code>cooked_055521.A10.B02</code>	51 Mb	
Histogram Files	<code>anaist_055521_A10.hbook</code>	11 Mb	AnaHistFiles
Log File	<code>run_055521_rmA10.err</code>	11 Kb	LOGS
	<code>run_055521_A10.log</code>	8 Kb	
	<code>run_055521_A10.out</code>	55 Kb	
Root File (for analysis)	<code>DST_055521.A10.B00.root</code>	408 Mb	ROOT
	<code>DST_055521.A10.B01.root</code>	408 Mb	
	<code>DST_055521.A10.B02.root</code>	11 Mb	

## 3.2 Calibration

During the data acquisition and while the trigger is open, a hit in the Start Counter surrounding the target starts a time measurement until a signal is detected in the CLAS spectrometer. Then the time is stopped and the information of the event is read out and recorded. A general feature in the calibration of all detector components is the need to align their timing with the beam radio frequency (RF or accelerator time)<sup>3</sup> time. The T-counter plane of the CLAS tagging system measures the travel time of the scattered electron from the T-counter plane to the radiator (backwards), as shown in Figure 2.4. The photon corresponding to this travel time of the scattered electron is identified and triggers an event in the target at the cen-

---

<sup>3</sup>The accelerator at JLab produces an electron beam with buckets a period of 2.004 ns, which defines the machine RF time; that is, an electron beam bucket is supplied to the target about every 2 ns.

ter of the CLAS spectrometer. The "RF vertex time"<sup>4</sup> for the identified photon is calculated. The start counter, TOF scintillators and the electromagnetic calorimeter (EC) of the CLAS spectrometer have their distinct vertex times. These vertex times are synchronized against the RF vertex time. Since the start counter is the closest sub-detector to the event vertex, its timing is the most reliable for any given track. First, the "ST vertex time"<sup>5</sup> for any given final particle is aligned with the "RF vertex time" for the photon. That is, the start-counter detector provides the first time reference and the TOF scintillators provide the second time reference. The distinct timings measured in all the components of the CLAS spectrometer are aligned together. Table 3.2 shows the role of each part of the CLAS detector in the calibration.

Table 3.2: The purpose of each calibration.

Detector	Calibration procedure
Tagger	Align T-counter and E-counter timing against the RF beam signal.
Time-of-flight (TOF) Counters	Optimize the time and hit position reconstruction, align the 57 paddle timings with each other and within the CLAS detection timing scheme.
Drift Chambers (DC)	Optimize charged track reconstruction.
Electromagnetic Calorimeter (EC)	Optimize the time and energy reconstruction.
Start-Counter (ST) Calibration	Align the ST paddles reconstructed within the CLAS detection timing.

Calibration programs generally read files of raw or reconstructed data in BOS format and typically produce some calibration constants. Calibration is an iterative process. When the calibration of one component is improved, it allows further improvement in another component. For example, if a TOF scintillator measures the time of flight of particles more precisely, the EC time can be calibrated more accurately. The CLAS spectrometer can be divided roughly into five parts: tagger, start counter (ST), drift chamber (DC), TOF counters, and EC. Each part of the calibration has a prerequisite stage; that is, the calibration of certain detector components can commence start only after other calibrations are finalized. The order of the calibration in the FROST experiment is Tagger, TOF, ST, DC and EC. A set of representative runs dispersed evenly throughout the beam time is generally selected for calibration. These runs are calibrated and reconstructed over several iterations

<sup>4</sup>The RF vertex time is the time of a photon calculated from the radiator at the event vertex.

<sup>5</sup>The ST vertex time is the time of the detected track calculated from the start counter (ST) at the event vertex.

until all subsystems are considered to be satisfactorily calibrated. The calibrations are then applied to the entire run period, and a larger subset of the entire dataset is reconstructed to check the quality and consistency of the calibrations. Typically, at this stage, two files per run would be reconstructed, resumming 5-10 % of the total run statistics. When the conditions of all calibrations are satisfied, the final reconstruction is commenced to prepare the data analysis.

I was responsible for the DC calibration [24] in the g9a and g9b experiments. Figure 3.2 shows how the regions and superlayers in DC are arranged. The sectors are six azimuthal segments divided by six superconducting coils, as shown in Figure 2.2. Each sector of the chambers is classified radially into three regions, and each region is composed of two superlayers. Superlayer 1 contains four layers, and the other superlayers each has six layers of sense wires.

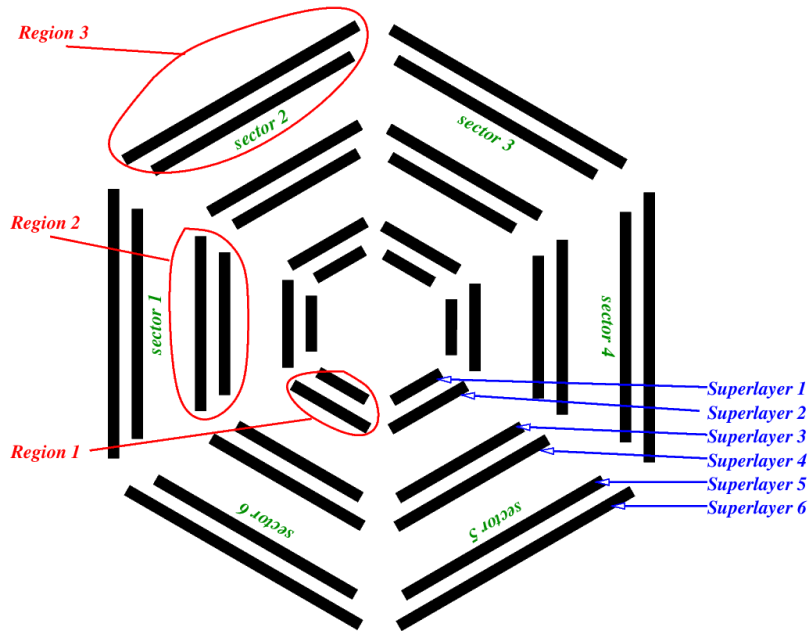


Figure 3.2: Schematic view of regions and superlayers in CLAS DC.

The DC are in a magnetic field and produce the curvature of the particle from which we can determine its momentum. For this purpose, thin wires are fixed in a volume filled with a special gas (the CLAS spectrometer uses a mixture of 90 % argon and 10 % CO<sub>2</sub> as a gas system) and form cells, as shown in Figure 3.3. The DC of the CLAS spectrometer uses a quasi-hexagonal pattern as the cell form with six field wires (cathodes) surrounding one sense wire (anode), as shown in Figure 3.4. A

traversing charged particle ionizes the gas inside these cells. Owing to the electrical potentials applied to the field-shaping wires, the electrons drift to the sense wire, and the connected electronics measure this current.

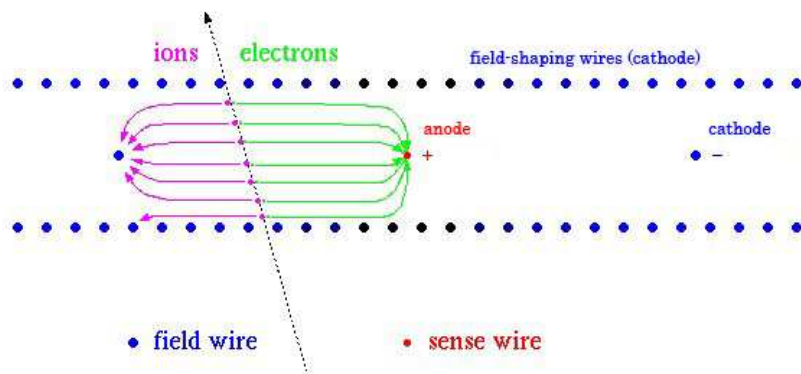


Figure 3.3: Typical arrangement of electrodes in a drift-chamber cell.

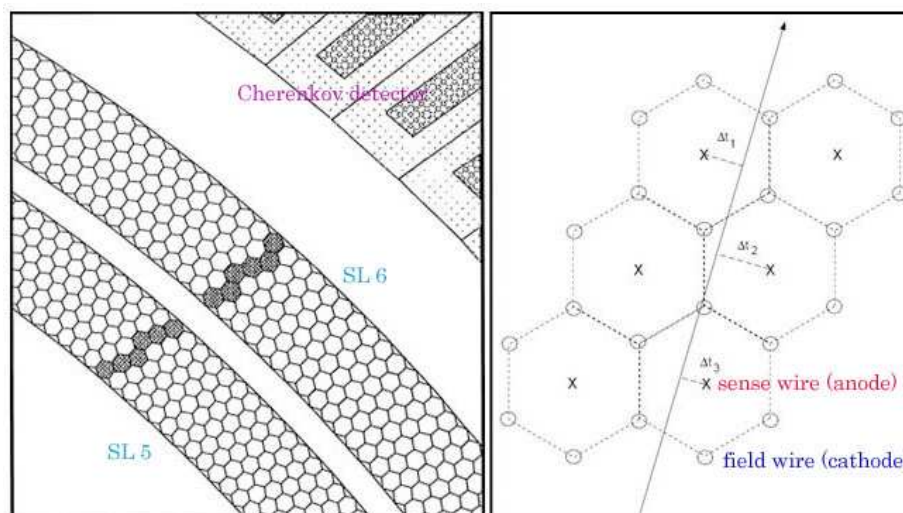


Figure 3.4: Left: Portion of a Region 3 sector showing the layout of its two superlayers. A passing charged particle is indicated by the highlighted drift cells that have fired. Right: Schematic diagram showing a charged particle track. The individual hexagonal drift cells are identified by a dashed line around the perimeter of each.

A software package entitled "dc3" is used at JLab to calibrate the CLAS DC. To determine the particle's track, the measured drift time should be used. The drift time

refers to the time required for electrons to drift to the nearest sense wire from the place where a charged final particle has crossed. An example of a drift time distributions is shown in Figure 3.5 (a). Any three sense wires are only nearby in one place, so a set of "hits" on these three sense wires fixes a particle track in this region via a least-squares fit done inside the CLAS reconstruction program. By measuring this drift time the location of the original track can be determined with much greater precision than that of the actual spacing between the wires. The "dc3" software package uses two terms to describe the distance of a charged particle track from a sense wire: *DOCA* and *DIST*. *DOCA* (distance of closest approach) is the distance from the fitted track to the sense wire; *DIST* is the distance from the sense wire to the track calculated from the drift time. The fitted *DOCA* values are obtained from fits to global tracks (i.e. fits that include all layers); That is, the trajectory in a DC can be rebuilt in the first stage without information from the other detectors in a hit-based track. These trajectory data constitute a fitted *DOCA*.

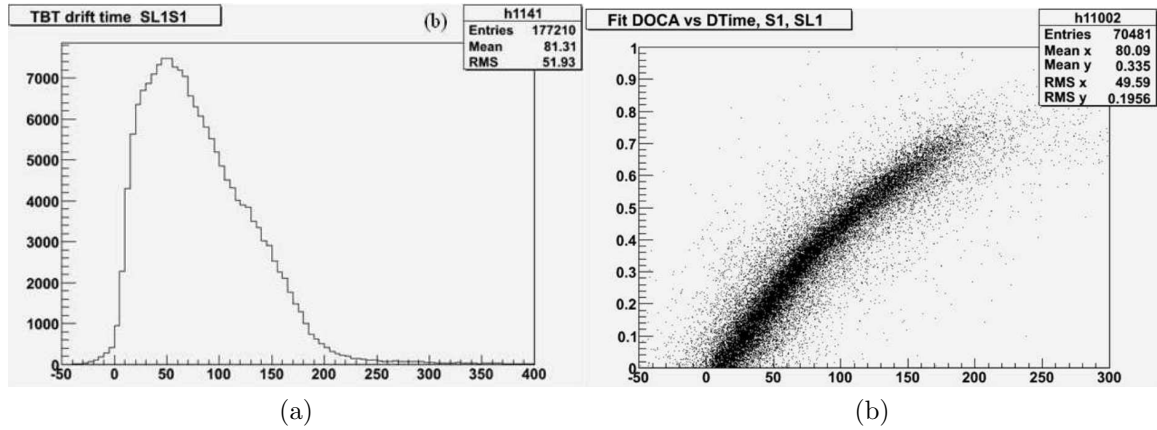


Figure 3.5: (a) Drift time measured in superlayer 1 of sector 1. (b) Relation between fitted *DOCA* and drift times in superlayer 1 of sector 1.

The "dc3" software package calculates the drift velocity function for every superlayer in every sector by using a fitting, as shown in Figure 3.6 (a). This software marks the calculated *DIST* from the relation of the drift velocity function and the drift time. It also obtains the time residual, defined as the difference between the absolute values of *DOCA* and *DIST*. Its sign is determined by the sign of any systematic time shift. The goal in DC calibration is that the value of the residual in each superlayer become approximately zero, as shown in Figure 3.6 (b). Therefore, moving from the rough hit-based track to a complete time-based track requires timing alignment of the TOF measurement.

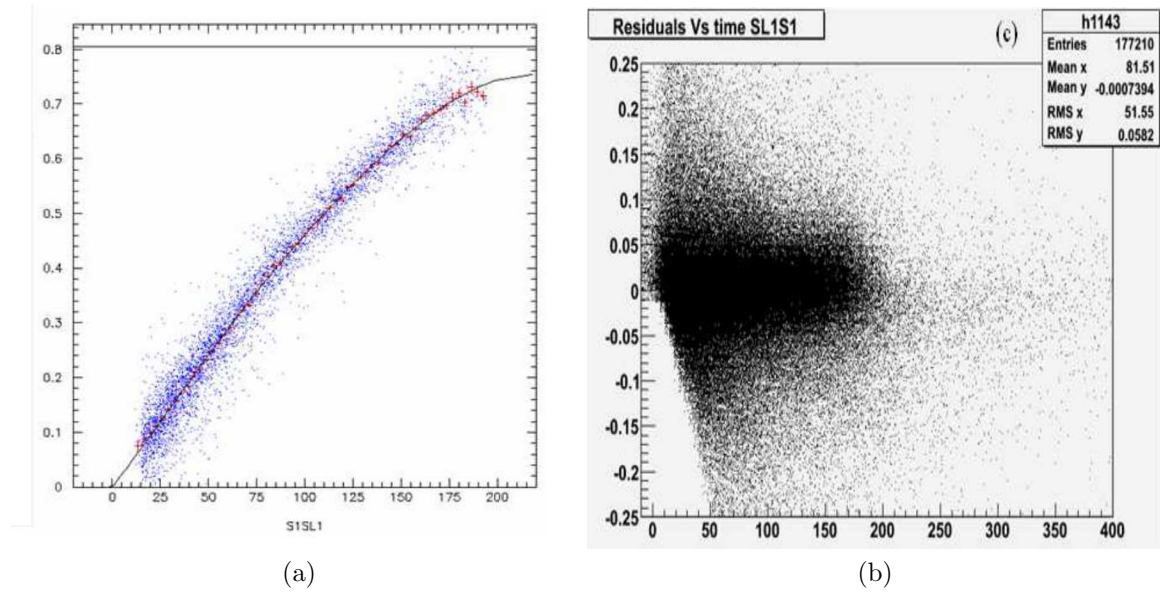


Figure 3.6: (a) Fitting the plot between fitted *DOCA* and drift times in superlayer 1 of sector 1, as shown in Figure 3.5 (b), to calculate the drift velocity function in the "dc3" software package. (b) Relation between drift times and the residual in superlayer 1 of sector 1.

Figure 3.7 shows the residual before starting the DC calibration and after finishing the final iteration of the calibration for every superlayer in every sector. The residual values tend to approach zero when the new ones are compared with the old. However, the residuals of superlayers 5 and 6 are not stable, but fluctuate with values far from zero.

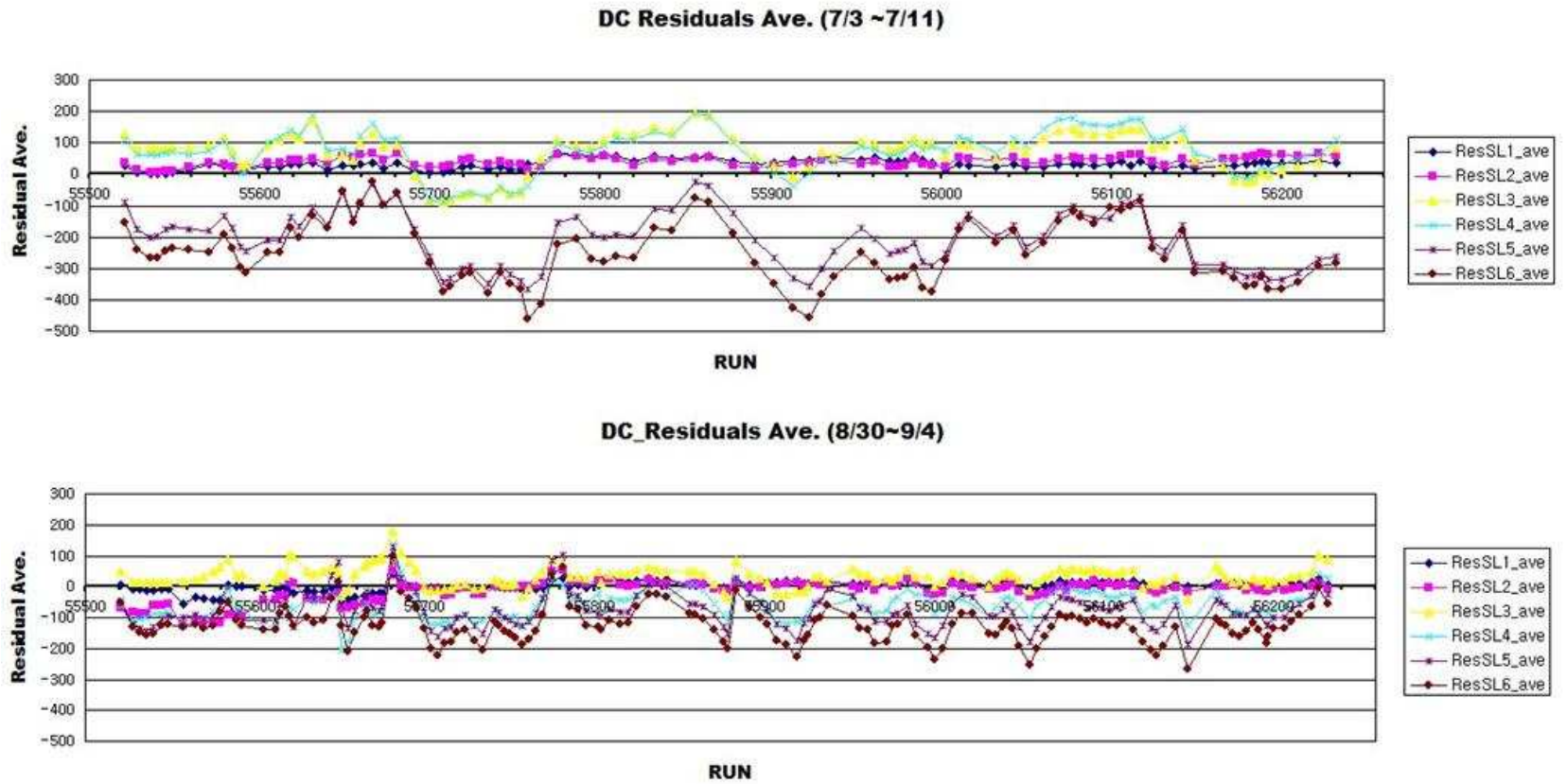


Figure 3.7: Average DC residuals before starting (the top) and after finishing (the bottom) DC calibration in the g9a dataset.

# CHAPTER 4

## DATA SELECTION

### 4.1 Pre-Event Selection

The data for the g9a experiment (FROST-g9a) were taken between November 3th, 2007 and February 12th, 2008. The g9a data are divided into two major parts according to the polarization type of the incident photon beam: circular and linear polarization. In this analysis, the data with a circularly polarized photon beam and a longitudinally polarized target were used. The circularly-polarized dataset is categorized into two parts according to the electron beam energy: one is the data from  $E_{e^-} = 1.645$  GeV and another is from  $E_{e^-} = 2.478$  GeV. These data are broken up into seven different periods.<sup>1</sup> Table 4.1 shows the different experimental conditions of the g9a data.

The information included in the raw data of the g9a experiment consists of QDC (Charge to Digital Converter) and TDC (Time to Digital Converter) channel IDs and values. The data must then undergo reconstruction, or be cooked (converting these data into physical quantities like particle IDs, positions, angles, energies, and momenta) in order to be ready for a physics analysis, as referenced in Chapter 3. Therewith the data calibration is carried out for each detector component of CLAS independently. After the detectors have been calibrated and the particle tracks have been reconstructed, the cooking of the data is complete and the data are made available for analysis. Each event has its information organized in data banks. These data banks hold not only the properties of the particles involved in the reaction but also information about detector hits.

---

<sup>1</sup>A period is defined as a group of runs with similar conditions like the same target polarization or 1/2 wave plate status in the data with a circularly-polarized photon beam and longitudinally-polarized target.

Table 4.1: The dataset of the g9a experiment classified according to a wide variety of characteristics, such as the target polarization, the beam polarization, the electron beam energy, dates, and run numbers. The data with the circularly-polarized beam is grouped in periods with similar run conditions.

Target Polarization	Beam Polarization	Electron Beam Energy (GeV)	Dates	Run Range	Period
Longitudinal	Circular	1.645	11/10/07 - 11/10/07	55521 - 55536	1
			11/11/07 - 11/13/07	55537 - 55555	2
			11/14/07 - 11/20/07	55556 - 55595	3
	Circular	2.478	11/27/07 - 11/30/07	55604 - 55625	4
			11/30/07 - 12/07/07	55630 - 55678	5
			02/04/08 - 02/07/08	56164 - 56193	6
			02/07/08 - 02/11/08	56196 - 56233	7
Linear	Linear	3.539	12/07/07 - 12/20/07	55678 - 55844	
		2.751	01/05/08 - 01/11/08	55854 - 55938	
		4.599	01/17/08 - 02/03/08	55945 - 56152	

## 4.2 Reaction Channel and General Event Selection

The reaction channel of interest in this analysis is  $\gamma p \rightarrow p\pi^+\pi^-$  using a circularly-polarized photon beam and this channel is broken up into different topologies, as shown in Table 4.2. A topology is defined according to the detected particles in the final state: the two-particle final states (Topology 1-3) and all three-particles in the final state (Topology 4). A particle which is not detected in a given topology can be identified through the missing-mass technique. For this method, the Lorentz vectors of the incoming beam and the target should be used. The four-momentum of an identified particle in the reaction  $\gamma p \rightarrow p\pi^+\pi^-$  is determined from the measured three momentum and the particle energy. The missing four-momentum is given by :

$$x^\mu = k^\mu + P^\mu - \sum_{i=1}^{2,3} p_i^\mu, \quad (4.1)$$

where  $k^\mu$  and  $P^\mu$  are the photon and proton-target four-momenta, and  $p_i^\mu$  are the four-momenta of the two or three detected particles. The missing mass  $m_X$  is defined as :

$$m_X^2 = x^\mu x_\mu. \quad (4.2)$$

The missing mass distribution is used to check the condition of the data after applying corrections and cuts. The four-momentum vector  $x^\mu$  of Equation 4.1 is used to complete the set of four-momentum vectors for events of Topologies 1, 2, or 3, as referenced in Table 4.2.

Table 4.2: Identification of the  $\gamma p \rightarrow p\pi^+\pi^-$  channel using different topologies. Reconstructed particles are identified by the **PID** information from the **GPID** bank.

Topology	Reconstructed particles				Missing mass of interest
	total	p	$\pi^+$	$\pi^-$	$m_X$
1	2	1	1	0	$m_{\pi^-}$
2	2	1	0	1	$m_{\pi^+}$
3	2	0	1	1	$m_p$
4	3	1	1	1	0

Since the g9a experiment has used a trigger which required at least one charged particle in CLAS, the trigger file used during data-taking allowed for the recording of a large variety of events. In order to analyze only the specific topologies of the reaction  $\gamma p \rightarrow p\pi^+\pi^-$ , events possessing the final-state particles of interest should be filtered using the particle's identification number (PID), which is determined during

the cooking process. Events that do not meet this requirement are ignored and subsequently omitted from the analysis. The calculation of the detected particles' mass, which is necessary to determine the PIDs of the final particles, uses two independently measured quantities, momentum ( $p$ ) and velocity as fraction of the speed of light ( $\beta$ ). The magnitude of the particle's momentum ( $p$ ) is determined with an error of  $< 1\%$  using the measurements made by the Drift Chambers [14]. The  $\beta$  of the detected final-state particle is determined using a combination of the Start Counter (SC), The Time of Flight (TOF), and the particle's detected trajectory through CLAS with an error of up to  $5\%$  [14]. A detected particle's mass can then be calculated by :

$$m_{particle\ X}^2 = \frac{p^2(1 - \beta^2)}{\beta^2}. \quad (4.3)$$

After the particle's mass has been calculated, it is compared to the masses of known particles (hadrons and leptons). If this calculated mass matches that of a known particle (within resolution errors), the PID associated with that mass is assigned to the final-state particle. This value can then be used to select certain final-state particles for analysis. Therefore, to select events that match one of the four topologies, the PID value is used and the necessary final-state particles are detected. Information regarding the properties of these final-state particles (their 4-vectors, vertex information, etc.) is then extracted from the GPID [25] data bank and used for kinematic fitting and application of cuts and systematic corrections, and the extraction of the polarization observables.

## 4.3 Photon and Particle Identification

### 4.3.1 Photon Selection

The electrons, which are used to produce the beam of polarized photons, are delivered from the accelerator into Hall B. They are carried in the form of 2 ns bunches. The circularly-polarized photon beam is also produced in the form of 2 ns bunches by directing the bunch of longitudinally-polarized electrons to the amorphous radiator. It is very important to determine the correct photon in each event because the photon energy is key to understand the initial state of the event. To determine the exact photon corresponding to a physics event, a timing window can be used which satisfies the consistency check between the tagger and start counter times.

The event-start-time difference at the interaction point between the tagger and the start counter,  $\Delta t_{TGPB}$ , is defined as the coincidence time between the tagger and CLAS spectrometer. Figure 4.1 shows the distribution of tagged photons as a function of the coincidence time,  $\Delta t_{TGPB}$ , on a logarithmic scale. In the central peak, there are events with the true tagger-CLAS coincidence time. Accidental coincidences

can be seen as a series of other peaks associated with different beam buckets. Only coincident events determined by :

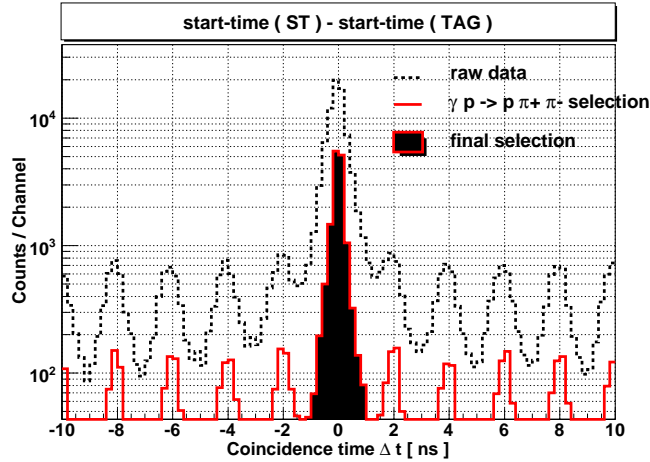


Figure 4.1: Coincidence-time distribution of tagged photons for the raw data (dotted histogram) and after applying all  $\gamma p \rightarrow p\pi^+\pi^-$  selection cuts (solid histogram). Events of the center bins filled in black indicate the candidates for the final selection.

$$|\Delta t_{TGPB}| < 1.2 \text{ ns}, \quad (4.4)$$

are selected. The tagged energy of that photon will be used as the photon energy for the event. The fraction of accidental coincidences remaining in the central peak is  $< 3\%$  and is calculated from the comparison in the yields between the central peak and neighboring beam buckets. When the “true” photon has been undetected, these events are considered accidental events. If events with only a “true” photon are selected, the fraction of accidental coincidences in the data is reduced strongly. In this analysis, events with a “true” photon are selected using  $NGRF = 1$  and  $TAGRID$  the same for all detected particles. These variables are from the GPID bank and introduced and described in more detail in Section 4.6.2.

### 4.3.2 Proton and Pion Selection

The reaction channel of interest in this analysis is  $\gamma p \rightarrow p\pi^+\pi^-$  and the photon energy for each event is selected according to the procedure outlined in section 4.3.1. In the next step, the identification of the proton,  $\pi^+$ , and  $\pi^-$  as the final-state particles of  $\gamma p \rightarrow p\pi^+\pi^-$  is needed using the GPID bank. The GPID bank has the CLAS-measured momentum of a particle and a theoretical  $\beta_c$  value for that particle can be calculated from this measured momentum. This theoretically calculated  $\beta_c$  value for all possible hadron particle types is compared to the CLAS-measured empirical  $\beta_m$

value. Particle identification is then determined based on matching the calculated  $\beta_c$  closest to the empirical measured  $\beta_m$ . Figure 4.2 shows the difference  $\Delta\beta$  between the calculated  $\beta_c$  and measured  $\beta_m$ .  $\Delta\beta$  is given with its assumed mass  $m$  :

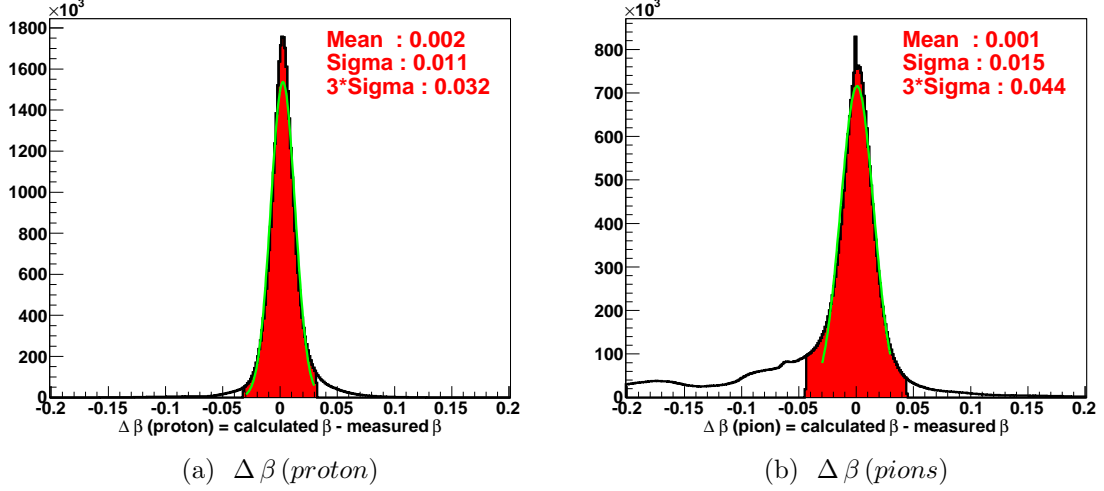


Figure 4.2: Distribution of  $\Delta\beta = \beta_c - \beta_m$  made from protons (a) and pions (plus and minus) (b), where  $\beta_c$  is calculated based on the particle's assumed mass. Events of the center peak filled in red are selected after applying the  $|\beta_c - \beta_m| \leq 3\sigma$  cut.

$$\Delta\beta = \beta_c - \beta_m = \sqrt{\frac{p^2}{m^2 + p^2}} - \beta_m. \quad (4.5)$$

The peak around  $\Delta\beta = 0$ , as shown in Figure 4.2, corresponds to the particles of interest.  $\Delta\beta$  for the pions in Figure 4.2 (b) is broader than for the proton in Figure 4.2 (a) and there is a long tail to negative values of  $\Delta\beta$  for the pions. When the GPID bank is made during the reconstruction, electrons are not separated from pions within the data. The long tail in the  $\Delta\beta$  distribution of the pion particles may represent electrons that need to be filtered out. To identify the proton and pion and correct this GPID problem, a  $|\beta_c - \beta_m|$  cut should be applied. This cut can be extracted by fitting the main peak near  $\Delta\beta = 0$  with a Gaussian function, discarding all events outside  $3\sigma$ , where  $\sigma$  is the width of the fitted Gaussian function. Thus, any events with a value of  $\Delta\beta$  greater than 0.032 for the proton and 0.044 for the pions are filtered out of the dataset. Figure 4.3 shows the measured momentum ( $p$ ) versus the empirical measured  $\beta_m$  for protons and pions (plus and minus) before (a) and after (b) applying the  $|\beta_c - \beta_m|$  cut. Due to the different rest masses, bands for pions and protons are clearly visible, especially after applying the  $|\beta_c - \beta_m|$  cut, and protons and pions are well identified.

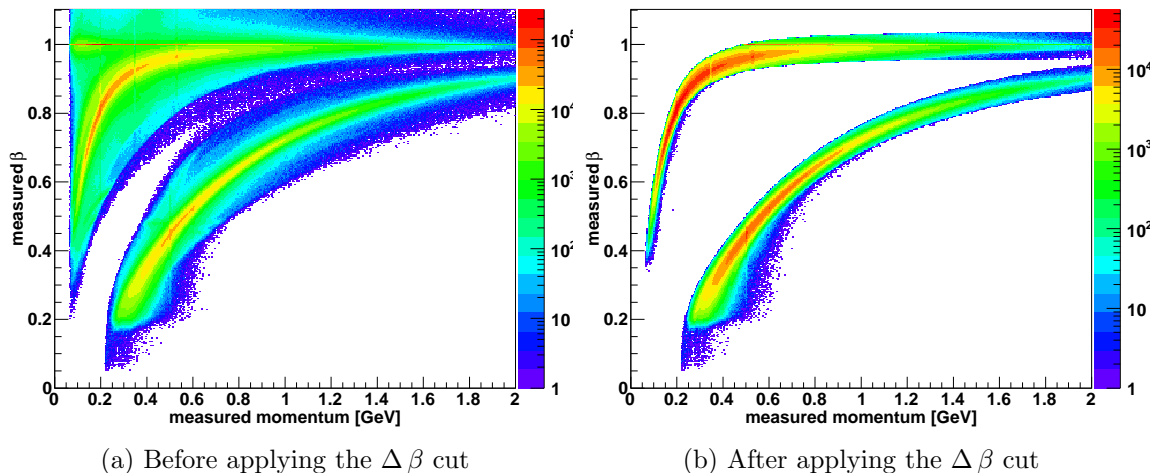


Figure 4.3: (a) Measured  $\beta_m$  versus the measured momentum for the double-pion photoproduction events read from GPID on a logarithmic color scale. Notice the stripes for pions at the top, followed by protons. (b) Measured  $\beta_m$  versus the measured momentum after applying the cut based on the difference  $\Delta\beta = \beta_c - \beta_m$ . Events with pions and protons are clearly distinguished after applying the cut.

## 4.4 Kinematic Fitting

The reconstruction process determines the 4-vectors of the final-state particles. Kinematic fitting [26] modifies these 4-vectors by imposing energy-momentum conservation on the event as a physical constraint. All components of these Lorentz 4-vectors and the photon energy are modified until the event satisfies energy-momentum conservation exactly, and then the kinematically fitted event has several quantities to inspect the quality of the kinematic fitting: a confidence level and pull distributions for each measured quantities. The confidence level is used to estimate the goodness-of-fit of the data to the hypothesized event. The pull distributions are used to evaluate the quality of the error estimation and check for systematics.

### 4.4.1 Confidence Level

After performing the fit, we need a way to check the agreement between the data and the hypothesis. The confidence level used as the primary method of the goodness-of-fit of an event is defined as :

$$CL = \int_{\chi^2}^{\infty} f(z; n) dz, \quad (4.6)$$

where  $f(z; n)$  is the  $\chi^2$  probability density function with  $n$  degrees of freedom. It denotes the probability that a given event obeys the constraint imposed on the event kinematics, e.g. energy-momentum conservation. In the ideal case of independent variables and gaussian errors, the confidence level of the events without background follows a flat distribution ranging from 0 to 1. However, the real data produce confidence level distributions which have a sharp rise near zero. The large number of events with low confidence level values represents events that do not satisfy the hypothesized constraint equations. These events include background events, poorly reconstructed events, or events with misidentified particles. Cutting out events with low confidence levels provides a reasonable way to eliminate the majority of the background while losing a relatively small amount of good events.

#### 4.4.2 Pulls

To effectively use the confidence level to cut out background events, a good understanding of each fit quantity's error is needed. The quality of the error estimation can be obtained by examining the pull distributions. All fit parameters for every detected final-state particle have pull distributions. A pull is a measure of how much and in what direction the kinematic fitting has to alter the measured parameters. The pull value for the  $i^{\text{th}}$  fit quantity is given by :

$$z_i = \frac{\epsilon_i}{\sigma(\epsilon_i)}, \quad (4.7)$$

where  $\epsilon_i = \eta_i - y_i$  is the difference between the fit value of the  $i^{\text{th}}$  parameter,  $\eta_i$ , and the measured value of the  $i^{\text{th}}$  parameter,  $y_i$ . The quantity  $\sigma$  represents the standard deviation of the parameter  $\epsilon_i$ . Therefore, the  $i^{\text{th}}$  pull can be written as:

$$z_i = \frac{\eta_i - y_i}{\sqrt{\sigma^2(\eta_i) - \sigma^2(y_i)}}. \quad (4.8)$$

The reaction channel  $\gamma p \rightarrow p\pi^+\pi^-$  has three final-state particles: proton,  $\pi^+$ , and  $\pi^-$ . There are three fit parameters for each particle in the kinematic fitting: a momentum and two angles,  $\lambda$  and  $\phi$ . Thus, this analysis has ten pull distributions including a pull for the photon energy if all particles in the final state are detected. Assuming that the errors of the parameters used for kinematic fitting are properly determined and all systematic errors have been corrected, the distribution of the pull values ( $z_i$  values) will be the Gaussian distribution in shape with a width of one ( $\sigma = 1$ ) and a mean value of zero ( $\mu = 0$ ); an example is shown in Figure 4.4. A systematic error in the quantity  $\eta_i$  can be seen as an overall shift in the distribution of the corresponding  $z_i$  away from zero. Similarly, if the error of  $\eta_i$  has been consistently (overestimated) underestimated, then the corresponding pull distribution will be too (narrow) broad. The error of the measured value  $\eta_i$  can be corrected from the pull distribution in an iterative procedure. Kinematic fitting provides an effective tool

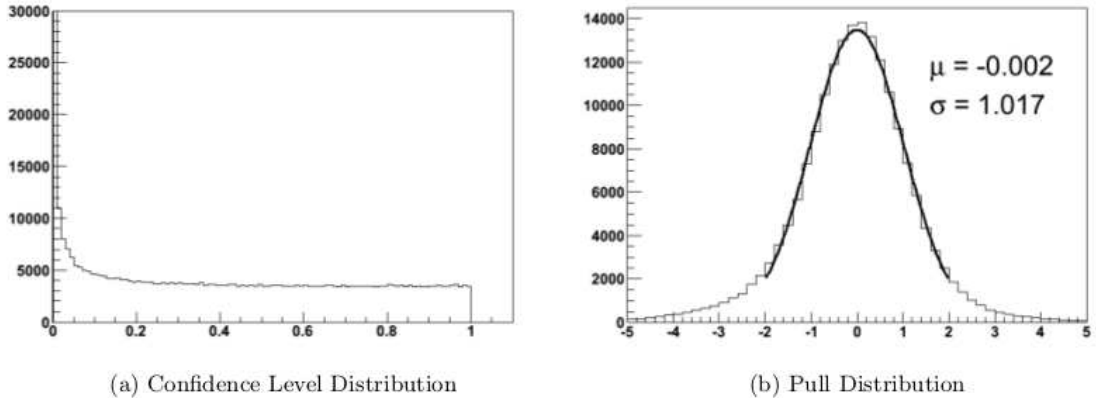


Figure 4.4: Example of fit results coming from a fit to a fully reconstructed  $\gamma p \rightarrow p\pi^+\pi^-$  final state. (a) Shows an example of a confidence level distribution. A confidence level distribution (working with real data) peaks toward zero but flattens out toward one. (b) Shows an example of a pull distribution (the photon energy pull). Ideally, a pull distribution has the Gaussian distribution in shape around the origin with a mean ( $\mu$ ) of zero and a sigma ( $\sigma$ ) of one.

also to determine corrections to the particles' energies and momenta. This will be described in the following sections.

## 4.5 Corrections

### 4.5.1 Energy Loss Correction (ELoss)

As charged particles from the decay of a resonance travel from the target cell to the Drift Chambers of CLAS, they lose energy through atomic excitations or ionizations when interacting with the three kinds of targets, target walls, support structures, beam pipe, start counter, and the air gap between the start counter and the Region 1 Drift Chambers. Therefore, the reconstructed momentum seen in the Drift Chambers is actually less than the momentum of the particle at the production vertex. To account and correct for this, the 4-vectors of the final-state particles taken from the data were corrected event-by-event according to the ELoss package developed for charged particles moving through CLAS [27]. This ELoss package calculates the lost momentum of each particle in several materials which the charged particle has interacted with. To perform this calculation, the particle's 4-momentum measured by the Region 1 of the Drift Chamber is used to track the particle back to the reaction vertex in the target cell. As the particle is tracked back to the reaction vertex, the materials and distances it traverses are considered and the energy loss of the detected particle is also calculated. The 4-vector of the particle is corrected by multiplying an

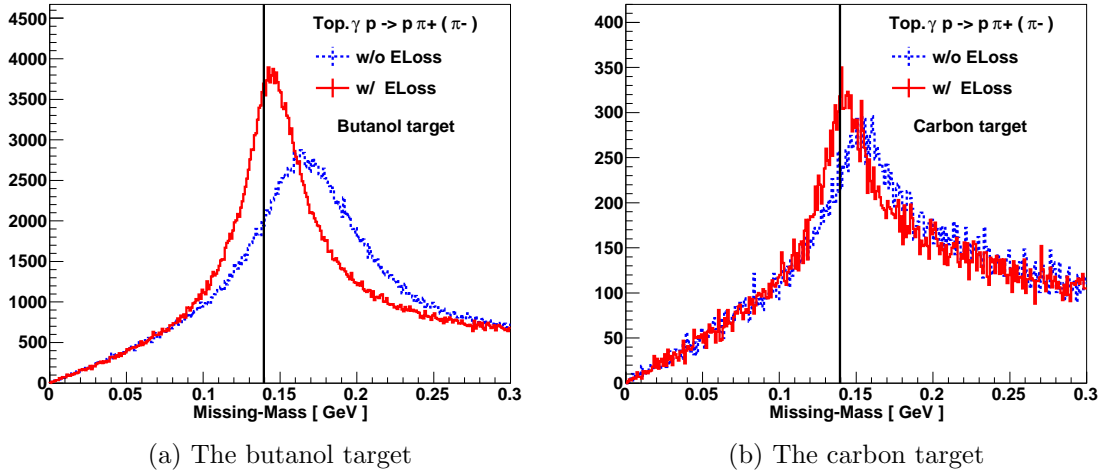


Figure 4.5: Missing-mass distributions before (dotted blue histogram) and after (solid red histogram) applying energy-loss-correction made in Topology  $\gamma p \rightarrow p \pi^+ (\pi^-)$  from the butanol target (a) and carbon target (b). The vertical lines denote the mass of the  $\pi^-$ . The energy-loss correction makes the peak shape noticeably narrower and the peak position is also corrected. Since, however, the peak position is not positioned at the  $\pi^-$  mass exactly, another correction is needed in the butanol target.

energy loss correction factor to the momentum of this vector like :

$$\begin{aligned}
 P_{(p, ELoss)} &= \eta_p \cdot P_{(p, CLAS)} \\
 P_{(\pi^+, ELoss)} &= \eta_{\pi^+} \cdot P_{(\pi^+, CLAS)} \\
 P_{(\pi^-, ELoss)} &= \eta_{\pi^-} \cdot P_{(\pi^-, CLAS)},
 \end{aligned} \tag{4.9}$$

where  $P_{(x, ELoss)}$  is the momentum of the particle  $x$  after applying the energy loss correction,  $P_{(x, CLAS)}$  is the raw momentum measured in CLAS and  $x$  is the proton,  $\pi^+$ , or  $\pi^-$ . Parameters  $\eta_p$ ,  $\eta_{\pi^+}$ , and  $\eta_{\pi^-}$  are the correction factors of the energy loss correction. The energy-loss-corrected 4-vectors are then used in the analysis with the corrections being on the order of a few MeV. The energy loss correction produces a shift in mass as can be seen for the missing-mass calculations in Figure 4.5.

## 4.5.2 Photon Beam Correction

The energy of the photons that are incident on the target is determined in the Hall B tagging system. The photon energy measured in this tagging system should be also checked for consistency with the final state after applying the energy loss correction in Section 4.5.1. It has been seen in past experiments that a physical sagging of the support structures for the E-counter scintillator bars in the tagger hodoscope could be attributed to gravitational forces [28]. The consequence of this

sagging is a misalignment of the scintillator bars which leads to a mis-measurement of the scattered electron's energy [29]. In the g9a experiment, this sagging problem has been already corrected when the data was reconstructed. However, whether the sagging problem still exists or not in the g9a dataset should be checked and minor corrections need to be applied to the photon beam if necessary.

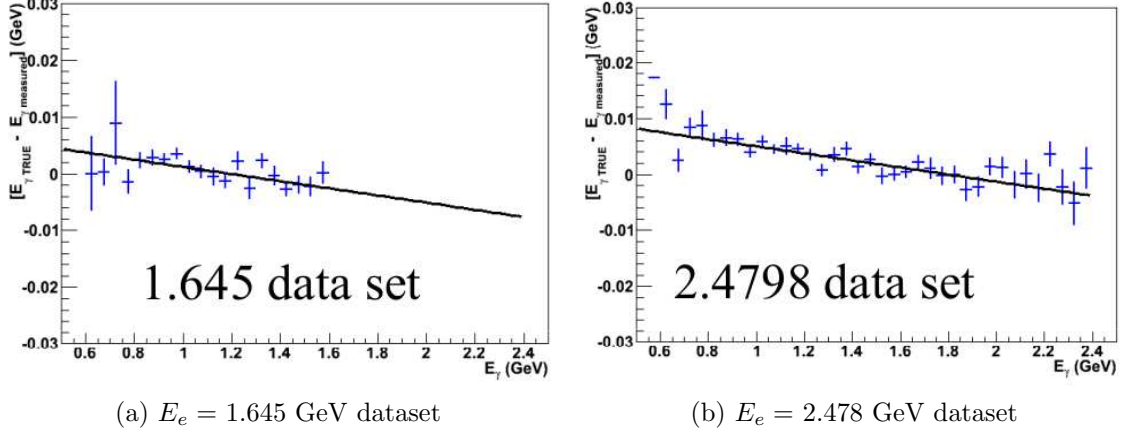


Figure 4.6: The photon beam correction on  $E_e = 1.645$  GeV dataset at ASU (a) and  $E_e = 2.478$  GeV dataset (b).  $E_{\gamma TRUE}$  is the photon energy returned by the kinematic fitting and  $E_{\gamma measured}$  is the measured photon energy from the data [30].

The photon beam energy can be calculated from the information of particles in the reaction  $\gamma p \rightarrow p\pi^+\pi^-$  using the energy conservation law like :

$$E_{(cal.\gamma)} = \sqrt{m_p^2 + P_{(p, E_{Loss})}^2} + \sqrt{m_{\pi^+}^2 + P_{(\pi^+, E_{Loss})}^2} + \sqrt{m_{\pi^-}^2 + P_{(\pi^-, E_{Loss})}^2} - m_p, \quad (4.10)$$

where  $P_{(p, E_{Loss})}$ ,  $P_{(\pi^+, E_{Loss})}$  and  $P_{(\pi^-, E_{Loss})}$  are the ELoss-corrected momenta of the final particles shown in Equation 4.13. The status of the photon beam energy can be checked by comparing the calculated photon energy  $E_{cal.\gamma}$  as seen in Equation 4.10 with the measured photon energy  $E_{mea.\gamma}$  given in the g9a dataset.

The initial photon beam correction, as shown in Figure 4.6, was given by :

$$E_{out} = E_{in} + a_1 \cdot E_{in} + a_0 \cdot E_{e-}, \quad \text{with} \quad \begin{aligned} a_0 &= 0.00456797 \text{ and} \\ a_1 &= -0.00630536, \end{aligned} \quad (4.11)$$

where  $E_{in}$  is the photon energy before the correction and  $E_{out}$  is the photon energy with the ASU correction.  $E_{e-}$  is the electron beam energy used in this analysis. Figure 4.7 shows the comparison of the calculated photon energy  $E_{cal.\gamma}$  to the measured photon energy  $E_{mea.\gamma}$  after applying the ASU photon correction. In the low energy, there is an overall shift in the distribution of the corresponding energy difference away

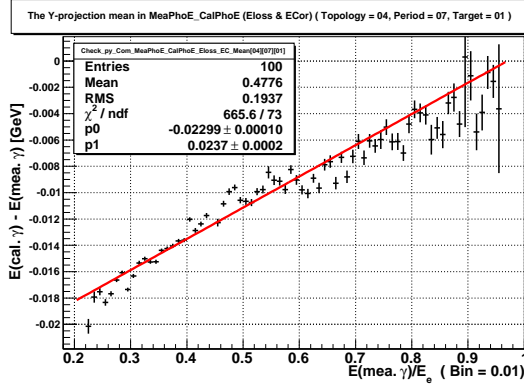


Figure 4.7: The difference between the calculated photon energy  $E_{cal,\gamma}$  and measured photon energy  $E_{mea,\gamma}$  after applying the ASU photon beam correction.

from zero: the measured photon energy is bigger than the calculated photon energy. The ASU photon energy correction needs to be supplemented and was improved by Florida State University (FSU) applying the fitting, as shown in Figure 4.7. The FSU photon energy correction is given by :

$$E_{out} = \left( a_1 \cdot E_{in} + a_0 \cdot E_e \right) \cdot \left( 1 + \frac{p_1}{E_e} \right) + p_0. \quad (4.12)$$

Table 4.3: The parameters used in the FSU photon beam correction.

target	$p_0$	$p_1$
butanol	-0.02299	0.0237
carbon	-0.01533	0.02012
polyethylene	-0.01539	0.02413

The three kinds of targets have different values for the parameters,  $p_0$ ,  $p_1$ , and  $p_2$ , as referenced in Table 4.3. The parameters  $a_1$  and  $a_2$  are from Equation 4.11.  $E_{out}$  is the photon energy after applying the final photon energy correction. After the photon beam correction is applied to the photon energy measured in the CLAS spectrometer, we can compare the difference between the calculated and measured photon energy. This is shown in Figure 4.8. After applying energy-loss and photon beam correction, 4-vectors of the final-state particles and the photon beam energy are corrected very well except for the regions of very high and low energies.

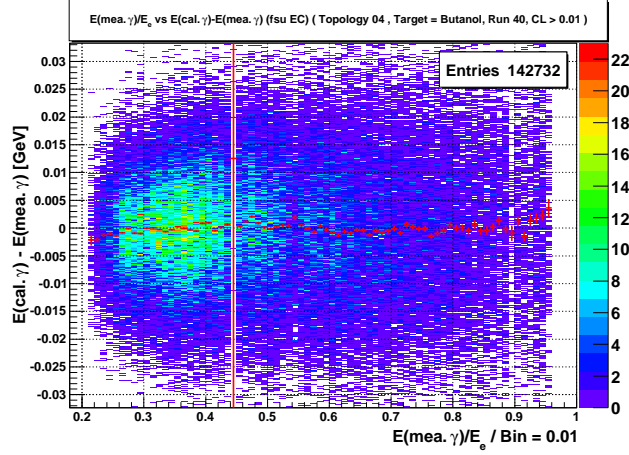


Figure 4.8: The difference between the calculated photon energy  $E_{cal.\gamma}$  and measured photon energy  $E_{mea.\gamma}$ , after applying energy-loss correction and all photon-beam correction. This figure is made for the topology  $\gamma p \rightarrow p\pi^+\pi^-$  with no missing mass and the data from the butanol target. On the  $x$ -axis,  $E_{e^-}$  is the electron beam energy used in the g9a experiment. As the tagging system of the Hall-B can tag photon energies from 20% to 95% of the incident electron beam energy, the data on the  $x$ -axis covers a range from 0.2 to 0.95.

### 4.5.3 Momentum Correction

Since the CLAS spectrometer used in the g9a experiment is not a perfect detector, corrections for particles' momenta must be determined for the g9a dataset. This mainly is a result of unknown variations in the magnetic field provided by the Torus Magnet as well as inefficiencies and misalignments of the Drift Chambers. The momentum correction in the g9a experiment was determined using the kinematic fitting. The final particle' 4-vector is corrected by multiplying a correction factor of the momentum correction to the momentum of this vector like :

$$\begin{aligned}
 P_{(p, MomC)} &= \xi_p \cdot P_{(p, ELoss)} \\
 P_{(\pi^+, MomC)} &= \xi_{\pi^+} \cdot P_{(\pi^+, ELoss)} \\
 P_{(\pi^-, MomC)} &= \xi_{\pi^-} \cdot P_{(\pi^-, ELoss)},
 \end{aligned}
 \tag{4.13}$$

where  $P_{(x, ELoss)}$  is the momentum of the particle  $x$  after applying the energy loss correction,  $P_{(x, MomC)}$  is the momentum of the particle  $x$  after applying the momentum correction and  $x$  is the proton,  $\pi^+$ , or  $\pi^-$ . Parameters  $\xi_p$ ,  $\xi_{\pi^+}$ , and  $\xi_{\pi^-}$  are the correction factors of the momentum correction. To properly determine correction factors of the proton and pion for the momentum correction using the kinematic fitting, pull distributions must be evaluated for different momentum bins. The binning of the momentum was determined based upon the observed distributions of the proton and pion momenta, as shown in Figure 4.9.

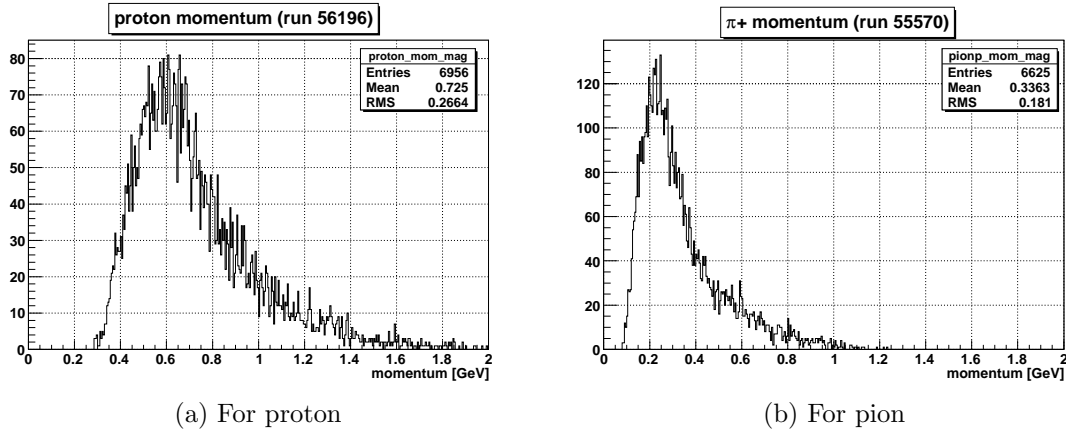


Figure 4.9: Examples of momentum distributions of final-state particles in the g9a dataset.

The momentum binning utilized 5 momentum bins for the proton and pion, which are referenced in Table 4.4.

Table 4.4: The momentum binning of the proton and pion for the momentum correction and the correction factors applied in this analysis.

particle	momentum bin	range [GeV]	correction factor
proton	1	0.2 - 0.5	1.012011
	2	0.5 - 0.6	1.002014
	3	0.6 - 0.7	0.999716
	4	0.7 - 0.9	1.000439
	5	0.9 - 1.7	0.999975
$\pi^+$	1	0.05 - 0.2	1.005510
	2	0.20 - 0.27	0.998049
	3	0.27 - 0.35	0.998151
	4	0.35 - 0.53	1.000716
	5	0.53 - 1.40	1.001858
$\pi^-$	1	0.05 - 0.2	1.018893
	2	0.20 - 0.27	0.987956
	3	0.27 - 0.35	0.986561
	4	0.35 - 0.53	1.010072
	5	0.53 - 1.40	0.992872

The final goal of the momentum correction is to obtain pull distributions, which are a Gaussian distribution in shape with  $\sigma = 1$  and mean = 0. Only small correction factors are applied to the momenta used in the kinematic fitting process to adjust the positions of the pull distributions. This iterative process is repeated until the pull distributions for proton,  $\pi^+$ , and  $\pi^-$  are centered at zero with a symmetric shape. Pull distributions and confidence-level distribution after applying the energy-loss correction, the photon-beam correction, and the momentum correction are shown in Figure 4.10. Means and sigmas of these pull distributions are acquired by fitting pull distributions with all corrections to a Gaussian curve and are referenced in Table 4.5.

Table 4.5: Means and  $\sigma$ 's of pull distributions made to integrate with the momentum bins referenced in Table 4.4 after applying all corrections.

particle		mean	$\sigma$
proton	mom	-0.012	1.029
	$\lambda$	+0.205	0.983
	$\phi$	-0.050	0.991
$\pi^+$	mom	-0.086	1.002
	$\lambda$	+0.099	1.004
	$\phi$	-0.098	0.990
$\pi^+$	mom	-0.090	1.023
	$\lambda$	-0.371	0.976
	$\phi$	-0.085	0.987
photon		+0.088	1.035

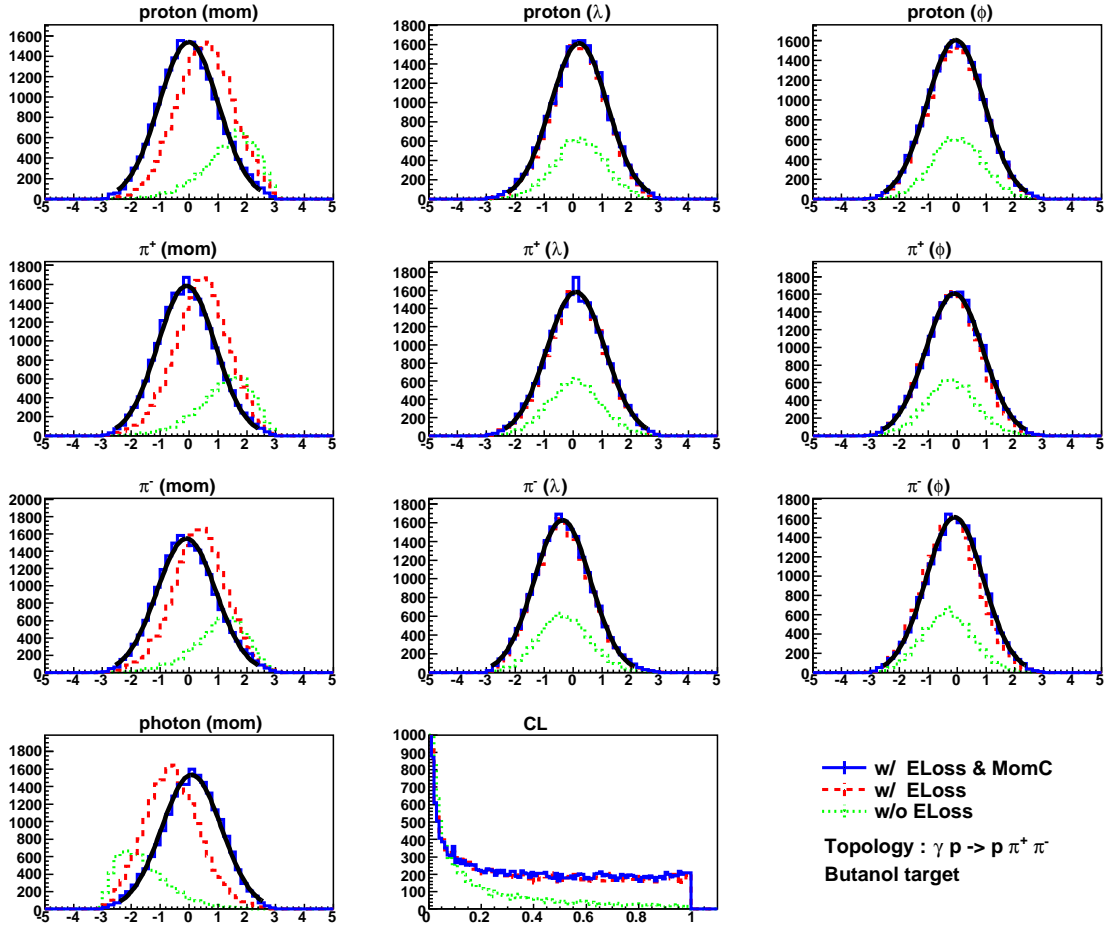


Figure 4.10: Pull and confidence-level distributions after applying all corrections in the butanol target. The green dotted line is made from the raw data. After the energy-loss correction is applied to the raw data, the red dashed line is obtained. One after another, photon-beam correction and momentum-correction are applied on the dataset and the blue solid histograms are obtained. These pulls and the confidence-level distribution are from Topology  $\gamma p \rightarrow p \pi^+ \pi^-$  ( $\gamma p \rightarrow p \pi^+ \pi^-$ ) with a 5 % confidence level cut applied. The lines represent fitting the data to a Gaussian function, the mean and  $\sigma$  of which can be found in Table 4.5.

## 4.6 Basic Cuts

The events of one of the four topologies were kinematically fitted after applying all corrections. In the next step, it is necessary to impose a series of cuts before extracting polarization observables. These cuts will serve to further refine the data sample and help remove events with accidental particles and other things that corrupt the dataset.

### 4.6.1 Vertex Cut

The g9a experiment has three kinds of targets such as a butanol, carbon, and polyethylene target. The butanol target is 5 cm long and 3 cm in diameter with its center located at the center of the CLAS spectrometer. The carbon target is located at 6 cm from the CLAS center downstream with 0.15 cm in length. The polyethylene target is located at 16 cm from the CLAS center downstream with 0.35 cm in length. The required vertex cuts therefore are:  $-3 \text{ cm} < z_{\text{all particles}} < +3 \text{ cm}$  for the butanol target,  $+5 \text{ cm} < z_{\text{all particles}} < +7.5 \text{ cm}$  for the carbon target, and  $+15 \text{ cm} < z_{\text{all particles}} < +18 \text{ cm}$  for the polyethylene target. The vertex cut involving the  $x$ - and  $y$ - components selects those events, which originated no more than 2 cm from the  $z$  axis (beam line).

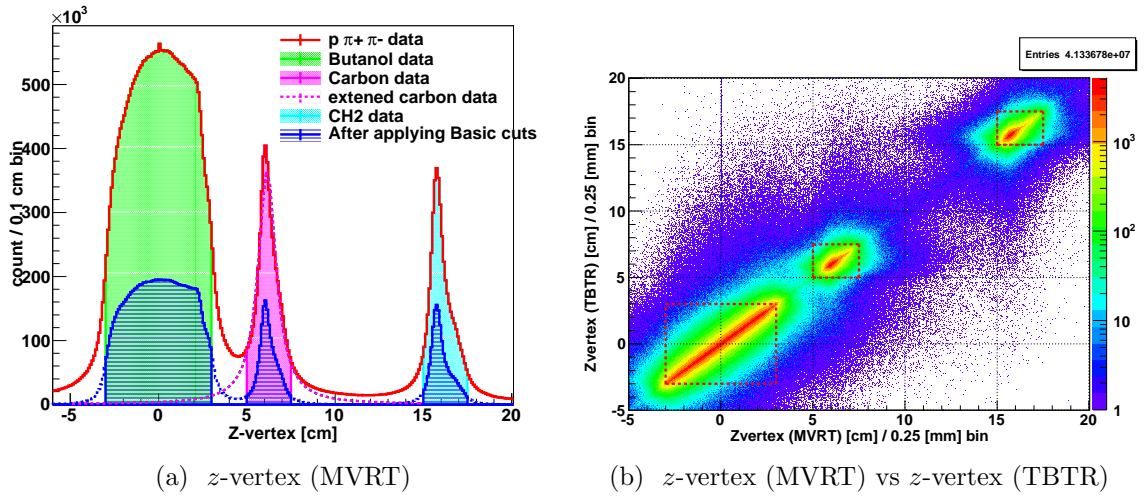


Figure 4.11: (a) The vertex  $z$ -position (axis along the beam line) of all reconstructed particles showing the positions of the three kinds of targets. The red line denotes the data with all  $p\pi^+\pi^-$  events. The blue line denotes events after applying basic cuts. The carbon data with all  $p\pi^+\pi^-$  events is fitted with a Breit-Wigner to check the distribution of carbon events. (b) A comparison of the  $z$ -vertex reconstruction from the MVRT and TBTR bank is shown on a log- $z$  color scale. Lines indicating the target cut regions are shown in the dashed red boxes.

Since the target vertex distributions of butanol and carbon targets are very close, as shown in Figure 4.11 (a), the overlap between both targets needs to be checked when determining event yields. To check the contamination of the butanol events with carbon events, the total distribution of the carbon data with all  $p\pi^+\pi^-$  events has been fitted with a Breit-Wigner function. We observe little interference of the carbon events with the butanol data. After applying basic cuts, the butanol and carbon events are clearly distinguished and there is no contamination of carbon events in the butanol events.

The vertex information in this analysis can be taken from either of the two banks, TBTR or MVRT. The difference of the vertex information between the TBTR and MVRT bank comes from the number of particles used to reconstruct the vertex. The reconstruction from the TBTR bank uses the vertex position for a particle based solely on CLAS information regarding the particle, whereas the MVRT bank assigns a single vertex information from the tracking information of all available charged particles in CLAS to calculate the best estimate of the vertex location. The MVRT vertex reconstruction is usually more accurate than the TBTR vertex when there are multiple tracks like in double-pion photoproduction since more tracks included in the reconstruction of the vertex location will determine the vertex with a higher degree of accuracy. In an ideal situation, both TBTR and MVRT vertex would give identical results, which seems to be a good approximation when looking at the vertex information for the entire dataset, as shown in Figure 4.11 (b). This plot shows single thin straight lines with  $V_z(TBTR) = V_z(MVRT)$  like an ideal situation. This analysis will use the vertex information from the MVRT bank.

## 4.6.2 Accidental Cuts

Accidental events can occur as a result of a number of factors, such as human error, detector error, natural events (e.g. cosmic ray), or a combination of these. Cuts to remove the accidental events imposed on the g9a dataset during this analysis use specific bank variables. These variables can be found in the GPID bank with the names 'NGRF' and 'TAGRID' and are shown in Figure 4.12 [25]. The NGRF variable indicates how many candidate photons were found in the reconstruction, which passed the reconstruction timing cut to find the incident photon. The TAGRID provides an index to the location of the photon related to a particle in the TAGR bank. The NGRF cut imposed on all final-state particles requires that they all have a value of one (NGRF=1). This means that for every final-state particles, there was only one photon found which passes the timing requirements. For the TAGRID cut, the requirement is that values of this variable for all final-state particles are the same and this guarantees that the reconstruction code found the same photon for all final state particles. These accidental cuts ensure that the events analyzed include a successful determination of the incident photon and that this photon is the same for all final-

state particles thus leading to a well-defined initial state.

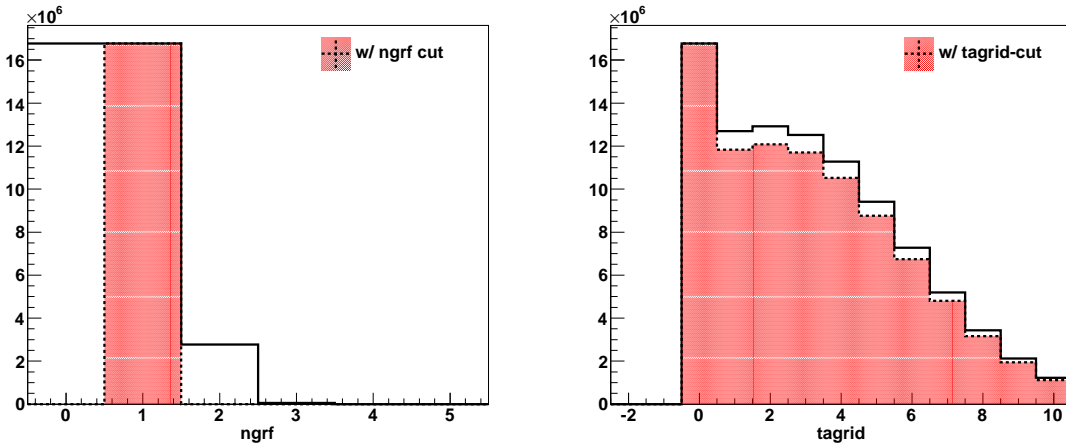


Figure 4.12: The distributions of the variable NGRF and TAGRID used in the g9a experiment.

### 4.6.3 Confidence Level Cut

By performing a cut on the confidence level, the background events, poorly reconstructed events as well as events with misidentified particles can be significantly removed from the g9a dataset. Figure 4.13 (a) shows the confidence level distribution in the topology  $\gamma p \rightarrow p\pi^+(\pi^-)$  before and after applying the confidence-level cut of 5% and Figure 4.13 (b) describes the missing mass distribution before and after applying the confidence-level cut of 5%. This confidence-level cut removes much of the background events while ideally only cutting out 5% of the good events.

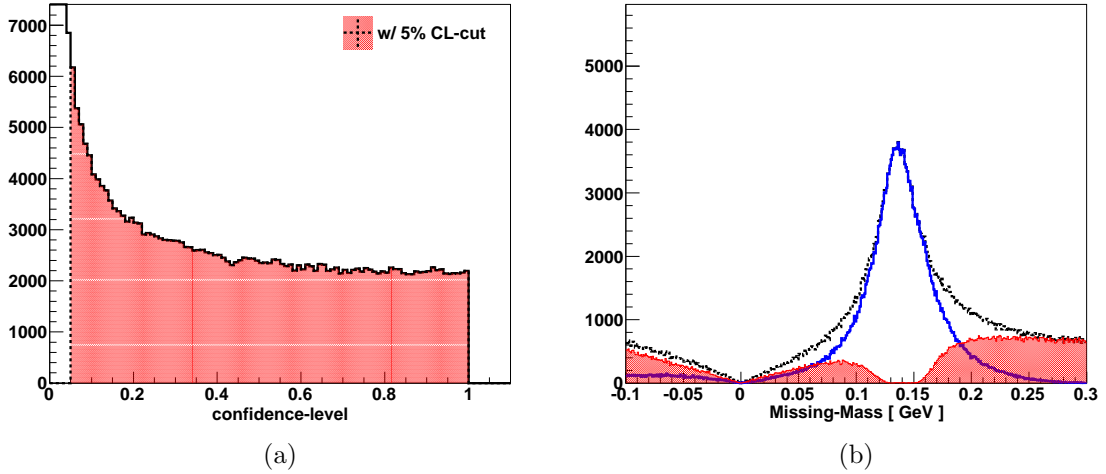


Figure 4.13: (a) The distribution of confidence level values for the topology  $\gamma p \rightarrow p\pi^+(\pi^-)$  generated from the butanol target. The confidence-level cut selects the events whose confidence level is greater than 0.05, as shown in the colored region. (b) The missing mass distribution made from the same topology and target as in Figure 4.13 (a). The black dashed line is made after applying all cuts and corrections without the confidence-level cut and the blue solid histogram indicates the good events after applying the confidence-level cut of 5% on the black dashed histogram. The colored area includes events whose confidence level is less than 0.05.

#### 4.6.4 Removing Bad Time-of-flight Paddles

Since some paddles of the time-of-flight (TOF) in the CLAS spectrometer are dead or malfunctioning, the information from these bad TOF paddles should be removed from the g9a dataset. The number of counts for each scintillator paddle is plotted in Figure 4.14. The bad paddles are identified by comparing the TOF paddle with very low counts to the average value of the sectors. The identified bad TOF paddles are listed in Table 4.6.

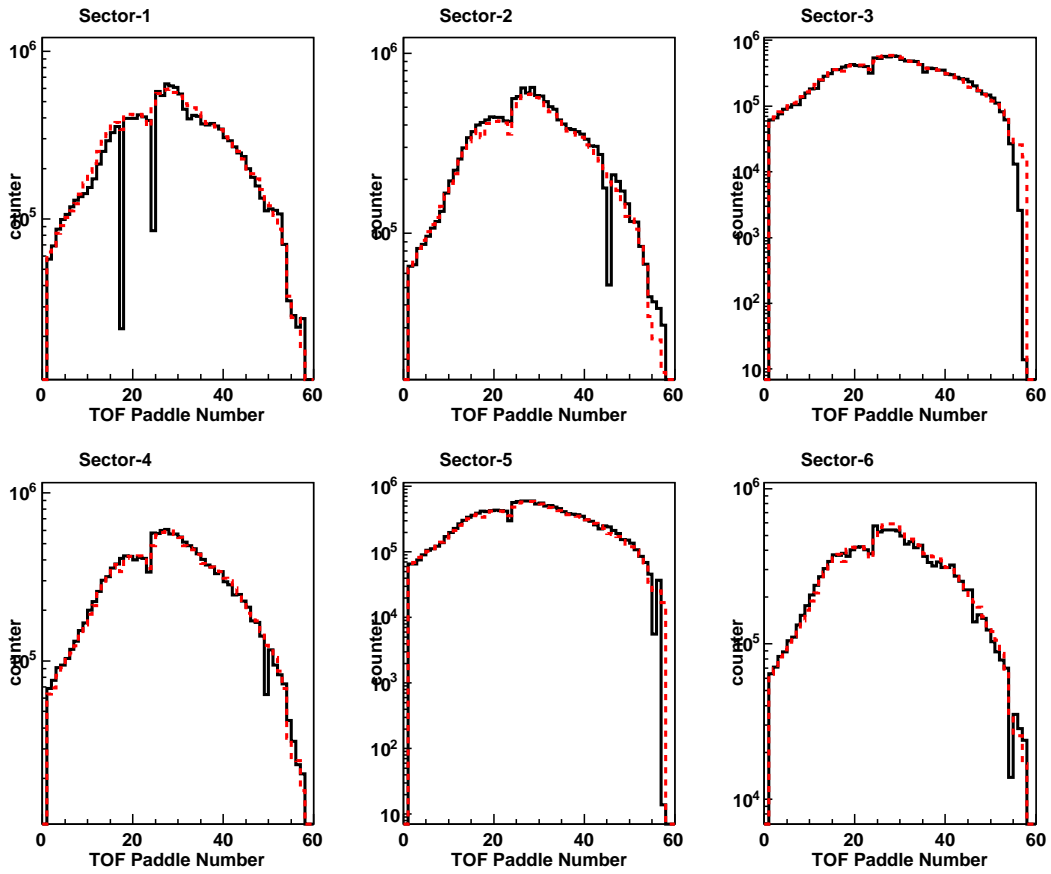


Figure 4.14: The paddle distributions of the time-of-flight counters in the six sectors. The red dashed line is the average of the six sectors' counts in the paddle distribution.

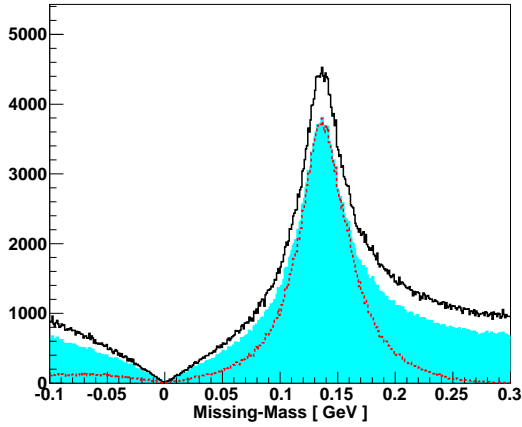
Table 4.6: The information of the bad time-of-flight paddles.

sector number	bad TOP paddles
1	17, 24
2	45
3	23, 35
4	23, 49
5	23, 55
6	54

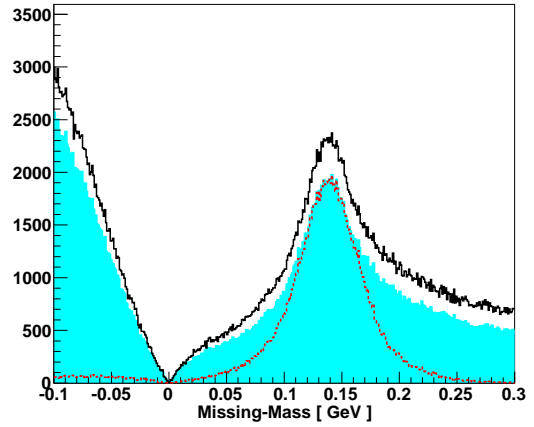
### 4.6.5 Event Distributions after Applying All Cuts and Corrections

The process of developing and applying energy and momentum corrections during the course of an analysis serves the purpose of correcting for the effects of the experimental setup, therefore resulting in a dataset that is as nature intended it. Additionally, determining and enforcing cuts used in an analysis serves not only to remove the remaining effects of the experimental setup but also to remove the contribution to the dataset from physics events not of interest to the analysis (the hadronic background). Figure 4.15 shows missing mass distributions and a squared missing mass distribution for the four kinds of topologies in the reaction  $\gamma p \rightarrow p\pi^+\pi^-$ , respectively. In this figure, missing-mass distributions after applying energy and momentum corrections for the 4-vectors in the reaction  $\gamma p \rightarrow p\pi^+\pi^-$  are described and the change of histograms after applying all cuts with and without the confidence-level cut are also shown in Figure 4.15.

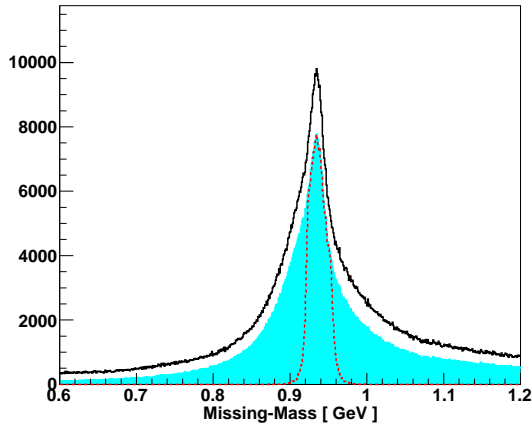
The remaining background may be comprised of accidental events where a detected particle was attributed to an event to which it does not belong, events with an incorrect initial state like a misidentification of a photon and events originating from interactions with matter other than the target materials. A typical method of observing the background is to choose a final state topology and construct the missing mass of that topology, as shown in Figure 4.13 (b). A single cut on the confidence level greatly reduces this background but does not entirely remove it. Through the application of vertex position, photon and particles identification variables, this background may be reduced even further. Because the g9a experiment uses a “dirty” polarized target, the free-proton events from the butanol after removing some of the background still have contributions from bound nucleons. These bound-nucleon contributions still need to be taken care of.



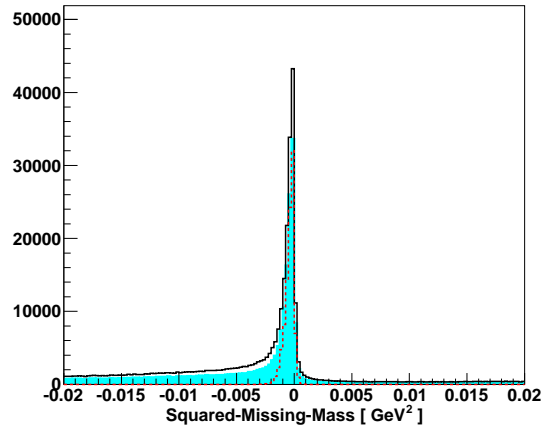
(a) Topology:  $\gamma p \rightarrow p \pi^+ (\pi^-)$



(b) Topology:  $\gamma p \rightarrow p \pi^- (\pi^+)$



(c) Topology:  $\gamma p \rightarrow \pi^+ \pi^- (p)$



(d) Topology:  $\gamma p \rightarrow p \pi^+ \pi^- ( )$

Figure 4.15: Missing-mass distributions for the four different topologies. The  $\pi^-$  particle is missing in all  $p \pi^+ \pi^-$  events (a), the  $\pi^+$  particle is missing (b), the  $p$  particle is missing (c), and there are no particles missing (d). The black solid line is made from the butanol target after applying all corrections. The histogram filled in light blue indicates the good events after applying all basic and accidental cuts and corrections without the confidence-level cut. The red dashed histogram includes events whose confidence level is greater than 0.05. The distribution in (d) is made as a function of the squared missing mass.

## 4.7 Beam and Target Polarization

### 4.7.1 Photon Beam Polarization

Circularly-polarized photons are produced by bremsstrahlung of longitudinally-polarized electrons from an amorphous radiator. The degree of circular polarization of the bremsstrahlung photons  $\delta_{\odot}$  can be calculated from the longitudinal polarization of the electron beam  $\delta_e$  multiplied by a numerical factor. In particular, with  $x = E_{\gamma}/E_e$ , the degree of circular polarization of bremsstrahlung from longitudinally-polarized electrons is given by [31] :

$$\delta_{\odot} = \delta_e \cdot \frac{4x - x^2}{4 - 4x + 3x^2}. \quad (4.14)$$

Figure 4.16, made from Equation 4.14, shows that the circular polarization of the photon beam and the photon beam energy are roughly proportional to each other. In the figure, the photon energy  $E_{\gamma}$  is described in proportion of the amount of the electron-beam energy  $E_e$ .

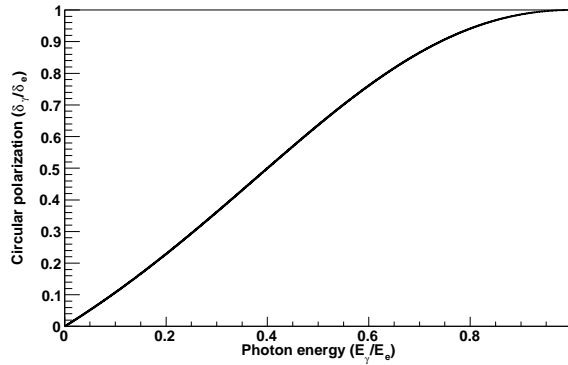


Figure 4.16: Circular polarization of the photon beam as a function of photon energy.

The data with a circularly-polarized photon beam in the g9a experiment have two kinds of electron beam energies, 1.645 GeV and 2.478 GeV, as referenced in Table 4.1. Runs with different electron beam energies have different circular polarizations for the same photon energy  $E_{\gamma}$ . Thus, the circular polarization of the photon beam should be calculated separately in runs with different electron beam energies, as shown in Figure 4.17. As the first step in calculating the circular polarization of the photon beam, the longitudinal polarization of the electron beam  $\delta_e$  should be found in runs with different electron beam energies. Table 4.7 summarizes the Møller measurements of the electron-beam polarization  $\delta_e$  in the g9a experiment and their average values in runs with different electron beam energies.

Table 4.7: Møller measurements of the electron-beam polarization.

Electron-beam energy $E_e$	Date	Run number	Electron-beam polarization $\delta_e$	
				Average
1.645 GeV	Nov. 12, 2007	55544	$+85.228 \pm 1.420$	$84.789 \pm 0.470$
			$-78.523 \pm 1.350$	
			$-79.150 \pm 1.26$	
			$+88.700 \pm 1.480$	
	Nov. 13, 2007	55552	$+84.167 \pm 1.330$	
			$-84.725 \pm 1.530$	
Nov. 19, 2007	55588	$-86.531 \pm 1.380$		
		$+88.409 \pm 1.440$		
		$+87.753 \pm 1.480$		
2.478 GeV	Nov. 28, 2007	55608	$-82.534 \pm 1.400$	$83.016 \pm 0.789$
	Nov. 28, 2007	55608	$-79.450 \pm 1.410$	
			$+80.060 \pm 1.400$	
	Jan. 07, 2008	56194	$-83.267 \pm 1.380$	
	Feb. 08, 2008	56202	$-83.248 \pm 1.320$	

An average value of 84.798 % and 83.016 % with an uncertainty of 0.470 % and 0.789 %, respectively, is used for the degree of the electron-beam polarization  $\delta_e$ . Since the center-of-mass energy is used as an independent kinematic variable, the circular polarization cannot be a continuous function. The average values of the circular polarization for a specific phase-space volume  $\Delta\tau$  in each center-mass-of-energy bin are given by :

$$\bar{\delta}_\odot = \frac{1}{N^+ + N^-} \sum_{i \in \Delta\tau} \delta_\odot(W). \quad (4.15)$$

$N^\pm$  are the total number of  $\gamma p \rightarrow p\pi^+\pi^-$  events for the two helicity states and  $W$  is the center-of-mass energy. These average values are calculated in each center-of-mass energy bin, shown in Table 4.8. Figure 4.17 shows circular polarizations and their averages for the two electron beam energies, 1.645 GeV and 2.478 GeV.

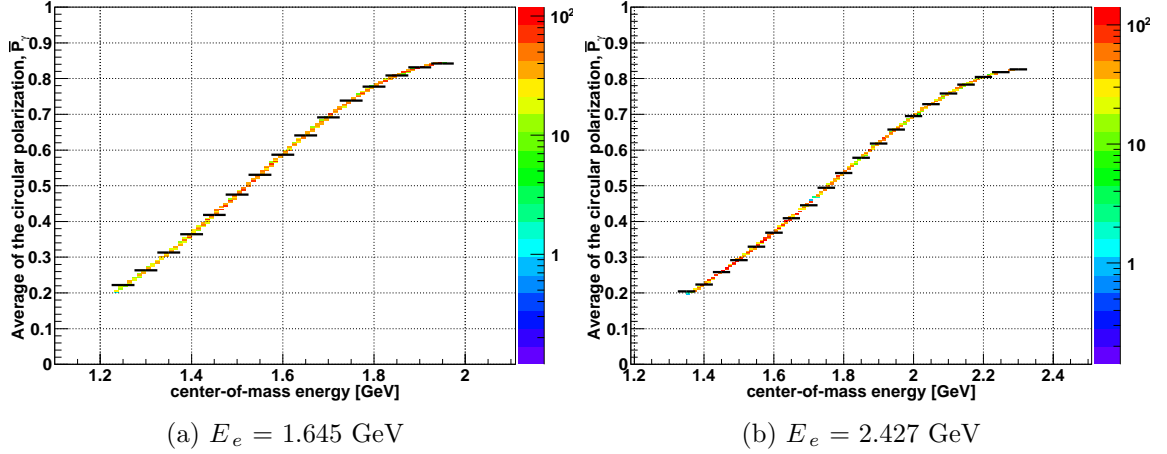


Figure 4.17: The average degree of circular polarization of the photon beam as a function of the center-of-mass energy for electron beam energies 1.645 GeV (a) and 2.427 GeV (b).

Table 4.8: The average degrees of circular polarization in FROST g9a.

The center of mass energy [GeV]	The average circular polarization, $\delta_{\odot}$	
	$E_e = 1.645$ GeV	$E_e = 2.427$ GeV
1.25	$0.22172 \pm 0.00007$	
1.30	$0.26349 \pm 0.00006$	
1.35	$0.31319 \pm 0.00007$	$0.20442 \pm 0.00019$
1.40	$0.36416 \pm 0.00008$	$0.22325 \pm 0.00007$
1.45	$0.41810 \pm 0.00008$	$0.25841 \pm 0.00008$
1.50	$0.47551 \pm 0.00009$	$0.29194 \pm 0.00010$
1.55	$0.53077 \pm 0.00010$	$0.32929 \pm 0.00010$
1.60	$0.58695 \pm 0.00013$	$0.36861 \pm 0.00012$
1.65	$0.64083 \pm 0.00015$	$0.40909 \pm 0.00014$
1.70	$0.69159 \pm 0.00017$	$0.44555 \pm 0.00021$
1.75	$0.73866 \pm 0.00019$	$0.49416 \pm 0.00020$
1.80	$0.77739 \pm 0.00022$	$0.53564 \pm 0.00022$
1.85	$0.80903 \pm 0.00024$	$0.57837 \pm 0.00031$
1.90	$0.83162 \pm 0.00025$	$0.61849 \pm 0.00029$
1.95	$0.84239 \pm 0.00034$	$0.65746 \pm 0.00031$
2.00		$0.69530 \pm 0.00035$
2.05		$0.72835 \pm 0.00037$
2.10		$0.75822 \pm 0.00040$
2.15		$0.78291 \pm 0.00045$
2.20		$0.80441 \pm 0.00051$
2.25		$0.81792 \pm 0.00059$
2.30		$0.82581 \pm 0.00065$

### 4.7.2 Beam Charge Asymmetry

The electron beam polarization is toggled between the  $h^+$  helicity state and the  $h^-$  helicity state at a 30 Hz rate. Therefore, the photon-beam flux for both helicity states should be identical on average. Small beam-charge asymmetries of the electron beam, however, can cause instrumental asymmetries in the observed  $\gamma p \rightarrow p\pi^+\pi^-$  asymmetries, and need to be taken into account. This beam-charge asymmetry can be calculated by considering the luminosities for helicity-plus and -minus events :

$$\Gamma^\pm = \alpha^\pm \Gamma = \frac{1}{2}(1 \pm \bar{a}_c)\Gamma, \quad (4.16)$$

where  $\Gamma$  is the total luminosity. The parameter  $\alpha^\pm$  is used to find the helicity plus and minus luminosity,  $\Gamma^\pm$ , from the total luminosity. This parameter depends on the mean value of the electron-beam charge asymmetry  $\bar{a}_c$ . Figure 4.18 shows the beam-charge asymmetry,  $a_c$ , for the g9a runs used in this analysis.

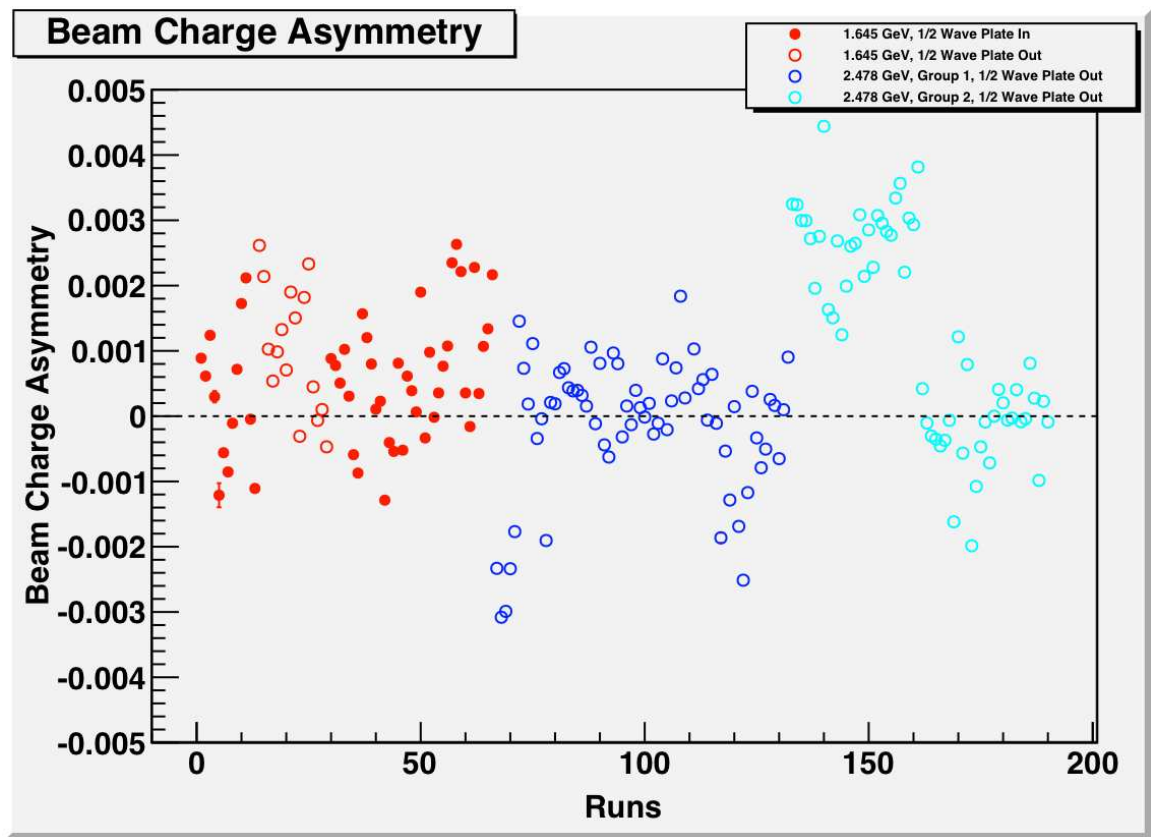


Figure 4.18: Distribution of beam-charge asymmetries for the analyzed runs.

Their averages and errors calculated for different periods are referenced in Table 4.9. These beam-charge asymmetries do not affect the final result of this analysis since these asymmetries are very small.

Table 4.9: The mean and error of the beam-charge asymmetries,  $\bar{a}_c$ , calculated in each period.

Period	Average of the beam-charge asymmetry, $\bar{a}_c$	$\sigma$
1, 2, and 3	$7 \times 10^{-4}$	$1 \times 10^{-3}$
4 and 5	$3 \times 10^{-5}$	$3 \times 10^{-3}$
6 and 7	$1 \times 10^{-3}$	$4 \times 10^{-3}$

### 4.7.3 Target Polarization

The target polarization has the magnitude and the direction, as shown in Figure 4.19. The polarization direction is defined by two quantities: the direction of the holding magnetic field with respect to the beam and the direction of the proton polarization with respect to the holding field. Table 4.10 shows how the direction of the target polarization is defined in the FROST g9a experiment.

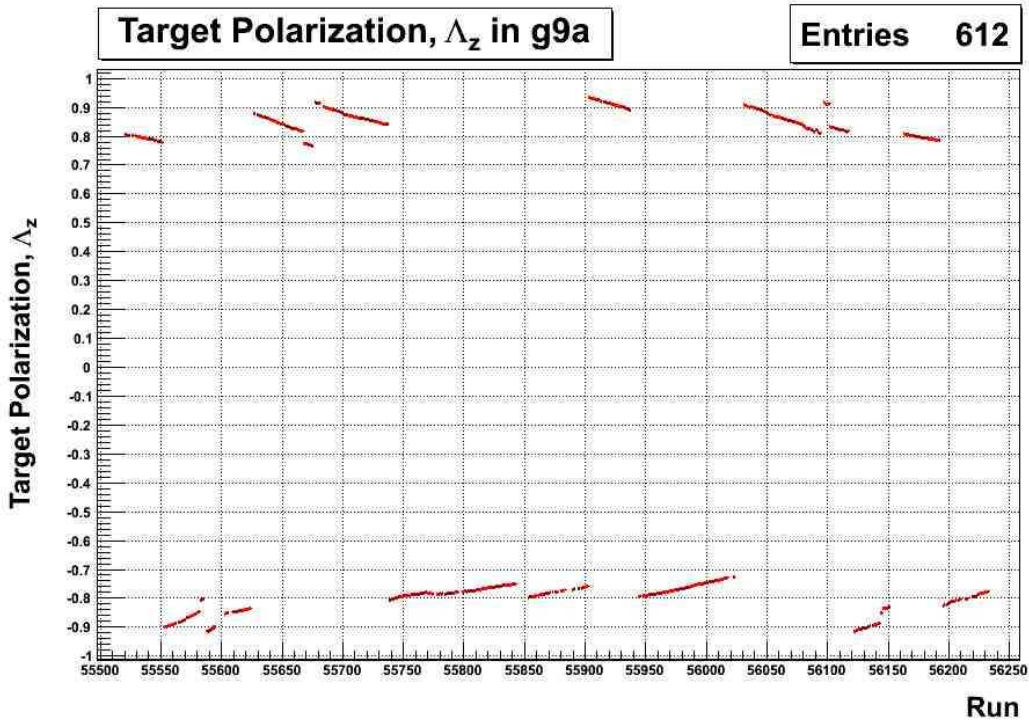


Figure 4.19: Target polarization versus run number measured in the g9a experiment.

Table 4.10: The definition of the direction of the target polarization used in the g9a experiment. The first plus sign in L++ means the direction of the holding magnet and the second indicates the direction of the proton polarization.

L++	: Positive target polarization
L+-	: Negative target polarization
L-+	: Negative target polarization
L--	: Positive target polarization

The plus (minus) sign in the direction of the holding field means the field is parallel (anti-parallel) to the beam direction. The plus (minus) sign in the direction of the proton polarization indicates the protons are polarized parallel (anti-parallel) to the holding field. It turned out later that the directions of the target polarization between the NMR data and the run table are not consistent. The exact directions of the target polarization are checked from the target asymmetry in the reaction  $\gamma p \rightarrow p\pi^+\pi^-$  based on the information of the run table (see Appendix A). Table 4.11 shows the information of the direction of the target polarization before and after correcting the inconsistency using the target asymmetry.

Table 4.11: The direction of the target polarization before and after correcting initial inconsistencies. After the correction, the direction of the target polarization in period 4 and 5 is reversed. The arrow  $\Rightarrow$  ( $\Leftarrow$ ) means the target polarization is parallel (anti-parallel) to the beam direction.

Period	The target polarization	
	Before the correction	After the correction
1	L+-( $\Leftarrow$ )	$\Leftarrow$
2	L+-( $\Leftarrow$ )	$\Leftarrow$
3	L++( $\Rightarrow$ )	$\Rightarrow$
4	L-+( $\Leftarrow$ )	$\Rightarrow$
5	L--( $\Rightarrow$ )	$\Leftarrow$
6	L++( $\Rightarrow$ )	$\Rightarrow$
7	L+-( $\Leftarrow$ )	$\Leftarrow$

Each run has a different value of the target polarization and in order to be used in the asymmetry equation, averages per period value should be calculated.  $\bar{\Lambda}_z$  is the mean value of the longitudinal target polarization :

$$\bar{\Lambda}_z^\pm = \frac{1}{N^\pm} \sum_{run} \Lambda_z^\pm(run), \quad (4.17)$$

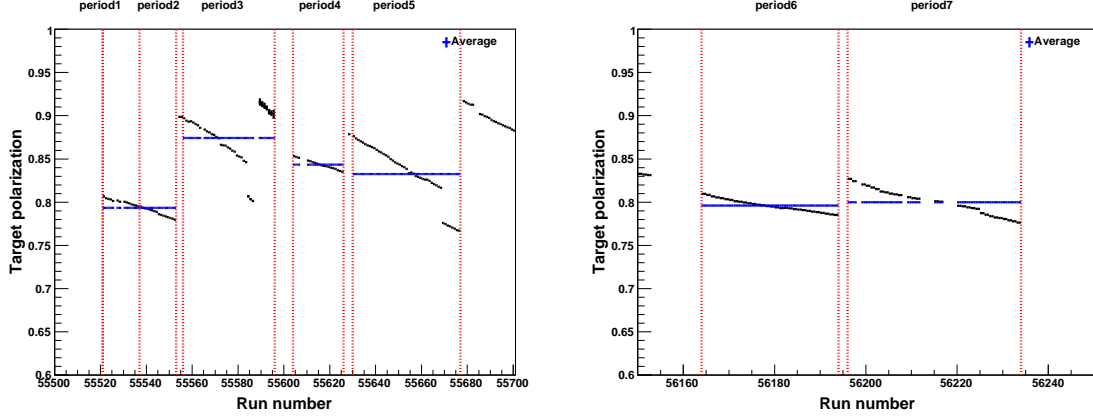


Figure 4.20: Values of target polarization versus run number measured in the g9a experiment and their averages (the blue line) made per period.

where  $\pm$  means the target polarization is parallel/anti-parallel to the beam and  $N^\pm$  is the total numbers of observed counts in the different target polarization. Figure 4.20 shows the distribution of target polarizations used in the dataset with the circularly-polarized beam and longitudinally-polarized target. The average values are calculated by using Equation 4.17 and their mean values are described in Table 4.12 with the statistical errors and systematic errors calculated by standard error propagation.

Table 4.12: Average target polarization with the statistical and systematic error per period and the ratio between the different target polarizations. This ratio of the different target polarization is used in Equation 5.12.

Period	Average target polarization			Ratio of target polarization		
	$\Lambda_z$	error		$\Lambda_z(=>)/\Lambda_z(<=)$	error	
		statistical	systematic		statistical	systematic
2	0.793	4.503e-05	1.685e-03	1.102	3.592e-04	2.350e-03
3	0.874	2.806e-04	1.736e-04			
4	0.843	5.165e-05	2.575e-04	1.013	7.402e-05	3.631e-04
5	0.833	3.321e-05	1.565e-04			
6	0.796	3.079e-05	2.136e-04	0.995	5.777e-05	3.781e-04
7	0.800	3.461e-05	2.150e-04			

#### 4.7.4 Confirm the Information of the Beam and Target Polarization

In the next step, we should assure that the directions of the determined beam and target polarizations are credible. The direction of the target polarization is mentioned in Table 4.11. Therewith, the direction of the beam polarization depends on the condition of the half-wave plate (HWP): IN or OUT. The longitudinal polarization of the electron beam is flipped pseudo-randomly with 30 sequences of helicity (+,−) or (−,+) signals per second. Occasionally the HWP is inserted in the circularly-polarized laser beam of the electron gun to reverse helicities and the beam polarization phase should be changed by 180°. The HWP is inserted and removed at semi-regular intervals throughout the experimental run to ensure that no polarity-dependent bias is manifested in the measured asymmetry. The electron-beam helicity information is stored in the level1-trigger-latch word of the TGBI bank. Bit 16 in the level1-trigger-latch word is the helicity-state bit. It indicates the sign of the electron-beam polarization, as shown in Table 4.13.

Table 4.13: Helicity signal from the TGBI-bank latch1 for the two half-wave-plate positions. In the table, the sign +(−) means the beam polarization is parallel (anti-parallel) to the beam direction.

TGBI latch1 bit-16	Beam helicity	
	$\lambda/2$ (OUT)	$\lambda/2$ (IN)
1	+	−
0	−	+

When the half-wave plate is OUT, the number 1 in bit 16 of the level1-trigger latch means the beam polarization is parallel to the beam direction and the number 0 means the beam polarization is antiparallel to the beam. When this plate is IN, the directions of the beam polarization related to the number 1 and 0 are switched. Table 4.14 shows the information of the condition of the half-wave plate and the direction of the target polarization used in this analysis. The reliability of the information, as referenced in Table 4.14, is confirmed by the beam and target asymmetry (see Appendix A).

Table 4.14: The condition of the beam and target polarization of each period used in this analysis.

Period	Run range	Beam polarization	Target polarization
		The condition of the half-wave plate	
1	55521 - 55536	IN	$\leftarrow$
2	55537 - 55555	OUT	$\leftarrow$
3	55556 - 55595	IN	$\Rightarrow$
4	55604 - 55625	IN	$\Rightarrow$
5	55630 - 55678	IN	$\leftarrow$
6	56164 - 56193	OUT	$\Rightarrow$
7	56196 - 56233	OUT	$\leftarrow$

## 4.8 Normalization Factor

As mentioned earlier, the g9a experimental data with the circularly-polarized beam can be divided into seven groups of runs with similar conditions called periods and each period has a different direction of the target polarization, as referenced in Table 4.14.

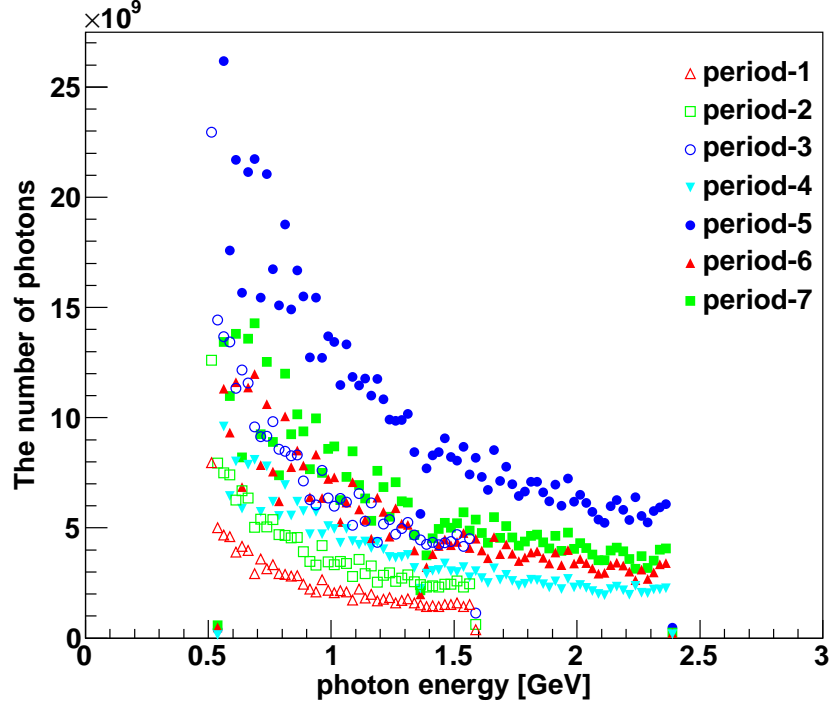


Figure 4.21: The distribution of the number of photons as a function of photon energy saved in the “gflux” file. In this picture, there are seven periods and each period has 100 and 25-MeV wide bins in the range from 0.4875 to 2.9875 GeV, respectively. Period 5 has the largest number of photons.

Datasets with different target polarizations should be combined to calculate the asymmetry in the reaction  $\gamma p \rightarrow p\pi^+\pi^-$ . Since, however, the number of runs included in each period is different and each run has a different number of events, a normalization factor is needed to adjust the imbalance of the number of events between periods. The events included in the data are roughly proportional to the initial number of photons. The normalization factors can be found from comparing the number of photons between periods. The information about the number of photons in Hall-B is saved in “gflux” files. The gflux files contain the number of photons and their uncertainties in a given bin, as shown in Figure 4.21. The g9a data with the circularly-polarized beam can be divided largely into two datasets according to the electron beam energy

$E_{e^-}$ . One dataset includes period 1, 2, and 3 with  $E_{e^-} = 1.645$  GeV and another dataset has period 4, 5, 6, and 7 with  $E_{e^-} = 2.427$  GeV. In the first dataset, Period 1 and Period 2 have very similar conditions except the condition of the half-wave plate. Because of statistics, the data of Period 1 and Period 2 will be combined after considering the difference of the half-wave plate between two periods and these combined data will then be defined as Period 2.

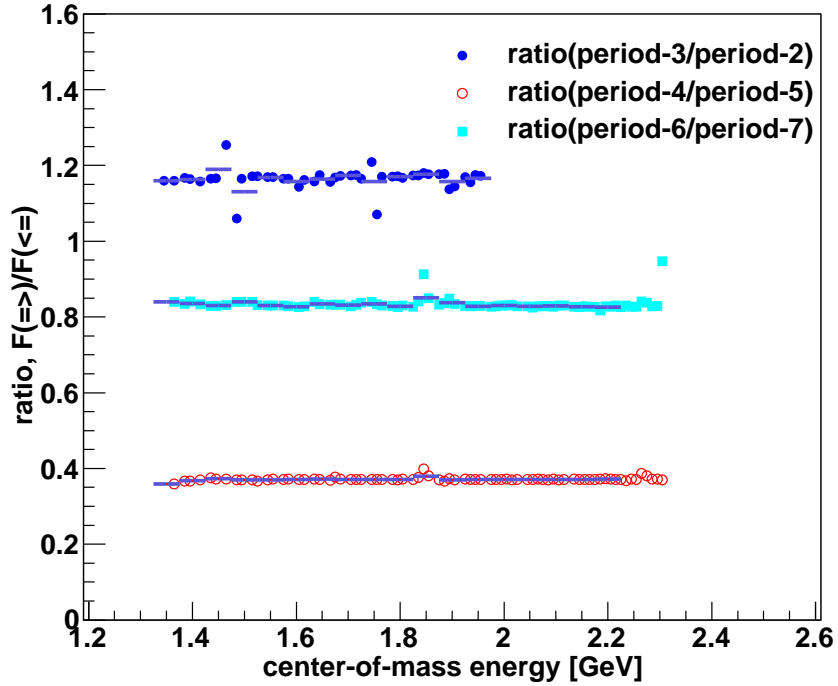


Figure 4.22: The ratio of the number of photons between periods with the target polarizations parallel ( $\Rightarrow$ ) and anti-parallel ( $\Leftarrow$ ) to the beam.

As mentioned before, the normalization factor is defined as the ratio of the number of photons between datasets with different directions of the target polarization, as shown in Figure 4.22. The periods 3, 4, and 6 have the target polarization direction parallel to the beam direction, as shown in Table 4.14 and the other periods have an opposite direction of the target polarization. There are three kinds of period-combinations to calculate the polarization observables in this analysis: combination-32 with period 3 and 2, combination-45 with period 4 and 5, and combination-67 with period 6 and 7.

Table 4.15: The normalization factor used in combination-32, combination-45, and combination-67.

The center of mass energy [GeV]	ratio, $F(\Rightarrow)/F(\Leftarrow)$		
	per-3/per-2	per-4/per-5	per-6/per-7
1.35	1.160	0.359	0.840
1.40	1.163	0.368	0.836
1.45	1.190	0.373	0.830
1.50	1.131	0.370	0.840
1.55	1.168	0.370	0.830
1.60	1.157	0.371	0.828
1.65	1.164	0.372	0.834
1.70	1.174	0.371	0.831
1.75	1.158	0.371	0.835
1.80	1.171	0.371	0.828
1.85	1.177	0.380	0.851
1.90	1.157	0.370	0.837
1.95	1.166	0.371	0.828
2.00		0.371	0.830
2.05		0.371	0.828
2.10		0.371	0.829
2.15		0.371	0.827
2.20		0.372	0.826

## 4.9 Dilution Factor

The g9a experiment utilizes butanol ( $C_4H_9OH$ ) as the main target material. When this main target is polarized, only the hydrogen component of the butanol can be polarized. Polarized free-proton events from the butanol target can be separated from bound-nucleon events, which are subject to Fermi motion, and other background events by using a dilution factor. This is illustrated in Figure 4.23. The dilution factor is generally defined as the ratio between the free proton and the full butanol contribution to the cross section. A simple calculation based on the chemical formula of butanol ( $C_4H_9OH$ ) yields  $10/74 = 0.135$  as the ideal dilution factor. In practice, dilution factors are reaction dependent and are generally larger than the ideal factor after the application of the selection cuts.

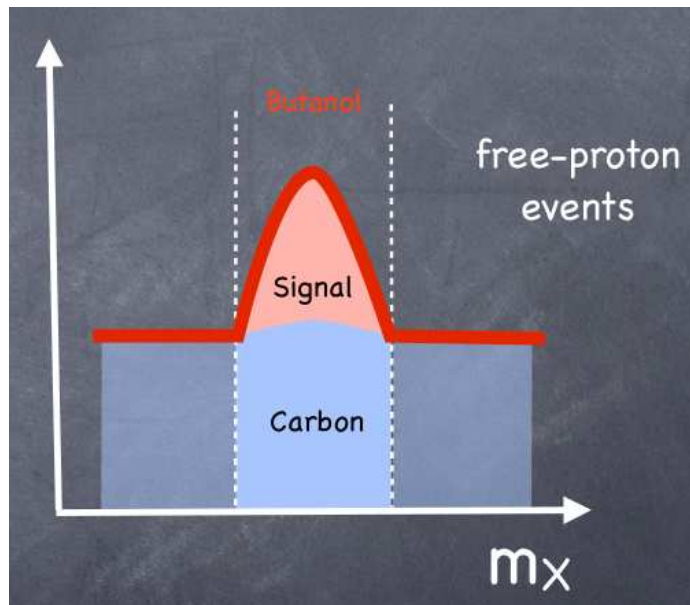


Figure 4.23: Illustration of the signal and background events in the butanol data from the g9a experiment.

To determine the dilution factor in this analysis, it was necessary to evaluate the contribution of the bound-nucleon events to the reaction  $\gamma p \rightarrow p\pi^+\pi^-$ . In the g9a experiment, the carbon target is used as a known source of bound nucleons to estimate the contribution of bound-nucleon and background events in the butanol data, as shown in Figure 4.23. It is assumed that bound-nucleon events from  $^{12}C$  and  $^{16}O$  nuclei in the butanol behave similarly, and can be appropriately subtracted using the data from the carbon target.

Figure 4.24 (a) illustrates an example of the missing  $\pi^-$  mass distribution using butanol (in black) and carbon (in red) data for the topology  $\gamma p \rightarrow p\pi^+(\pi^-)$ . Since the carbon events from the g9a experiment have the hydrogen contamination [32], the carbon events from the g9b experiment are used in this analysis. Figure 4.24 (b) shows the same butanol distribution where the bound-nucleon and background events are described with a Chebyshev polynomial. To isolate the free-proton events in the butanol data more accurately, the carbon distribution should be scaled and then subtracted from the butanol distribution. The equation to calculate the dilution factor is :

$$D(W) = 1 - \frac{\mathbf{s} \cdot N_C(W)}{N_{C_4H_9OH}(W)}, \quad (4.18)$$

where  $N_C$  is the number of events from the carbon target and  $N_{C_4H_9OH}$  is the number of events from the butanol target. In Equation 4.18,  $\mathbf{s}$  is the parameter to scale the carbon distribution and  $\mathbf{s} \cdot N_C$  is the number of events from the scaled carbon distribution, i.e., the true contribution of bound-nucleon and background events in the butanol data. In Section 4.9.1, the method to determine the scale parameters referred to as "phase space scale factors" will be described [33].

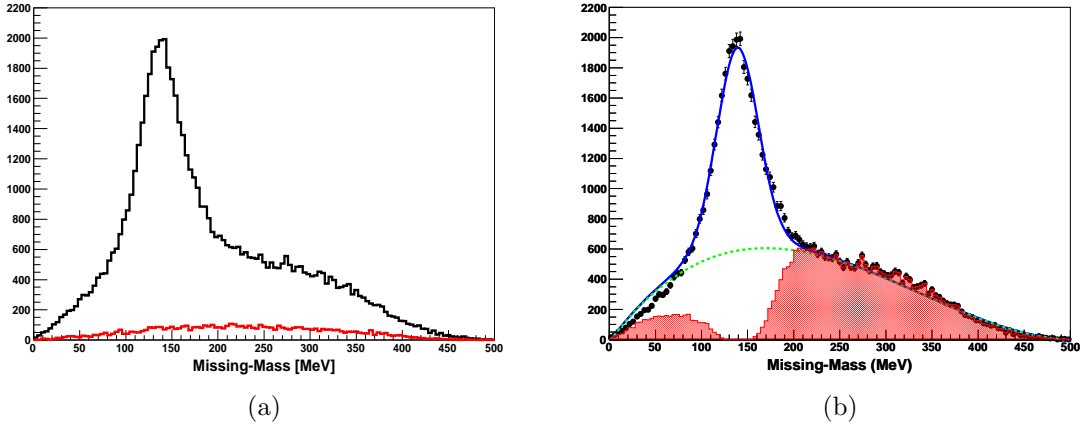


Figure 4.24: (a) The missing mass distribution for the topology  $\gamma p \rightarrow p\pi^+(\pi^-)$  from the butanol and carbon target. The black line describes the butanol events from the g9a experiment and the red line denotes the carbon events from the g9b experiment. (b) The fitted missing mass distribution using a mixed function of a Gaussian and a Chebyshev polynomial (blue line). The green dotted line denotes the Chebyshev polynomial in the mixed fitting function. The colored area includes events whose confidence level is less than 0.05. The data are selected from  $W \in [1.575, 1.625]$  GeV; the beam polarization is anti-parallel to the beam and the target polarization is anti-parallel to the beam direction.

## 4.9.1 Phase Space Scale Factor

The scale factors or the "phase space scale factors" are used to produce the scaled carbon distributions from the carbon data. They are determined by comparing the bound-nucleon events in the butanol data with the carbon data. In order to accomplish this, it is necessary to isolate the bound-nucleon events from the butanol data. The free proton events in the butanol data are from protons "at rest", that is, these events are not subject to Fermi motion. Energy conservation for the topology  $\gamma p \rightarrow p' \pi^+ (\pi^-)$  requires :

$$E_{\pi^-} = (E_\gamma + E_p) - (E_{p'} + E_{\pi^+}), \quad (4.19)$$

where  $(E_\gamma + E_p)$  is the energy of the initial state, and  $(E_{p'} + E_{\pi^+})$  is the energy of the final state. The free proton events obey the relation  $E_p = m_p$  and are distributed near the missing-pion peak, as shown in Figure 4.25 (a). Since the bound-nucleon events have additional Fermi motion, they obey the relation  $E_p = \sqrt{m_p^2 + p_F^2}$ , where  $p_F$  is the Fermi momentum, and can be distributed far from the peak. In the squared missing-mass distribution of the butanol data, free-proton events in the butanol data cannot have the negative values, but the squared missing-masses of bound-nucleon events can be the negative. The squared missing-mass distribution can be classified as a region that is possible for free proton reactions and that can only contain events from bound nucleons. In Figure 4.25, a loose cut at  $MM^2 < -0.2 \text{ GeV}^2$  can isolate bound-nucleon events in butanol data.

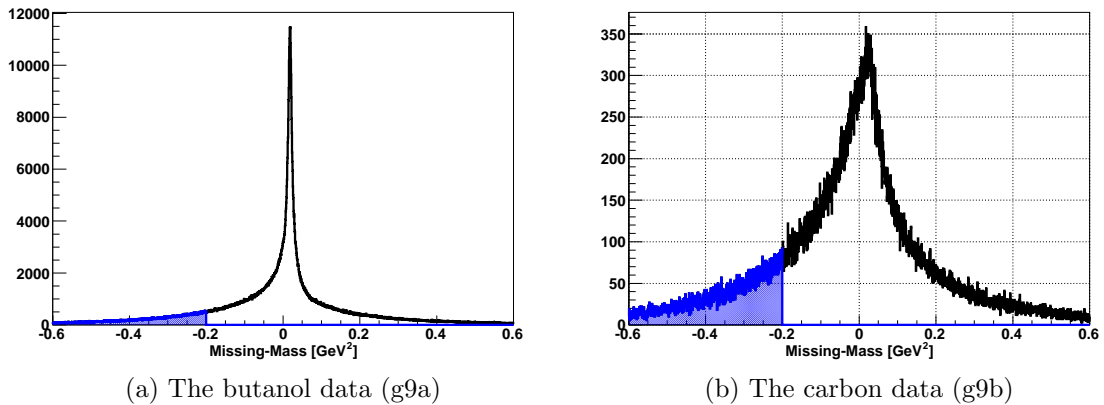


Figure 4.25: The missing squared-mass distribution for Topology  $\gamma p \rightarrow p \pi^+ (\pi^-)$  from the butanol target (a) and from the carbon target (b). The blue-shaded regions indicate  $MM^2 < -0.2 \text{ GeV}^2$  and should contain only events for bound nucleons.

Figure 4.26 shows the two dimensional distribution of two kinematic variables: center-of-mass energy,  $W$ , versus the azimuthal angle,  $\phi_{\pi^+}^*$ , after applying the loose

cut at  $MM^2 < -0.2 \text{ GeV}^2$  in the squared missing-mass distribution of the butanol and carbon data.

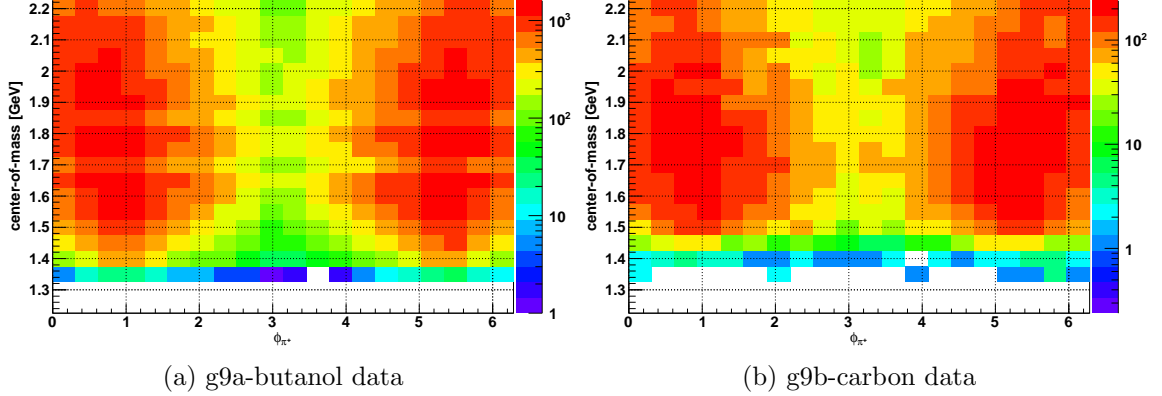


Figure 4.26: The comparison of the  $\pi^+$   $W$  versus  $\phi_{\pi^+}^*$  from the butanol and carbon data in the reaction  $\gamma p \rightarrow p\pi^+(\pi^-)$ . The phase space (a) is from the butanol data of the g9a experiment, and the phase space (b) is from the carbon data of the g9b experiment.

The phase space scale factor is calculated by simply dividing the two histograms in Figure 4.26. Figure 4.27 (a) shows that the resulting phase space scale factors exhibit a very flat distribution and are independent of the azimuthal angle  $\phi_{\pi^+}^*$ . Figure 4.27 (b) shows the free-proton distribution and scaled carbon distribution calculated by the method described in this section.

## 4.9.2 Q-factor Method

Another approach, called the Q-factor method, has been used to separate the signal events from the background events. The Q-factor method assigns each event in the butanol data an event-based quality factor which denotes the probability that an event is a signal event [34]. The contribution of the bound-nucleon and background events can be removed from the butanol events by weighting each event with this Q-factor. In order to determine the Q-factors, the following 5 kinematic variables, used to define the 5-dimensional kinematic phase space of the reaction  $\gamma p \rightarrow p\pi^+\pi^-$ , have been chosen:  $\cos \Theta_{c.m.}^{proton}$ , a mass ( $m_{p\pi^+}$ ,  $m_{p\pi^-}$ , or  $m_{\pi^+\pi^-}$ ), the center-of-mass energy  $W$ , the polar and azimuthal angle  $\theta_{\pi^+}^*$  and  $\phi_{\pi^+}^*$  in the rest frame of the  $\pi^+\pi^-$  system. For each event (seed event), events closest in the kinematic phase space defined by 4 of the 5 independent variables are selected to perform event-based unbinned maximum

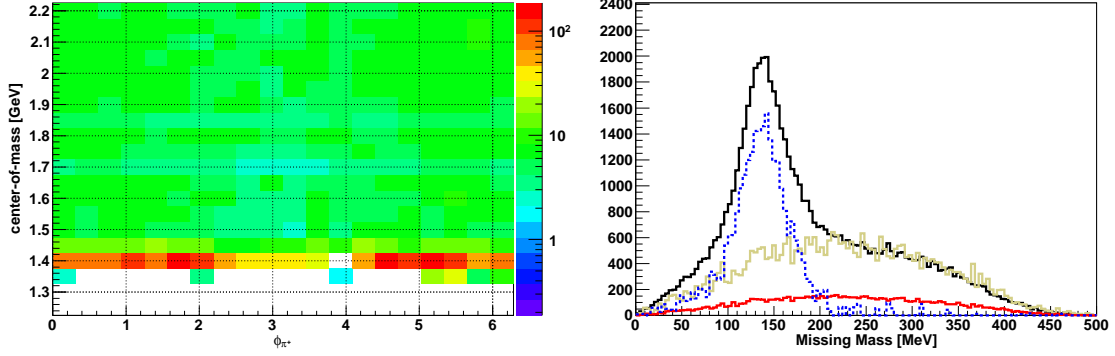


Figure 4.27: (a) The  $\pi^+$  phase space scale factor on two dimensional distribution of the  $\pi^+$   $W$  versus  $\phi_{\pi^+}^*$  (b) The missing mass distribution with the free-proton and bound-nucleon distribution calculated using the phase space scale factors given in (a). The black line describes the butanol events for Topology  $\gamma p \rightarrow p\pi^+(\pi^-)$  and the center-of-mass energy  $W \in [1.575, 1.625]$  GeV from the g9a experiment, and the red line is the carbon events from the g9b experiment. The yellow line is the scaled carbon distribution, and the blue dashed line is the free-proton distribution made by the phase space scale factors.

likelihood fits [35] in the remaining fifth variables. In this analysis, we have performed fits on the missing pion mass in Topology 1 or 2. To locate the nearest neighbor events, the following equation describing the distance between event  $a$  and  $b$ ,  $D_{a,b}$  has been used :

$$D_{a,b}^2 = \sum_{i=1}^4 \left( \frac{\Gamma_i^a - \Gamma_i^b}{\Delta_i} \right)^2, \quad (4.20)$$

where  $\Gamma$  is a kinematic variable and  $\Delta_i$  is the maximum range of the kinematic variable  $\Gamma$ . Table 4.16 shows the specific kinematic variables and their maximum ranges used in the Q-factor method.

Table 4.16: The kinematic variables  $\Gamma_i$  and their ranges  $\Delta_i$  used in the Q-factor method.

$\Gamma_i$	Kinematic variable	Their maximum ranges, $\Delta_i$
$\Gamma_0$	center-of-mass energy, $W$	50 [MeV]
$\Gamma_1$	$\cos \Theta_{c.m.}^{proton}$	2
$\Gamma_2$	$\phi_{\pi^+}^*$	$2\pi$ [radian]
$\Gamma_3$	$\cos \theta_{\pi^+}^*$	2

The distances of all other events from a seed event are computed using Equation 4.20, and then the 300 nearest neighbors are selected to form a missing-mass distribution for fitting. The missing-mass distribution made from the carbon data is used as the background distribution in the fitting function of the Q-factor method. The total fit function utilizes a signal function for the missing-pion peak and the carbon distribution from the g9b experiment for the description of the background. For the latter, a seed event in the carbon sample is chosen which is kinematically closest to the butanol seed event and the 300 nearest neighbors for the carbon seed events are selected. Figure 4.28 (a) shows an example of the missing mass distributions for a particular pair of a butanol and carbon seed event. These distributions will be used as the input for the Q-factor method.

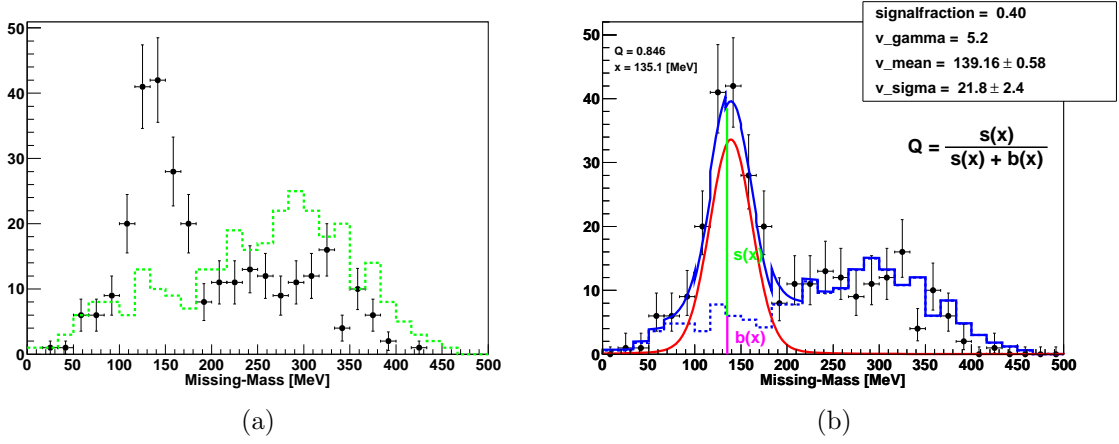


Figure 4.28: (a) The missing mass distributions made from the 300 nearest events selected from butanol (black dots) and carbon (green line) data in Topology  $\gamma p \rightarrow p\pi^+(\pi^-)$ ,  $W \in [1.575, 1.625]$  GeV, and Period 7. (b) Fitting the butanol's missing mass distribution (black dots) using a combination of the signal (red line) and carbon background (blue dashed line) function.

In the missing  $\pi^-$  mass distribution from the butanol target for Topology  $\gamma p \rightarrow p\pi^+(\pi^-)$ , a clear peak near 139.5 MeV for the  $\pi^-$  can be seen. Since the peak is much broader than the natural width of the  $\pi^-$ , a Gaussian resolution function should be used to describe the shape of the peak. Unfortunately, a Gaussian could not describe very well the high-mass tail of the signal; for this reason, a Voigt function with a very small Breit-Wigner component is used for the signal. The true carbon distribution of the g9b experiment is used for the background shape which describes a smooth non-peaking distribution underneath the peak. For this analysis, the total function is defined as :

$$f(x) = N \cdot [f_s \cdot S(x) - (1 - f_s) \cdot B(x)]. \quad (4.21)$$

$S(x)$  denotes the signal and  $B(x)$  the background function.  $N$  is a normalization constant and  $f_s$  is the signal fraction with a value between 0 and 1. The RooFit package of the CERN ROOT software package [35] is used for the fit procedure. The Q-factor itself is then given by :

$$Q = \frac{s(x)}{s(x) + b(x)}, \quad (4.22)$$

where  $x$  is the missing mass of the seed event and  $s(x) = f_s \cdot S(x)$  and  $b(x) = (1 - f_s) \cdot B(s)$ . The total fitting function  $f(x)$  in Equation 4.21 has four parameters:  $\Gamma$ , mean, and  $\sigma$  of the Voigt function and  $f_s$  (the signal fraction). The mean of the Voigt function has been fixed to 139.5 MeV; the sigma of the Voigt function has no limitation. The  $\Gamma$  parameter of the Voigt function has been fixed to a very small value, which was derived from a similar fit to the fully integrated distribution (summed over all events, as shown in Figure 4.29).

The signal fraction  $f_s$  is the most important parameter and is related to the event based scale factor.

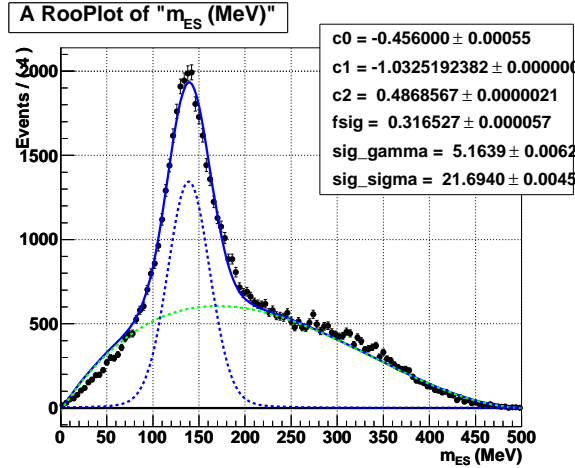


Figure 4.29: Fitting the missing-mass distribution from the butanol data in Topology  $\gamma p \rightarrow p\pi^+(\pi^-)$ ,  $W \in [1.575, 1.625]$  GeV, and Period 7 using a Voigt function. The  $\Gamma$  parameter taken in this fitting is used as a fixed value in the Q-factor method.

The event-based scale factor,  $\mathbf{s}$ , is given by (similar to Equation 4.21) :

$$\mathbf{s} = \frac{(1 - f_s) \cdot (\# \text{ of nearest butanol events})}{(\# \text{ of nearest carbon events})} = 1 - f_s, \quad (4.23)$$

where the number of nearest butanol events is equal to the number of nearest carbon events. The event-based scale factors are assumed to be the same for all butanol seed events. Similar phase space scale factor, as discussed in Section 4.9.1, can be derived from the Q-factor method. The peak of the  $\chi^2$  distribution derived from the all Q-factor fits should have a value near one, as shown in Figure 4.30 (a), to guarantee good quality fitting. Figure 4.30 (b) shows the ratio of the phase space scale factors derived from kinematics (Section 4.9.1) to the phase space scale factors derived from the Q-factor method. Figure 4.30 (b) shows a fairly flat distribution, close to one. Figure 4.31 shows the free-proton distribution and scaled carbon distribution calculated by the Q-factor method. The results of the Q-factor method applied in the whole energy range  $W \in [1.375, 2.125]$  are shown in Figure 4.32-4.35.

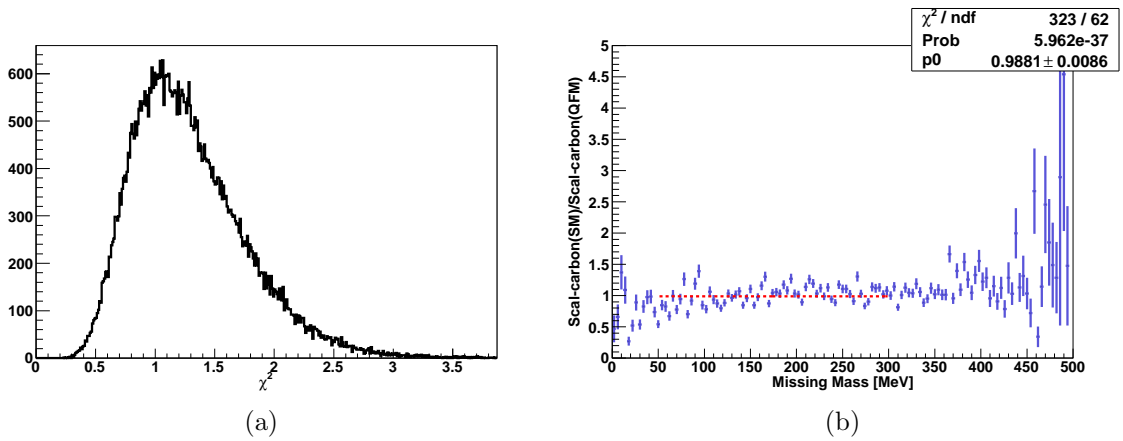


Figure 4.30: (a) The normalized  $\chi^2$  distribution from the Q-factor method (b) The comparison of scaled carbon distribution between the phase space scale factor and Q-factor method.

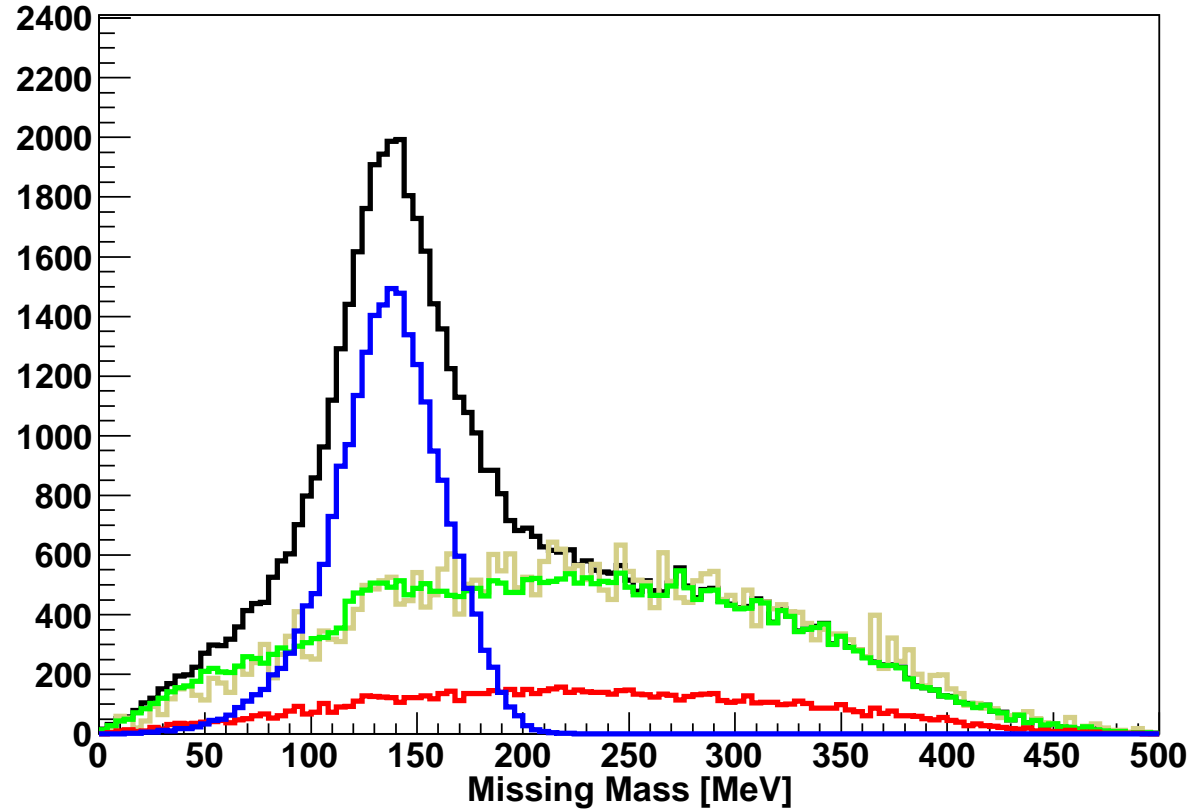
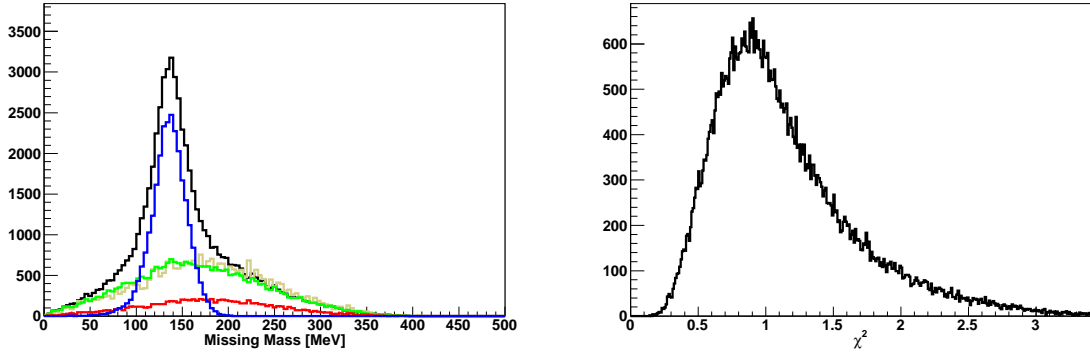
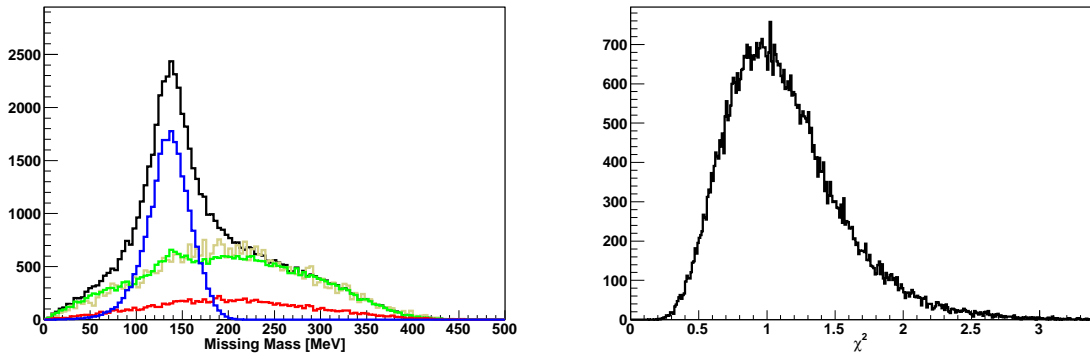


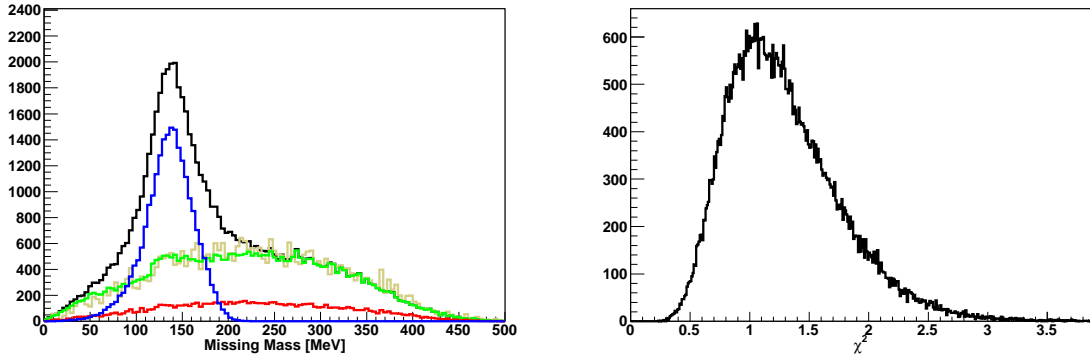
Figure 4.31: The missing-mass distribution with the free-proton and bound-nucleon distribution calculated by the Q-factor method. The black and red line denote the butanol (the g9a experiment) and carbon (the g9b experiment) data for Topology  $\gamma p \rightarrow p\pi^+(\pi^-)$  and  $W \in [1.575, 1.625]$  GeV used in Figure 4.27, respectively. The yellow line and the green line denote the scaled carbon distribution and the free-proton distribution by the method described in Section 4.9.1, respectively.



(a)  $W \in 1.50$  GeV

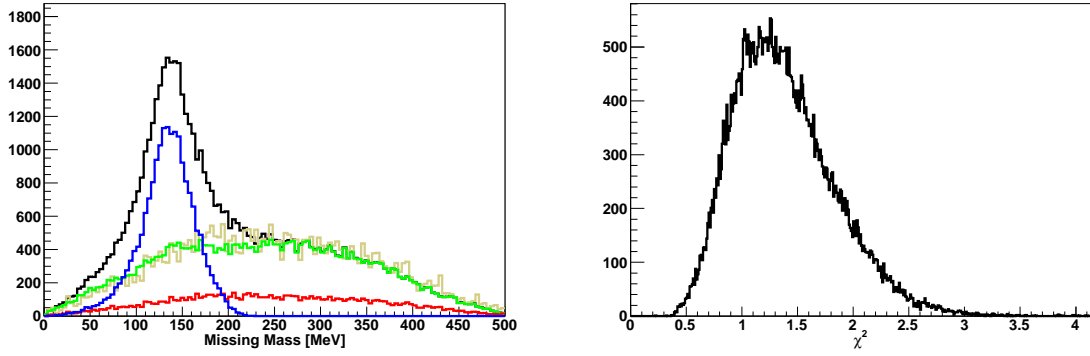


(b)  $W \in 1.55$  GeV

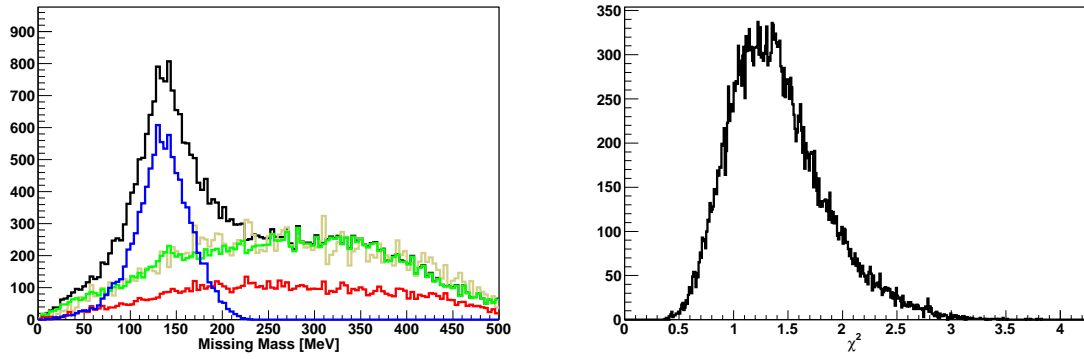


(c)  $W \in 1.60$  GeV

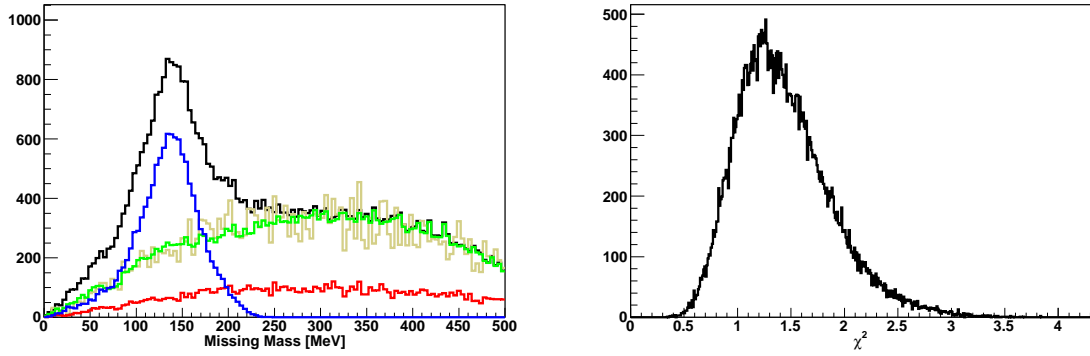
Figure 4.32: The missing-mass distribution with the free-proton and bound-nucleon distribution calculated in Q-factor method in Topology  $\gamma p \rightarrow p\pi^+(\pi^-)$ , the center-of-mass energy range  $W \in [1.475, 1.625]$  GeV, and Period 7, and their  $\chi^2$  distribution.



(a)  $W \in 1.65$  GeV

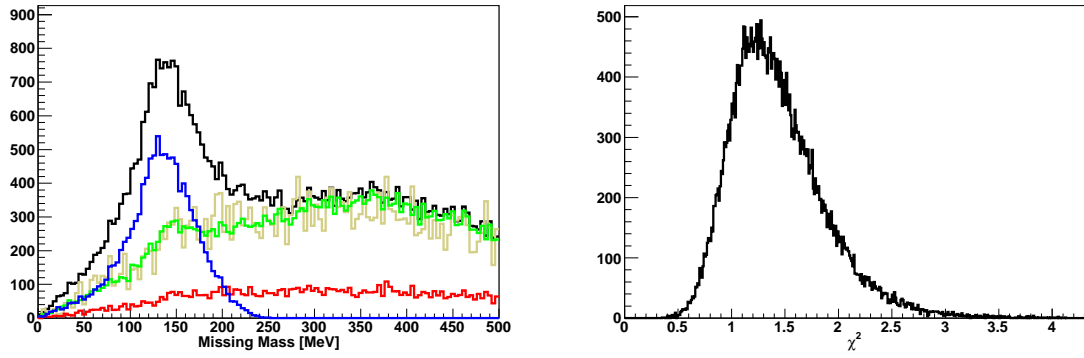


(b)  $W \in 1.70$  GeV

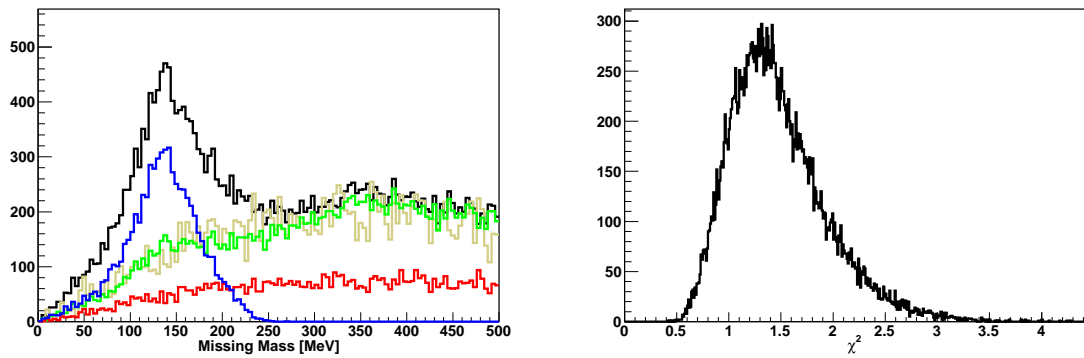


(c)  $W \in 1.75$  GeV

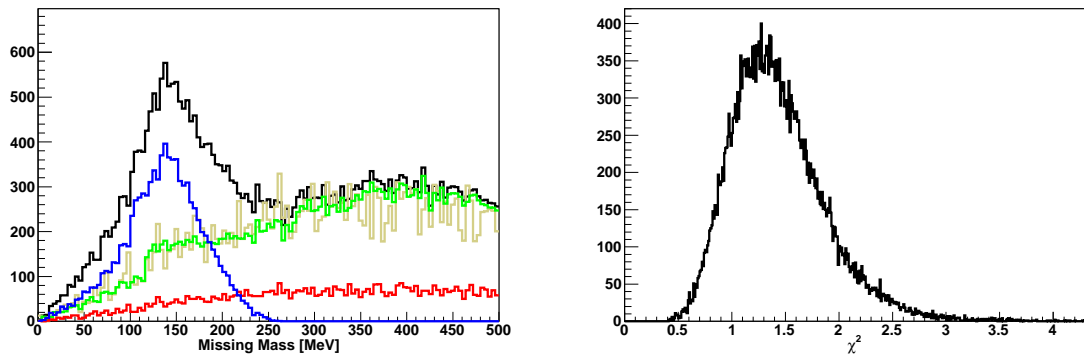
Figure 4.33: The missing-mass distribution with the free-proton and bound-nucleon distribution calculated in Q-factor method in Topology  $\gamma p \rightarrow p\pi^+(\pi^-)$ , the center-of-mass energy range  $W \in [1.625, 1.775]$  GeV, and Period 7, and their  $\chi^2$  distribution.



(a)  $W \in 1.80$  GeV

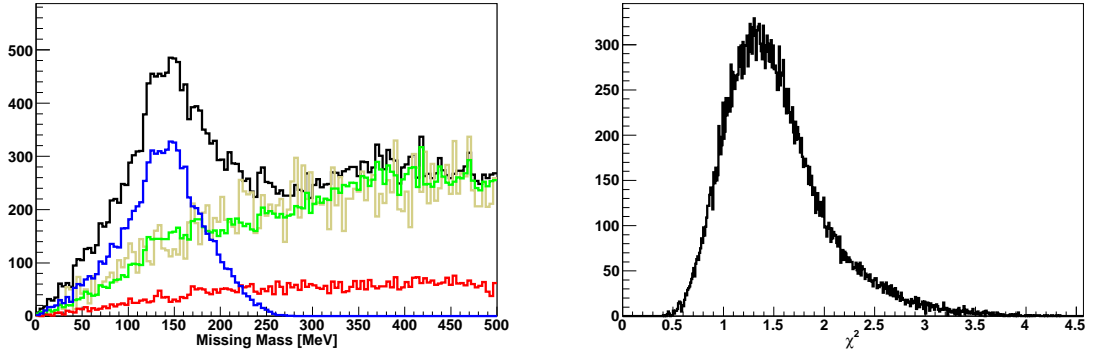


(b)  $W \in 1.85$  GeV

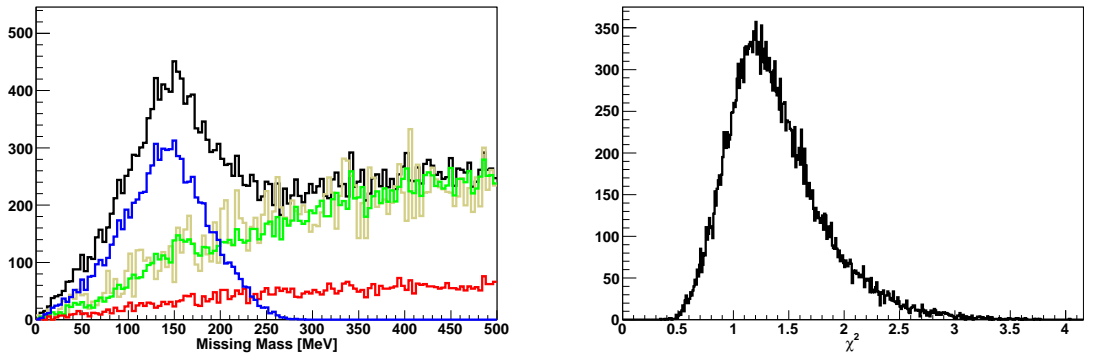


(c)  $W \in 1.90$  GeV

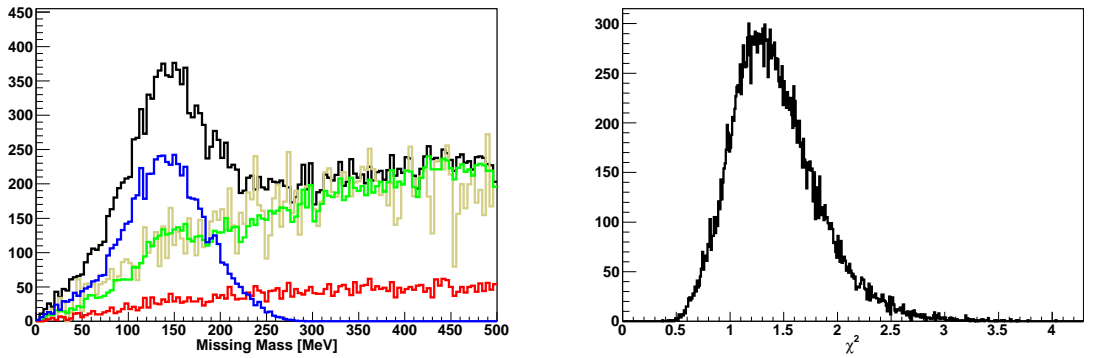
Figure 4.34: The missing-mass distribution with the free-proton and bound-nucleon distribution calculated in Q-factor method in Topology  $\gamma p \rightarrow p\pi^+(\pi^-)$ , the center-of-mass energy range  $W \in [1.775, 1.925]$  GeV, and Period 7, and their  $\chi^2$  distribution.



(a)  $W \in 1.95$  GeV



(b)  $W \in 2.00$  GeV



(c)  $W \in 2.05$  GeV

Figure 4.35: The missing-mass distribution with the free-proton and bound-nucleon distribution calculated in Q-factor method in Topology  $\gamma p \rightarrow p\pi^+(\pi^-)$ , the center-of-mass energy range  $W \in [1.925, 2.075]$  GeV, and Period 7, and their  $\chi^2$  distribution.

# CHAPTER 5

## DATA ANALYSIS

After all corrections, cuts and kinematic fitting were applied, the different possible final-state topologies for the reaction  $\gamma p \rightarrow p\pi^+\pi^-$  have been selected and the extraction of polarization observable commenced. The polarization observables  $\mathbf{I}^\odot$ ,  $\mathbf{P}_z$ , and  $\mathbf{P}_z^\odot$  (Equation 1.4) were extracted from the double-pion photoproduction data utilizing circular beam and longitudinal target polarization. This chapter presents the methodology utilized in the extraction of these polarization observables from the experimental data.

### 5.1 General Data Analysis

#### 5.1.1 Binning and Definition of Angles

In order for an analysis to be conducted, the kinematics of the reaction must be understood. First, the kinematics of  $\gamma p \rightarrow p\pi^+\pi^-$  require a selection of five independent kinematic variables, as referenced in Section 1.3.3. The kinematic variables chosen for this analysis are  $\cos\Theta_{c.m.}$  of the proton, a mass ( $m_{p\pi^+}$ ,  $m_{p\pi^-}$ , or  $m_{\pi^+\pi^-}$ ), the center-of-mass energy  $W$ ,  $\theta_{\pi^+}^*$ , and  $\phi_{\pi^+}^*$ , where the latter two angles denote the polar and azimuthal angles of the  $\pi^+$  in the rest frame of the  $\pi^+\pi^-$  system. A diagram showing the kinematics of the reaction  $\gamma p \rightarrow p\pi^+\pi^-$  can be seen in Figure 5.1, while the blue plane represents the center-of-mass production plane composed of the initial photon and proton, while the red plane represents the decay plane formed by two of the final-state particles.

The angle  $\phi_{\pi^+}^*$  is a kinematic variable unique to a final state containing two pseudoscalar mesons. It describes the orientation of the decay plane containing the two pions (or another pair of the particles) with respect to the production plane, which is defined by the incident photon and recoiling proton. It is also given as the azimuthal angle with respect to the  $\pi^+$  meson. This azimuthal angle,  $\phi_{\pi^+}^*$ , is calculated via two boosts, the first being a boost along the beam line into the overall center-of-mass frame. The second boost occurs along the axis that is antiparallel to the recoiling pro-

ton and results in the rest frame wherein the two final-state pions occur back-to-back. Mathematically, the angle  $\phi_{\pi^+}^*$  is uniquely determined by the following expression:

$$\cos\phi^* = \frac{(\vec{p} \times \vec{a}) \cdot (\vec{b}_2 \times \vec{b}_1)}{|\vec{p} \times \vec{a}| |\vec{b}_2 \times \vec{b}_1|}. \quad (5.1)$$

In this analysis the data are then binned in two of the five independent kinematical variables. These binning variables are the center-of-mass energy,  $W$ , and the azimuthal angle,  $\phi_{\pi^+}^*$ . In order to compare the polarization observable  $\mathbf{I}^\odot$  (Equation 1.4), with the results from the CLAS g1c analysis [11], the center-of-mass energy  $W$  is divided into bins of 50 MeV wide. This results in a total of 20 bins in the center-of-mass energy, covering an energy range from 1.225 GeV to 2.225 GeV. For the angle,  $\phi_{\pi^+}^*$ , 20 bins are used, covering a range from  $0 \leq \phi_{\pi^+}^* \leq 2\pi$ , to describe the structure of the observable more clearly than in the CLAS g1c analysis, which used 11 bins in the same angle range. This choice of binning using two variables results in a total of 400 bin combinations per final-state topology.

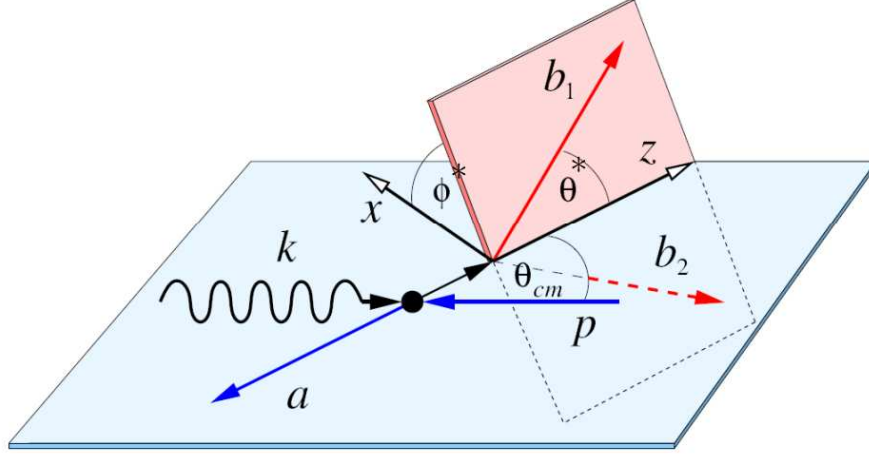


Figure 5.1: A diagram describing the kinematics of the reaction  $\gamma p \rightarrow p\pi^+\pi^-$ . The blue plane represents the center-of-mass production plane composed of the initial photon and proton, while the red plane represents the decay plane formed by two of the final-state particles. In the diagram,  $k$  is the initial photon and the particle  $p$  denotes the polarized target proton.  $a$ ,  $b_1$ , and  $b_2$  are the three particles of the final state. If we assume that particle  $a$  is the recoiling proton,  $b_1$  and  $b_2$  should be the two pions:  $\pi^+$  and  $\pi^-$ .  $\Theta_{c.m.}$  denotes the angle between the initial proton and the particle  $a$  in the center-of-mass system.  $\phi^*$  and  $\theta^*$  indicate the azimuthal and polar angles of the particle  $b_1$  in the rest frame of  $b_1$  and  $b_2$ .

## 5.1.2 Observables with Circular Beam and Longitudinal Target Polarization

The reaction rate for  $\gamma p \rightarrow p \pi \pi$ , in the case of a circularly-polarized beam on a longitudinally-polarized target, is by [10] :

$$\frac{d\sigma}{dx_i} = \sigma_0 \{ (1 + \bar{\Lambda}_z \cdot \mathbf{P}_z) + \bar{\delta}_\odot (\mathbf{I}^\odot + \bar{\Lambda}_z \cdot \mathbf{P}_z^\odot) \}, \quad (5.2)$$

and results in the polarization observable  $\mathbf{I}^\odot$ , the beam-helicity asymmetry, the observable  $\mathbf{P}_z$ , target asymmetry, and the observable  $\mathbf{P}_z^\odot$ , to the helicity difference, which can be determined from this dataset.

## 5.2 Polarization observable $\mathbf{I}^\odot$

### 5.2.1 Beam Helicity Asymmetry

The differential cross section for  $\gamma p \rightarrow p \pi \pi$  (Equation 5.2) is experimentally given by :

$$\frac{d\sigma}{dx_i} = \frac{N_{data}}{A \cdot F \cdot \rho \cdot \Delta x_i}, \quad (5.3)$$

where  $N_{data}$  is the number of data events measured in the g9a experiment,  $A$  is the acceptance,  $F$  is the photon flux,  $\rho$  is the target area density parameter, and  $\Delta x_i$  is the width of the kinematic bin. Therefore, the number of measured data events,  $N_{data}$ , can be also defined as :

$$N_{data} = \sigma_0 \cdot (A \cdot F \cdot \rho \cdot \Delta x_i) \{ (1 + \bar{\Lambda}_z \cdot \mathbf{P}_z) + \bar{\delta}_\odot (\mathbf{I}^\odot + \bar{\Lambda}_z \cdot \mathbf{P}_z^\odot) \}. \quad (5.4)$$

Since the beam and target polarization of each  $N_{data}$  in the g9a dataset have a certain direction, a definition of this direction is required. In the following,  $\rightarrow$  and  $\leftarrow$  indicate the circular beam polarization parallel and antiparallel to the beam axis;  $\Rightarrow$  and  $\Leftarrow$  indicate the longitudinally target polarization parallel and antiparallel to the beam axis. In this analysis, we use four different dataset with the following beam and target polarizations :

$$N(\rightarrow\Rightarrow), N(\leftarrow\Rightarrow), N(\rightarrow\Leftarrow), \text{ and } N(\leftarrow\Leftarrow). \quad (5.5)$$

In the process of calculating the asymmetry, the product  $\sigma_0 \cdot A \cdot \rho \cdot \Delta x_i$  will cancel out. Moreover, each combination (Equation 5.5) has a different photon flux  $F$ , average beam polarization  $\bar{\delta}_\odot$ , and average target polarization  $\bar{\Lambda}_z$  :

$$N_{combination} \sim F \{ (1 + \bar{\Lambda}_z \cdot \mathbf{P}_z) + \bar{\delta}_\odot (\mathbf{I}^\odot + \bar{\Lambda}_z \cdot \mathbf{P}_z^\odot) \}. \quad (5.6)$$

The distributions of events with these four different polarization settings, as a function of  $\phi^*$ , have the form :

$$\begin{aligned}
N(\phi^*, \sigma(\rightarrow\Rightarrow)) &\sim F(\rightarrow\Rightarrow) \left\{ 1 + \bar{\Lambda}_z(\Rightarrow) \mathbf{P}_z + \bar{\delta}_\odot(\rightarrow) \left( \mathbf{I}^\odot + \bar{\Lambda}_z(\Rightarrow) \mathbf{P}_z^\odot \right) \right\} \\
N(\phi^*, \sigma(\leftarrow\Rightarrow)) &\sim F(\leftarrow\Rightarrow) \left\{ 1 + \bar{\Lambda}_z(\Rightarrow) \mathbf{P}_z - \bar{\delta}_\odot(\leftarrow) \left( \mathbf{I}^\odot + \bar{\Lambda}_z(\Rightarrow) \mathbf{P}_z^\odot \right) \right\} \\
N(\phi^*, \sigma(\rightarrow\Leftarrow)) &\sim F(\rightarrow\Leftarrow) \left\{ 1 - \bar{\Lambda}_z(\Leftarrow) \mathbf{P}_z + \bar{\delta}_\odot(\rightarrow) \left( \mathbf{I}^\odot - \bar{\Lambda}_z(\Leftarrow) \mathbf{P}_z^\odot \right) \right\} \\
N(\phi^*, \sigma(\leftarrow\Leftarrow)) &\sim F(\leftarrow\Leftarrow) \left\{ 1 - \bar{\Lambda}_z(\Leftarrow) \mathbf{P}_z - \bar{\delta}_\odot(\leftarrow) \left( \mathbf{I}^\odot - \bar{\Lambda}_z(\Leftarrow) \mathbf{P}_z^\odot \right) \right\}.
\end{aligned} \tag{5.7}$$

In the ideal case, the photon flux will be well known, and flux parameters from the four different data combinations will have the same value:  $F(\rightarrow\Rightarrow) = F(\leftarrow\Rightarrow) = F(\rightarrow\Leftarrow) = F(\leftarrow\Leftarrow) = F$ . Similarly, the ideal experiment setup makes it possible to use  $\bar{\Lambda}_z(\Rightarrow) = \bar{\Lambda}_z(\Leftarrow) = \bar{\Lambda}_z$  and  $\bar{\delta}_\odot(\rightarrow) = \bar{\delta}_\odot(\leftarrow) = \bar{\delta}_\odot$ , and the datasets can be reliably scaled. Since the polarization observable  $I^\odot$  refers to unpolarized target data, a dataset with the unpolarized target nucleons and a circularly-polarized beam is needed. We can produce unpolarized target data by adding the data with different target polarizations :

$$\begin{aligned}
N(\phi^*, \sigma(\rightarrow)) &\sim N(\phi^*, \sigma(\rightarrow\Rightarrow)) + N(\phi^*, \sigma(\rightarrow\Leftarrow)) \sim F \left( 2 + 2 \cdot \bar{\delta}_\odot \mathbf{I}^\odot \right) \\
N(\phi^*, \sigma(\leftarrow)) &\sim N(\phi^*, \sigma(\leftarrow\Rightarrow)) + N(\phi^*, \sigma(\leftarrow\Leftarrow)) \sim F \left( 2 - 2 \cdot \bar{\delta}_\odot \mathbf{I}^\odot \right),
\end{aligned} \tag{5.8}$$

and the beam asymmetry derived from the unpolarized target data can be expressed as :

$$\frac{N(\phi^*, \sigma(\rightarrow)) - N(\phi^*, \sigma(\leftarrow))}{N(\phi^*, \sigma(\rightarrow)) + N(\phi^*, \sigma(\leftarrow))} = \bar{\delta}_\odot \mathbf{I}^\odot. \tag{5.9}$$

However, in the more general situation [36],  $\bar{\Lambda}_z(\Rightarrow) \neq \bar{\Lambda}_z(\Leftarrow)$ . As the polarization of the JLab electron beam in each period is flipped 30 times per second, we can assume that the flux parameters between the different beam polarizations are the same,  $F(\rightarrow) = F(\leftarrow)$ , and the beam polarization between the different beam directions is also the same,  $\bar{\delta}_\odot(\rightarrow) = \bar{\delta}_\odot(\leftarrow) = \bar{\delta}_\odot$ . In reality, the flux parameters between the different target polarizations are different, and we have  $F(\Rightarrow) \neq F(\Leftarrow)$ . In this analysis, the four different dataset (Equation 5.5) were scaled with the target polarization and photon flux, as shown in Figure 5.2 :

$$\begin{aligned}
\frac{N(\phi^*, \sigma(\rightarrow\Rightarrow))}{\Lambda_z(\Rightarrow)F(\Rightarrow)} &\sim \left\{ \left( \frac{1}{\Lambda_z(\Rightarrow)} + \mathbf{P}_z \right) + \frac{\bar{\delta}_\odot}{\Lambda_z(\Rightarrow)} \mathbf{I}^\odot + \bar{\delta}_\odot \mathbf{P}_z^\odot \right\} \\
\frac{N(\phi^*, \sigma(\leftarrow\Rightarrow))}{\Lambda_z(\Rightarrow)F(\Rightarrow)} &\sim \left\{ \left( \frac{1}{\Lambda_z(\Rightarrow)} + \mathbf{P}_z \right) - \frac{\bar{\delta}_\odot}{\Lambda_z(\Rightarrow)} \mathbf{I}^\odot - \bar{\delta}_\odot \mathbf{P}_z^\odot \right\} \\
\frac{N(\phi^*, \sigma(\rightarrow\Leftarrow))}{\Lambda_z(\Leftarrow)F(\Leftarrow)} &\sim \left\{ \left( \frac{1}{\Lambda_z(\Leftarrow)} - \mathbf{P}_z \right) + \frac{\bar{\delta}_\odot}{\Lambda_z(\Leftarrow)} \mathbf{I}^\odot - \bar{\delta}_\odot \mathbf{P}_z^\odot \right\} \\
\frac{N(\phi^*, \sigma(\leftarrow\Leftarrow))}{\Lambda_z(\Leftarrow)F(\Leftarrow)} &\sim \left\{ \left( \frac{1}{\Lambda_z(\Leftarrow)} - \mathbf{P}_z \right) - \frac{\bar{\delta}_\odot}{\Lambda_z(\Leftarrow)} \mathbf{I}^\odot + \bar{\delta}_\odot \mathbf{P}_z^\odot \right\}.
\end{aligned} \tag{5.10}$$

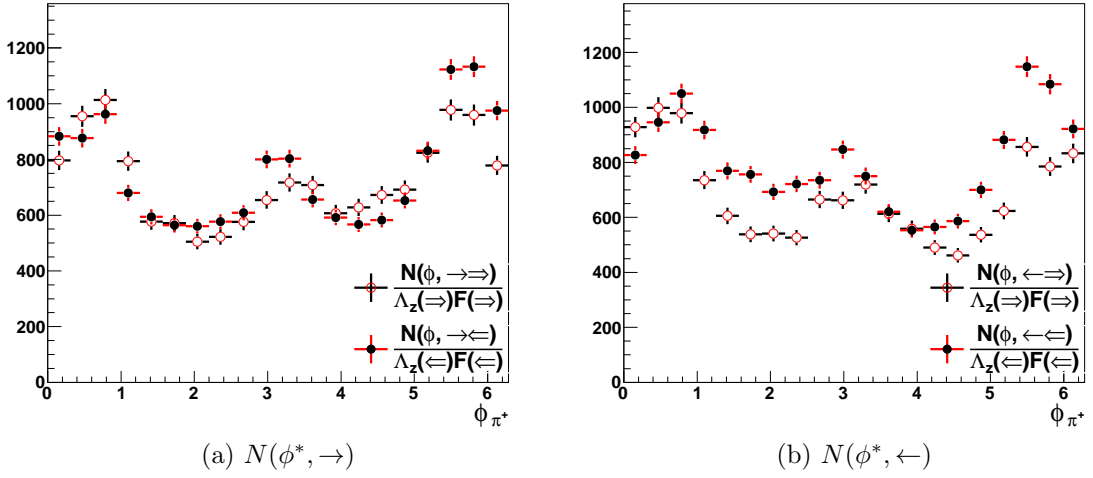


Figure 5.2: Examples of  $\phi^*$  angular distributions in the helicity frame of the beam polarization parallel (a) and anti-parallel (b) to the beam axis for the center-of-mass energy  $W \in [1.675, 1.725]$  GeV in the topology  $\gamma p \rightarrow p\pi^+(\pi^-)$ . The data with the target polarization parallel (antiparallel) to the beam axis are from Period 6 (Period 7).

Figure 5.2 shows examples of angular distributions in the four different polarization combinations (Equation 5.5). In the next step, distributions in Figure 5.2 (a) and (b) have been added, respectively, to produce an unpolarized target. Figure 5.3 shows examples of these distributions:  $N(\phi^*, \sigma(\rightarrow))$  and  $N(\phi^*, \sigma(\leftarrow))$  :

$$\begin{aligned}
N(\phi^*, \sigma(\rightarrow)) &\sim \frac{N(\phi^*, \sigma(\rightarrow\Rightarrow))}{\Lambda_z(\Rightarrow)F(\Rightarrow)} + \frac{N(\phi^*, \sigma(\rightarrow\Leftarrow))}{\Lambda_z(\Leftarrow)F(\Leftarrow)} \sim \left( \frac{1}{\Lambda_z(\Rightarrow)} + \frac{1}{\Lambda_z(\Leftarrow)} \right) \left( 1 + \bar{\delta}_\odot \mathbf{I}^\odot \right) \\
N(\phi^*, \sigma(\leftarrow)) &\sim \frac{N(\phi^*, \sigma(\leftarrow\Rightarrow))}{\Lambda_z(\Rightarrow)F(\Rightarrow)} + \frac{N(\phi^*, \sigma(\leftarrow\Leftarrow))}{\Lambda_z(\Leftarrow)F(\Leftarrow)} \sim \left( \frac{1}{\Lambda_z(\Rightarrow)} + \frac{1}{\Lambda_z(\Leftarrow)} \right) \left( 1 - \bar{\delta}_\odot \mathbf{I}^\odot \right).
\end{aligned} \tag{5.11}$$

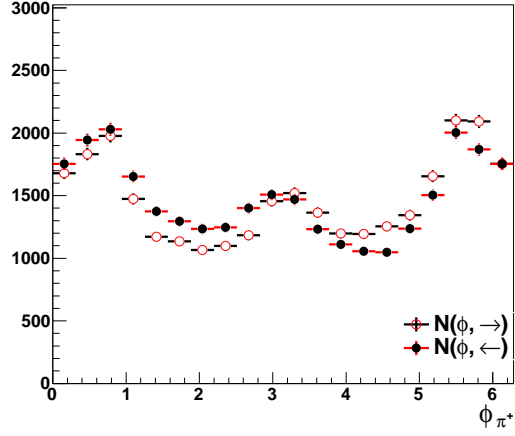


Figure 5.3: CLAS-integrated azimuthal angular distributions in the helicity frame of helicity-plus events  $N(\phi^*, \rightarrow)$  and helicity-minus events  $N(\phi^*, \leftarrow)$  for the center-of-mass energy  $W \in [1.675, 1.725]$  GeV in the topology  $\gamma p \rightarrow p\pi^+(\pi^-)$ .

The beam asymmetry can be calculated using the number of events for the helicity plus and minus from Equation 5.11. Since the effect for the electron beam charge asymmetry in the g9a dataset is negligible, it is not applied to the beam asymmetry (see Appendix B). The polarization observable  $\mathbf{I}^\odot$ , as shown in Figure 5.4, with the normalization factor  $F(\Rightarrow)/F(\Leftarrow)$ , introduced in Table 4.15 is given by :

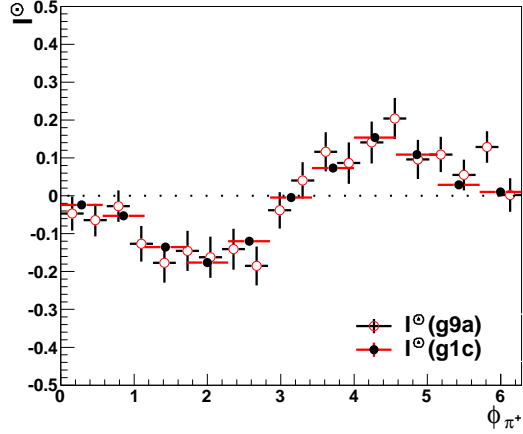


Figure 5.4: The polarization observable  $\mathbf{I}^\odot$  calculated from Equation 5.12 is compared with the same observable published in the g1c experiment. The dataset is the same as in Figure 5.2.

$$\mathbf{I}^\odot = \frac{1}{\bar{\delta}_\odot} \frac{\left( \frac{N(\phi^*, \sigma(\rightarrow\Rightarrow))}{\Lambda_z(\Rightarrow) \cdot F(\Rightarrow)/F(\Leftarrow)} + \frac{N(\phi^*, \sigma(\rightarrow\Leftarrow))}{\Lambda_z(\Leftarrow)} \right) - \left( \frac{N(\phi^*, \sigma(\Leftarrow\Rightarrow))}{\Lambda_z(\Rightarrow) \cdot F(\Rightarrow)/F(\Leftarrow)} + \frac{N(\phi^*, \sigma(\Leftarrow\Leftarrow))}{\Lambda_z(\Leftarrow)} \right)}{\left( \frac{N(\phi^*, \sigma(\rightarrow\Rightarrow))}{\Lambda_z(\Rightarrow) \cdot F(\Rightarrow)/F(\Leftarrow)} + \frac{N(\phi^*, \sigma(\rightarrow\Leftarrow))}{\Lambda_z(\Leftarrow)} \right) + \left( \frac{N(\phi^*, \sigma(\Leftarrow\Rightarrow))}{\Lambda_z(\Rightarrow) \cdot F(\Rightarrow)/F(\Leftarrow)} + \frac{N(\phi^*, \sigma(\Leftarrow\Leftarrow))}{\Lambda_z(\Leftarrow)} \right)}. \quad (5.12)$$

## 5.2.2 Average Beam Asymmetry

Since the g9a dataset is broken up the different periods (Table 4.14), we can use three kinds of period-combinations to calculate the beam asymmetry: Period 3 and 2 (called combination-32), Period 4 and 5 (called combination-45), and Period 6 and 7 (called combination-67). As reminded, the double-pion photoproduction data have also four kinds of topologies:

- Topology 1:  $\bar{\gamma}\bar{p} \rightarrow p\pi^+(\pi^-)$  ( $\pi^-$  not detected)
- Topology 2:  $\bar{\gamma}\bar{p} \rightarrow p\pi^-(\pi^+)$  ( $\pi^+$  not detected)
- Topology 3:  $\bar{\gamma}\bar{p} \rightarrow \pi^+\pi^-(p)$  (proton not detected)
- Topology 4:  $\bar{\gamma}\bar{p} \rightarrow p\pi^+\pi^-$  (all particles detected)

Since the CLAS spectrometer is designed to detect charged particles, we cannot distinguish between the reaction  $\gamma p$  and  $\gamma n$  using the butanol target. The missing-mass distribution for the topology  $\gamma p \rightarrow \pi^+\pi^-(p)$ , as shown in Figure 4.15, includes the data from the reaction  $\gamma p \rightarrow \pi^+\pi^-(p)$  and from the reaction  $\gamma n \rightarrow \pi^+\pi^-(n)$  together, and this analysis cannot separate dataset between the reaction  $\gamma p$  and  $\gamma n$ . For this reason, the topology  $\gamma p \rightarrow \pi^+\pi^-(p)$  has been excluded in this analysis. The beam asymmetries from three kinds of period-combinations and three kinds of topologies, as referenced in Table 5.1, are calculated.

Figure 5.4 shows the comparison of the observable  $\mathbf{I}^\odot$  from the g9a and g1c experiments. In the figure, the polarization observable  $\mathbf{I}^\odot$  from the g9a dataset is made from combination-67 and Topology  $\gamma p \rightarrow p\pi^+(\pi^-)$ . In the next step, the average of the observables from the three different period-combinations in each topology has been calculated to improve statistics. This is shown in Figure 5.5. These observables of the combination-32, combination-45, and combination-67, as shown in Figure 5.5, have statistical errors of different magnitudes. When the average of these observables is calculated, the errors have been used as weighting parameters :

$$\bar{x} = \frac{\sum_i x_i \cdot \frac{1}{\sigma_i^2}}{\sum_i \frac{1}{\sigma_i^2}}, \quad (5.13)$$

where  $x_i$  is the observable and  $\sigma_i$  is its error.

Table 5.1: The dataset used to calculate the average observable  $\mathbf{I}^\odot$ .

Topology 1: $\gamma p \rightarrow p\pi^+(\pi^-)$	combination-32
	combination-45
	combination-67
Topology 2: $\gamma p \rightarrow p\pi^-(\pi^+)$	combination-32
	combination-45
	combination-67
Topology 4: $\gamma p \rightarrow p\pi^+\pi^-$	combination-32
	combination-45
	combination-67

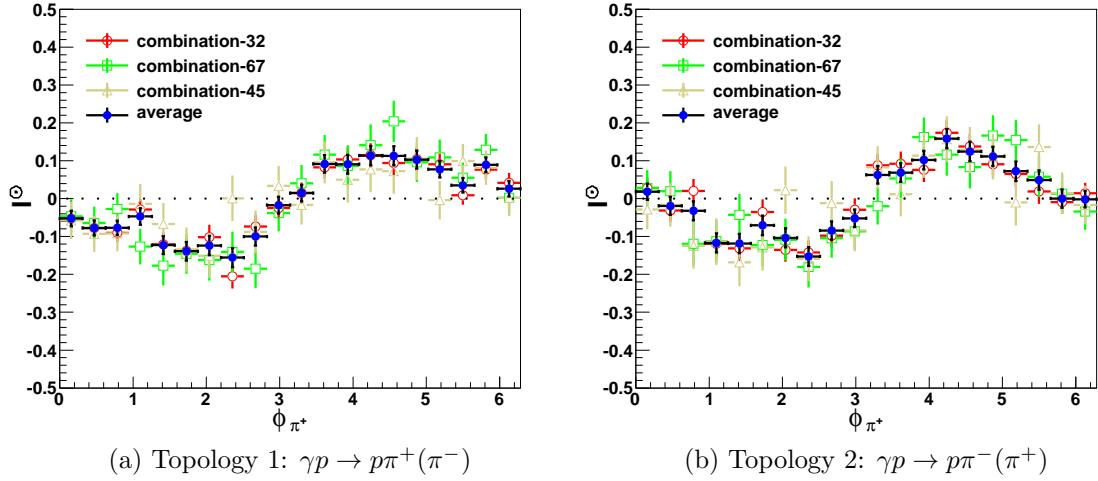


Figure 5.5: Polarization observables  $\mathbf{I}^\odot$  from the three kinds of period-combinations in the topology  $\gamma p \rightarrow p\pi^+(\pi^-)$  (a) and the topology  $\gamma p \rightarrow p\pi^-(\pi^+)$  (b) for the center-of-mass energy  $W \in [1.675, 1.725]$  GeV and their average in each topology. The polarization observable  $\mathbf{I}^\odot$  in each period-combination and each topology is derived from Equation 5.12.

To improve further the statistics and obtain better kinematic coverage, the results from the topology 1, 2, and 4 have been averaged using Equation 5.13. This final observable from the butanol data is shown in Figure 5.6, together with the data published from the g1c experiment. Results of this analysis are in general agreement with the data published in [11] (See Appendix C).

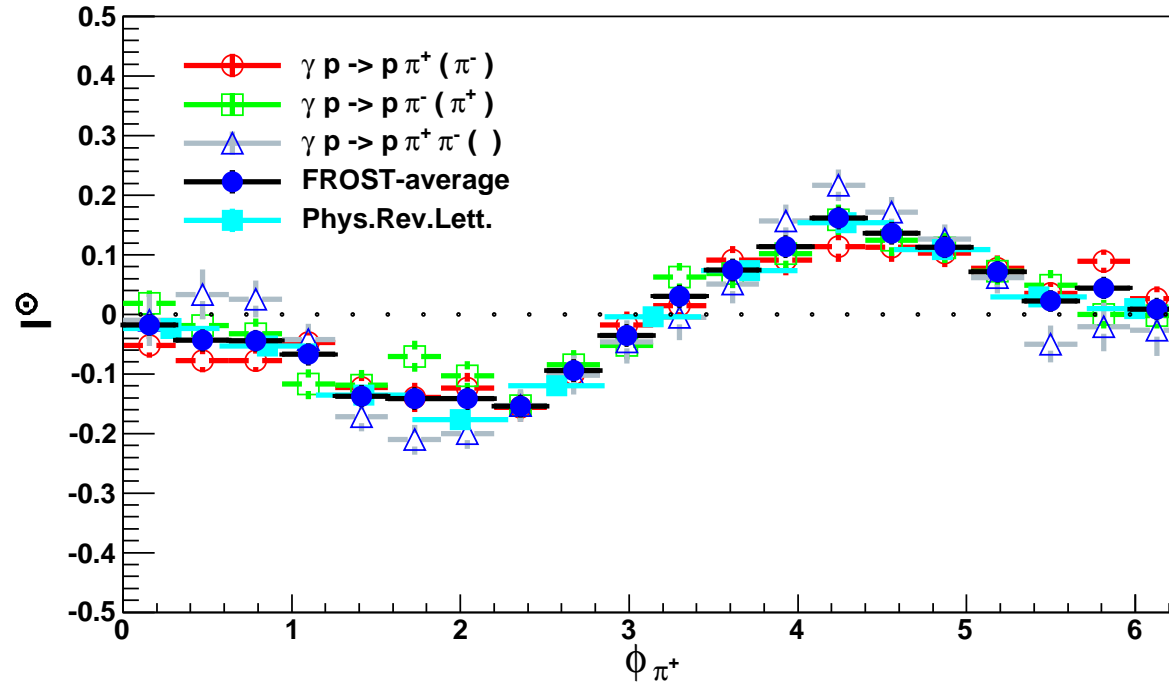


Figure 5.6: The beam asymmetries from the topology 1, 2, and 4 and average, called FROST-average, for the center-of-mass energy  $W \in [1.675, 1.725]$  GeV. The polarization observable  $I^\circ$  analyzed in the g9a experiment is also compared with data published in [11].

### 5.2.3 Comparison

For different period-combinations and topologies, we have compared the results to check consistency. Figure 5.7 (a)-(c) shows the differences ( $I_{\text{combination X}}^{\odot} - I_{\text{combination Y}}^{\odot}$ ) for three kinds of period-combinations; Figure 5.8 (a)-(c) shows the differences ( $I_{\text{Topology X}}^{\odot} - I_{\text{Topology Y}}^{\odot}$ ) between different topologies integrated over all kinematic bins. Figure 5.8 (d) shows the differences ( $I_{g9a}^{\odot} - I_{g1c}^{\odot}$ ) of the polarization observable  $\mathbf{I}^{\odot}$  from this analysis and previous published CLAS data. The distributions are all centered at zero and show generally good agreement.

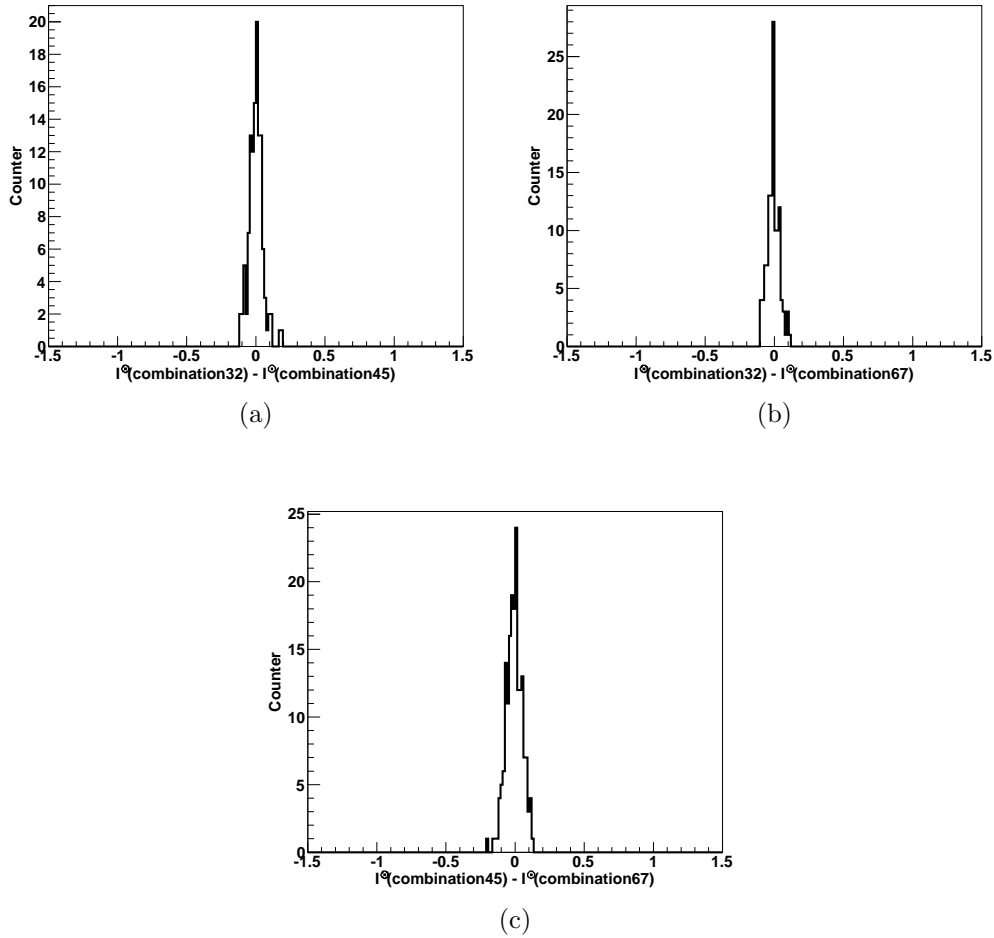


Figure 5.7: (a)-(c) Comparisons (differences) between results for the polarization observables  $\mathbf{I}^{\odot}$  from different period-combinations integrated over all energies in Topology  $\gamma p \rightarrow p\pi^+(\pi^-)$ . The distributions are centered at zero, suggesting consistency among the results from different period-combinations.

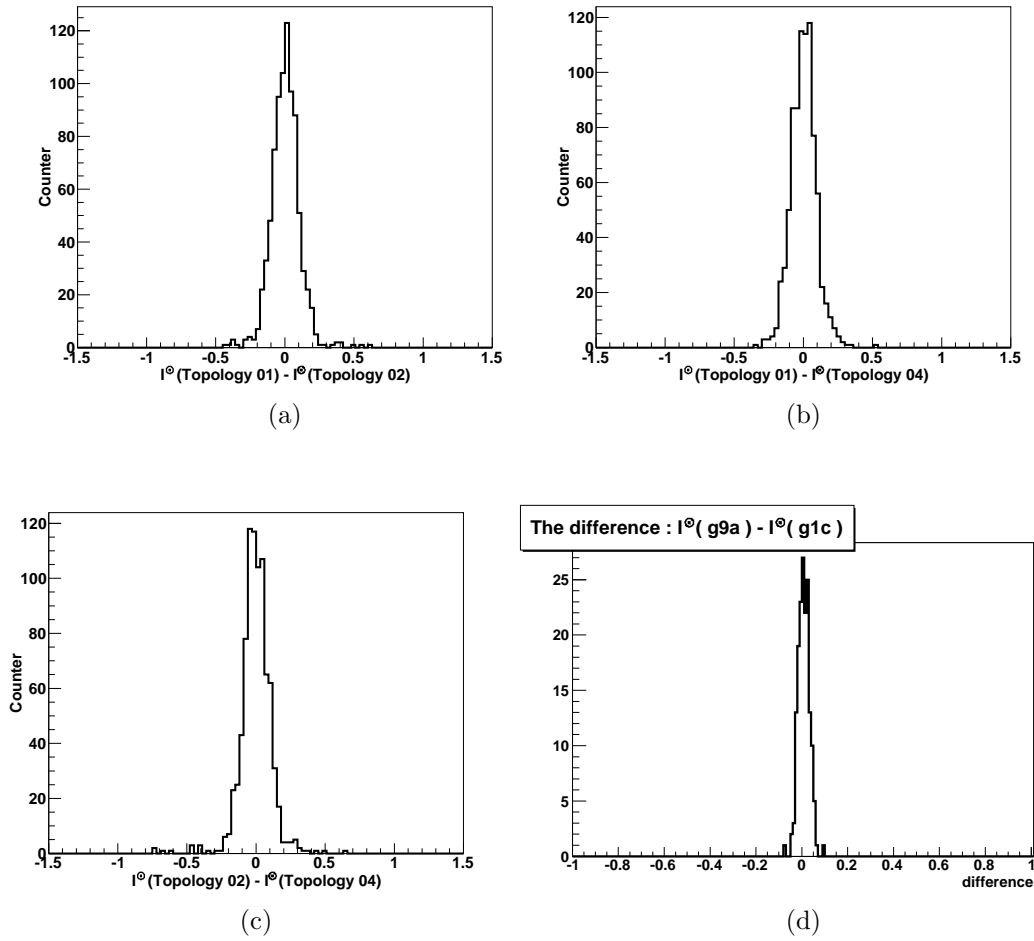


Figure 5.8: (a)-(c) Comparisons (differences) between results for the polarization observables  $I^\ominus$  from different topologies integrated over all energies. The distributions are centered at zero, suggesting consistency among the results from different topologies. (d) Comparisons (differences) between results for the polarization observables  $I^\ominus$  from the g9a experiment and the g1c experiment, integrated over all energies.

## 5.3 Polarization Observable $\mathbf{P}_z$

### 5.3.1 Target Asymmetry

The target asymmetry derived from the different target polarization data, as a function of  $\phi^*$ , is given by :

$$\mathbf{T.Asy.} = \frac{N(\phi^*, \sigma(\Rightarrow)) - N(\phi^*, \sigma(\Leftarrow))}{N(\phi^*, \sigma(\Rightarrow)) + N(\phi^*, \sigma(\Leftarrow))}. \quad (5.14)$$

In order to calculate the target asymmetry, the polarized free-proton data of the full butanol data must be extracted. In the numerator of Equation 5.14, unpolarized data effect of the butanol events will cancel out. However, there are still unpolarized events in the denominator of Equation 5.14 (normalization). Since the Q-factor is defined as an event-based dilution factor, the Q-factor weighted event  $N(\phi^*, \sigma(\rightarrow\Rightarrow))$ <sup>Q</sup> denotes the number of the free-proton events. The event distributions of the four different data combinations, as shown in Figure 5.9, are given by (similar to the beam asymmetry in Equation 5.2) :

$$\begin{aligned} \frac{N(\phi^*, \sigma(\rightarrow\Rightarrow))}{F(\Rightarrow)} &\sim \left(1 + \Lambda_z(\Rightarrow) \cdot \mathbf{P}_z\right) + \delta_{\odot} \cdot \mathbf{I}^{\odot} + \delta_{\odot} \cdot \Lambda_z(\Rightarrow) \cdot \mathbf{P}_z^{\odot} \\ \frac{N(\phi^*, \sigma(\leftarrow\Rightarrow))}{F(\Rightarrow)} &\sim \left(1 + \Lambda_z(\Rightarrow) \cdot \mathbf{P}_z\right) - \delta_{\odot} \cdot \mathbf{I}^{\odot} - \delta_{\odot} \cdot \Lambda_z(\Rightarrow) \cdot \mathbf{P}_z^{\odot} \\ \frac{N(\phi^*, \sigma(\rightarrow\Leftarrow))}{F(\Leftarrow)} &\sim \left(1 - \Lambda_z(\Leftarrow) \cdot \mathbf{P}_z\right) + \delta_{\odot} \cdot \mathbf{I}^{\odot} - \delta_{\odot} \cdot \Lambda_z(\Leftarrow) \cdot \mathbf{P}_z^{\odot} \\ \frac{N(\phi^*, \sigma(\leftarrow\Leftarrow))}{F(\Leftarrow)} &\sim \left(1 - \Lambda_z(\Leftarrow) \cdot \mathbf{P}_z\right) - \delta_{\odot} \cdot \mathbf{I}^{\odot} + \delta_{\odot} \cdot \Lambda_z(\Leftarrow) \cdot \mathbf{P}_z^{\odot}. \end{aligned} \quad (5.15)$$

Since the polarization observable  $\mathbf{P}_z$  refers to unpolarized beam data, a dataset with a longitudinally-polarized target and an unpolarized beam is required. We can produce an unpolarized beam data by adding the data with different beam polarizations from Equation 5.15. Figure 5.10 shows examples of these distributions,  $N(\phi^*, \sigma(\Rightarrow))$ <sup>Q</sup> and  $N(\phi^*, \sigma(\Leftarrow))$ <sup>Q</sup> :

$$\begin{aligned} N(\phi^*, \sigma(\Rightarrow)) &\sim \frac{N(\phi^*, \sigma(\rightarrow\Rightarrow))}{F(\Rightarrow)} + \frac{N(\phi^*, \sigma(\leftarrow\Rightarrow))}{F(\Rightarrow)} \sim 2 + 2 \cdot \Lambda_z(\Rightarrow) \cdot \mathbf{P}_z \\ N(\phi^*, \sigma(\Leftarrow)) &\sim \frac{N(\phi^*, \sigma(\rightarrow\Leftarrow))}{F(\Leftarrow)} + \frac{N(\phi^*, \sigma(\leftarrow\Leftarrow))}{F(\Leftarrow)} \sim 2 - 2 \cdot \Lambda_z(\Leftarrow) \cdot \mathbf{P}_z. \end{aligned} \quad (5.16)$$

The target asymmetry derived from the unpolarized beam data is given by:

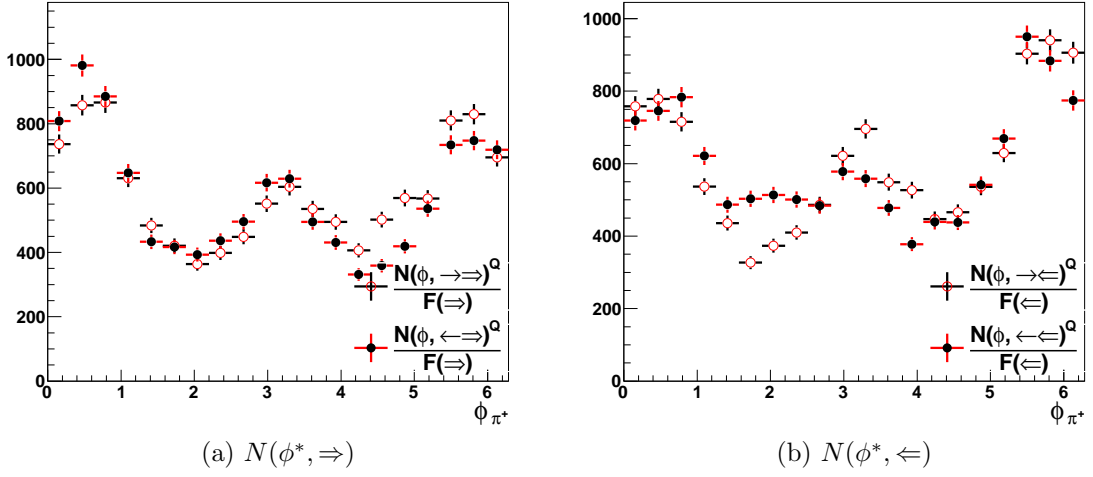


Figure 5.9: Example of the  $\phi^*$  angular distributions in the helicity frame of the target polarization parallel (a) and antiparallel (b) to the beam axis. The data are selected for  $W \in [1.725, 1.775]$  GeV, combination-67, and Topology  $\gamma p \rightarrow p\pi^+(\pi^-)$ .

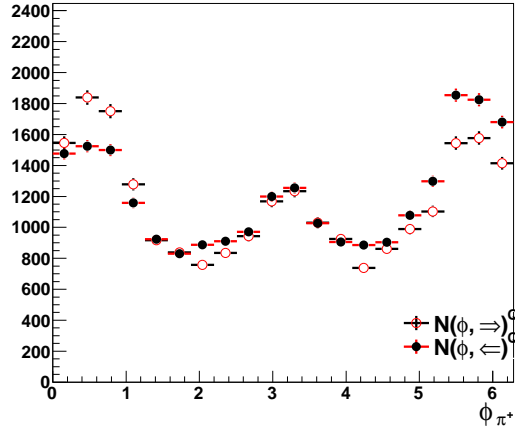


Figure 5.10: CLAS-integrated azimuthal angular distribution in  $N(\phi^*, \Rightarrow)^Q$  and  $N(\phi^*, \Leftarrow)^Q$  for the center-of-mass energy  $W \in [1.725, 1.775]$  GeV and the topology  $\gamma p \rightarrow p\pi^+(\pi^-)$ .

$$\begin{aligned}
 \mathbf{T.Asy.} &= \frac{\left( \frac{N(\phi^*, \sigma(\rightarrow\Rightarrow))}{F(\Rightarrow)/F(\Leftarrow)} + \frac{N(\phi^*, \sigma(\leftarrow\Rightarrow))}{F(\Rightarrow)/F(\Leftarrow)} \right) - \left( \frac{N(\phi^*, \sigma(\rightarrow\Leftarrow))}{1} + \frac{N(\phi^*, \sigma(\leftarrow\Leftarrow))}{1} \right)}{\left( \frac{N(\phi^*, \sigma(\rightarrow\Rightarrow))^Q}{F(\Rightarrow)/F(\Leftarrow)} + \frac{N(\phi^*, \sigma(\leftarrow\Rightarrow))^Q}{F(\Rightarrow)/F(\Leftarrow)} \right) + \left( \frac{N(\phi^*, \sigma(\rightarrow\Leftarrow))^Q}{1} + \frac{N(\phi^*, \sigma(\leftarrow\Leftarrow))^Q}{1} \right)} \\
 &= \frac{\Lambda_z(\Rightarrow) + \Lambda_z(\Leftarrow)}{2} \cdot \mathbf{P}_z
 \end{aligned} \tag{5.17}$$

and the polarization observable  $\mathbf{P}_z$ , as shown in Figure 5.11, is given by:

$$\mathbf{P}_z = \frac{1}{\bar{\Lambda}_z} \frac{\left( \frac{N(\phi^*, \sigma(\rightarrow\Rightarrow))}{F(\Rightarrow)/F(\Leftarrow)} + \frac{N(\phi^*, \sigma(\Leftarrow\Rightarrow))}{F(\Rightarrow)/F(\Leftarrow)} \right) - \left( \frac{N(\phi^*, \sigma(\rightarrow\Leftarrow))}{1} + \frac{N(\phi^*, \sigma(\Leftarrow\Leftarrow))}{1} \right)}{\left( \frac{N(\phi^*, \sigma(\rightarrow\Rightarrow))^Q}{F(\Rightarrow)/F(\Leftarrow)} + \frac{N(\phi^*, \sigma(\Leftarrow\Rightarrow))^Q}{F(\Rightarrow)/F(\Leftarrow)} \right) + \left( \frac{N(\phi^*, \sigma(\rightarrow\Leftarrow))^Q}{1} + \frac{N(\phi^*, \sigma(\Leftarrow\Leftarrow))^Q}{1} \right)}. \quad (5.18)$$

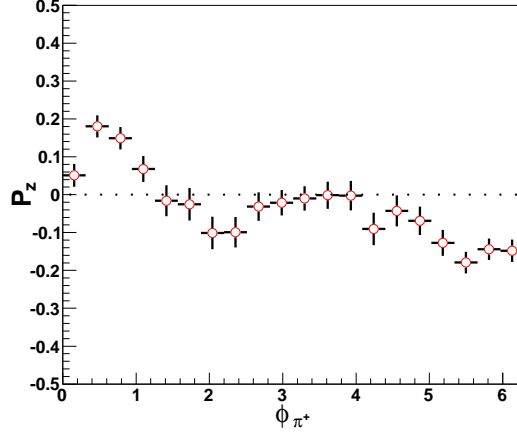


Figure 5.11: The polarization observable  $\mathbf{P}_z$  calculated from Equation 5.18. The dataset is the same as that used in Figure 5.10.

### 5.3.2 Average Target Asymmetry

The target asymmetry can be calculated from three kinds of period-combinations and two kinds of topologies, as referenced in Table 5.2, which is similar to calculating the average of the observable  $\mathbf{I}^\odot$  in Section 5.2.2.

Table 5.2: The dataset used to calculate the average observable  $\mathbf{P}_z$ .

Topology 1: $\gamma p \rightarrow p\pi^+(\pi^-)$	combination-32
	combination-45
	combination-67
Topology 2: $\gamma p \rightarrow p\pi^-(\pi^+)$	combination-32
	combination-45
	combination-67

Figure 5.11 shows the polarization observable  $\mathbf{P}_z$  from combination-67 and Topology  $\gamma p \rightarrow p\pi^+(\pi^-)$  of the g9a dataset. In Figure 5.12, each topology is based on the average of the combination-32, combination-45, and combination-67 using Equation 5.13. Figure 5.13 shows the average value of observables  $\mathbf{P}_z$  calculated in Topology  $\gamma p \rightarrow p\pi^+(\pi^-)$  and Topology  $\gamma p \rightarrow p\pi^-(\pi^+)$ , as shown in Figure 5.12 for the center-of-mass energy  $W \in [1.725, 1.775]$  GeV.

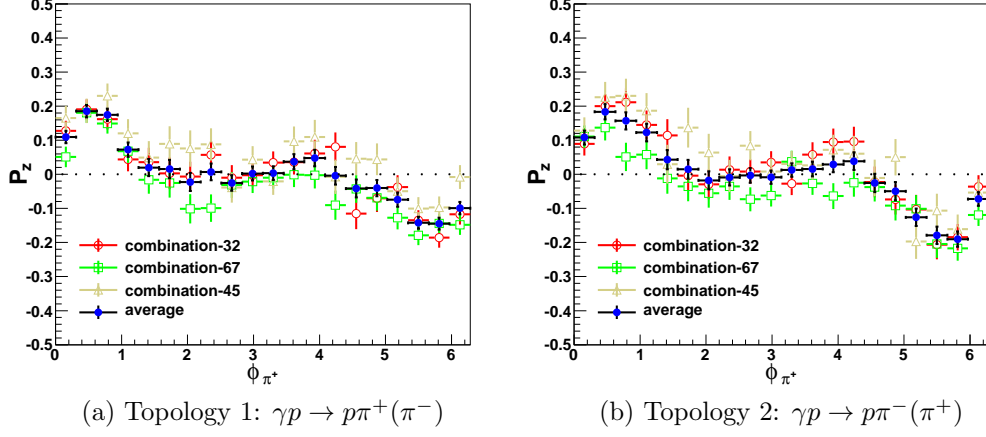


Figure 5.12: Polarization observables  $\mathbf{P}_z$  of three kinds of period-combinations in Topology  $\gamma p \rightarrow p\pi^+(\pi^-)$  (a) and Topology  $\gamma p \rightarrow p\pi^-(\pi^+)$  (b) for the center-of-mass energy  $W \in [1.725, 1.775]$  GeV and their average in each topology.

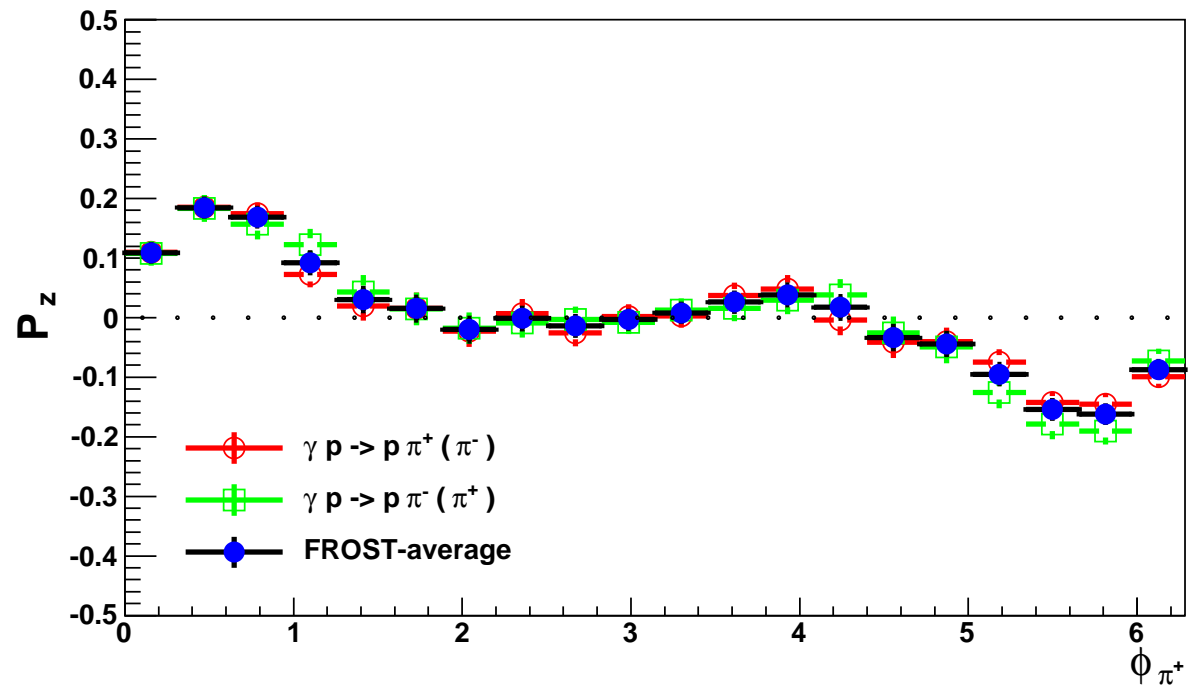


Figure 5.13: The average target asymmetry of the topology 1 and topology 2 and their average, called FROST-average. The data are shown for the center-of-mass energy  $W \in [1.725, 1.775]$  GeV.

### 5.3.3 Comparison

For different period-combinations and topologies, we have compared the results to ensure a consistency. Figure 5.14 shows the differences ( $P_{z\text{combination X}} - P_{z\text{combination Y}}$ ) for three kinds of period-combinations, and Figure 5.15 the differences ( $P_{z\text{Topology X}} - P_{z\text{Topology Y}}$ ) between different topologies integrated across all kinematic bins. The distributions are all centered at zero and show generally good agreement.

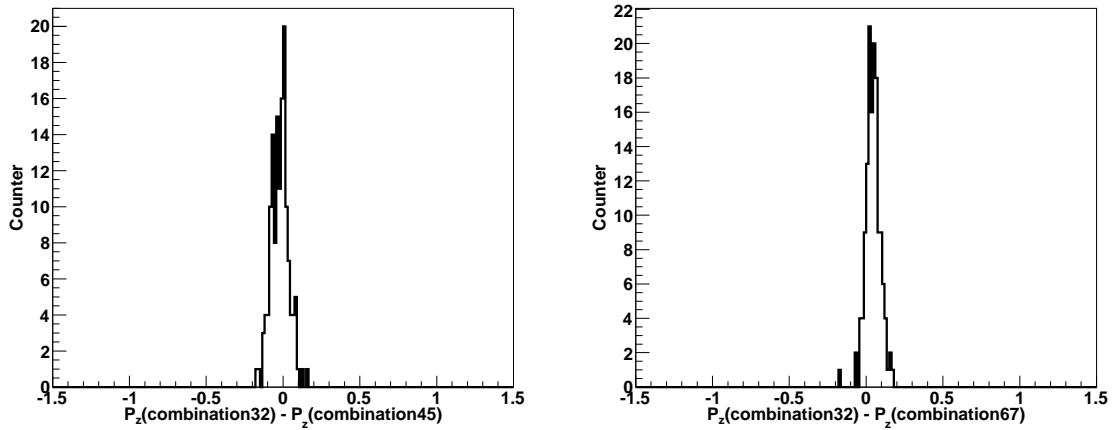


Figure 5.14: Comparisons (differences) between results for the polarization observables  $\mathbf{P}_z$  from different period-combinations integrated across all energies in Topology  $\gamma p \rightarrow p\pi^+(\pi^-)$ .

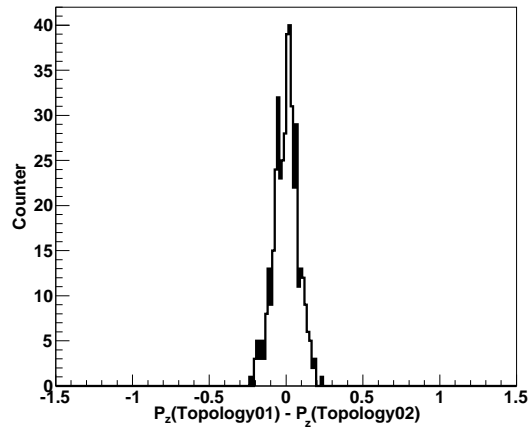


Figure 5.15: Comparisons (differences) between results for the polarization observables  $\mathbf{I}^\odot$  from different topologies integrated across all energies.

## 5.4 Polarization Observable $\mathbf{P}_z^\odot$

### 5.4.1 Helicity Difference

In the calculation of the helicity difference, the average target polarization was used. Table 4.12 shows the average degree of target polarization in all periods. The degree of target polarization of periods 4 and 5 is similar with each other. Periods 6 and 7 are also have similar values. However, polarization between periods 2 and 3 are a slightly different. If the average target polarization between  $\Lambda_z(\Rightarrow)$  and  $\Lambda_z(\Leftarrow)$  is applied to the calculation of the helicity difference, the influence of the observable  $\mathbf{P}_z^\odot$  from combination-32 has only a small influence on the observable  $\mathbf{P}_z^\odot$ . Its effect will be estimated in systematic uncertainties (Section 5.5). The event distributions of four different data combination sets in the general case are given by Equation 5.15.

The double polarization observable  $\mathbf{P}_z^\odot$  refers to the data with the longitudinally-polarized target and the circularly-polarized beam. The events with the spin 3/2  $N(\phi^*, \sigma_{3/2})$  and spin 1/2  $N(\phi^*, \sigma_{1/2})$  are given by :

$$\begin{aligned} N(\phi^*, \sigma_{3/2}) &\sim \frac{N(\phi^*, \rightarrow\Rightarrow)}{F(\Rightarrow)} + \frac{N(\phi^*, \leftarrow\Leftarrow)}{F(\Leftarrow)} \sim 2 + 2 \cdot \bar{\delta}_\odot \cdot \bar{\Lambda}_z \cdot \mathbf{P}_z^\odot \\ N(\phi^*, \sigma_{1/2}) &\sim \frac{N(\phi^*, \leftarrow\Rightarrow)}{F(\Rightarrow)} + \frac{N(\phi^*, \rightarrow\Leftarrow)}{F(\Leftarrow)} \sim 2 - 2 \cdot \bar{\delta}_\odot \cdot \bar{\Lambda}_z \cdot \mathbf{P}_z^\odot. \end{aligned} \quad (5.19)$$

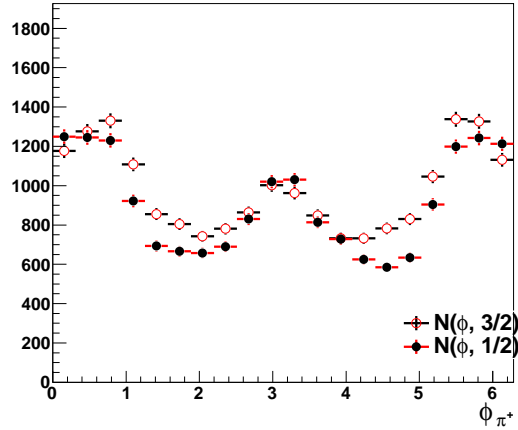


Figure 5.16: CLAS-integrated azimuthal angular distribution in  $N(\phi^*, 3/2)$  and  $N(\phi^*, 1/2)$  for the center-of-mass energy  $W \in [1.675, 1.725]$  GeV and the topology  $\gamma p \rightarrow p\pi^+(\pi^-)$ .

The polarization observable  $\mathbf{P}_z^\odot$ , as shown in Figure 5.17 is given by :

$$\mathbf{P}_{\mathbf{z}}^{\odot} = \frac{1}{\bar{\delta}_{\odot} \cdot \bar{\Lambda}_z} \frac{\left( \frac{N(\phi^*, \rightarrow \Rightarrow)}{F(\Rightarrow)/F(\Leftarrow)} + \frac{N(\phi^*, \Leftarrow \Leftarrow)}{1} \right) - \left( \frac{N(\phi^*, \Leftarrow \Rightarrow)}{F(\Rightarrow)/F(\Leftarrow)} + \frac{N(\phi^*, \rightarrow \Leftarrow)}{1} \right)}{\left( \frac{N(\phi^*, \rightarrow \Rightarrow)^Q}{F(\Rightarrow)/F(\Leftarrow)} + \frac{N(\phi^*, \Leftarrow \Leftarrow)^Q}{1} \right) + \left( \frac{N(\phi^*, \Leftarrow \Rightarrow)^Q}{F(\Rightarrow)/F(\Leftarrow)} + \frac{N(\phi^*, \rightarrow \Leftarrow)^Q}{1} \right)}. \quad (5.20)$$

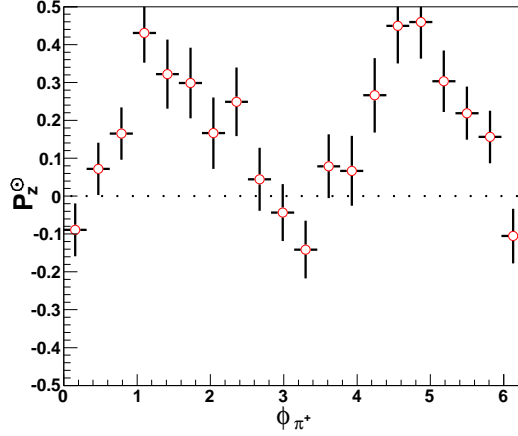


Figure 5.17: The polarization observable  $\mathbf{P}_{\mathbf{z}}^{\odot}$  calculated from Equation 5.20. The dataset is the same as in Figure 5.16.

## 5.4.2 Average Helicity Difference

The helicity difference can also be calculated from three kinds of period-combinations and two kinds of topologies, which is referenced in Table 5.3, similar to calculating the average of observable  $\mathbf{P}_{\mathbf{z}}$  in section 5.3.2.

Table 5.3: The dataset used to calculate the average observable  $\mathbf{P}_{\mathbf{z}}^{\odot}$ .

Topology 1: $\gamma p \rightarrow p\pi^+(\pi^-)$	combination-32
	combination-45
	combination-67
Topology 2: $\gamma p \rightarrow p\pi^-(\pi^+)$	combination-32
	combination-45
	combination-67

Figure 5.17 shows the polarization observable  $\mathbf{P}_{\mathbf{z}}^{\odot}$  from combination-67 and Topology  $\gamma p \rightarrow p\pi^+(\pi^-)$  of the g9a dataset. In Figure 5.18, each topology is based on

the average of the combination-32, combination-45, and combination-67 using Equation 5.13. Figure 5.19 shows the average value of observables  $\mathbf{P}_z^\ominus$  calculated in Topology  $\gamma p \rightarrow p\pi^+(\pi^-)$  and Topology  $\gamma p \rightarrow p\pi^-(\pi^+)$ , as shown in Figure 5.18 for the center-of-mass energy  $W \in [1.675, 1.725]$  GeV. Figure 6.6 shows the average value of the observable  $\mathbf{P}_z^\ominus$  for the whole energy range  $W \in [1.375, 2.125]$  GeV.

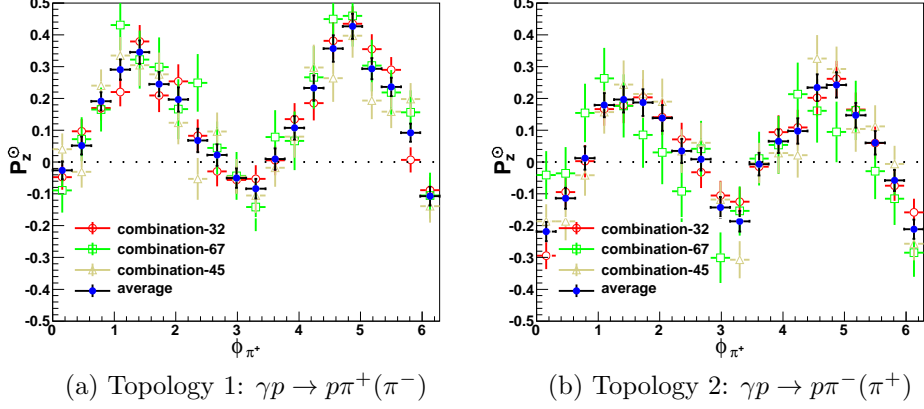


Figure 5.18: Polarization observables  $\mathbf{P}_z^\ominus$  of three kinds of period-combinations in Topology  $\gamma p \rightarrow p\pi^+(\pi^-)$  (a) and Topology  $\gamma p \rightarrow p\pi^-(\pi^+)$  (b) for the center-of-mass energy  $W \in [1.675, 1.725]$  GeV and their average in each topology.

Figure 5.19 shows the average value of observables  $\mathbf{P}_z^\ominus$  calculated in Topology  $\gamma p \rightarrow p\pi^+(\pi^-)$  and Topology  $\gamma p \rightarrow p\pi^-(\pi^+)$ , as shown in Figure 5.18 for the center-of-mass energy  $W \in [1.725, 1.775]$  GeV.

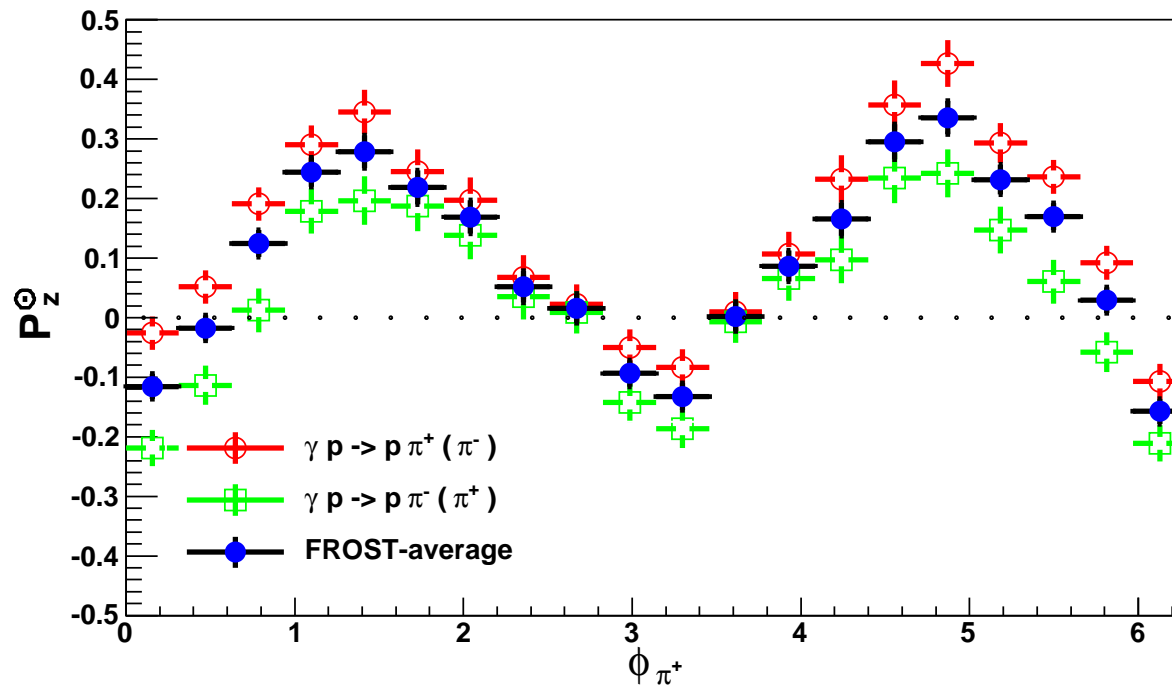


Figure 5.19: The average helicity difference of the topology 1 and topology 2 and their average, called FROST-average. The data are shown for the center-of-mass energy  $W \in [1.675, 1.725]$  GeV.

### 5.4.3 Comparison

For different period-combinations and topologies, we have compared the results to confirm consistency. Figure 5.20 shows the differences ( $P_z^\odot_{\text{combination X}} - P_z^\odot_{\text{combination Y}}$ ) for three kinds of period-combinations, and Figure 5.21 shows the differences ( $P_z^\odot_{\text{Topology X}} - P_z^\odot_{\text{Topology Y}}$ ) between different topologies integrated across all kinematic bins. The distributions are all centered at zero and show generally good agreement.

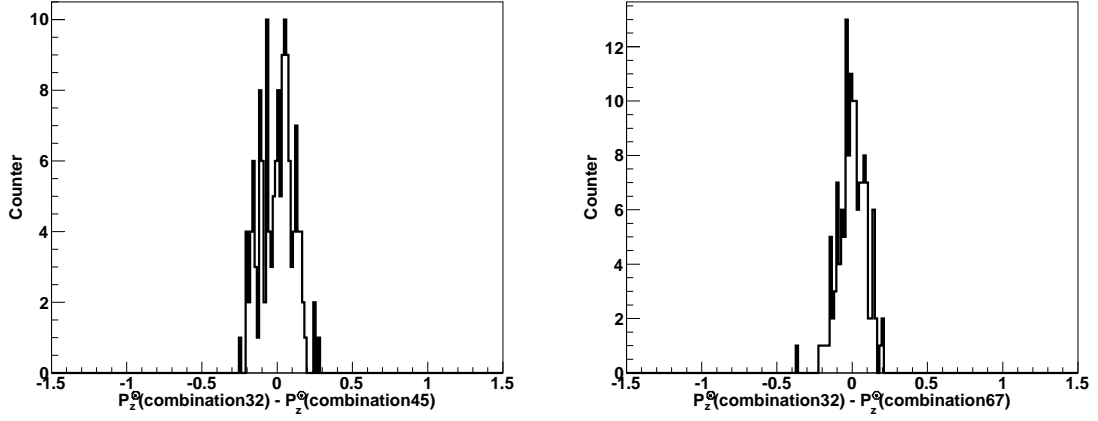


Figure 5.20: Comparisons (differences) between results for the polarization observables  $P_z^\odot$  from different period-combinations integrated over all energies in Topology  $\gamma p \rightarrow p\pi^+(\pi^-)$ .

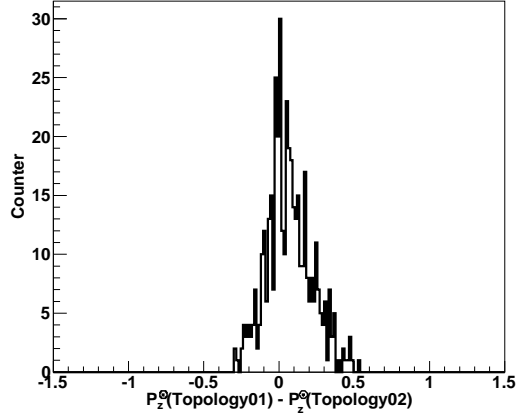


Figure 5.21: Comparisons (differences) between results for the polarization observables  $P_z^\odot$  from different topologies integrated over all energies.

## 5.5 Systematic Uncertainties

Systematic uncertainties define errors which are not determined by statistics but are introduced by an inaccuracy in the measurement inherent in the system. Systematic errors in experimental observations of the g9a experiment are usually based on instrumental effects. The polarization observables have several variables from the measuring instruments: beam polarization  $\delta_{\odot}$ , target polarization  $\Lambda_z$ , and normalization factor  $F$  from the photon beam flux. These systematic uncertainties and their systematic errors affect the polarization observables. The integrated effect of these systematic errors on the observables can be calculated by applying the error propagation. (See Appendix D).

The beam helicity is flipped in the injector of the electron accelerator. Small beam-charge asymmetries of the electron beam can be one component of the systematic error. The error of beam-charge asymmetry can be calculated from the difference between polarization observables  $\mathbf{I}^{\odot}$  before and after applying the effect of the electron beam charge asymmetry (See Appendix B). Other systematic errors, as referenced in Table 5.4, should be studied for publishing.

Table 5.4: Systematic contributions to the uncertainties in polarization observables. There is the list of systematic errors studied for publishing.

Contribution	$\Delta\mathbf{O}$	$\Delta\mathbf{O}/\mathbf{O}$
Circular polarization of photon beam		< 1.8 %
Target polarization		< 4.33 %
Electron beam-charge asymmetry	< 0.004	
Accidentals		
Normalization (photon flux)		
Q-factor method : nearest neighbors		
Q-factor method : scale factor		
Kinematic fitting : different CL		
Average target polarization in $\mathbf{P}_z^{\odot}$		

# CHAPTER 6

## CONCLUSIONS

### 6.1 Systematic check of the Symmetry of the Observables

In this analysis, the dataset has been binned in two independent kinematical variables: the center-of-mass energy,  $W$ , and the azimuthal angle,  $\phi_{\pi^+}^*$ . As previously mentioned, the variable  $\phi_{\pi^+}^*$  is the angle between the production plane (blue plane in Figure 5.1) and the decay plane (red plane in the same figure). Observables as function of  $\phi_{\pi^+}^*$  exhibit either an odd or an even symmetry.

Figure 6.1 shows the polarization observable  $\mathbf{I}^\odot$  for the whole energy range  $W \in [1.375, 2.125]$  GeV. To check the symmetry of the observable  $\mathbf{I}^\odot$ , the transition  $\phi_{\pi^+}^* \rightarrow 2\pi - \phi_{\pi^+}^*$  is performed, i.e.  $-\mathbf{I}^\odot(2\pi - \phi_{\pi^+}^*)$ . This is equivalent to applying a mirror operation with respect to the production plane, and then changing the sign of the asymmetry (Figure 6.1). The observable  $\mathbf{I}^\odot$  obeys the odd symmetry constraints because the differences between the observables  $\mathbf{I}^\odot(\phi_{\pi^+}^*)$  and  $-\mathbf{I}^\odot(2\pi - \phi_{\pi^+}^*)$  are comparably small values.

Figure 6.2 and 6.3 represent the polarization observables  $\mathbf{P}_z$  and  $\mathbf{P}_z^\odot$  for the whole energy range  $W \in [1.375, 2.125]$  GeV, respectively. To also check the symmetries of the observables  $\mathbf{P}_z$  and  $\mathbf{P}_z^\odot$ , the transition  $\phi_{\pi^+}^* \rightarrow 2\pi - \phi_{\pi^+}^*$  should be applied like for the observable  $\mathbf{I}^\odot$ . Because the observable  $\mathbf{P}_z$  is an odd symmetry like the observable  $\mathbf{I}^\odot$ ,  $-\mathbf{P}_z(2\pi - \phi_{\pi^+}^*)$  is applied (Figure 6.2). Since, however,  $\mathbf{P}_z^\odot$  is an even function, the mirror operation with respect to the production plane does not require a sign change as in the case of  $\mathbf{I}^\odot$  and  $\mathbf{P}_z$ , i.e.  $\mathbf{P}_z^\odot(2\pi - \phi_{\pi^+}^*)$  (Figure 6.3). The polarization observables  $\mathbf{P}_z$  and  $\mathbf{P}_z^\odot$  have overall well defined symmetry constraints because the differences between the observable and the observable applied the transition  $\phi_{\pi^+}^* \rightarrow 2\pi - \phi_{\pi^+}^*$  have the reasonable small values.

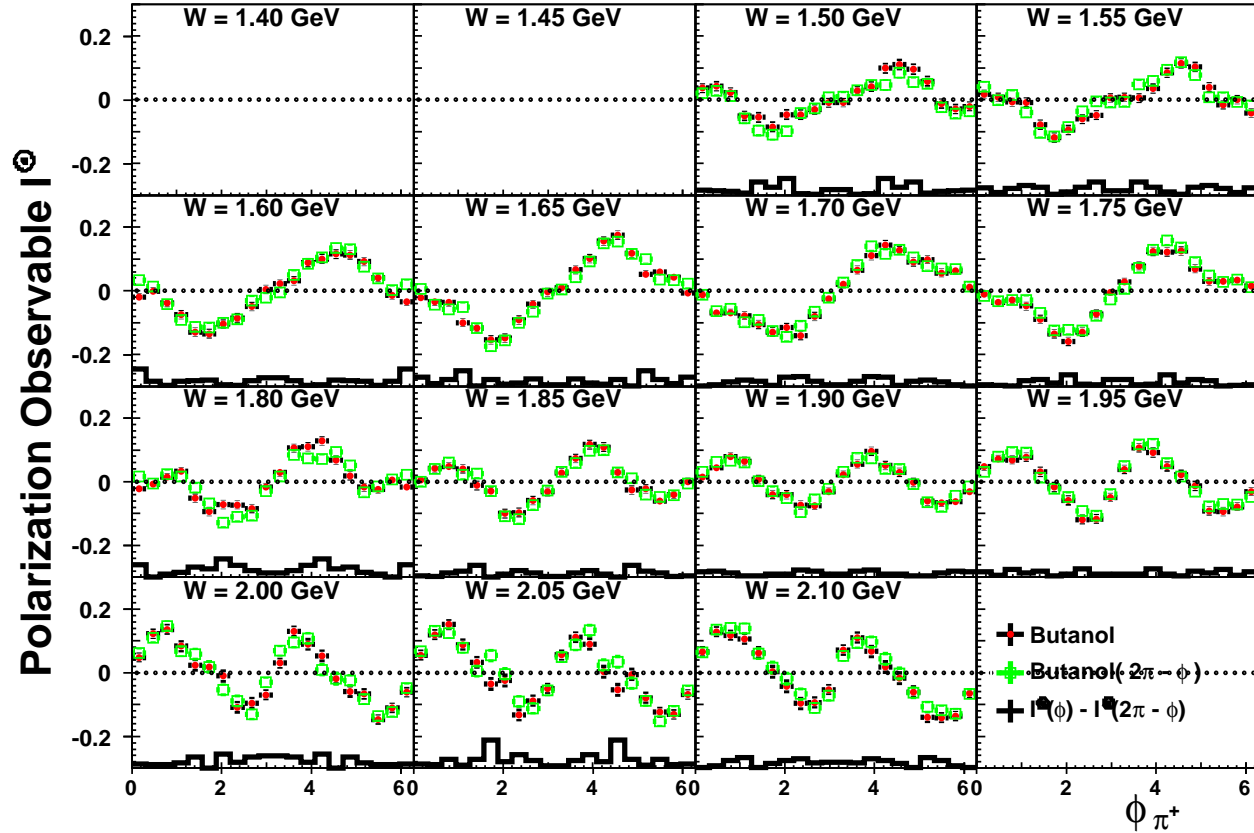


Figure 6.1: Measured beam-helicity asymmetry  $I^\odot$  in the reaction  $\vec{\gamma}p \rightarrow p\pi^+\pi^-$  for the whole center-of-mass energy range  $W \in [1.375, 2.125]$  GeV. The filled symbols denote the average observable  $I^\odot$  from the butanol data and the open symbol the observable  $-I^\odot(2\pi - \phi_{\pi^+}^*)$  from the same dataset. The distribution at the bottom of each energy is the difference between the observable  $I^\odot$  and the observable  $-I^\odot(2\pi - \phi_{\pi^+}^*)$ .

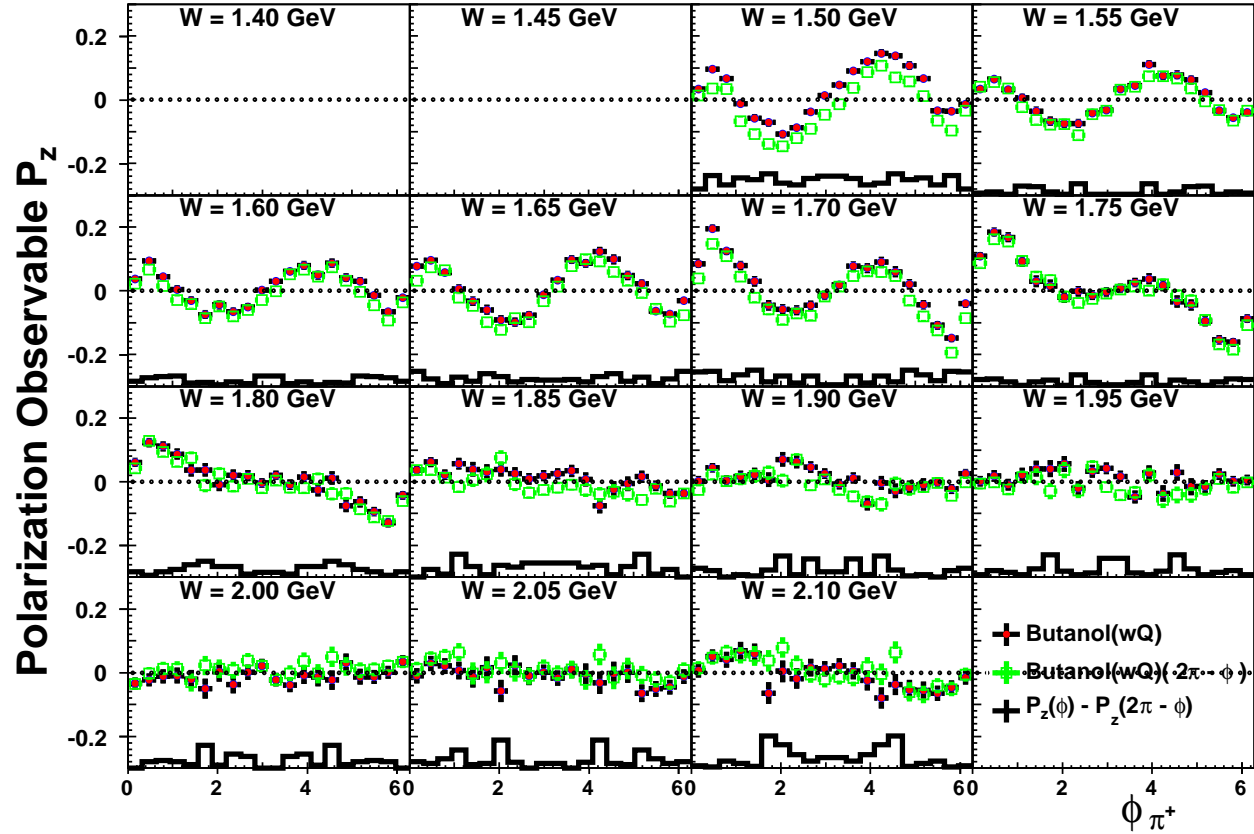


Figure 6.2: Measured beam-helicity asymmetry  $\mathbf{P}_z$  in the reaction  $\gamma\vec{p} \rightarrow p\pi^+\pi^-$  for the whole center-of-mass energy range  $W \in [1.375, 2.125]$  GeV. The filled symbols denote the average observable  $\mathbf{P}_z$  from the butanol data weighted by the Q-factor (Section 4.9.2) and the open symbol the observable  $-\mathbf{P}_z(2\pi - \phi_{\pi^+}^*)$  from the same dataset. The distribution at the bottom of each energy is the difference between the observable  $\mathbf{P}_z$  and the observable  $-\mathbf{P}_z(2\pi - \phi_{\pi^+}^*)$ .

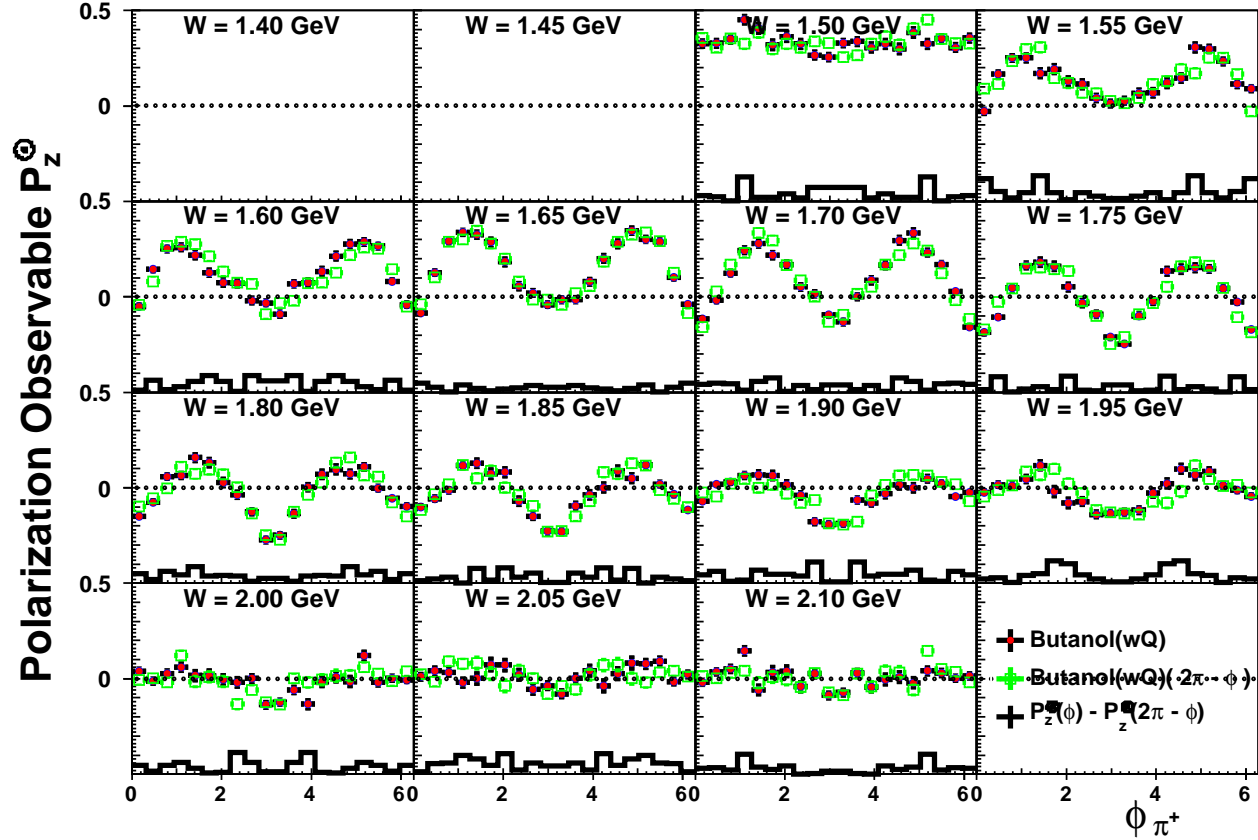


Figure 6.3: Measured beam-helicity asymmetry  $\mathbf{P}_z^{\odot}$  in the reaction  $\vec{\gamma}\vec{p} \rightarrow p\pi^+\pi^-$  for the whole center-of-mass energy range  $W \in [1.375, 2.125]$  GeV. The filled symbols denote the average observable  $\mathbf{P}_z^{\odot}$  from the butanol data weighted by the Q-factor (Section 4.9.2) and the open symbol the observable  $\mathbf{P}_z^{\odot}(2\pi - \phi_{\pi^+}^*)$  from the same dataset. The distribution at the bottom of each energy is the difference between the observable  $\mathbf{P}_z^{\odot}$  and the observable  $\mathbf{P}_z^{\odot}(2\pi - \phi_{\pi^+}^*)$ .

## 6.2 Comparison of the Polarization Observables with Models

Figure 6.4 shows the comparison of the observable  $\mathbf{I}^\odot$  from this analysis with the results from the CLAS-g1c experiment for the entire center-of-mass energy range,  $W \in [1.375, 2.125]$  GeV. The observable  $\mathbf{I}^\odot$  from the g9a experiment (in red) is overall very good agreement with the published data (in light blue) [11] for the whole energy range. In addition, the observable from the CLAS-g9a experiment with 20 bins in the azimuthal angle  $\phi_{\pi^+}^*$  has the better resolution than from the CLAS-g1c experiment with 11 bins. Since the  $x$ -axis in this figure denotes the azimuthal angle between the center-of-mass production plane (blue plane in Figure 5.1) and the decay plane (red plane in the same figure), the observable  $\mathbf{I}^\odot$  must have a value of zero in this representation for  $\phi_{\pi^+}^* = 0, \pi,$  and  $2\pi$  due to the odd symmetry. This nicely observed in the data. Moreover, the results from the butanol data (in red, no background subtraction) and the butanol data weighted by the Q-factor (in deep blue, background subtraction) coincide very well for the whole  $\phi_{\pi^+}^*$  angle range. The discrepancy between these two results is happened due to the low statistic.

The measurements of the observable  $\mathbf{I}^\odot$  are then compared to the results from the models of A. Fix [37] and W. Roberts [10], which are available from threshold of the double pion photoproduction up to the center-of-mass energy,  $W = 1.775$  GeV. The observables calculated by A. Fix and W. Roberts show the odd symmetry as the result from this analysis in shape and magnitude to be observed. Overall agreement, however, is not very good and there is even the big discrepancy between them.

Figure 6.5 shows the polarization observable  $\mathbf{P}_z$  for the whole center-of-mass energy range  $W \in [1.375, 2.125]$  GeV. For the polarization observable  $\mathbf{P}_z$ , there are no experimentally published data. However, results from the models of A. Fix [37] and W. Roberts [10] exist in the low-energy region ( $W \in [1.375, 1.1775]$  GeV). All these model predictions provide a good estimation of the magnitude of the observable. However, they appear to be a sign issue. Therefore, the observables analyzed here can serve as the guideline to improve predictions.

Figure 6.6 shows the polarization observable  $\mathbf{P}_z^\odot$  for the whole energy range  $W \in [1.375, 2.125]$  GeV. Since the published data for the observable  $\mathbf{P}_z^\odot$  [13] only shows the helicity-dependent total cross-section difference,  $\Delta\sigma = (\sigma_{3/2} - \sigma_{1/2})$ , but not the observable, the results published in [13] are not shown in Figure 6.6. The polarization observable  $\mathbf{P}_z^\odot$  from the g9a experiment is overall good agreement with the models predictions by A. Fix [37] and W. Roberts [10] in shape, but not amplitude. It is worth noting that the A. Fix model knows about these results from the isospin related channel,  $n\pi^+\pi^0$  and  $p\pi^0\pi^0$ , measured at MAMI.

In summary, we have given a brief overview of precise measurements of the beam-helicity asymmetry, the target asymmetry, and the helicity difference for photoproduction of two charge pions off the longitudinally-polarized proton using circularly-polarized photons. The comparison between results from the butanol target and the butanol weighted by the Q-factor (event-based background subtraction) also shows that the Q-factor method is a very useful tool to extract the polarization observables. The general lack of agreement between experiment and the theory signals severe shortcomings in the theoretical models existed. Therefore, the comparison with model predictions provides the basis for significant improvements for the models. A proper understanding of the  $\pi^+\pi^-N$  channel in the region of overlapping nucleon resonances can serve as an important contribution to solving the missing resonance problem.

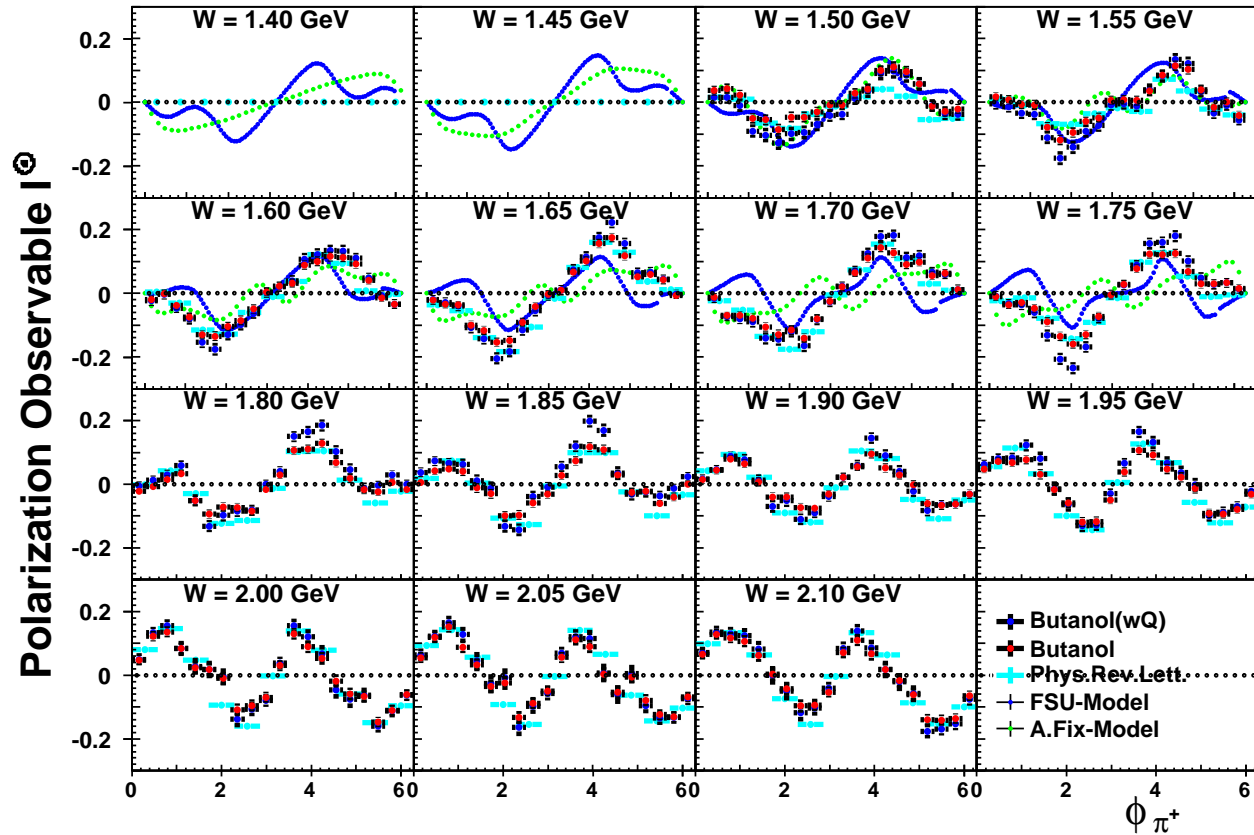


Figure 6.4: Comparison between the polarization observable  $I^\circ$  analyzed in the g9a experiment, and the polarization observable  $I^\circ$  published in the g1c experiment (light blue). The data are shown for the whole center-of-mass energy range  $W \in [1.375, 2.125]$  GeV. All kinematic variables except  $\phi_{\pi^+}^*$  and  $W$  are integrated over. The red datapoint denotes the observable  $I^\circ$  from the butanol data, and the deep blue datapoint denotes the same observable from the butanol weighted by the Q-factor (Section 4.9.2). The green dots indicate model calculations provided by A. Fix [37], and the blue dots by W. Roberts [10].

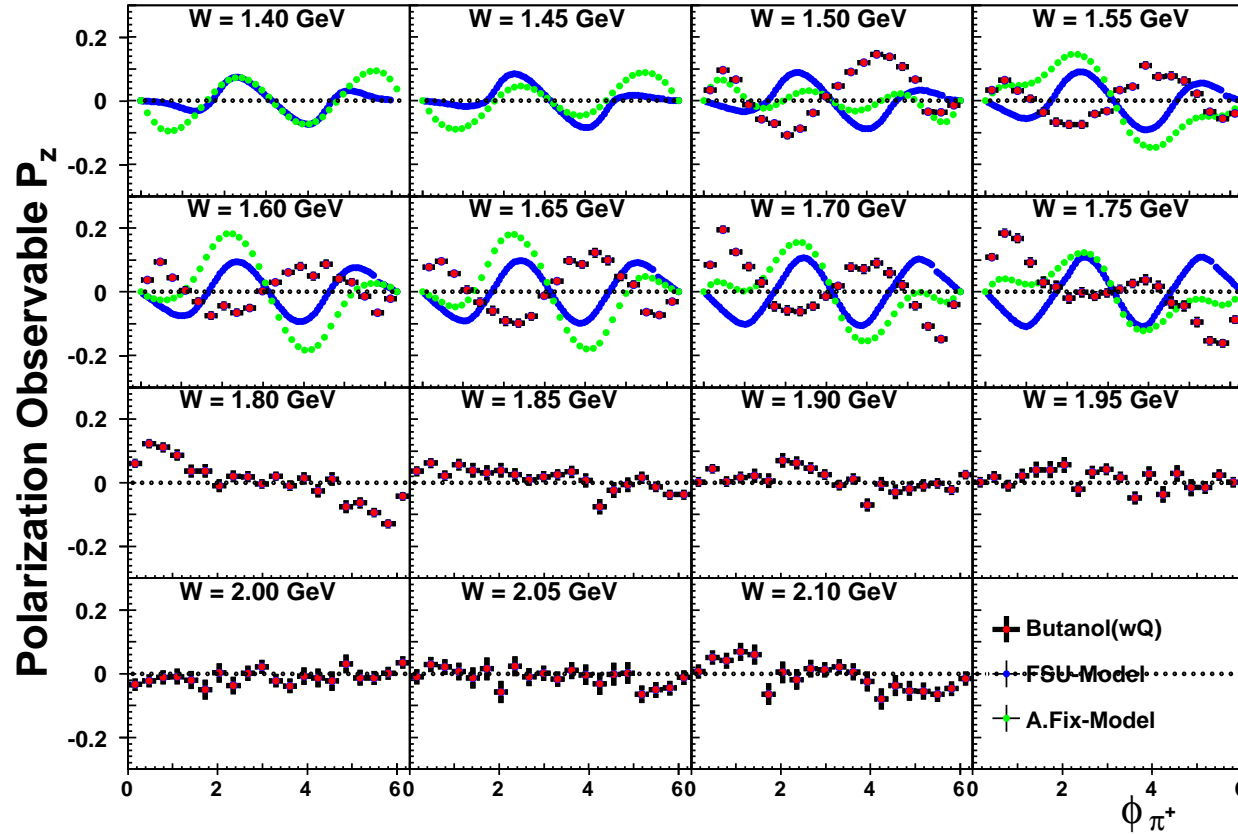


Figure 6.5: The polarization observable  $\mathbf{P}_z$  from the g9a experiment for the whole center-of-mass energy range  $W \in [1.375, 2.125]$  GeV. All kinematic variables except  $\phi_{\pi^+}^*$  and  $W$  are integrated over. The blue denotes the observable  $\mathbf{I}^\odot$  from the butanol weighted by the Q-factor (Section 4.9.2). The green dots indicate model calculations provided by A. Fix [37], and the blue dots by W. Roberts [10].

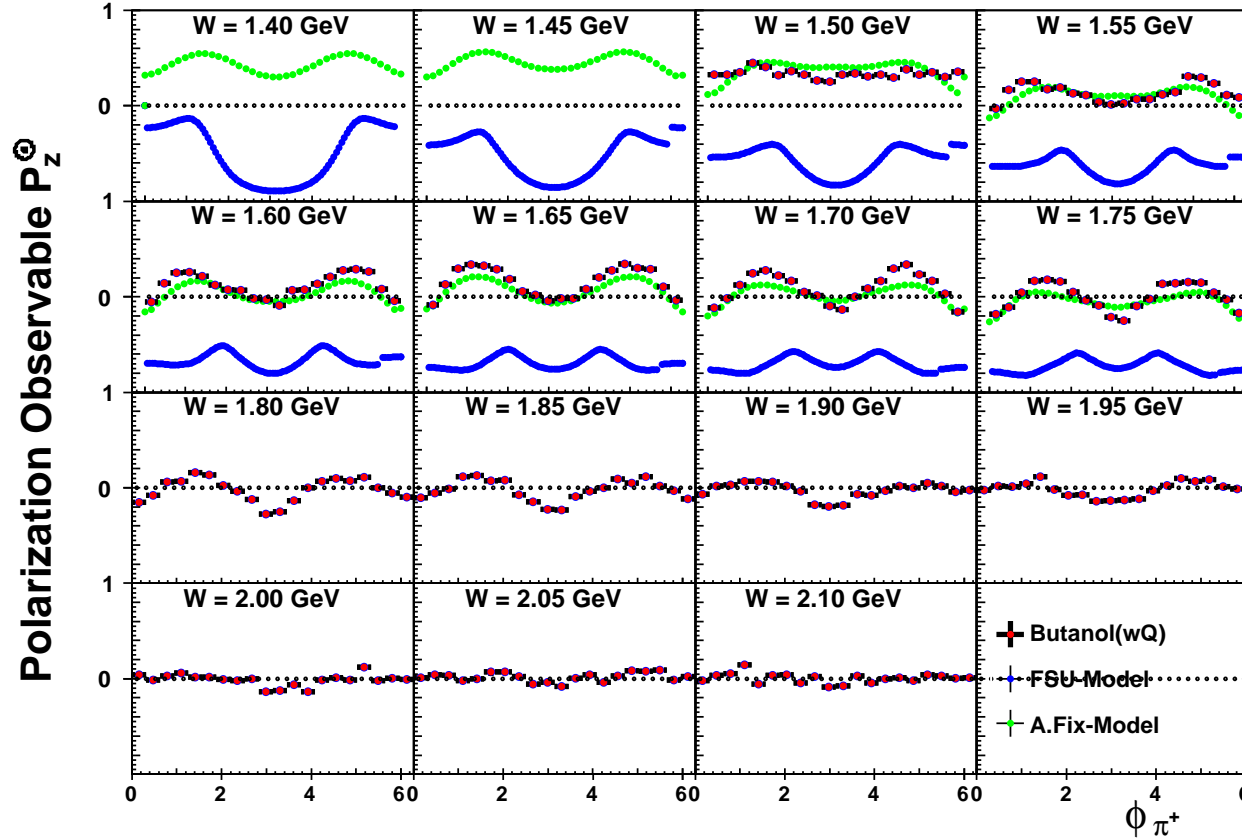


Figure 6.6: The polarization observable  $\mathbf{P}_z^\odot$  from the g9a experiment for the whole center-of-mass energy range  $W \in [1.375, 2.125]$  GeV. All kinematic variables except  $\phi_{\pi^+}^*$  and  $W$  are integrated over. The blue fullcross denotes the observable  $\mathbf{I}^\odot$  from the butanol weighted by the Q-factor (Section 4.9.2). The green dots indicate model calculations provided by A. Fix [37], and the blue dots by W. Roberts [10].

# APPENDIX A

## BEAM AND TARGET POLARIZATION

### A.1 Beam and Target Polarization

Table 4.14 illustrates the condition of the half-wave plate and the direction of the target polarization in the seven periods. The information in Table 4.14 should be confirmed. The condition of the half-wave plate is used for the beam polarization, as referenced in Table 4.13. If the condition of the half-wave-plate in Table 4.14 per period may be wrong, beam asymmetries from three period-combinations will not coincide. In conclusion, beam asymmetries made from three different period-combinations show good agreement, as shown in Figure A.1.

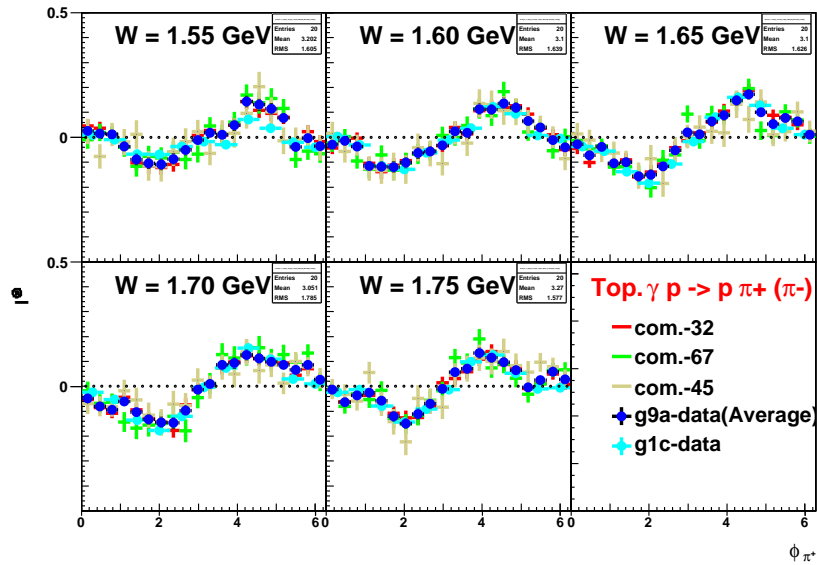
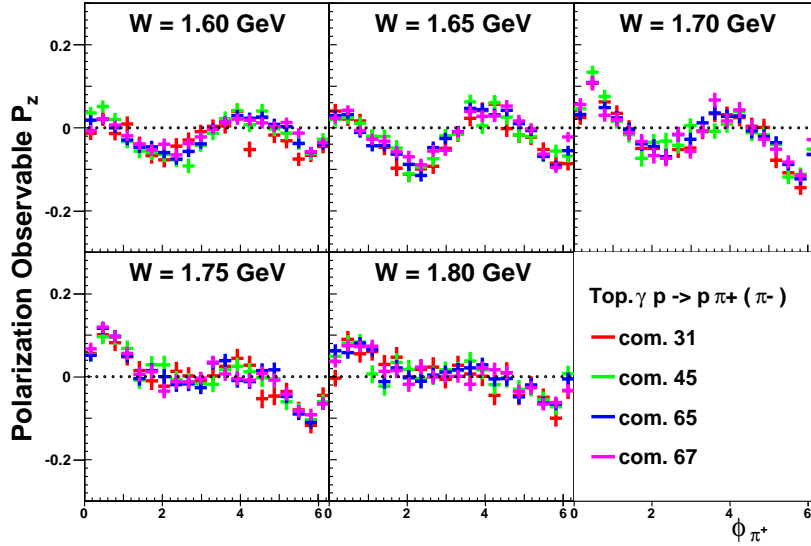
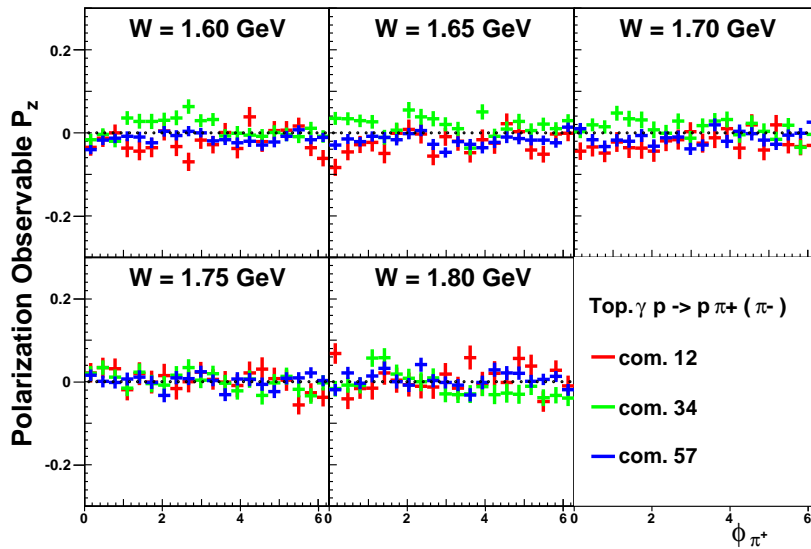


Figure A.1: The beam asymmetries of three period-combinations in topology  $\gamma p \rightarrow p\pi^+(\pi^-)$  and an average beam asymmetry.

The direction of the target polarization in Table 4.14 can also be checked using the target asymmetry. Target asymmetries made in the different directions of the target polarizations will have some structure and beam asymmetries in the same directions will not have any structures, as shown in Figure A.2.



(a) Combinations among different polarizations.



(b) Combinations among same polarizations.

Figure A.2: The target asymmetry made from different target polarizations (a) and from the same target polarization (b).

# APPENDIX B

## BEAM CHARGE ASYMMETRY

### B.1 Beam Charge Asymmetry

Table 4.9 shows the electron beam charge asymmetry in the g9a dataset and the total number of  $\gamma p \rightarrow p\pi^+\pi^-$  events for the two helicity states. The electron beam charge asymmetry can be defined by

$$Y^\pm = N^\pm/\alpha^\pm \quad (\text{B.1})$$

$$\begin{aligned}
 Y^+ &= \frac{1}{\alpha^+} \left( \frac{N(\phi, \rightarrow\Rightarrow)}{\Lambda_z(\Rightarrow)F(\Rightarrow)} + \frac{N(\phi, \rightarrow\Leftarrow)}{\Lambda_z(\Leftarrow)F(\Leftarrow)} \right) \sim \frac{A(\phi)}{\alpha^+} \left( \frac{1}{\Lambda_z(\Rightarrow)} + \frac{1}{\Lambda_z(\Leftarrow)} \right) (1 + \delta_\odot \mathbf{I}^\odot) \\
 Y^- &= \frac{1}{\alpha^-} \left( \frac{N(\phi, \leftarrow\Rightarrow)}{\Lambda_z(\Rightarrow)F(\Rightarrow)} + \frac{N(\phi, \leftarrow\Leftarrow)}{\Lambda_z(\Leftarrow)F(\Leftarrow)} \right) \sim \frac{A(\phi)}{\alpha^-} \left( \frac{1}{\Lambda_z(\Rightarrow)} + \frac{1}{\Lambda_z(\Leftarrow)} \right) (1 - \delta_\odot \mathbf{I}^\odot)
 \end{aligned} \quad (\text{B.2})$$

and the asymmetry can be calculated using the corrected number of events for the helicity plus and minus. The beam asymmetry  $A^{beam}$  considering the effect of the electron beam charge asymmetry is given by

$$\begin{aligned}
 A^{beam} &= \frac{Y^+ - Y^-}{Y^+ + Y^-} = \frac{\frac{1}{\alpha^+} \left( \frac{N(\phi, \rightarrow\Rightarrow)}{\Lambda_z(\Rightarrow)F(\Rightarrow)} + \frac{N(\phi, \rightarrow\Leftarrow)}{\Lambda_z(\Leftarrow)F(\Leftarrow)} \right) - \frac{1}{\alpha^-} \left( \frac{N(\phi, \leftarrow\Rightarrow)}{\Lambda_z(\Rightarrow)F(\Rightarrow)} + \frac{N(\phi, \leftarrow\Leftarrow)}{\Lambda_z(\Leftarrow)F(\Leftarrow)} \right)}{\frac{1}{\alpha^+} \left( \frac{N(\phi, \rightarrow\Rightarrow)}{\Lambda_z(\Rightarrow)F(\Rightarrow)} + \frac{N(\phi, \rightarrow\Leftarrow)}{\Lambda_z(\Leftarrow)F(\Leftarrow)} \right) + \frac{1}{\alpha^-} \left( \frac{N(\phi, \leftarrow\Rightarrow)}{\Lambda_z(\Rightarrow)F(\Rightarrow)} + \frac{N(\phi, \leftarrow\Leftarrow)}{\Lambda_z(\Leftarrow)F(\Leftarrow)} \right)} \\
 &= \frac{\frac{1 + \delta_\odot \mathbf{I}^\odot}{\alpha^+} - \frac{1 - \delta_\odot \mathbf{I}^\odot}{\alpha^-}}{\frac{1 + \delta_\odot \mathbf{I}^\odot}{\alpha^+} + \frac{1 - \delta_\odot \mathbf{I}^\odot}{\alpha^-}}
 \end{aligned} \quad (\text{B.3})$$

The polarization observable  $\mathbf{I}^\odot$  is given by

$$I^{\odot} = \frac{1}{\delta_{\odot}} \frac{A^{beam} \left( \frac{1}{\alpha^+} + \frac{1}{\alpha^-} \right) - \left( \frac{1}{\alpha^+} - \frac{1}{\alpha^-} \right)}{\left( \frac{1}{\alpha^+} + \frac{1}{\alpha^-} \right) - A^{beam} \left( \frac{1}{\alpha^+} - \frac{1}{\alpha^-} \right)} \quad (\text{B.4})$$

Equation 5.12 shows the polarization observable  $\mathbf{I}^{\odot}$  without the effect of the beam charge asymmetry, and equation B.4 shows the polarization observable  $\mathbf{I}^{\odot}$  with the effect of the beam charge asymmetry. Figure B.1 shows their difference. The electron beam charge asymmetry can be neglected in this analysis.

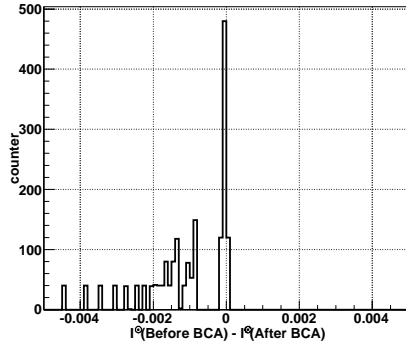


Figure B.1: Comparisons between the polarization observables  $\mathbf{I}^{\odot}$  before and after applying the beam charge asymmetry.

# APPENDIX C

## BACKGROUND EFFECT IN THE BUTANOL TARGET

### C.1 Background Effect in the Butanol Target

The butanol data are composed of the free-proton, bound-nucleon, and background data. We cannot distinguish precisely between the free-proton events and the rest of the events in the butanol data. The confidence-level cut in the g9a analysis can make it possible to classify the butanol data.

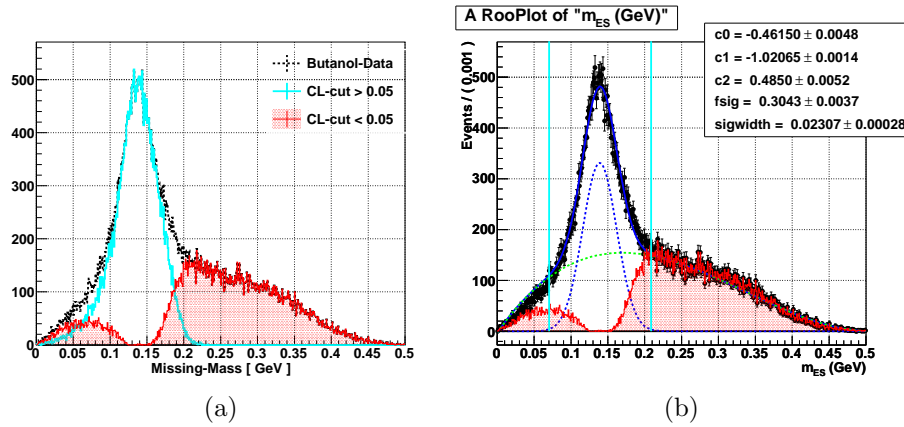


Figure C.1: (a) The missing mass distribution with the 5 % confidence-level cut for the butanol target. (b) The missing mass distribution fitted with a Gaussian and the second-order Chebyshev polynomial. The data are selected for the center-of-mass energy  $W \in [1.575, 1.625]$  GeV and the topology  $\gamma p \rightarrow p\pi^+(\pi^-)$ . The hatched area includes events whose the confidence-level is less than 0.05. The light blue line is located at the  $\pi^+$  mass  $\pm 3\sigma$  of the fitted Gaussian function. The dashed green line is the second-order Chebyshev polynomial function.

Figure C.1 (a) shows the missing mass distribution with the 5 % confidence-level cut. In Figure C.1 (b), the free-proton data are expressed as the Gaussian function. The bound-nucleon and background data are described using the second-order Chebyshev polynomial function. The missing mass distribution of the g1c dataset after applying all cuts and corrections had no background for double-pion photoproduction because the g1c experiment use the hydrogen target. In the g9a dataset, however, the missing mass plot has the background with the free-proton events as the shape of the Gaussian, as shown in Figure C.1 (b). We may assume that the background events of the missing mass distribution, as shown in Figure C.1 (a), stems from carbon parts of the butanol target. However, the mixture of "good" carbon events and garbage events, which is badly reconstructed, is unknown. We also assume that the beam asymmetry made from the free-proton events is similar for bound nucleons, and that g9a dataset is not sensitive to distinguish between the beam asymmetries for free-proton and bound-nucleon events.

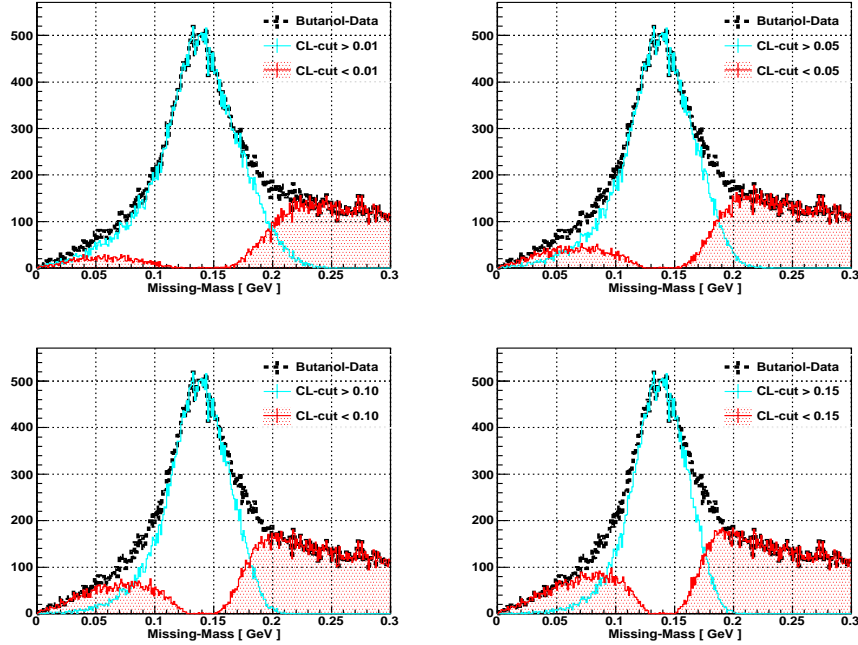


Figure C.2: The missing mass distribution of the butanol target made in different CL-cuts. The data are selected for the center-of-mass energy  $W \in [1.575, 1.625]$  GeV and the topology  $\gamma p \rightarrow p\pi^+(\pi^-)$ .

Figure C.2 shows the missing mass distribution of Topology  $\gamma p \rightarrow p\pi^+(\pi^-)$  in the confidence-level cut 1 %, 5 %, 10 %, and 15 %. When the confidence-level cut is increased, more and more background events are cut out, along with the small

amounts of the good signal events. These different amounts of background events under the free-proton events in Figure C.2 can have an effect on the amplitude of our modulation in the beam asymmetry. Figure C.3 shows the comparison between the polarization observables  $I^\ominus$  made in the confidence-level cut 1 %, 5 %, 10 %, and 15 % with the published g1c data. Figure C.3 shows the beam asymmetry is more or less independent of the confidence-level cut. The different sizes of background events under the free-proton events apparently have no significant effect on the structure of the beam asymmetry.

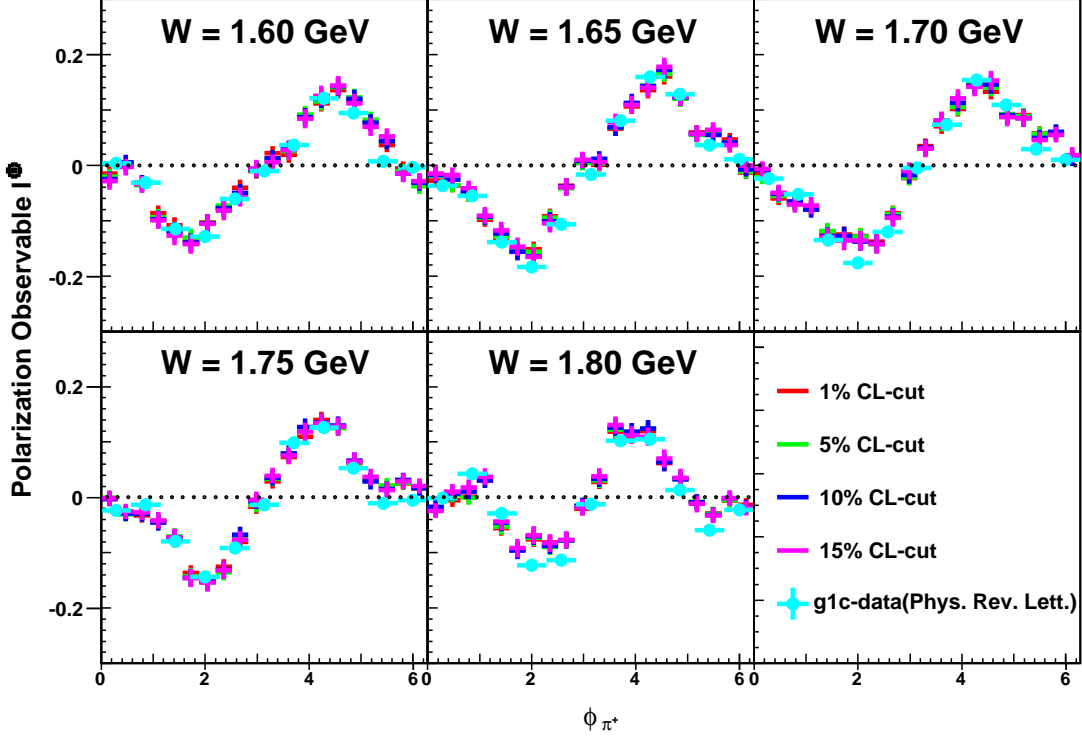
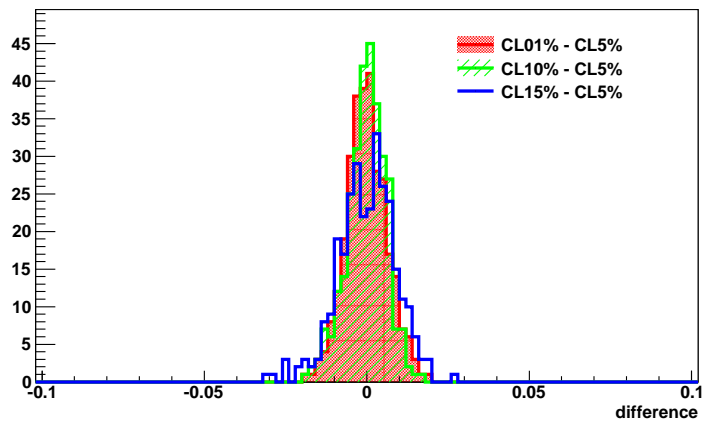
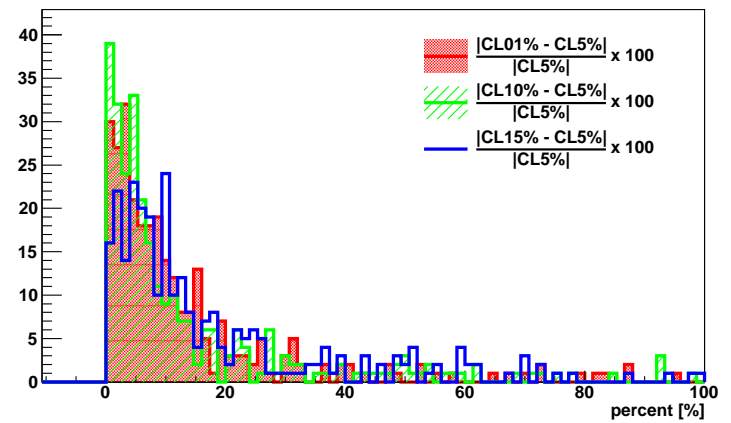


Figure C.3: The average beam asymmetries made in 1 % CL-cut, 5 % CL-cut, 10 % CL-cut, and 15 % CL-cut and the polarization observable  $I^\ominus$  published in g1c experiment.

Our conclusion is that, after applying the confidence-level cut, the "garbage" background events can be almost negligible; That is, events under the free-proton events are from the bound-nucleon data. Polarization observables  $I^\ominus$  from free-proton and bound-nucleon events have similar values. Figure C.4 (a) shows differences  $(I_{X\% \text{ CLcut}}^\ominus - I_{5\% \text{ CLcut}}^\ominus)$  and Figure C.4 (b) describes the percent error between  $X\%$  CL-cut and 5 % CL-cut when  $X$  is 1 % CL-cut, 10 % CL-cut, and 15 % CL-cut.



(a) Difference



(b) Percent error

Figure C.4: Difference and percent error between polarization observable  $I^{\odot}$  for 5% CL-cut and other CL-cuts.

# APPENDIX D

## ERROR PROPAGATION

### D.1 Error Propagation

The target polarization  $\Lambda_z$ , normalization factor  $F$ , and beam polarization  $\delta_{\odot}$  in Equation 5.12 also have statistical errors and their effects on the polarization observable  $\mathbf{I}^{\odot}$  should also be considered. Polarization observable  $\mathbf{I}^{\odot}$  can be given by:

$$\mathbf{I}^{\odot} = \frac{1}{\bar{\delta}_{\odot}} \frac{N(\rightarrow) - N(\leftarrow)}{N(\rightarrow) + N(\leftarrow)} \quad (\text{D.1})$$

Where

$$N(\rightarrow) = \frac{N(\rightarrow\Rightarrow)}{\{\Lambda(\Rightarrow)/\Lambda(\Leftarrow)\}\{F(\Rightarrow)/F(\Leftarrow)\}} + N(\rightarrow\Leftarrow) \quad (\text{D.2})$$

and

$$N(\leftarrow) = \frac{N(\leftarrow\Rightarrow)}{\{\Lambda(\Rightarrow)/\Lambda(\Leftarrow)\}\{F(\Rightarrow)/F(\Leftarrow)\}} + N(\leftarrow\Leftarrow). \quad (\text{D.3})$$

For a calculative expedience, we assume  $A = \Lambda(\Rightarrow)/\Lambda(\Leftarrow)$  and  $B = F(\Rightarrow)/F(\Leftarrow)$ . The errors of  $N(\rightarrow)$  and  $N(\leftarrow)$  for the target polarization and normalization factor can be calculated using the formulation of the error propagation:

$$\Delta N(\rightarrow) = \sqrt{\left(\frac{N(\rightarrow\Rightarrow) \cdot \Delta A}{A^2 \cdot B}\right)^2 + \left(\frac{N(\rightarrow\Rightarrow) \cdot \Delta B}{A \cdot B^2}\right)^2} \quad (\text{D.4})$$

and

$$\Delta N(\leftarrow) = \sqrt{\left(\frac{N(\leftarrow\Rightarrow) \cdot \Delta A}{A^2 \cdot B}\right)^2 + \left(\frac{N(\leftarrow\Rightarrow) \cdot \Delta B}{A \cdot B^2}\right)^2}. \quad (\text{D.5})$$

The error of polarization observable  $\mathbf{I}^\odot$  is also given using the formulation of the error propagation:

$$\begin{aligned}\Delta I^\odot &= \sqrt{\left(\frac{\partial I^\odot \cdot \Delta N(\rightarrow)}{\partial N(\rightarrow)}\right)^2 + \left(\frac{\partial I^\odot \cdot \Delta N(\leftarrow)}{\partial N(\leftarrow)}\right)^2 + \left(\frac{\partial I^\odot \cdot \Delta \bar{\delta}_\odot}{\partial \bar{\delta}_\odot}\right)^2} \\ &= \sqrt{\frac{(2N(\leftarrow))^2(\Delta N(\rightarrow))^2}{(\bar{\delta}_\odot)^2(N(\rightarrow) + N(\leftarrow))^4} + \frac{(2N(\rightarrow))^2(\Delta N(\leftarrow))^2}{(\bar{\delta}_\odot)^2(N(\rightarrow) + N(\leftarrow))^4} + \frac{(N(\rightarrow) - N(\leftarrow))^2(\Delta \bar{\delta}_\odot)^2}{(\bar{\delta}_\odot)^4(N(\rightarrow) + N(\leftarrow))^2}}.\end{aligned}\quad (\text{D.6})$$

The error of polarization observable  $\mathbf{I}^\odot$  given in Equation D.6 consists of three parts: the error from the target polarization, the error from the normalization factor, and the error from the beam polarization. Figure D.1 shows the error distribution about polarization observable  $\mathbf{I}^\odot$  in the three parts.

The error from the target polarization is given by:

$$\Delta I_{Tar.Pol.}^\odot = \sqrt{\frac{2N(\leftarrow)^2 \cdot N(\rightarrow \Rightarrow)^2 + 2N(\rightarrow)^2 \cdot N(\leftarrow \Rightarrow)^2}{(\bar{\delta}_\odot)^2 \cdot (N(\rightarrow) + N(\leftarrow))^4 \cdot (A^2 \cdot B)^2}} \cdot (\Delta A)^2 \quad (\text{D.7})$$

The error from the normalization factor is given by:

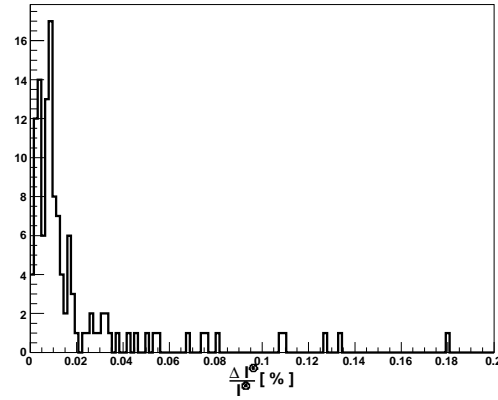
$$\Delta I_{Nor.Fac.}^\odot = \sqrt{\frac{2N(\leftarrow)^2 \cdot N(\rightarrow \Rightarrow)^2 + 2N(\rightarrow)^2 \cdot N(\leftarrow \Rightarrow)^2}{(\bar{\delta}_\odot)^2 \cdot (N(\rightarrow) + N(\leftarrow))^4 \cdot (A \cdot B^2)^2}} \cdot (\Delta B)^2 \quad (\text{D.8})$$

The error from the beam polarization is given by:

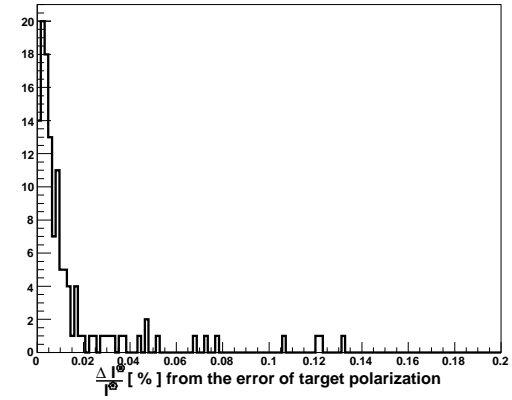
$$\Delta I_{Beam.Pol.}^\odot = \sqrt{\frac{1}{(\bar{\delta}_\odot)^4} \cdot \left(\frac{N(\rightarrow) - N(\leftarrow)}{N(\rightarrow) + N(\leftarrow)}\right)^2} \cdot (\Delta \bar{\delta}_\odot)^2 \quad (\text{D.9})$$

and the error of polarization observable  $\mathbf{I}^\odot$  is given by

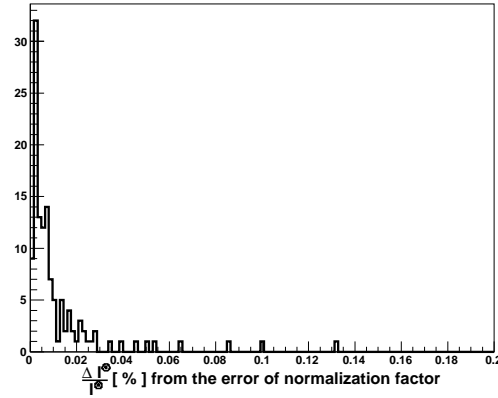
$$\Delta I^\odot = \sqrt{\left(\Delta I_{Tar.Pol.}^\odot\right)^2 + \left(\Delta I_{Nor.Fac.}^\odot\right)^2 + \left(\Delta I_{Beam.Pol.}^\odot\right)^2} \quad (\text{D.10})$$



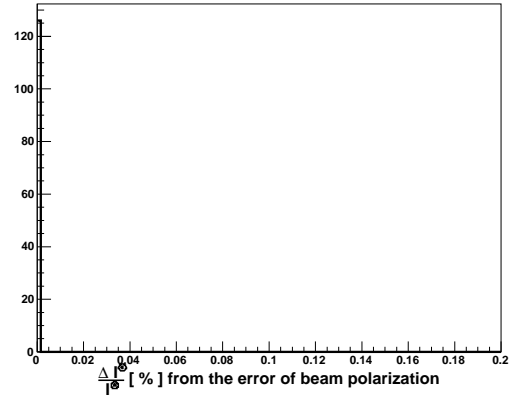
(a)



(b)



(c)



(d)

Figure D.1: The statistical error contribution on observable  $\mathbf{I}^\odot$  from the target polarization (b), from the normalization factor (c), and the beam polarization (d). The sum of these errors is shown in (a).

# APPENDIX E

## AVERAGE POLARIZATION OBSERVABLES

### E.1 Average Polarization Observable $I^\odot$

#### E.1.1 Average Polarization Observable $I^\odot$ for the Butanol Data

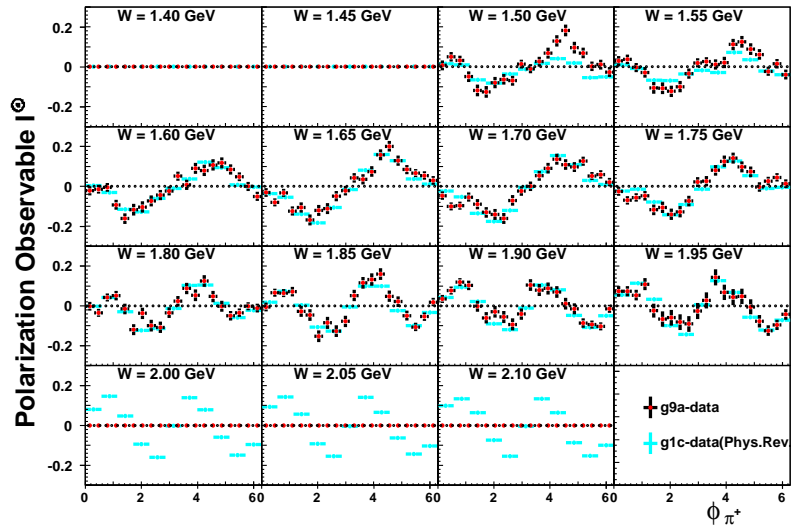


Figure E.1: The beam asymmetries for the topology  $\gamma p \rightarrow p\pi^+(\pi^-)$  and the combination-32. The dataset is for the whole center-of-mass energy range  $W \in [1.375, 2.125]$  GeV and the butanol data.

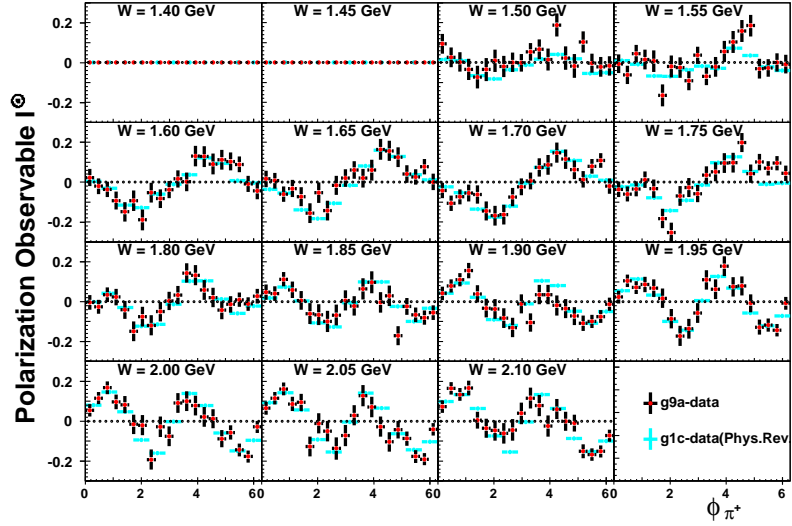


Figure E.2: The beam asymmetries for the topology  $\gamma p \rightarrow p\pi^+(\pi^-)$  and the combination-45. The dataset is for the whole center-of-mass energy range  $W \in [1.375, 2.125]$  GeV and the butanol data.

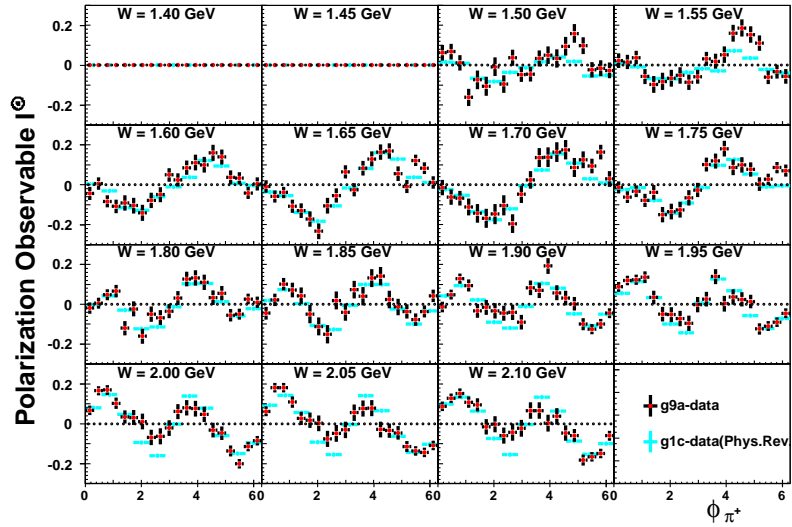


Figure E.3: The beam asymmetries for the topology  $\gamma p \rightarrow p\pi^+(\pi^-)$  and the combination-67. The dataset is for the whole center-of-mass energy range  $W \in [1.375, 2.125]$  GeV and the butanol data.

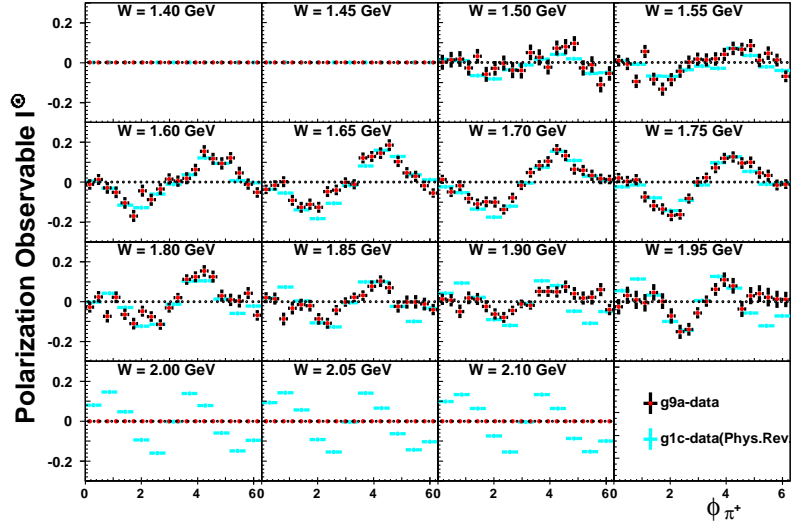


Figure E.4: The beam asymmetries for the topology  $\gamma p \rightarrow p\pi^-(\pi^+)$  and the combination-32. The dataset is for the whole center-of-mass energy range  $W \in [1.375, 2.125]$  GeV and the butanol data.

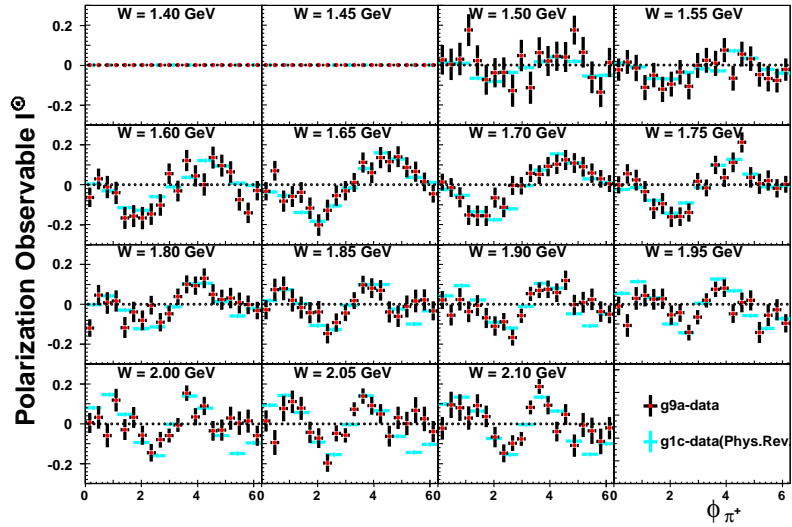


Figure E.5: The beam asymmetries for the topology  $\gamma p \rightarrow p\pi^-(\pi^+)$  and the combination-45. The dataset is for the whole center-of-mass energy range  $W \in [1.375, 2.125]$  GeV and the butanol data.

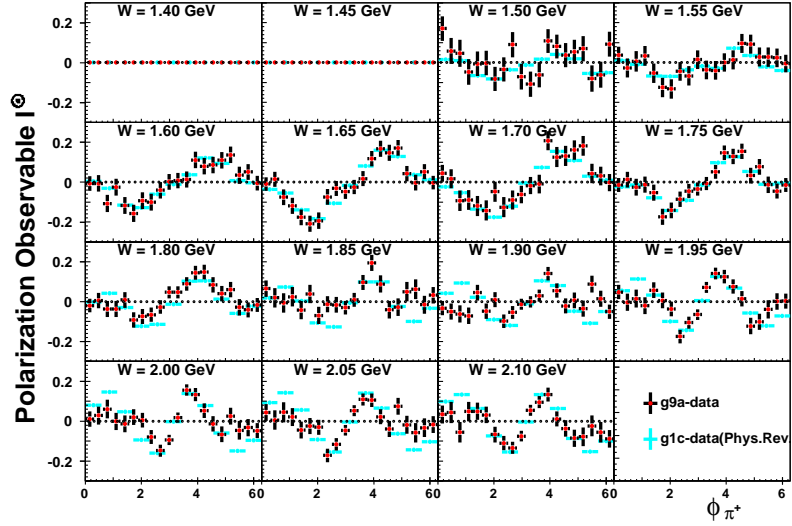


Figure E.6: The beam asymmetries for the topology  $\gamma p \rightarrow p\pi^-(\pi^+)$  and the combination-67. The dataset is for the whole center-of-mass energy range  $W \in [1.375, 2.125]$  GeV and the butanol data.

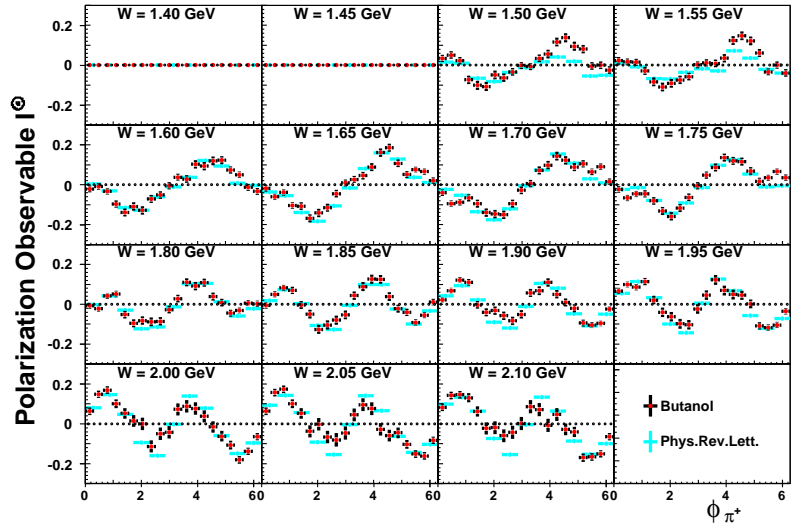


Figure E.7: The beam asymmetries for the topology  $\gamma p \rightarrow p\pi^+(\pi^-)$  and the average combination. The dataset is for the whole center-of-mass energy range  $W \in [1.375, 2.125]$  GeV and the butanol data.

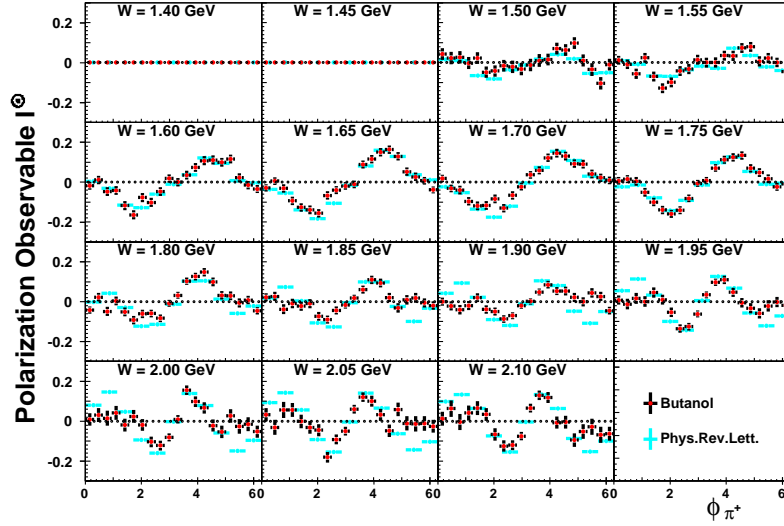


Figure E.8: The beam asymmetries for the topology  $\gamma p \rightarrow p\pi^-(\pi^+)$  and the average combination. The dataset is for the whole center-of-mass energy range  $W \in [1.375, 2.125]$  GeV and the butanol data.

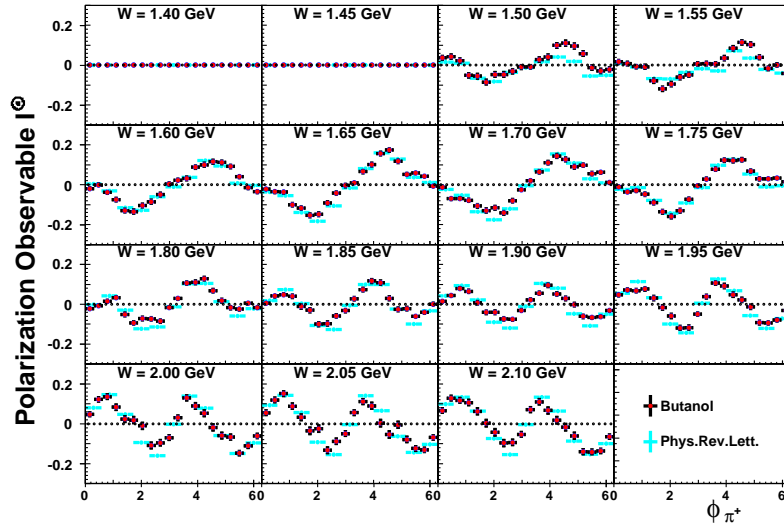


Figure E.9: The beam asymmetries for the average topology and the average combination. The dataset is for the whole center-of-mass energy range  $W \in [1.375, 2.125]$  GeV and the butanol data.

## E.1.2 Average Polarization Observable $I^\ominus$ for the Butanol Data Weighted by Q-factor

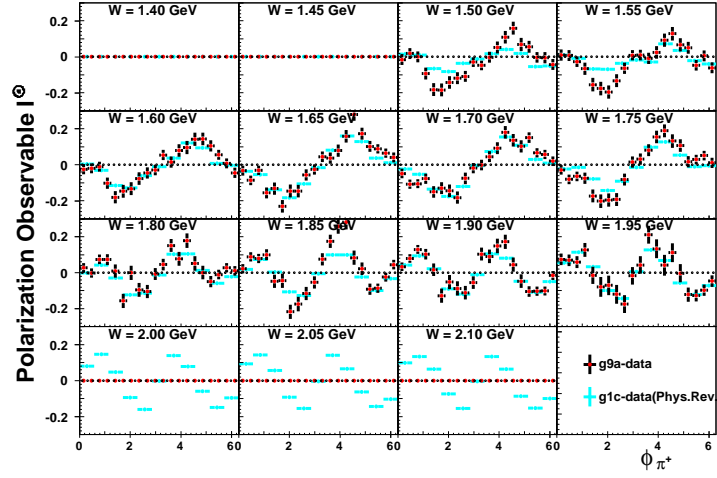


Figure E.10: The beam asymmetries for the topology  $\gamma p \rightarrow p\pi^+(\pi^-)$  and the combination-32. The dataset is for the whole center-of-mass energy range  $W \in [1.375, 2.125]$  GeV and the butanol data weighted by Q-factor.

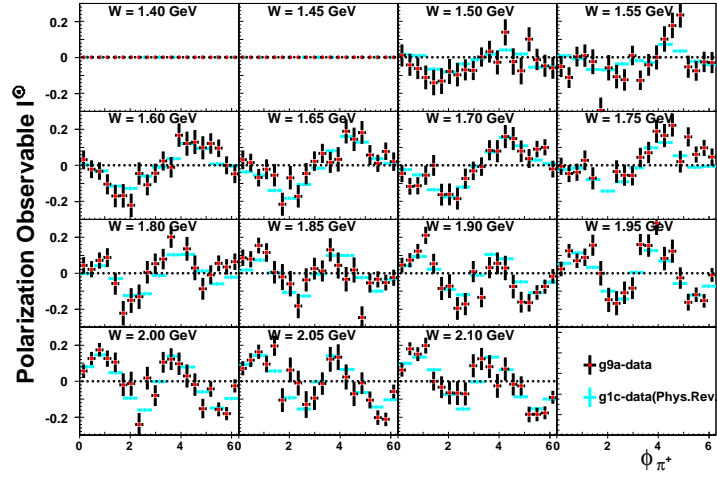


Figure E.11: The beam asymmetries for the topology  $\gamma p \rightarrow p\pi^+(\pi^-)$  and the combination-45. The dataset is for the whole center-of-mass energy range  $W \in [1.375, 2.125]$  GeV and the butanol data weighted by Q-factor.

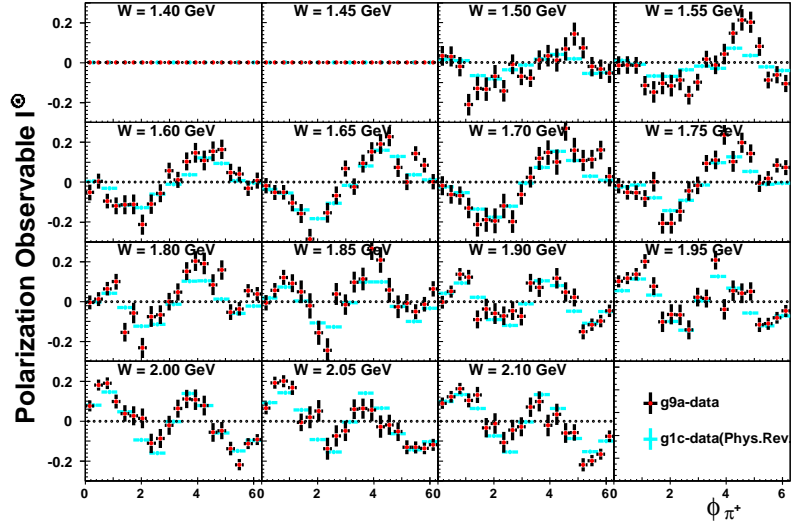


Figure E.12: The beam asymmetries for the topology  $\gamma p \rightarrow p\pi^+(\pi^-)$  and the combination-67. The dataset is for the whole center-of-mass energy range  $W \in [1.375, 2.125]$  GeV and the butanol data weighted by Q-factor.

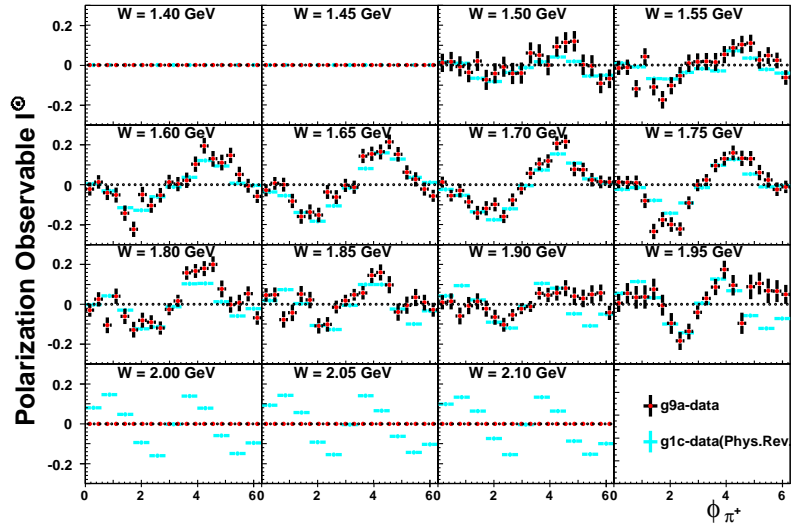


Figure E.13: The beam asymmetries for the topology  $\gamma p \rightarrow p\pi^-(\pi^+)$  and the combination-32. The dataset is for the whole center-of-mass energy range  $W \in [1.375, 2.125]$  GeV and the butanol data weighted by Q-factor.

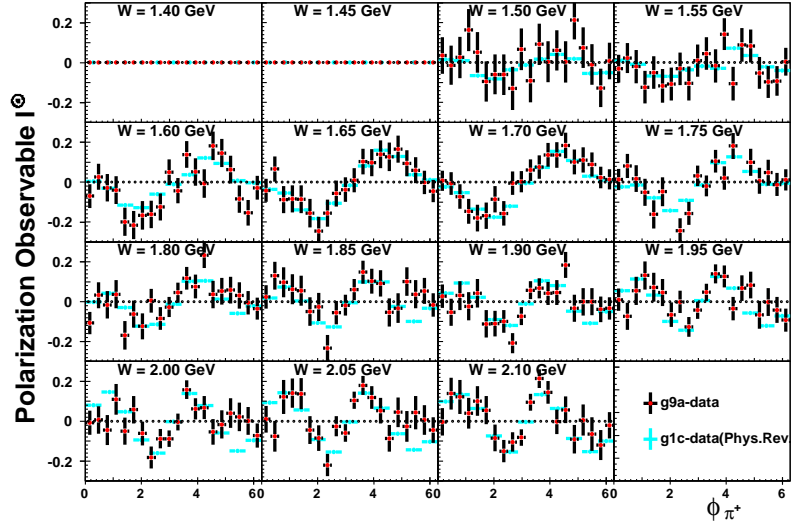


Figure E.14: The beam asymmetries for the topology  $\gamma p \rightarrow p\pi^-(\pi^+)$  and the combination-45. The dataset is for the whole center-of-mass energy range  $W \in [1.375, 2.125]$  GeV and the butanol data weighted by Q-factor.

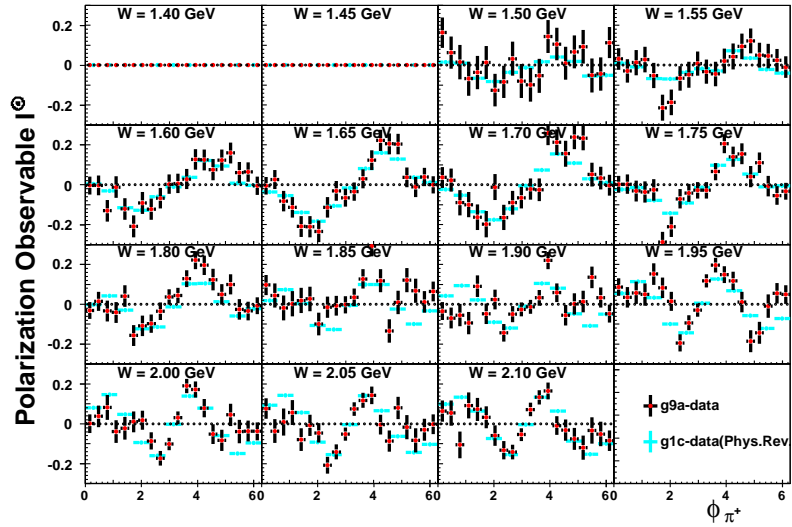


Figure E.15: The beam asymmetries for the topology  $\gamma p \rightarrow p\pi^-(\pi^+)$  and the combination-67. The dataset is for the whole center-of-mass energy range  $W \in [1.375, 2.125]$  GeV and the butanol data weighted by Q-factor.

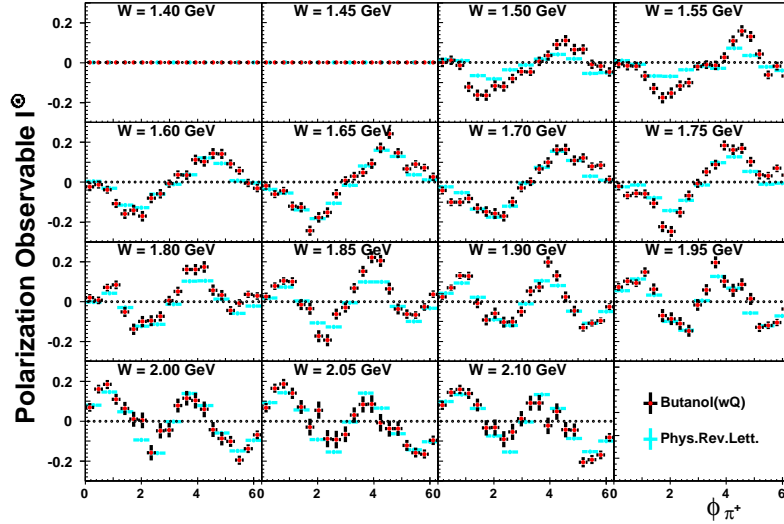


Figure E.16: The beam asymmetries for the topology  $\gamma p \rightarrow p\pi^+(\pi^-)$  and the average combination. The dataset is for the whole center-of-mass energy range  $W \in [1.375, 2.125]$  GeV and the butanol data weighted by Q-factor.

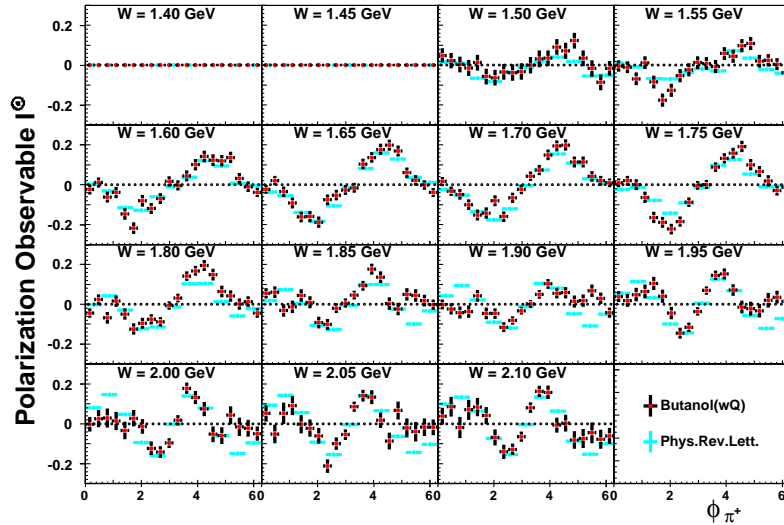


Figure E.17: The beam asymmetries for the topology  $\gamma p \rightarrow p\pi^-(\pi^+)$  and the average combination. The dataset is for the whole center-of-mass energy range  $W \in [1.375, 2.125]$  GeV and the butanol data weighted by Q-factor.

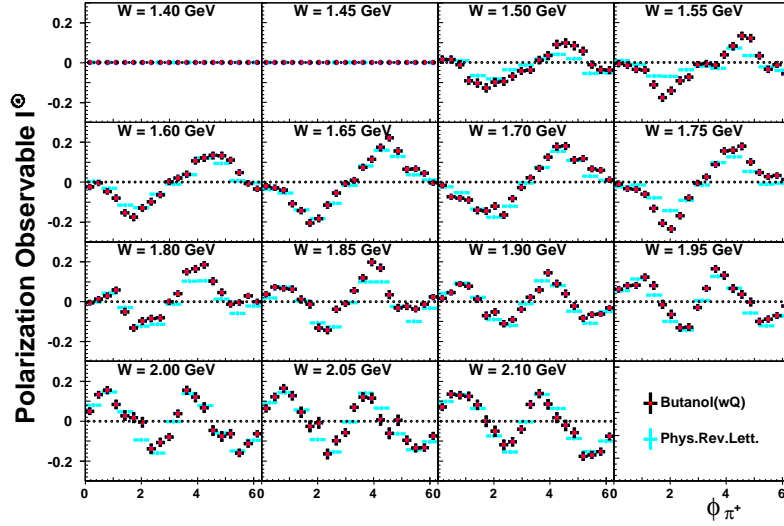


Figure E.18: The beam asymmetries for the average topology and the average combination. The dataset is for the whole center-of-mass energy range  $W \in [1.375, 2.125]$  GeV and the butanol data weighted by Q-factor.

## E.2 Average Polarization Observable $P_z$

### E.2.1 Average Polarization Observable $P_z$ for the Butanol Data Weighted by Q-factor

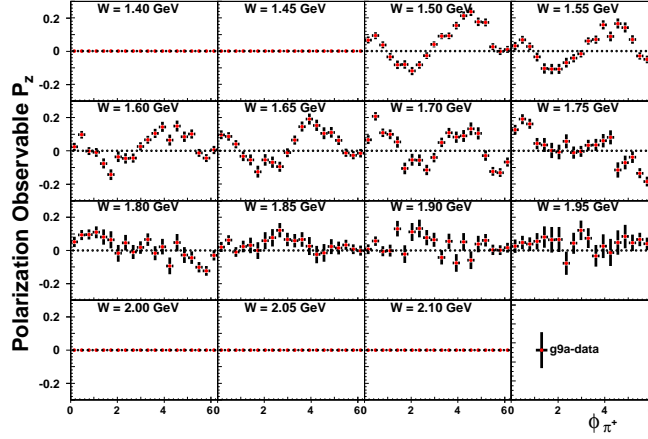


Figure E.19: The target asymmetries for the topology  $\gamma p \rightarrow p\pi^+(\pi^-)$  and the combination-32. The dataset is for the whole center-of-mass energy range  $W \in [1.375, 2.125]$  GeV and the butanol data weighted by Q-factor.

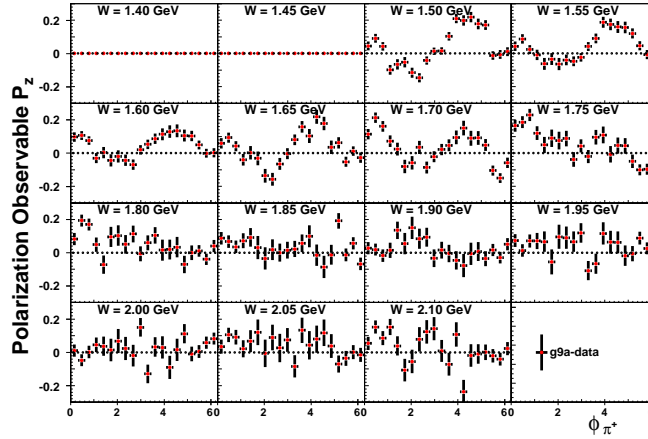


Figure E.20: The target asymmetries for the topology  $\gamma p \rightarrow p\pi^+(\pi^-)$  and the combination-45. The dataset is for the whole center-of-mass energy range  $W \in [1.375, 2.125]$  GeV and the butanol data weighted by Q-factor.

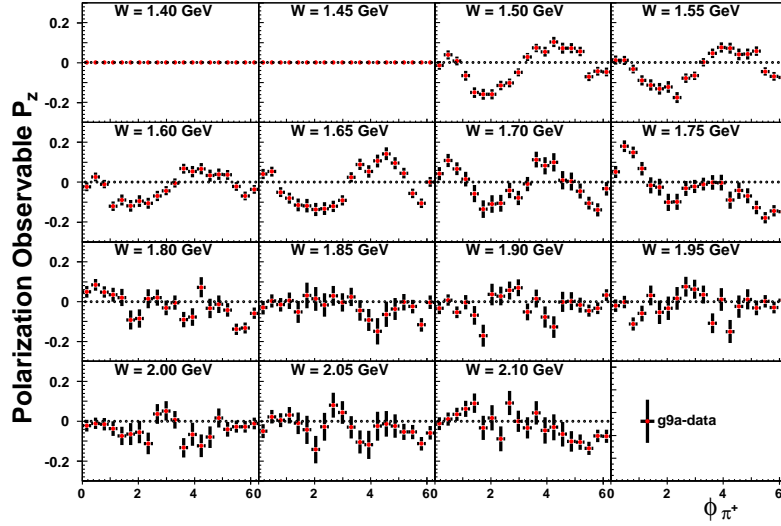


Figure E.21: The target asymmetries for the topology  $\gamma p \rightarrow p\pi^+(\pi^-)$  and the combination-67. The dataset is for the whole center-of-mass energy range  $W \in [1.375, 2.125]$  GeV and the butanol data weighted by Q-factor.

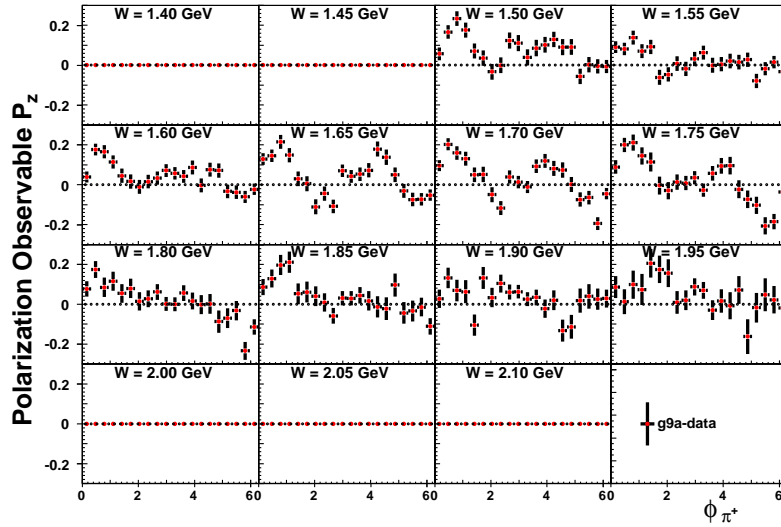


Figure E.22: The target asymmetries for the topology  $\gamma p \rightarrow p\pi^-(\pi^+)$  and the combination-32. The dataset is for the whole center-of-mass energy range  $W \in [1.375, 2.125]$  GeV and the butanol data weighted by Q-factor.

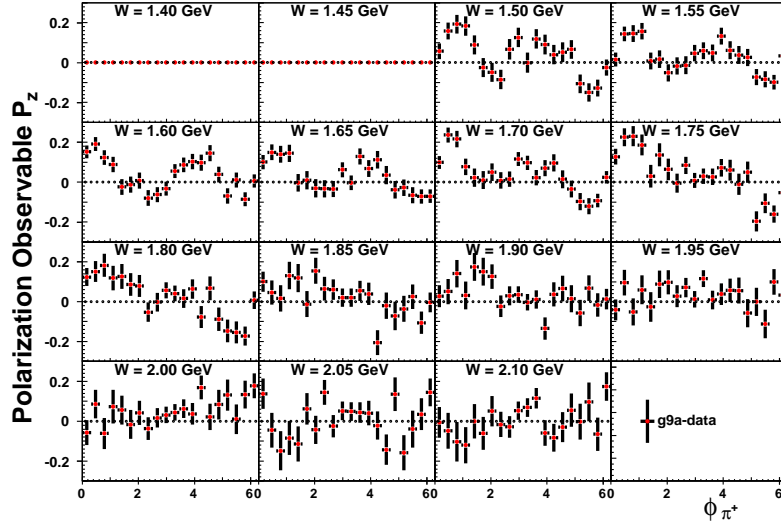


Figure E.23: The target asymmetries for the topology  $\gamma p \rightarrow p\pi^-(\pi^+)$  and the combination-45. The dataset is for the whole center-of-mass energy range  $W \in [1.375, 2.125]$  GeV and the butanol data weighted by Q-factor.

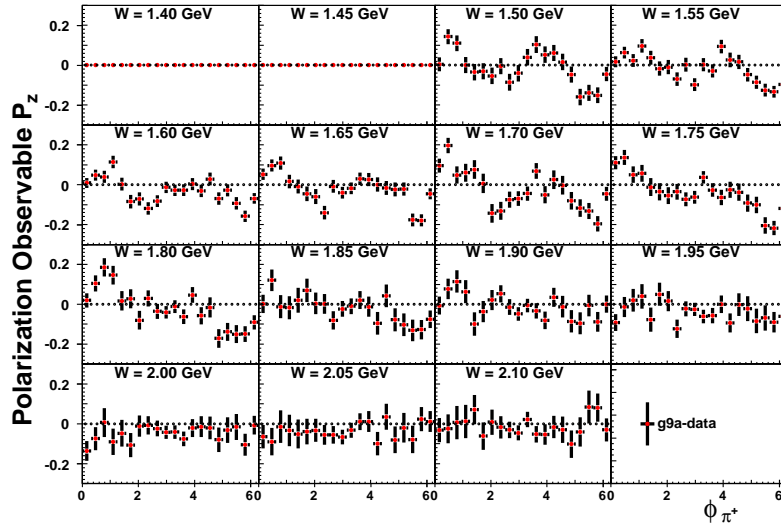


Figure E.24: The target asymmetries for the topology  $\gamma p \rightarrow p\pi^-(\pi^+)$  and the combination-67. The dataset is for the whole center-of-mass energy range  $W \in [1.375, 2.125]$  GeV and the butanol data weighted by Q-factor.

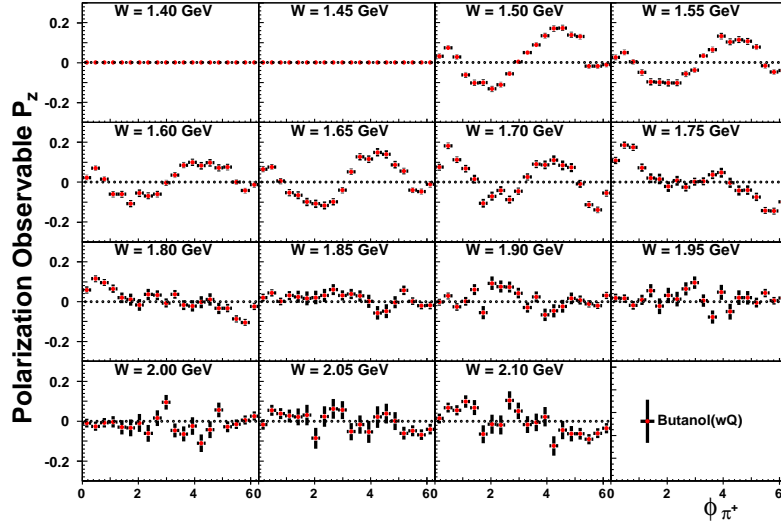


Figure E.25: The target asymmetries for the topology  $\gamma p \rightarrow p\pi^+(\pi^-)$  and the average combination. The dataset is for the whole center-of-mass energy range  $W \in [1.375, 2.125]$  GeV and the butanol data weighted by Q-factor.

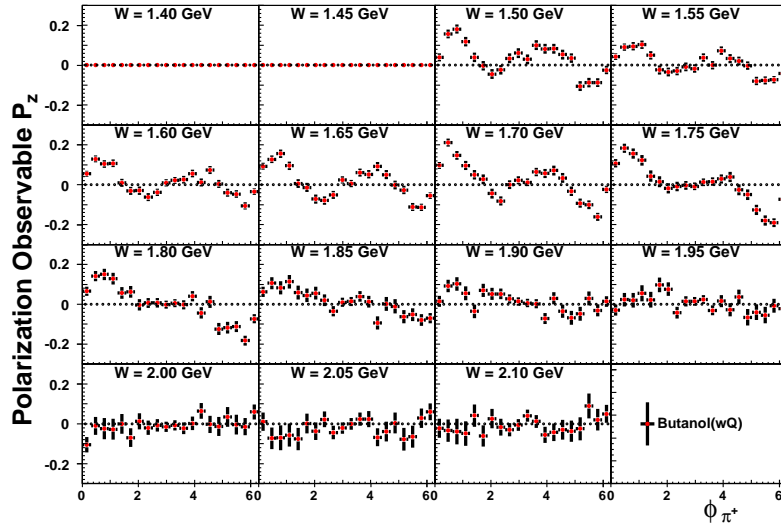


Figure E.26: The target asymmetries for the topology  $\gamma p \rightarrow p\pi^-(\pi^+)$  and the average combination. The dataset is for the whole center-of-mass energy range  $W \in [1.375, 2.125]$  GeV and the butanol data weighted by Q-factor.

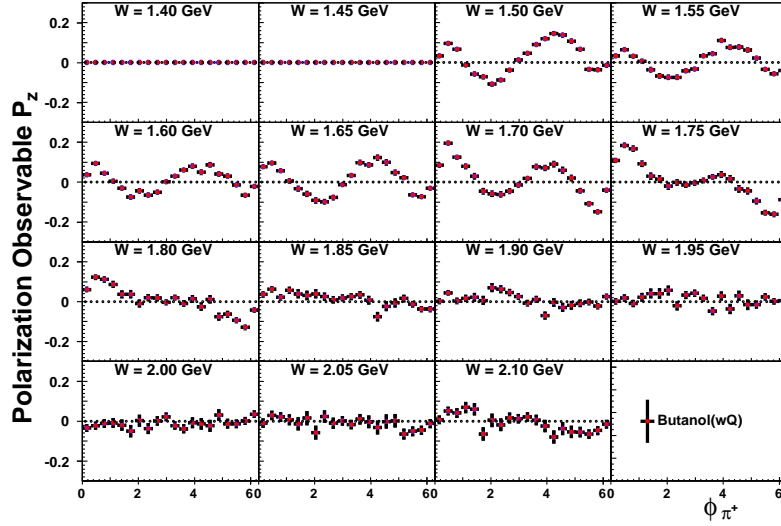


Figure E.27: The target asymmetries for the average topology and the average combination. The dataset is for the whole center-of-mass energy range  $W \in [1.375, 2.125]$  GeV and the butanol data weighted by Q-factor.

## E.3 Average Polarization Observable $P_z^\odot$

### E.3.1 Average Polarization Observable $P_z^\odot$ for the Butanol Data Weighted by Q-factor

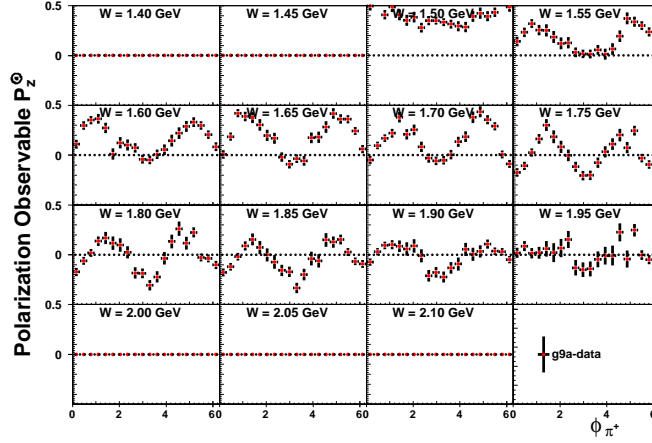


Figure E.28: The helicity differences for the topology  $\gamma p \rightarrow p\pi^+(\pi^-)$  and the combination-32. The dataset is for the whole center-of-mass energy range  $W \in [1.375, 2.125]$  GeV and the butanol data weighted by Q-factor.

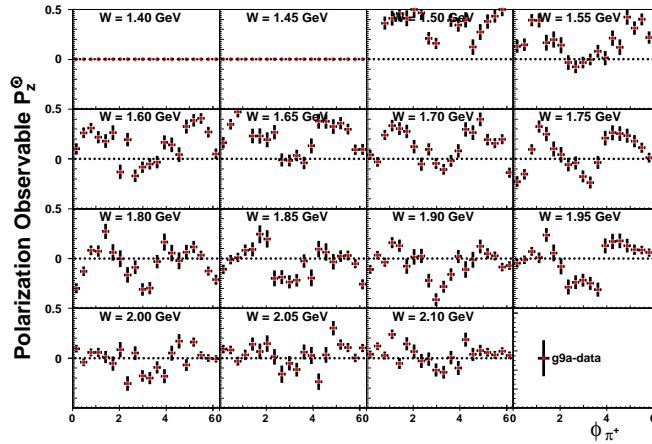


Figure E.29: The helicity differences for the topology  $\gamma p \rightarrow p\pi^+(\pi^-)$  and the combination-45. The dataset is for the whole center-of-mass energy range  $W \in [1.375, 2.125]$  GeV and the butanol data weighted by Q-factor.

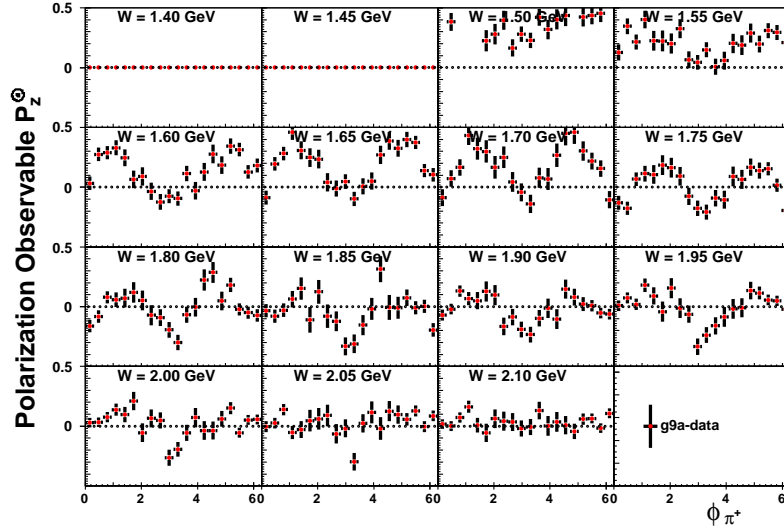


Figure E.30: The helicity differences for the topology  $\gamma p \rightarrow p\pi^+(\pi^-)$  and the combination-67. The dataset is for the whole center-of-mass energy range  $W \in [1.375, 2.125]$  GeV and the butanol data weighted by Q-factor.

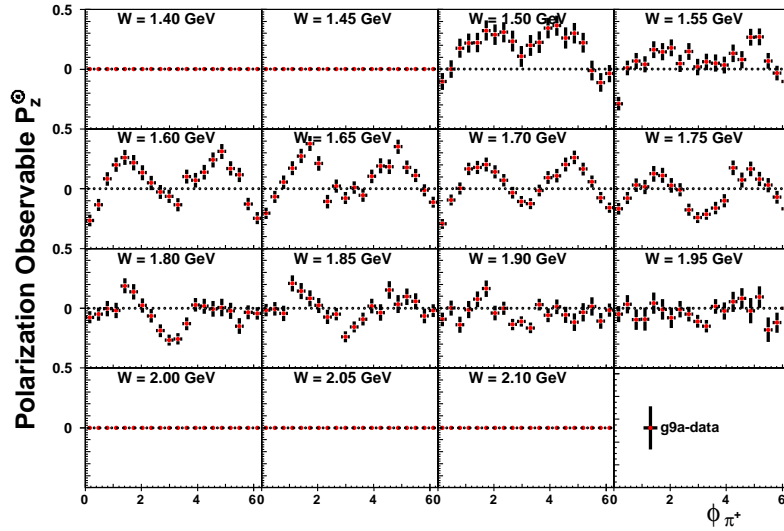


Figure E.31: The helicity differences for the topology  $\gamma p \rightarrow p\pi^-(\pi^+)$  and the combination-32. The dataset is for the whole center-of-mass energy range  $W \in [1.375, 2.125]$  GeV and the butanol data weighted by Q-factor.

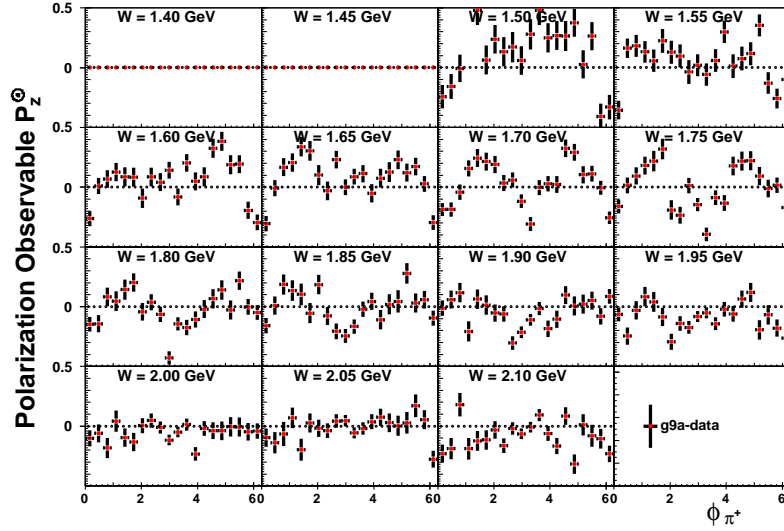


Figure E.32: The helicity differences for the topology  $\gamma p \rightarrow p\pi^-(\pi^+)$  and the combination-45. The dataset is for the whole center-of-mass energy range  $W \in [1.375, 2.125]$  GeV and the butanol data weighted by Q-factor.

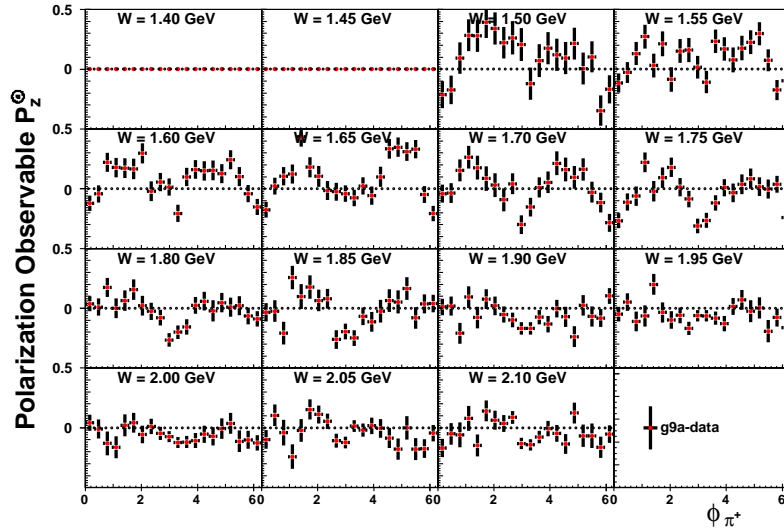


Figure E.33: The helicity differences for the topology  $\gamma p \rightarrow p\pi^-(\pi^+)$  and the combination-67. The dataset is for the whole center-of-mass energy range  $W \in [1.375, 2.125]$  GeV and the butanol data weighted by Q-factor.

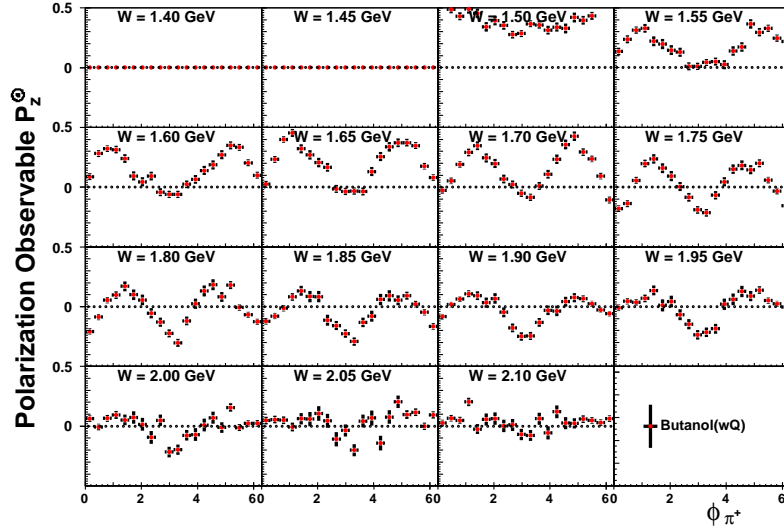


Figure E.34: The helicity differences for the topology  $\gamma p \rightarrow p\pi^+(\pi^-)$  and the average combination. The dataset is for the whole center-of-mass energy range  $W \in [1.375, 2.125]$  GeV and the butanol data weighted by Q-factor.

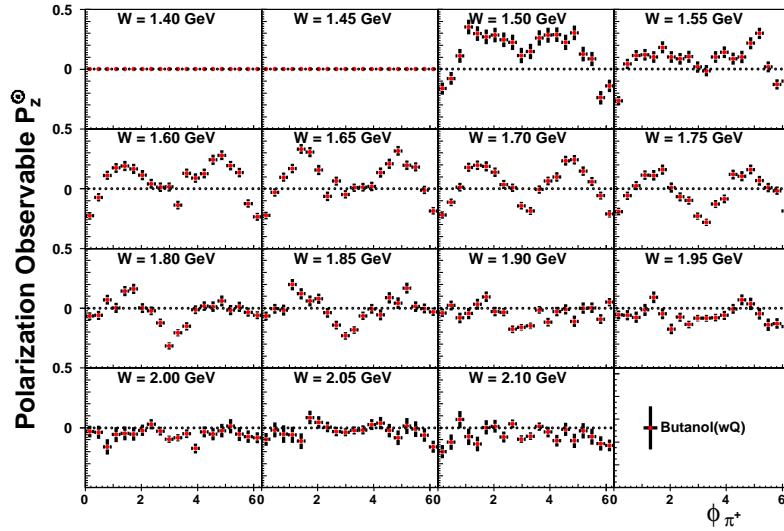


Figure E.35: The helicity differences for the topology  $\gamma p \rightarrow p\pi^-(\pi^+)$  and the average combination. The dataset is for the whole center-of-mass energy range  $W \in [1.375, 2.125]$  GeV and the butanol data weighted by Q-factor.

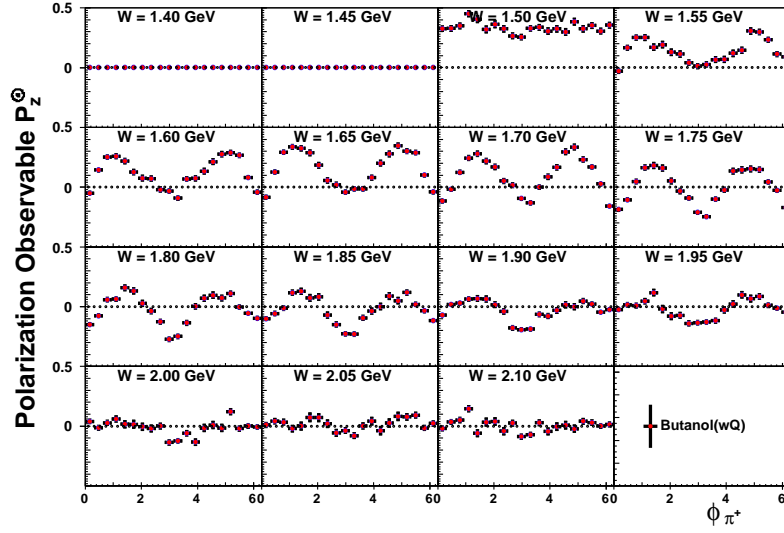


Figure E.36: The helicity differences for the average topology and the average combination. The dataset is for the whole center-of-mass energy range  $W \in [1.375, 2.125]$  GeV and the butanol data weighted by Q-factor.

# BIBLIOGRAPHY

- [1] J. Beringer *et al.*, "Review of particle physics (RPP)", *Phys. Rev.*, D86, p.010001, 2012.
- [2] E. D. Bloom *et al.*, "High-energy inelastic  $e$ - $p$  scattering at  $6^\circ$  and  $10^\circ$ ", *Phys. Rev. Lett.*, vol. 23, pp. 930-934, Oct 1969.
- [3] S. Bethke, "Experimental tests of asymptotic freedom", *Progress in particle and Nuclear Physics*, vol. 58, no. 2, pp. 351 - 386, 2007.
- [4] S. Capstick and N. Isgur, "Baryons in a relativized quark model with chromodynamics", *Phys. Rev. D*, vol. 34, pp. 2809-2835, Nov 1986.
- [5] L.Ya. Glozman and D.O. Riska, "The spectrum of the nucleons and the strange hyperons and chiral dynamics", *Physics Reports*, vol. 268, no. 4, pp. 263-303, 1996.
- [6] U. Loring, K. Kretzschmar, B. Metsch, and H. Petry, "Relativistic quark models of baryons with instantaneous forces", *Eur. Phys. J.*, A10, pp. 309, 2001.
- [7] C. Hanretty, "Measurement of the polarization observables  $I^S$  and  $I^C$  for  $\vec{\gamma}p \rightarrow p\pi^+\pi^-$  using the CLAS spectrometer", *A Dissertation thesis*, Spring Semester, 2011.
- [8] B. Krusche and S. Schadmand, "Study of non-strange baryon resonances with meson photoproduction", *Progress in Particle and Nuclear Physics*, vol. 51, no. 2, pp. 399-485, 2003.
- [9] F. Zehr, "Double pion photoproduction off the proton at threshold and in the second resonance region", *A Dissertation thesis*, February, 2008.
- [10] W. Roberts and T. Oed, "Polarization observables for two-pion production off the nucleon", *Phys. Rev. C*, vol. 71, pp. 055201, 2005.
- [11] S. Strauch *et al.*, "Beam-helicity asymmetries in double-charged-pion photoproduction on the proton", *Phys. Rev. Lett.*, vol. 95, pp. 162003, 2005.
- [12] D. Krambrich *et al.*, "Beam-helicity asymmetries in double-pion photoproduction off the proton", *Phys. Rev. Lett.*, vol. 103, pp. 052002, 2009.

- [13] J. Ahrens, "First measurement of the helicity dependence for the  $\gamma p \rightarrow p\pi^+\pi^-$  reaction", *Eur. Phys. J.*, A34, pp. 11, 2007.
- [14] B. A. Mecking *et al.*, "The CEBAF large acceptance spectrometer (CLAS)", *Nucl. Instrum. Meth.*, A503, pp. 513 - 553, 2006.
- [15] D. I. Sober *et al.*, "The bremsstrahlung tagged photon beam in Hall B at JLab", *Nucl. Instrum. Meth.*, A440, pp. 263 - 284, 2000.
- [16] C. D. Keith, "The JLab frozen spin target", *SPIN PHYSICS : 18th International Spin Physics Symposium, AIP Conference Proceedings*, vol. 1149, pp. 886-889, 2009.
- [17] M. Crofford, C. Hovater, G. Lahti, C. Piller, and M. Poelker, "The RF System for the CEBAF polarized photoinjector", *Jefferson Lab. Technical Report*, 2993.
- [18] C. D. Keith, *et al.*, "A polarized target for the CLAS detector", *Nucl. Instrum. Meth.*, A501, pp. 327 - 339, 2003.
- [19] C. D. Keith, "Freezing the spin of the proton", *JLab Seminar*, 2004
- [20] C. D. Keith, "Polarized solid targets: recent progress and future prospects", *Polarized Sources, Targets and Polarimetry :Proceedings of the 13th International Workshop*, pp. 113-122, 2011.
- [21] Ch. Bradtke, *Ph. D. Thesis*, BONN-IR-99-nn, 1999.
- [22] L. Todor, "G1c data calibration and cooking procedures, characteristics, information" CLAS Note 2002-017, 2002.
- [23] D. Cords, "CLAS event format with BOS" CLAS Note 1994-012, 1994.
- [24] D. Lawrence and M. Mestayer, "CLAS drift chamber calibration: software and procedures" CLAS Note 1999-018, 1999.
- [25] E. Pasyuk, "Brief user guide to GPID" CLAS Note 2007-008, 2007.
- [26] M. Williams and C. A. Meyer, "Kinematic fitting in CLAS" CLAS Note 2003-017, 2003.
- [27] E. Pasyuk, "Energy loss corrections for charged particles in CLAS" CLAS Note 2007-016, 2007.
- [28] S. Stepanyan *et al.*, "Energy calibration of the JLab bremsstrahlung tagging system", *Nucl. Instrum. Meth.*, A572, pp. 654 - 661, 2007.
- [29] M. Dugger and C. Hanretty, "Correction to the incident photon energy for g8b data", CLAS Note 2009-030, 2009.

- [30] M. Dugger, "Check of tagger photon energy for g9a (version 2)", FROST Group Meeting, July 27th, 2010.
- [31] H. Olsen and L. C. Maximon, "Photon and electron polarization in high-energy bremsstrahlung and pair production with screening", *Phys. Rev.*, vol. 114, pp. 887-904, 1959.
- [32] E. Pasyuk, "The hydrogen contamination of the carbon data in g9a experiment", FROST Group Meeting, March 13th, 2013.
- [33] M. Dugger, B. G. Ritchie, "DRAFT of CLAS-notw: Phase space dependent scale factors fro FROST g9a data".
- [34] M. Williams, M. Belis, and C. A. Meyer, "Separating signals from non-interfering backgrounds using probabilistic event weightings", arXiv:0804.3382.
- [35] W. Verkerke, D. Kirkby, "Roofit users manual v2.91", Document vesion 2.91-33, October 14th, 2008.
- [36] K. Livingston, "Binned fitting techniques for measuring photon beam asymmetry" CLAS Note 2012-010, 2012.
- [37] A. Fix and H. Arenhovel, "Double pion photoproduction on nucleon and deuteron", *Eur. Phys. J*, A25, pp. 115, 2005.

# BIOGRAPHICAL SKETCH

Sungkyun Park was born in Pusan, South Korea on November 30th, 1976 to Youngsik Park and Yangsoon Kang. He has enrolled at the Korea University, Seoul, South Korea in March 1996, where he received a Bachelor of Science in February 2003. That spring he entered Elementary Particle Physics Laboratory at Korea University and began work with his advisor, Dr. JooSang Kang, and received his Master of Science in February 2005. He was accepted in the doctoral program of the physics department at Florida State University in Fall 2006. In the Summer of 2007 he joined the Experimental Hadronic Physics Group at Florida State University and began work with his advisor, Dr. Volker Credé. He received a Master of Science degree in spring 2012 from Florida State University. This dissertation was defended on July 1, 2013 at Florida State University.